Discovery of bioactive lipids and lipid pathways in cell death and disease

Discovery of bioactive lipids and lipid pathways in cell death and disease

A dissertation presented

by

Tejia Zhang

to

The Department of Chemistry and Chemical Biology

In partial fulfillment of the requirements

for the degree of

Doctor of Philosophy

in the subject of

Chemistry

Harvard University

Cambridge, Massachusetts

April 2014

Dissertation Advisor: Professor Alan Saghatelian Tejia Zhang

Discover of bioactive lipids and lipid pathways in cell death and disease

Abstract

Apoptosis is an intricately regulated cellular process required for the health and homeostasis of living systems [1]. The mitochondrial apoptotic pathway depends on the BCL-2 family of pro- and anti-apoptotic members whose interactions regulate cell fate [1]. BAX and BAK are key pro-apoptotic proteins required for mitochondrial permeabilization during apoptosis [1]. While the mitochondrial death program relies heavily on its protein components, evidences support equally crucial roles for lipids and lipid metabolism in promoting or hindering apoptosis at the mitochondria [2-4]. To gain insight into the interplay between lipids and BCL-2 proteins we used a liquid chromatography (LC)–mass spectrometry (MS)-based comparative lipidomics approach to uncover lipid changes in the absence of BAX and/or BAK. Our analysis revealed novel functions for BAX and BAK in inflammation and ceramide metabolism.

In response to inflammatory stimuli, prostaglandins are synthesized from arachidonic acid by cyclooxygenase (COX), the target of non-steroidal anti-inflammatory drugs [5, 6]; different prostaglandins exhibit a wide range of functions including vasodilation, fever generation and bone reabsorption [6]. Absence of BAX and/or BAK led to prostaglandin down-regulation, arachidonic acid accumulation, and reduced expression of the inducible cyclooxygenase isoform COX-2. *Bax*$^{-/-}$ fibroblasts displayed blunted COX-2 response to the inflammatory agent bacterial lipopolysaccharide through altered kinetics of NFκB and MAPK

signaling. To our knowledge this is the first report of a role for BAX and BAK in COX-2 regulation.

Absence of BAX and BAK also led to selective upregulation of unsaturated ceramides with additional degree of unsaturation in the sphingoid backbone; unsaturated ceramides were significantly more potent in reducing cellular viability than saturated species. Up until now, almost all studies on the pro-apoptotic functions of ceramides have focused on saturated species [7-10]; our discovery of a different ceramide pool regulated by BAX and BAK implies the synergistic effects between BAX and ceramides in apoptosis could be more complex than previously known.

A targeted LC–MS workflow was also developed for characterization of a novel lipid class involved in type 2 diabetes. Targeted LC–MS revealed altered oxysterol metabolism following perturbation of the Sonic hedgehog pathway. Taken together, our findings demonstrate interesting connections among lipids, cell death and disease.

References

[1] L.D. Walensky, BCL-2 in the crosshairs: tipping the balance of life and death, Cell Death Differ, 13 (2006) 1339-1350.

[2] V.E. Kagan, V.A. Tyurin, J. Jiang, Y.Y. Tyurina, V.B. Ritov, A.A. Amoscato, A.N. Osipov, N.A. Belikova, A.A. Kapralov, V. Kini, I.I. Vlasova, Q. Zhao, M. Zou, P. Di, D.A. Svistunenko, I.V. Kurnikov, G.G. Borisenko, Cytochrome c acts as a cardiolipin oxygenase required for release of proapoptotic factors, Nat Chem Biol, 1 (2005) 223-232.

[3] M. Crimi, M.D. Esposti, Apoptosis-induced changes in mitochondrial lipids, Biochimica et Biophysica Acta (BBA) - Molecular Cell Research, 1813 (2011) 551-557.

[4] Jerry E. Chipuk, Gavin P. McStay, A. Bharti, T. Kuwana, Christopher J. Clarke, Leah J. Siskind, Lina M. Obeid, Douglas R. Green, Sphingolipid Metabolism Cooperates with BAK and BAX to Promote the Mitochondrial Pathway of Apoptosis, Cell, 148 (2012) 988-1000.

[5] D.L. Simmons, D. Wagner, K. Westover, Nonsteroidal Anti-Inflammatory Drugs, Acetaminophen, Cyclooxygenase 2, and Fever, Clinical Infectious Diseases, 31 (2000) S211-S218.

[6] C.D. Funk, Prostaglandins and Leukotrienes: Advances in Eicosanoid Biology, Science, 294 (2001) 1871-1875.

[7] L.J. Siskind, M. Colombini, The Lipids C2- and C16-Ceramide Form Large Stable Channels: Implications for Apoptosis, Journal of Biological Chemistry, 275 (2000) 38640-38644.

[8] L.J. Siskind, T.D. Mullen, K. Romero Rosales, C.J. Clarke, M.J. Hernandez-Corbacho, A.L. Edinger, L.M. Obeid, The BCL-2 Protein BAK Is Required for Long-chain Ceramide Generation during Apoptosis, Journal of Biological Chemistry, 285 (2010) 11818-11826.

[9] J. Stiban, D. Fistere, M. Colombini, Dihydroceramide hinders ceramide channel formation: Implications on apoptosis, Apoptosis, 11 (2006) 773-780.

[10] H. Lee, J.A. Rotolo, J. Mesicek, T. Penate-Medina, A. Rimner, W.-C. Liao, X. Yin, G. Ragupathi, D. Ehleiter, E. Gulbins, D. Zhai, J.C. Reed, A. Haimovitz-Friedman, Z. Fuks, R. Kolesnick, Mitochondrial Ceramide-Rich Macrodomains Functionalize Bax upon Irradiation, PLoS ONE, 6 (2011) e19783.

Acknowledgement

First, I would like to acknowledge Prof. Alan Saghatelian. His scientific expertise and kind support have made every day of my Ph.D. an incredibly fruitful and fun experience. I have become a better scientist because of Alan's guidance, and what I have learned in the past six years will always stay with me as I continue to tackle the challenges of learning from the wonderfully complex biological systems that I have been introduced to in Alan's lab. I feel truly honored to have been given this opportunity and I could not have asked for a better Ph.D. experience.

I would like to thank members of my Dissertation Advisory Committee, Prof. David Liu and Prof. Daniel Kahne, for taking time out of their busy schedules to meet with me and for their helpful discussions. The metabolism of apoptosis project is a collaboration with the lab of Prof. Loren Walensky, and I greatly appreciate his ideas and insights that have yielded fruitful directions to take my project. I would also like to thank Prof. Barbara Kahn, for kindly taking the time to meet with me to discuss my career plans; her keen insights on type 2 diabetes in the FAHFA project have given me new perspectives on the study of metabolic syndrome.

It is incredibly exciting and deeply humbling to have worked with a group of very intelligent and fun colleagues. I owe a great deal of thanks to Dr. Nawaporn "Yui" Vinayavekhin, Dr. Edwin Homan, Dr. Anna Mari Lone, Dr. Whitney Nolte, Dr. Ranitendranath "Ranit" Tagore, Dr. Debarati "Debs" Mazumder, Dr. James Cardia, Jiao Ma, Amanda McFedries, Dr. Sarah Slavoff, Dr. Adam Schwaid, Prof. Arthur Tinoco, Prof. Yun-Gon Kim, Dr. Andrew Mitchell, Dr. Cammi Valdez and Mathias Leidl for their tremendous, indispensable help with different aspects of my projects and on general techniques; discussions scientific and

miscellaneous; Friday night dinners, weekend dim sum runs and spontaneous quests for food around the Square; the music, potlucks and graduation hats; and the challenges that we helped each other through. There is a lot that I could say, but I could summarize it all to the fact that I wish to thank them for their friendship, for showing me how to be a stronger person who is not blind-sighted by success and who faces failure with grace and maturity. I have no doubt that they will become wonderful teachers, scientists or have very fulfilling careers in whichever paths they choose to take.

I would also like to thank Lauren Barclay, Joseph Bellairs, Marina Godes, Maguerite "Meg" Davis and Denis Reyna from the Walensky lab for taking their own research time to help me on the apoptosis project; members of the Kahn lab, especially Dr. Ismail Syed, Dr. Mark Yore, Dr. Pedro Moraes-Vieira and Dr. Odile Peroni, for insightful discussions on the FAHFA project and inflammation; Carl Ward, who worked with Jiao and contributed a great deal to the RNA-Seq data; Dr. Sherry Zhang and Dr. Yu Wang from the McMahon lab, and Clare Whitehead for their help on the oxysterol project; Dr. Bogdan Budnick and Dr. Sunia Trauger for their assistance with proteomics and lipidomics; Dr. Arthur Liberzon for help with GSEA; Dr. John Guilinger from the Liu lab for advice on CRISPR; Dr. Amélie Dion and Dr. Ge Zou from the Myers lab for advice on synthesis; and Dr. Alex Speed from the Evans lab for synthesis advice and always joining us on Friday night dinners. Members of the Liu lab have been very friendly and helpful in allowing us to use their instruments. Susan Kinsella's kindness, dedication and hard work made everything in lab run very smoothly. Our daily operations are possible thanks to Gina Tyros and Ian McKenna from Agilent, Chris Perry from shipping, Jerry Connors and Mike Paterno from facilities, John Randazzo at the mail room, Joe and Stanley at the Biological Stockroom, and Theresa Guzman-Peña and Maria from the custodial staff.

I owe special thanks to my friends Sharon Zhang and Ying Niu, whom I met in my freshman year at MIT. Despite our busy schedules they have kept in touch with me even when I was not good in return. Sharon, who was close by, always connected with me when I needed to relax the most. It takes a very caring heart to do what they have done, and I am so glad to have their friendship.

I will always be grateful to the many mentors in my life who helped with my initial transition to the United States and who inspired me to be a scientist.

Most importantly, I would not be here today without the hard work and sacrifices from my parents and grandparents. I am forever indebted to them for everything they did and have continued to do for me. I hope I have made them proud.

Table of Contents

List of Figures

List of Tables

Abbreviations

AA	arachidonic acid
ACD	actinomycin D
ACN	acetonitrile
AG4OX	adipose-specific GLUT4 overexpressor
ATP	adenosine triphosphate
BAD	BCL-2-associated agonist of cell death
BAT	brown adipose tissue
BAX	BCL-2-associated X protein
BAK	BCL-2 homologous antagonist killer
BCL-2	B cell lymphoma-2
BCL-xL	B cell lymphoma-extra large
cer	ceramide
cerS	dihydroceramide synthase
CE	collision energy
CID	collision-induced dissociation
CL	cardiolipin
CoA	coenzyme A
COX	cyclooxygenase
co-IP	co-immunoprecipitation
CPT1	carnitine palmitoyltransferase 1
CPT2	carnitine palmitoyltransferase 2

cyt c	cytochrome c
DAG	diacylglycerol
DCM	dichloromethane
DHA	docosahexaenoic acid
DKO	double knockout
DP	declustering potential
EIC	extracted ion chromatograph
ER	endoplasmic reticulum
ESI	electrospray
FA	fatty acid
FAAH	fatty acid amide hydrolase
FAHFA	fatty acid hydroxyl fatty acid
FBS	fetal bovine serum
FFA	free fatty acid
GNM	gastrocnemius muscle
GPCR	G-protein coupled receptor
GSEA	gene set enrichment analysis
GST	glutathione S transferase
HAA	hydroxyarachidonic acid
HCD	high-energy collisional dissociation
HDHA	hydroxydocosahexaenoic acid
HFA	hydroxy fatty acid
HFD	high fat diet

H/R	hypoxia/reoxygenation
HOA	hydroxyoleic acid
HPA	hydroxypalmitic acid
HPO	hydroxypalmitoleic acid
HSA	hydroxystearic acid
iBMK	immortalized baby mouse kidney (epithelial cells)
IDMS	isotope-dilution mass spectrometry
IRF	interferon recognition factor
KO	knockout
LC–MS	liquid chromatography–mass spectrometry
LPL	lipoprotein lipase
LPS	lipopolysaccharide
MAG	monoacylglycerol
MAM	mitochondria-associated membrane
MEF	mouse embryonic fibroblast
MOMP	mitochondrial outer membrane permeabilization
MRM	multiple reaction monitoring
m/z	mass/charge
NEFA	non-esterified fatty acid
NOD1	nucleotide-binding and oligomerization domain 1
NOD2	nucleotide-binding and oligomerization domain 2
NPD	Niemann-Pick Disease
OA	oleic acid

OHC	hydroxycholesterol
OMM	outer mitochondrial membrane
PA	phosphatidic acid (chapter 2)
PA	palmitic acid (chapter 4)
PAHSA	palmitic acid hydroxy stearic acid
PC	phosphatidylcholine
PCR	polymerase chain reaction
PE	phosphatidylethanolamine
PG	prostaglandin
PGHS	prostaglandin synthase
PG WAT	perigonadal white adipose tissue
PM	plasma membrane
PMA	phosphomolybdic acid
PO	palmitoleic acid
PPARα	nuclear hormone receptor peroxisome proliferator α
PPARγ	nuclear hormone receptor peroxisome proliferator γ
PRR	pattern recognition receptor
PS	phosphatidylserine
Ptc1	Patched1
Pyr	pyridine
RNA	ribonucleic acid
rt	room temperature
RT-PCR	real time-polymerase chain reaction

SA	stearic acid
sat	saturated
S1P	sphingosine-1-phosphate
SEM	standard error of the mean
Shh	Sonic hedgehog
SKO	single knockout
SM	sphingomyelin
SMase	sphingomyelinase
Smo	Smoothened
SPE	solid phase extraction
sph	sphingosine
SPK	sphingosine kinase
SPT	serine palmitoyltransferase
SQ WAT	subcutaneous white adipose tissue
SuFu	Suppressor of Fused
T2D	type 2 diabetes
TAG	triacylglycerol
TG	triglyceride
THF	tetrahydrofuran
TIC	total ion chromatograph
TLC	thin-layer chromatography
TLR	toll-like receptor
TMT	tandem affinity tag

TOF	time of flight
Q-TOF	quadrupole-time of flight
unsat	unsaturated
WAT	white adipose tissue
WT	wild type

Chapter 1

Emerging roles of lipids in apoptosis and metabolism

Adapted from:

T. Zhang, A. Saghatelian, Emerging roles of lipids in BCL-2 family-regulated apoptosis.

Biochim. Biophys. Acta. 1831 (2013) 1542-1554.

1.1. Apoptosis and lipid metabolism

Apoptosis is an intricately regulated process required for the health and homeostasis of living systems [1]. Apoptosis in mammalian cells proceeds through extrinsic and intrinsic pathways [2]. The extrinsic pathway involves binding of extracellular signaling factors to death receptors at the plasma membrane [2]. The intrinsic pathway is activated by intracellular stress and proceeds through the mitochondria [2]. The mitochondrial apoptotic pathway is regulated by the BCL-2 family whose members are classified based on structure and function (Figure 1.1);

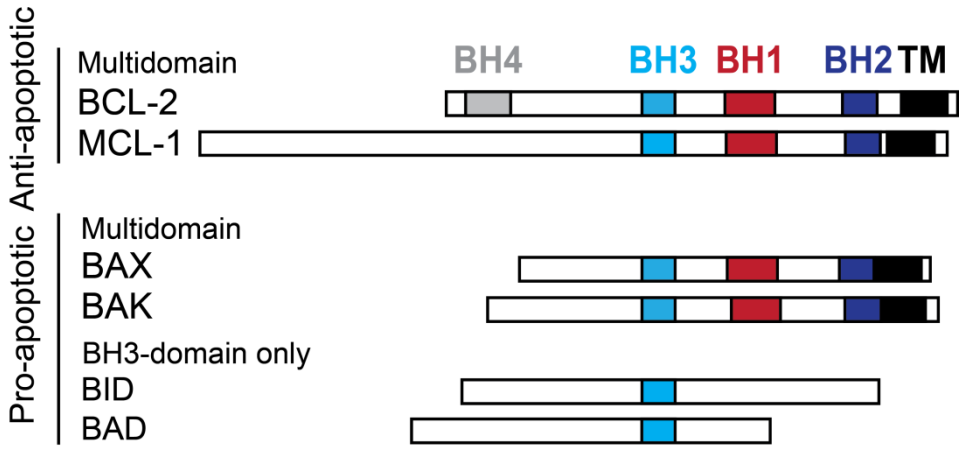

Figure 1.1. Selected members of the BCL-2 family. BCL-2 proteins are classified based on structure (multidomain or BH3 domain-only) and function (pro- or anti-apoptotic).

anti-apoptotic proteins such as BCL-2 and BCL-X_L share three to four conserved BCL-2 homology domains (BH1-4) while pro-apoptotic proteins such as BAX and BAK share three such domains [1]. A third group of pro-apoptotic BH3 domain-only proteins acts as stress sensors that communicate the apoptotic signal to multidomain proteins; BH3 domain-only messengers are organized into activators or derepressors based on their ability to either activate multidomain pro-apoptotic or deactivate multidomain anti-apoptotic BCL-2 members [1, 3].

In the mitochondrial apoptotic pathway, a diverse set of signals recruits distinct BH3 domain-only proteins to trigger activation of the executioner proteins BAX and BAK [1, 3]. BAX and BAK oligomerization in the outer mitochondrial membrane (OMM) leads to mitochondrial outer membrane permeabilization (MOMP) and release of cytochrome c (cyt c) along with other apoptogenic factors, a crucial step in apoptosis [1, 4, 5]. While the mitochondrial apoptotic program heavily relies on its protein components, mounting evidence pinpoints the membrane as an equally important factor in the successful propagation of the death response [6-8].

The lipid environment of the mitochondrial membrane is critical for BCL-2 protein translocation prior to MOMP, and perturbation in mitochondrial lipid composition can lead to phenotypes associated with dysregulated cell death [9-11]. The mitochondrial lipid cardiolipin (CL) plays an important role in the maintenance of mitochondrial bioenergetics [12], and sphingolipid metabolism has been shown to cooperate with BAX and BAK pore formation in the mitochondrial membrane [13]. These findings suggest that far beyond their role as inert structural elements, lipids and their metabolism can exert key points of control over the BCL-2 family-regulated apoptotic program. A review of recent literature on the link between BCL-2 proteins and metabolism, in particular the role of the sphingolipid metabolic hub ceramide in BCL-2 family-regulated apoptosis, will be presented in the following sections.

1.1.1. Ceramide in BCL-2 family-regulated apoptosis

1.1.1.1. Biosynthesis and the sphingolipid rheostat

The major pathways of ceramide generation are *de novo* biosynthesis, sphingomyelin (SM) hydrolysis and sphingosine salvage [14-17] (Figure 1.2). *De novo* biosynthesis begins with

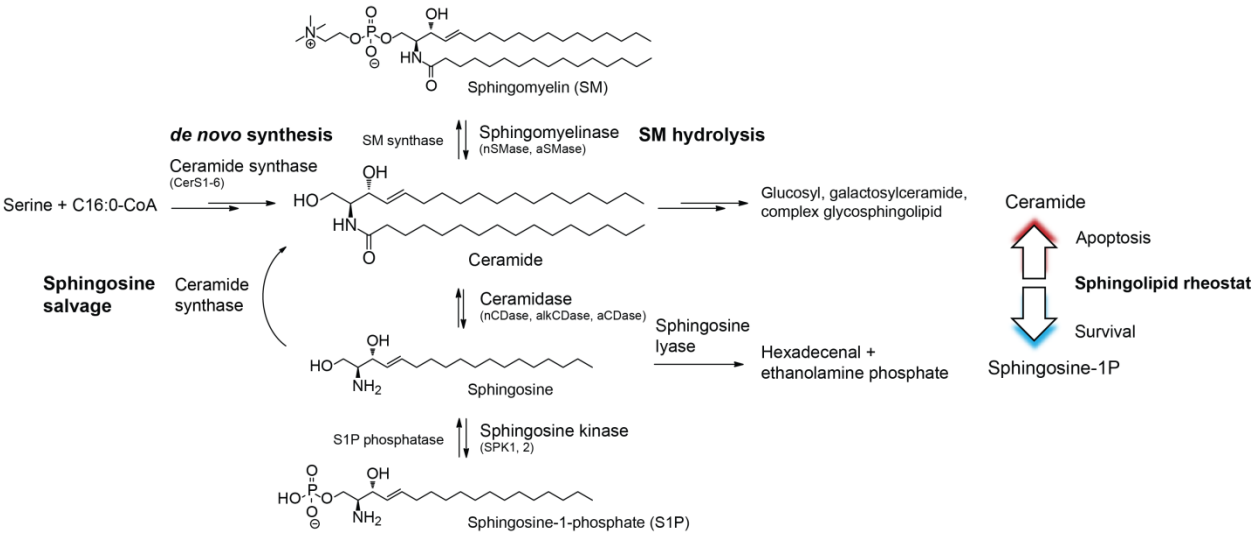

Figure 1.2. Ceramide is the hub of sphingolipid metabolism.

coupling of fatty acyl-CoA to serine *via* the pyridoxal 5-phosphate-dependent serine palmitoyltransferase (SPT) to generate 3-ketosphinganine, CoA and CO_2; palmitoyl (C16:0)-CoA is the predominant SPT substrate in mammalian cells and yeast [15, 18]. 3-Ketosphinganine is reduced to dihydrosphinganine by the NADPH-dependent 3-ketosphinganine reductase and subsequently acylated at the amine by the CoA-dependent dihydroceramide synthase (CerS) [14, 15, 18]. Dihydroceramide is reduced by dihydroceramide desaturase to yield mature ceramide, which contains a *trans* double bond at C4-C5 of the sphingosine chain [14, 15, 18, 19] (Figure 1.2). Six mammalian CerSs (CerS1-6) have been identified, each exhibiting specifity for distinct fatty acyl chains [14, 18].

SM hydrolysis by sphingomyelinases (SMases) also yields ceramide (Figure 1.2); a variety of neutral (n) and acid (a) SMases, each with its own pH optimum, operates in distinct cellular compartments [10, 20, 21]. Neutral, acid and alkaline ceramidases with different cellular localizations degrade ceramide to sphingosine [10], which can be reacylated to new ceramide *via* the salvage pathway [14], phosphorylated by sphingosine kinase (SPK) to sphingosine-1-

phosphate (S1P) [22] or irreversibly degraded by sphingosine lyase to ethanolamine phosphate and hexadecenal [23] (Figure 1.2). Ceramidases also possess reverse activity and can reform ceramide *via* a CoA-independent mechanism [24-26] (Figure 1.2).

Ceramide is the hub of sphingolipid metabolism. The diversity of cellular fatty acids translates into ceramide species with acyl chains of varying lengths and degrees of unsaturation, which are further reflected in the diversity of ceramide metabolites. More than 200 ceramides with distinct structural modifications are known and subject to metabolism by more than 28 enzymes [27, 28]. As a result of this diversity, different ceramide metabolites or even ceramides with different acyl chain lengths can exert opposing influences over key cellular processes such as apoptosis [27-30]. The sphingolipid rheostat model states that the balance among different sphingolipids, in particular the predominantly pro-apoptotic ceramide and the pro-survival S1P, regulates the balance between cell death and proliferation [11, 31]; modulation of enzymes that mediate metabolism between these two lipids could have significant impact on cell fate and has been demonstrated by the use of SPK and SMase inhibitors as anticancer and anti-inflammatory agents [10, 32].

The distinct compartmentalization of metabolic pathways surrounding ceramide also needs to be considered. CerS is localized to the ER and mitochondria-associated membranes (MAM) [14, 16, 33] while several studies have revealed microsomal, mitochondrial, nuclear and plasma membrane localizations for ceramidases and SMases [10, 16, 18, 19]. Consequently, interaction with components of the mitochondrial apoptotic machinery requires sphingolipid mobilization. The relative sphingolipid concentrations in the cell must also be tightly regulated to maintain the sphingolipid rheostat and homeostasis. Endogenous sphingolipid levels follow the scale S1P << ceramide << SM [34, 35]; however, presence of ceramide-enriched

macrodomains in the mitochondrial membrane during apoptosis implies local sphingolipid concentrations may be significantly higher than whole cell measurements [33, 36]. While the question of how sphingolipid metabolism accommodates these key factors in the context of BCL-2 family-regulated apoptosis remains to be fully addressed, we would like to review recent findings on two metabolic enzymes surrounding ceramide: SMase and CerS. Non-apoptotic roles of BCL-2 proteins in metabolism will also be addressed in subsequent sections.

1.1.1.2. Ceramide metabolism and apoptosis - sphingomyelinase

The concept of the "sphingomyelin cycle" as a regulator of important cellular processes arose several decades ago, when SM turnover was implicated in key pathways such as differentiation and protein kinase C regulation [37, 38]. aSMase deficiency due to mutations in the SM phosphodiesterase-1 gene leads to Niemann-Pick diseases with serious metabolic consequences ranging from hepatosplenomegaly to fatal neurological degeneration [39]. Distinct SMase populations regulate cell death at the plasma membrane and mitochondria [8, 40, 41]. BCL-2 family-dependent apoptosis *via* endogenous SMase-mediated ceramide elevation has been observed in different cell types in response to a diverse set of signals, with some of the more recent examples including etoposide in G6 glioma cells [42], galectin-1 in T cells [43], kainic acid in Sprague-Dawley [44] rats and gemcitabine in mouse astrocytoma and primary human glioma cells [45]. The antibiotic minocycline protected rat cortical neurons against bacterial sphingomyelinase (bSMase) by up-regulating BCL-2 expression [46]. It is worth noting that in some of these cases *de novo* synthesis and sphingosine salvage could not be completely ruled out as alternative pathways to ceramide production. Ceramide elevation and BAX translocation were also observed upon hypoxia/reoxygenation (H/R) of NT-2 human

neuronal precursor cells, with both aSMase and CerS5 contributing toward H/R-induced ceramide generation [47]. Treatment of leukemia cells with the anticancer agent N-(4-hydroxyphenyl)retinamide led to a biphasic increase in ceramide level where the first peak corresponded to SM hydrolysis and the second peak was attributable to CerS [48].

Modulation of SMase activity has been employed frequently in the study of ceramide function in BCL-2 family-regulated apoptosis. Birbes *et al*. observed that mitochondrial targeting of bSMase in MCF-7 breast cancer cells triggered ceramide elevation, BAX translocation and cyt c-mediated apoptosis that mimicked the phenotypes of TNFα treatment [40, 49]. BCL-2 overexpression conferred resistance to bSMase targeting [40]. bSMase addition increased BAX-membrane association in isolated mitochondria, and bSMase targeted to the cytosol, plasma membrane, ER, Golgi or nucleus raised ceramide level without triggering apoptosis [40]. These findings, taken together with the previous observation of both CerS and SMase-mediated ceramide generation in response to TNFα [50], suggest that a mitochondria-specific ceramide pool is necessary for mediating the TNFα apoptotic response in MCF-7 cells [40, 49]. aSMase was also indispensable for UV-induced BAX conformational change at the mitochondria of several cell types [51] (Figure 1.3). No UV-induced BAX conformational change and cyt c release were observed in siRNA knockdown of aSMase in HeLa cells relative to wild type (WT), or in lymphoblasts and fibroblasts from Niemann-Pick Disease (NPD) Type A patients, which are devoid of aSMase activity [51]. Exogenous C16 ceramide induced BAX conformational change in isolated mitochondria, and either exogenous C16 ceramide or aSMase overexpression could restore apoptotic phenotypes in NPD cells [51].

A murine knockout model has been developed for aSMase [52]. *aSMase*$^{-/-}$ mice appeared phenotypically normal at birth but gradually developed ataxia, reduced growth and

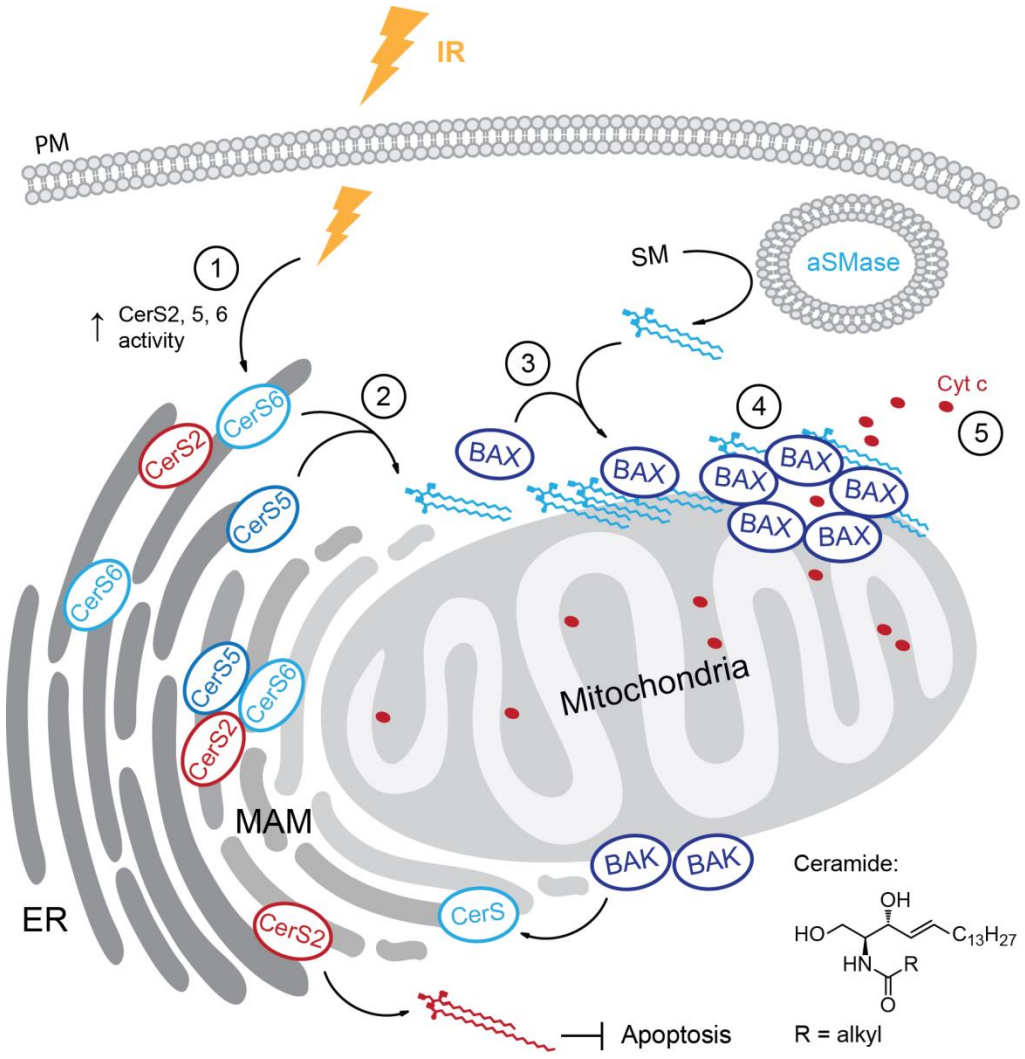

Figure 1.3. Ionizing radiation (IR)-induced ceramide generation and BCL-2 family-regulated apoptosis. IR (Cs-137)-triggered apoptosis of HeLa cells in the context of ceramides and BCL-2 proteins occurs through the following sequence: 1) IR-induced CerS 2, 5 and 6 activation, 2) ceramide generation, 3) ceramide macrodomain formation in mitochondrial membrane and preferential BAX insertion at ceramide-rich sites, 4) BAX oligomerization followed by 5) MOMP and cyt c release. CerS2 is required for IR-induced C24 ceramide biosynthesis while CerS5 and 6 are both required for IR-induced C16 ceramide biosynthesis. Overexpression studies reveal pro-survival function for CerS2 and pro-apoptotic function for CerS5. aSMase is also indispensable for UV-induced BAX conformational change at the mitochondria in HeLa, human fibroblasts and lymphoblasts. BAK, but not BAX, is required for CerS-mediated synthesis of long-chain ceramides (C16, 18 and 20) in UV-C-treated hematopoietic and baby mouse embryonic kidney cells. PM: plasma membrane.

neurodegeneration, leading to premature death [52]. *aSMase*$^{-/-}$ mice exhibited decreased radiation-induced pulmonary apoptosis and TNFα-induced liver damage with respect to WT [53, 54]. BAX translocation was unimpaired in TNFα-treated *aSMase*$^{-/-}$ mouse hepatocytes, suggesting that aSMase could mediate the TNFα response downstream of BCL-2 proteins. Interestingly, inhibition of glucosylceramide synthetase protected WT hepatocytes from TNFα-induced apoptosis despite raising ceramide levels [54]. The glycosphingolipid ganglioside GD3 localized to mitochondria during apoptosis in WT but not *aSMase*$^{-/-}$ hepatocytes, implying participation of additional ceramide metabolites in the aSMase-mediated TNFα response [54]. Thymol treatment of bone marrow-derived dendritic cells from WT but not *aSMase*$^{-/-}$ mice led to SMase-mediated ceramide elevation, BCL-2 and BCL-xL down-regulation, caspase activation and morphological changes associated with apoptosis [55].

1.1.1.3. Ceramide metabolism and apoptosis - ceramide synthase

Of the six mammalian CerSs, murine knockout models exist for CerS1, 2 and 3 [56-58]. *Cers1*$^{-/-}$ mice are characterized by neurodegeneration, cerebellar shrinkage and foliation defects [56]; *Cers2*$^{-/-}$ mice are characterized by neurodegeneration, cerebellar shrinkage, altered liver metabolism and hepatocarcinoma [57, 58]; and lethal skin barrier disruption occurs in *Cer3*$^{-/-}$ mice [59]. siRNA knockdown of individual CerS in MCF-7 cells led to selective up-regulation of the remaining CerSs and no change in total sphingolipids, implying a high degree of inter-regulation [14, 60]. BCL-2 family-regulated apoptosis *via* endogenous CerS-mediated ceramide elevation has been observed in multiple cell types in response to a wide range of stimuli, including gemcitabine in lung adenocarcinoma cells [61], saturated fatty acids in rat testicular Leydig cells [62], the anti-tumorigenic herb *P. urinaria* in leukemia cells [63], the AMPK

inhibitor Compound C in breast cancer cells [64] and UV-C irradiation of hematopoietic and baby mouse kidney cells [65]. A requirement for CerS in BCL-2 protein-dependent caspase activation was also observed in irradiated *C. elegans* germ cells [66]. It is worth noting that in some of these cases use of the CerS inhibitor fumonisin B_1 (FB_1) does not allow decoupling of *de novo* synthesis from the salvage pathway [67].

Another model system used in the study of CerS and ceramide interaction with the BCL-2 family-regulated apoptotic program is ionizing radiation (IR)-treated HeLa cells (Figure 1.3). Lee *et al*. observed mitochondria-specific elevation in CerS (but not SMase) activity and ceramide level in IR (Cs-137)-treated HeLa cells [33]. Ceramide elevation preceded BAX activation, and inhibition of either CerS or SPT led to significantly reduced BAX insertion, oligomerization and cyt c release, implying UV-induced *de novo* ceramide synthesis is required for BAX-dependent apoptosis in HeLa cells [33]. Confocal microscopy of mitochondria in irradiated HeLa cells revealed an endogenous increase in ceramide macrodomains and BAX-macrodomain co-localization [33], in agreement with previous finding of BAX association with ceramide and cholesterol-rich detergent-resistant mitochondrial membranes [36]. The authors calculated up to 80 % of *de novo* CerS-generated ceramide contributed toward macrodomain formation [33]. Macrodomain isolation and characterization confirmed the presence of BAX exclusively as a higher molecular weight oligomer, further supporting ceramide-rich mitochondrial domains as sites for preferential BAX activation [33].

Irradiation of HeLa cells also increased *de novo* ceramide generation *via* selective activation of CerS2, 5 and 6 [29] (Figure 1.3). CerS2 (C24 ceramide) overexpression protected HeLa cells from IR-induced apoptosis while CerS5 (C16 ceramide) overexpression enhanced cell death, with similar findings in MCF-7 and HCT-116 cells [29, 68, 69]. Both CerS5 and 6

were required for IR-induced C16 ceramide biosynthesis [29]. Co-immunoprecipitation revealed direct interactions among CerS2, 5 and 6, suggesting that the balance among different CerS activities could modulate cell fate toward apoptosis or survival [29]. Simultaneous knockdown of CerS5 and 6 in MCF-7 cells also inhibited UV-C-induced post-mitochondrial plasma membrane permeabilization; inhibitor studies revealed the source of the CerS5/6-generated ceramides as sphingosine salvage rather than *de novo* synthesis, implicating the existence of distinct ceramide pools in regulating different stages of the apoptotic program [14, 69]. Interestingly, CerS6-generated C16 ceramide protected human head and neck squamous cell carcinomas from ER stress-induced apoptosis *via* modulation of the ATF6/CHOP pathway, suggesting that a single ceramide may exert different functions in the context of different cell types and pathways [30].

1.1.2. BCL-2 proteins and metabolism

1.1.2.1. BCL-2 proteins and ceramide metabolism

Changes in the expression of BCL-2 proteins can alter apoptotic sensitivity *via* modulation of sphingolipid metabolism. BCL-2 overexpression in rat C6 glioma cells inhibited etoposide-induced nSMase activity, ceramide production, cyt c release and caspase activation [70]. Ceramide reduction was also observed in BCL-2-overexpressing C6 cells in response to TNFα or cisplatin, and in etoposide-treated C6 cells overexpressing BCL-xL; BAX overexpression promoted etoposide-induced apoptosis without altering ceramide production, suggesting that ceramide generation was not BAX-dependent in this context [70]. BCL-2 overexpression reduced Mg^{2+}-dependent nSMase activity in hypoxic PC12 cells [71]. Diamide treatment of MCF-7 cells led to SM hydrolysis *via* depletion of the nSMase inhibitor glutathione,

a phenotype that was blunted by BCL-xL overexpression; BCL-xL inhibited SM hydrolysis but not glutathione depletion, indicating BCL-xL exerted its effect upstream of ceramide metabolism but downstream of glutathione [72]. BCL-2 overexpression in human melanoma cells increased SPK1 expression while siRNA knockdown of BCL-2 induced the opposite effect [73], in agreement with previous finding of the role of BCL-2 in rescuing SPK1 activity from the DNA damaging agent ACD [74]. Interestingly, BCL-xL overexpression protected WEH1 cells from anti-immunoglobulin-induced apoptosis without altering ceramide level [75]. Similarly, in leukemia cells treated with the anticancer agent N-(4-hydroxyphenyl)retinamide, BCL-2 overexpression inhibited the phenotypes of mitochondrial apoptosis but not early reactive oxide species production, which was preceded by ceramide accumulation [48]. These findings suggest that overexpression of anti-apoptotic proteins could rescue cells from apoptosis by acting either up or downstream of ceramide metabolism.

BAX and BAK activity can also influence sphingolipid metabolism. Loss of BAX in HT116 and DU 145 cells conferred resistance to ceramide-induced cell death [76]. BAX and BAK deficiency individually mimicked aSMase deficiency by protecting mice from lethal gastrointestinal syndrome and crypt lethality following radiation exposure [77]. siRNA knockdown of BAK in MCF-7 cells inhibited UV-C-induced C18 and C20, but not C16 ceramide generation, suggesting that specific BCL-2 proteins could regulate distinct ceramide pools during apoptosis [69]. Using hematopoietic and baby kidney cells from WT and BAX, BAK double knockout (DKO) mice, Siskind *et al*. demonstrated that DKO cells were highly resistant to UV-C and did not up-regulate ceramide relative to WT [65]. Ceramide generation occurred independently of MOMP and required BAK but not BAX [65] (Figure 1.3). CerS activity was significantly decreased in BAK KO cells although the enzyme and mRNA levels

were unaltered, suggesting that BAK could be regulating CerS post-translationally [65]. Importantly, addition of BAK-containing microsomes to BAK KO microsomes restored CerS activity, implying non-redundant functions for BAX and BAK in apoptosis and metabolism [65].

1.1.2.2. BCL-2 proteins in glycolysis and fatty acid metabolism

In addition to sphingolipid metabolism, evidences support BCL-2 family involvement in glycolysis and fatty acid metabolism. The serine/threonine kinase Akt, which blocks apoptotic events preceding cyt c release in a similar fashion as some anti-apoptotic BCL-2 proteins, requires the first committed, hexokinase-catalyzed step of glycolysis for its anti-apoptotic function [78]. The inhibitory effect of Akt upon growth factor withdrawal occurred downstream of BID cleavage to active tBID, and overexpression of myristoylated Akt in growth factor-deprived rat fibroblasts blocked tBID-induced BAK oligomerization, a crucial step of the mitochondrial apoptotic program [79]. Importantly, proteomics revealed that the BH3-domain only pro-apoptotic protein BAD resided in a functional holoenzyme complex with protein kinase A, the A kinase anchoring protein WAVE-1, protein phosphatase 1 catalytic units and glucokinase [80]. *Bad*$^{-/-}$ mice failed to assemble this complex and displayed reduced glucose tolerance relative to WT [80]. Glucose induced BAD phosphorylation in hepatocytes, and reduced glucokinase activity was found in hepatocytes from mice expressing a non-phosphorylatable BAD, supporting regulation of glukokinase activity by BAD phosphorylation status [80, 81]. Glucokinase regulates glycogen synthesis and glucose production in hepatocytes, and glucose-dependent insulin secretion in pancreatic β cells [81, 82]; *Bad*$^{-/-}$ islets displayed impaired insulin secretion that could be rescued by treatment with BAD hydrocarbon-stapled BH3 helices [81, 83]. Impaired insulin secretion and calcium response, and reduced glucose

oxidation were also present in islets from founder 2 mice overexpressing the anti-apoptotic protein BCL-xL [84]. These findings implicate BAD, and potentially additional apoptotic proteins, in the coordination of major cellular pathways previously thought to be separate; BAD phosphorylation in response to cellular nutrient status could be a mechanism for tuning the protein's regulation of glycolysis or apoptosis.

BAD participation in glycolysis raises the question of whether other BCL-2 members could influence different branches of metabolism. While glucose deprivation induced apoptosis in fibroblasts [79], palmitic acid treatment of a murine T cell hybridoma cell line led to dose-dependent reduction of mitochondrial potential, reactive oxygen species release and nuclear apoptosis [85]; these effects were rescued by BCL-2 overexpression, suggesting potential crosstalk between fatty acid metabolism and BCL-2 family-regulated apoptosis [85]. Palmitic or stearic, but not lauric, myristic or palmitoleic acid, induced cell death with apoptotic morphology in murine hematopoietic precursor cells; cell death also correlated with carnitine palmitoyltransferase 1 (CPT1) upregulation [86]. Direct BCL-2-CPT1 binding has been demonstrated *via* glutathione S transferase binding assay and co-immunoprecipitation [87]. tBID treatment of permeabilized hepatocytes in the presence of caspase inhibitors and exogenous cyt c reduced fatty acid oxidation, resulting in palmitoyl-CoA accumulation and depletion of acetyl-carnitine and acylcarnitines [88]; similar to fatty acid treatment, effects of tBID were blunted by BCL-2 overexpression [88].

It is also worth noting that recent findings identified additional non-apoptotic functions for BAX and BAK in mitochondrial morphogenesis [89], and BID in innate immunity [90]. The interesting connections between BCL-2 proteins and metabolism prompted us to perform comparative global lipidomic analysis of WT and BAX, BAK-double knockout mouse

embryonic fibroblasts. BAX and BAK were selected given their crucial roles in mitochondrial permeabilization during apoptosis [1, 91] and mitochondrial morphogenesis under physiological conditions [89], both implying potential interactions between these two proteins and lipids at the mitochondria. As will be discussed in detail in Chapters 2 and 3, our analysis revealed novel functions for BAX and BAK in regulation of mitochondrial ceramide distribution and eicosanoid metabolism as further support for the interdependence of metabolism and BCL-2 family-regulated apoptosis.

1.2. Fatty acid and metabolic syndrome

Metabolic syndrome is a multi-component disorder characterized by insulin resistance, atherogenic dyslipidemia, obesity and hypertension; co-occurrence of these symptoms leads to increased risk for cardiovascular disease and type 2 diabetes (T2D) [92, 93]. Correlation between obesity and T2D implies a negative metabolic role for fatty acids, and the adverse effect of plasma non-esterified fatty acids (NEFAs), or free fatty acids (FFAs), on metabolic homeostasis was thought to be due to the lipid's promotion of insulin resistance [94, 95]. FFA circulation is a mechanism for shuttling FFAs to their site of utilization [94]. Circulating FFAs arise primarily from adipose tissue triglyceride (TG) hydrolysis during fasting [94, 96], and partially from spillover when dietary TGs are hydrolyzed by lipoprotein lipase (LPL) to FFAs that are taken up by adipocytes for storage [94, 97, 98]. Insulin inhibits lipolysis in adipose tissue [99], and FFAs increase insulin resistance *via* substrate saturation and modification of downstream signaling events [100]. Inhibition of the anti-lypolytic function of insulin by excessive circulating FFAs increases lipolysis, thereby releasing even more FFAs that adversely affect insulin signaling [94, 100]. Lipid infusion significantly reduced insulin stimulation of

PI3K, Akt1 and protein kinase Cλ/ζ in rat muscle [100, 101], and saturated FA inhibited insulin stimulation of Akt in murine myoblasts [100, 102].

While evidence supports a deleterious role for FAs in promoting insulin resistance, recent findings suggest that interaction between FA metabolism and insulin signaling depends on FA structure (Figure 1.4), and is more complex than previously believed [94]. Palmitic (16:0) or stearic (18:0) acid, but not palmitoleic (16:1) or oleic (18:1) acid, inhibited insulin signaling through Akt in murine myoblasts [102]. TG-palmitate infusion into mice inhibited insulin signaling while TG-palmitoleate infusion stimulated downstream insulin actions, strongly supporting 16:1 FA function as an insulin-sensitizing lipokine [103]. More recently, the G-protein coupled receptor GPR120 was identified as a sensor and receptor for ω3-FAs (20:5 and 22:6 FAs) [104]; receptor stimulation with ω3-FAs significantly reduced cellular inflammatory response in murine macrophages; dietary ω3-FAs enhanced insulin sensitivity in WT, but not *GPR120*$^{-/-}$ mice [105].

In addition, the nuclear hormone receptor peroxisome proliferator-activated receptor α stimulates FA oxidation to acetyl-CoA in liver during fasting [106]; fasting *PPARα*$^{-/-}$ mice exhibit elevated circulating FFAs and hypoglycemia [107, 108]. Linoleic (18:2) acid is an endogenous ligand of PPARα [106, 109], supporting a connection between glucose and FA metabolism, and a role for FFAs in inducing their own oxidation by acting as PPAR ligands [106]. 18:2 FA is also a ligand for the insulin sensitizer PPARγ [110]; 18:2 FA activation of PPARγ is reduced by inhibiting Δ^6 FA desaturase activity, indicating FA unsaturation is necessary for receptor interaction [110]. Dietary 18:2 FA delayed onset of T2D in Zucker rats in contrast to the insulin resistance role of 16:0 FA [102, 111] as additional evidence for the distinct metabolic functions of different FFAs.

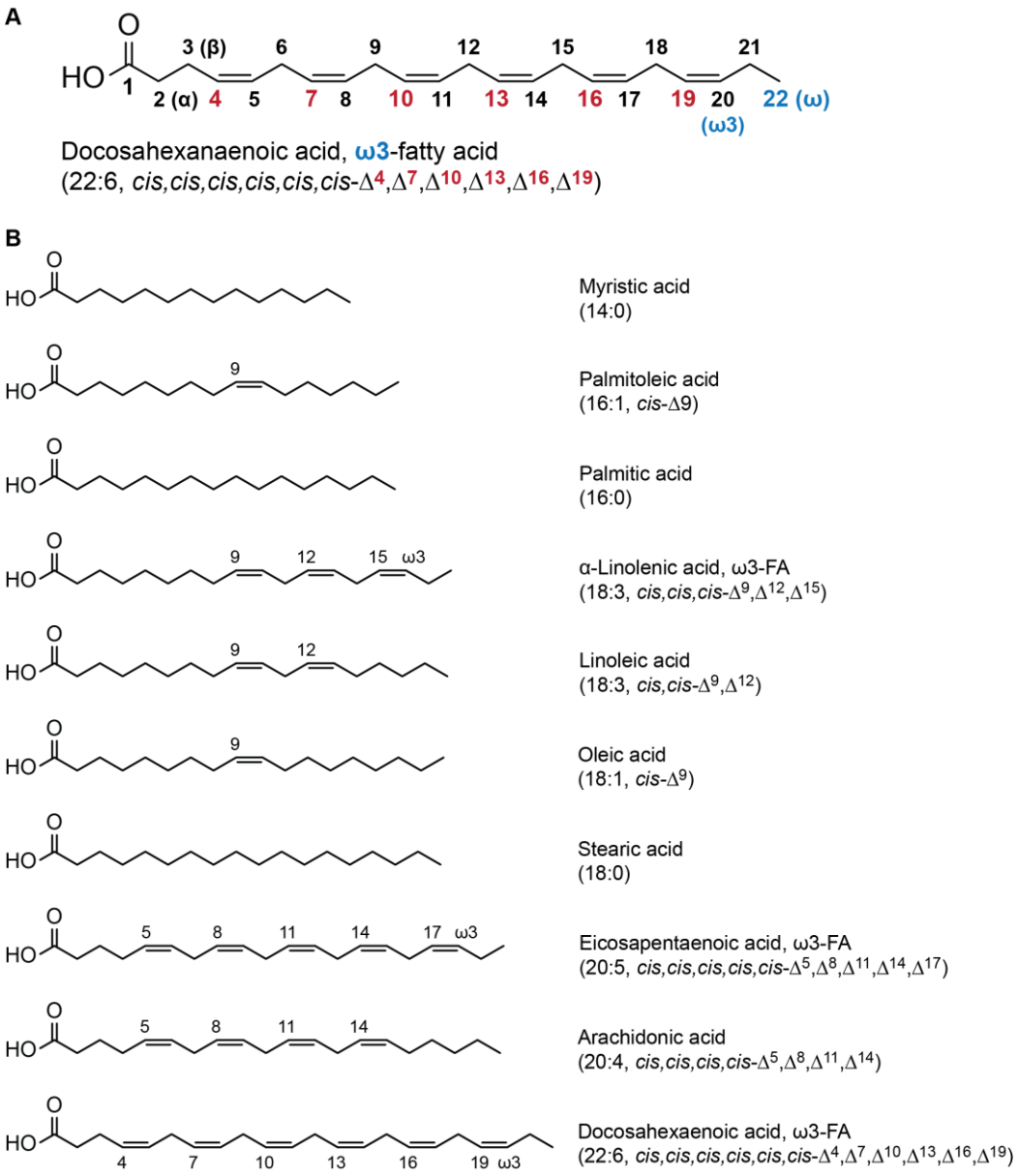

Figure 1.4. Structures of selected FFAs [15, 112]. A) Structure of docosahexaenoic acid. Docosahexaenoic acid is the trivial name of this FA. The C:D, *cis/trans*-Δ^x nomenclature containing information on degrees of unsaturation and double bond locations is in parenthesis [15, 113]. In the C:D notation (i.e. 22:6), C denotes total number carbons and D total number of double bonds. In the *cis/trans*-Δ^x notation each double bond is labeled *cis* or *trans*, and numbered based on its starting location (x) from the carbonyl carbon, which is numbered 1 [15, 113]. For all FAs the ω position refers to the terminal carbon farthest away from the carbonyl carbon [15]. Docosahexaenoic acid is a ω3-FA given the presence of a double bond starting at the third (ω3) carbon relative to the ω carbon [113]. B) Structures of commonly studied FFAs. Additional double bond isomers may be possible.

It is also important to note that in the context of T2D, mice overexpressing GLUT4, the major glucose transporter of insulin-sensitive tissues, in adipose tissue (AG4OX) exhibited enhanced insulin sensitivity but also increased lipogenesis and higher total body lipid content due to increased adipocyte number rather than size [114, 115]. Increased lipogenesis and insulin sensitivity in AG4OX mice suggest that the beneficial effect of GLUT4 upregulation could be carried out through modulation of lipid profile. In agreement with this hypothesis, LC–MS-based lipidomics of WT and AG4OX adipose tissues revealed AG4OX-induced upregulation of fatty acyl hydroxy fatty acid (FAHFA), a novel lipid class with beneficial effects in glucose tolerance and inflammation. These findings demonstrate that lipid structure could significantly affect the former's influence over insulin sensitivity, and lipid type should be carefully considered in addition to lipid quantity in the contexts of insulin signaling and T2D. Detailed optimization of a targeted LC–MS workflow for comprehensive analysis of FAHFA isomers and family members will be discussed in Chapter 4.

1.3. Conclusion

Far from inert structural elements of the membrane bilayer, lipids and their metabolism exert key points of control over crucial cellular processes such as apoptosis and insulin signaling [6, 94, 100]; dysregulated lipid metabolism can lead to metabolic syndrome and diseases of excessive cell death or survival [1, 94, 100, 116-118]. The diverse localization of sphingolipid metabolic enzymes and the equally diverse targeting of their lipid products bear significant impact over apoptosis and other cellular processes. Similarly, metabolism and mobilization of different fatty acid populations are necessary for receptor signaling and homeostasis. Difference in apoptotic potential among ceramides of varying acyl chain lengths [27, 29, 30] and the

selective role of unsaturated FAs in receptor binding [105, 109, 110] raises the important question of how different members of the same lipid class could be regulated by and interact with protein components *in vivo*, both spatially and temporally, to achieve the desired downstream effects. It is also important to note that while cellular metabolism can modulate apoptosis at the mitochondria, protein components of the apoptotic machinery are also regulators of cellular metabolism [88]. As is seen in the case of BAD, BAD phosphorylation is a mechanism for shifting the protein's activity toward either glycolysis or apoptosis, thereby linking two major cellular pathways previously believed to be separate [80, 81].

The notion that metabolism, and not just metabolites themselves, can interact with the protein machinery of key cellular processes also calls for a global, unbiased approach in quantifying complex metabolite changes in the context of protein deficiency or overexpression, which could be aided by recent advances in the field of metabolomics [119-121]. Oxidative lipidomics has become an useful tool in the study of lipid transformations during apoptosis [122-125] and traumatic brain injury [126], and targeted LC–MS has enabled sensitive quantification of large numbers of polar [127] or nonpolar metabolites [128, 129] from one biological sample. The increased sensitivity and resolution of LC–MS-based techniques also allow identification of lipids with subtle differences in chain length, stereochemistry and degrees of unsaturation [130-132]. As we will demonstrate through our studies of BAX, BAK-knockout MEFs and AG4OX mice in the following chapters, the combination of genetic knockout models, biochemical and metabolomic techniques could yield valuable information on the crosstalk among lipid metabolism, cell death and disease.

1.4. References

[1] L.D. Walensky, BCL-2 in the crosshairs: tipping the balance of life and death, Cell Death Differ, 13 (2006) 1339-1350.

[2] F. Gonzalvez, Z.T. Schug, R.H. Houtkooper, E.D. MacKenzie, D.G. Brooks, R.J.A. Wanders, P.X. Petit, F.M. Vaz, E. Gottlieb, Cardiolipin provides an essential activating platform for caspase-8 on mitochondria, The Journal of Cell Biology, 183 (2008) 681-696.

[3] J.I. Fletcher, D.C.S. Huang, BH3-only proteins: orchestrating cell death, Cell Death Differ, 13 (2006) 1268-1271.

[4] E. Gavathiotis, M. Suzuki, M.L. Davis, K. Pitter, G.H. Bird, S.G. Katz, H.-C. Tu, H. Kim, E.H.Y. Cheng, N. Tjandra, L.D. Walensky, BAX activation is initiated at a novel interaction site, Nature, 455 (2008) 1076-1081.

[5] G. van Loo, X. Saelens, M. van Gurp, M. MacFarlane, S.J. Martin, P. Vandenabeele, The role of mitochondrial factors in apoptosis: a Russian roulette with more than one bullet, Cell Death Differ, 9 (2002) 1031-1042.

[6] M. Crimi, M.D. Esposti, Apoptosis-induced changes in mitochondrial lipids, Biochimica et Biophysica Acta (BBA) - Molecular Cell Research, 1813 (2011) 551-557.

[7] Z.T. Schug, E. Gottlieb, Cardiolipin acts as a mitochondrial signalling platform to launch apoptosis, Biochimica et Biophysica Acta (BBA) - Biomembranes, 1788 (2009) 2022-2031.

[8] T.S. Tirodkar, C. Voelkel-Johnson, Sphingolipids in apoptosis, Experimental Oncology, 34 (2012) 231-242.

[9] S.M. Claypool, C.M. Koehler, The complexity of cardiolipin in health and disease, Trends in Biochemical Sciences, 37 (2012) 32-41.

[10] D. Canals, D.M. Perry, R.W. Jenkins, Y.A. Hannun, Drug targeting of sphingolipid metabolism: sphingomyelinases and ceramidases, British Journal of Pharmacology, 163 (2011) 694-712.

[11] J.R. Van Brocklyn, J.B. Williams, The control of the balance between ceramide and sphingosine-1-phosphate by sphingosine kinase: Oxidative stress and the seesaw of cell survival and death, Comparative Biochemistry and Physiology Part B: Biochemistry and Molecular Biology, 163 (2012) 26-36.

[12] N. Robinson, Functional binding of cardiolipin to cytochromec oxidase, J Bioenerg Biomembr, 25 (1993) 153-163.

[13] Jerry E. Chipuk, Gavin P. McStay, A. Bharti, T. Kuwana, Christopher J. Clarke, Leah J. Siskind, Lina M. Obeid, Douglas R. Green, Sphingolipid Metabolism Cooperates with BAK and BAX to Promote the Mitochondrial Pathway of Apoptosis, Cell, 148 (2012) 988-1000.

[14] T.D. Mullen, Y.A. Hannun, L.M. Obeid, Ceramide synthases at the centre of sphingolipid metabolism and biology, Biochemical Journal, 441 (2012) 789-802.

[15] The AOCS Lipid Library (2014), http://lipidlibrary.aocs.org.

[16] B.J. Pettus, C.E. Chalfant, Y.A. Hannun, Ceramide in apoptosis: an overview and current perspectives, Biochimica et Biophysica Acta (BBA) - Molecular and Cell Biology of Lipids, 1585 (2002) 114-125.

[17] T.D. Mullen, L. Obeid, Ceramide and apoptosis: exploring the enigmatic connections between sphingolipid metabolism and programmed cell death, Anticancer Agents Med Chem, 12 (2012) 340-363.

[18] A.H. Futerman, H. Riezman, The ins and outs of sphingolipid synthesis, Trends in Cell Biology, 15 (2005) 312-318.

[19] A.H. Futerman, Y.A. Hannun, The complex life of simple sphingolipids, EMBO Rep, 5 (2004) 777-782.

[20] F.M. Goñi, A. Alonso, Sphingomyelinases: enzymology and membrane activity, FEBS Letters, 531 (2002) 38-46.

[21] A.H. Merrill Jr, D.D. Jones, An update of the enzymology and regulation of sphingomyelin metabolism, Biochimica et Biophysica Acta (BBA) - Lipids and Lipid Metabolism, 1044 (1990) 1-12.

[22] D.L. Siow, C.D. Anderson, E.V. Berdyshev, A. Skobeleva, V. Natarajan, S.M. Pitson, B.W. Wattenberg, Sphingosine kinase localization in the control of sphingolipid metabolism, Advances in Enzyme Regulation, 51 (2011) 229-244.

[23] M. Serra, J.D. Saba, Sphingosine 1-phosphate lyase, a key regulator of sphingosine 1-phosphate signaling and function, Advances in Enzyme Regulation, 50 (2010) 349-362.

[24] S. El Bawab, H. Birbes, P. Roddy, Z.M. Szulc, A. Bielawska, Y.A. Hannun, Biochemical Characterization of the Reverse Activity of Rat Brain Ceramidase: A CoA-Independent and Fumonisin B1-Insensitive Ceramide Synthase, Journal of Biological Chemistry, 276 (2001) 16758-16766.

[25] M. Tani, N. Okino, S. Mitsutake, T. Tanigawa, H. Izu, M. Ito, Purification and Characterization of a Neutral Ceramidase from Mouse Liver: A Single Protein Catalyzes the

Reversible Reaction in which Ceramide is Both Hydrolyzed and Synthesized, Journal of Biological Chemistry, 275 (2000) 3462-3468.

[26] S.A. Novgorodov, B.X. Wu, T.I. Gudz, J. Bielawski, T.V. Ovchinnikova, Y.A. Hannun, L.M. Obeid, Novel Pathway of Ceramide Production in Mitochondria: Thioesterase and Neutral Ceramidase Produce Ceramide from Sphingosine and Acyl-CoA, Journal of Biological Chemistry, 286 (2011) 25352-25362.

[27] Y.A. Hannun, L.M. Obeid, Many Ceramides, Journal of Biological Chemistry, 286 (2011) 27855-27862.

[28] M.M. Young, M. Kester, H.-G. Wang, Sphingolipids: regulators of crosstalk between apoptosis and autophagy, Journal of Lipid Research, 54 (2013) 5-19.

[29] J. Mesicek, H. Lee, T. Feldman, X. Jiang, A. Skobeleva, E.V. Berdyshev, A. Haimovitz-Friedman, Z. Fuks, R. Kolesnick, Ceramide synthases 2, 5, and 6 confer distinct roles in radiation-induced apoptosis in HeLa cells, Cellular Signalling, 22 (2010) 1300-1307.

[30] C.E. Senkal, S. Ponnusamy, J. Bielawski, Y.A. Hannun, B. Ogretmen, Antiapoptotic roles of ceramide-synthase-6-generated C16-ceramide via selective regulation of the ATF6/CHOP arm of ER-stress-response pathways, The FASEB Journal, 24 (2010) 296-308.

[31] T.A. Taha, T.D. Mullen, L.M. Obeid, A house divided: Ceramide, sphingosine, and sphingosine-1-phosphate in programmed cell death, Biochimica et Biophysica Acta (BBA) - Biomembranes, 1758 (2006) 2027-2036.

[32] S. Pyne, R. Bittman, N.J. Pyne, Sphingosine Kinase Inhibitors and Cancer: Seeking the Golden Sword of Hercules, Cancer Research, 71 (2011) 6576-6582.

[33] H. Lee, J.A. Rotolo, J. Mesicek, T. Penate-Medina, A. Rimner, W.-C. Liao, X. Yin, G. Ragupathi, D. Ehleiter, E. Gulbins, D. Zhai, J.C. Reed, A. Haimovitz-Friedman, Z. Fuks, R. Kolesnick, Mitochondrial Ceramide-Rich Macrodomains Functionalize Bax upon Irradiation, PLoS ONE, 6 (2011) e19783.

[34] R. Kolesnick, The therapeutic potential of modulating the ceramide/sphingomyelin pathway, The Journal of Clinical Investigation, 110 (2002) 3-8.

[35] R.L. Shaner, J.C. Allegood, H. Park, E. Wang, S. Kelly, C.A. Haynes, M.C. Sullards, A.H. Merrill, Quantitative analysis of sphingolipids for lipidomics using triple quadrupole and quadrupole linear ion trap mass spectrometers, Journal of Lipid Research, 50 (2009) 1692-1707.

[36] E. Martínez-Abundis, F. Correa, N. Pavón, C. Zazueta, Bax distribution into mitochondrial detergent-resistant microdomains is related to ceramide and cholesterol content in postischemic hearts, FEBS Journal, 276 (2009) 5579-5588.

[37] Y.A. Hannun, R.M. Bell, Functions of Sphingolipids and Sphingolipid Breakdown Products in Cellular Regulation, Science, 243 (1989) 500-507.

[38] T. Okazaki, R.M. Bell, Y.A. Hannun, Sphingomyelin turnover induced by vitamin D3 in HL-60 cells. Role in cell differentiation, Journal of Biological Chemistry, 264 (1989) 19076-19080.

[39] P. Irun, M. Mallén, C. Dominguez, V. Rodriguez-Sureda, L.A. Alvarez-Sala, N. Arslan, N. Bermejo, C. Guerrero, I. Perez de Soto, L. Villalón, P. Giraldo, M. Pocovi, Identification of seven novel SMPD1 mutations causing Niemann–Pick disease types A and B, Clinical Genetics, (2013) n/a-n/a.

[40] H. Birbes, S. El Bawab, Y.A. Hannun, L.M. Obeid, Selective hydrolysis of a mitochondrial pool of sphingomyelin induces apoptosis, The FASEB Journal, 15 (2001) 2669-2679.

[41] P. Zhang, B. Liu, G.M. Jenkins, Y.A. Hannun, L.M. Obeid, Expression of Neutral Sphingomyelinase Identifies a Distinct Pool of Sphingomyelin Involved in Apoptosis, Journal of Biological Chemistry, 272 (1997) 9609-9612.

[42] M. Sawada, S. Nakashima, Y. Banno, H. Yamakawa, K. Hayashi, K. Takenaka, Y. Nishimura, H. Sakai, Y. Nozawa, Ordering of ceramide formation, caspase activation, and Bax/Bcl-2 expression during etoposide-induced apoptosis in C6 glioma cells, Cell Death Differ, 7 (2000) 761-772.

[43] G. Ion, R. Fajka-Boja, F. Kovács, G. Szebeni, I. Gombos, Á. Czibula, J. Matkó, É. Monostori, Acid sphingomyelinase mediated release of ceramide is essential to trigger the mitochondrial pathway of apoptosis by galectin-1, Cellular Signalling, 18 (2006) 1887-1896.

[44] M.A. Mikati, M. Zeinieh, R.A. Habib, J. El Hokayem, A. Rahmeh, M. El Sabban, J. Usta, G. Dbaibo, Changes in sphingomyelinases, ceramide, Bax, Bcl2, and caspase-3 during and after experimental status epilepticus, Epilepsy Research, 81 (2008) 161-166.

[45] C. Dumitru, I. Sandalcioglu, M. Wagner, M. Weller, E. Gulbins, Lysosomal ceramide mediates gemcitabine-induced death of glioma cells, J Mol Med, 87 (2009) 1123-1132.

[46] C.-M. Tang, C.-S. Hwang, S.-D. Chen, D.-I. Yang, Neuroprotective mechanisms of minocycline against sphingomyelinase/ceramide toxicity: Roles of Bcl-2 and thioredoxin, Free Radical Biology and Medicine, 50 (2011) 710-721.

[47] J. Jin, Q. Hou, T.D. Mullen, Y.H. Zeidan, J. Bielawski, J.M. Kraveka, A. Bielawska, L.M. Obeid, Y.A. Hannun, Y.-T. Hsu, Ceramide Generated by Sphingomyelin Hydrolysis and the Salvage Pathway Is Involved in Hypoxia/Reoxygenation-induced Bax Redistribution to Mitochondria in NT-2 Cells, Journal of Biological Chemistry, 283 (2008) 26509-26517.

[48] M.-C. Morales, G. Pérez-Yarza, N.N. Rementería, M.-D. Boyano, A. Apraiz, A. Gómez-Muñoz, E. Pérez-Andrés, A. Asumendi, 4-HPR-mediated leukemia cell cytotoxicity is triggered by ceramide-induced mitochondrial oxidative stress and is regulated downstream by Bcl-2, Free Radical Research, 41 (2007) 591-601.

[49] H. Birbes, C. Luberto, Y.-T. Hsu, S. El Bawab, Y.A. Hannun, L.M. Obeid, A mitochondrial pool of sphingomyelin is involved in TNFalpha-induced Bax translocation to mitochondria, Biochem. J., 386 (2005) 445-451.

[50] G.S. Dbaibo, W. El-Assaad, A. Krikorian, B. Liu, K. Diab, N.Z. Idriss, M. El-Sabban, T.A. Driscoll, D.K. Perry, Y.A. Hannun, Ceramide generation by two distinct pathways in tumor necrosis factor α-induced cell death, FEBS Letters, 503 (2001) 7-12.

[51] H. Kashkar, K. Wiegmann, B. Yazdanpanah, D. Haubert, M. Krönke, Acid Sphingomyelinase Is Indispensable for UV Light-induced Bax Conformational Change at the Mitochondrial Membrane, Journal of Biological Chemistry, 280 (2005) 20804-20813.

[52] K. Horinouchi, S. Erlich, D.P. Perl, K. Ferlinz, C.L. Bisgaier, K. Sandhoff, R.J. Desnick, C.L. Stewart, E.H. Schuchman, Acid sphingomyelinase deficient mice: a model of types A and B Niemann-Pick disease, Nat Genet, 10 (1995) 288-293.

[53] P. Santana, L.A. Peña, A. Haimovitz-Friedman, S. Martin, D. Green, M. McLoughlin, C. Cordon-Cardo, E.H. Schuchman, Z. Fuks, R. Kolesnick, Acid Sphingomyelinase–Deficient Human Lymphoblasts and Mice Are Defective in Radiation-Induced Apoptosis, Cell, 86 (1996) 189-199.

[54] C. García-Ruiz, A. Colell, M. Montserrat, A. Morales, M. Calvo, C. Enrich, J.C. Fernández-Checa, Defective TNF-α–mediated hepatocellular apoptosis and liver damage in acidic sphingomyelinase knockout mice, The Journal of Clinical Investigation, 111 (2003) 197-208.

[55] N.T. Xuan, E. Shumilina, E. Schmid, S.K. Bhavsar, R. Rexhepaj, F. Götz, E. Gulbins, F. Lang, Role of acidic sphingomyelinase in thymol-mediated dendritic cell death, Molecular Nutrition & Food Research, 54 (2010) 1833-1841.

[56] C. Ginkel, D. Hartmann, K. vom Dorp, A. Zlomuzica, H. Farwanah, M. Eckhardt, R. Sandhoff, J. Degen, M. Rabionet, E. Dere, P. Doermann, K. Sandhoff, K. Willecke, Ablation of neuronal Ceramide Synthase 1 in mice decreases ganglioside levels and expression of Myelin Associated Glycoprotein in oligodendrocytes, Journal of Biological Chemistry, (2012).

[57] Y. Pewzner-Jung, H. Park, E.L. Laviad, L.C. Silva, S. Lahiri, J. Stiban, R. Erez-Roman, B. Brügger, T. Sachsenheimer, F. Wieland, M. Prieto, A.H. Merrill, A.H. Futerman, A Critical Role for Ceramide Synthase 2 in Liver Homeostasis: I. ALTERATIONS IN LIPID METABOLIC PATHWAYS, Journal of Biological Chemistry, 285 (2010) 10902-10910.

[58] S. Imgrund, D. Hartmann, H. Farwanah, M. Eckhardt, R. Sandhoff, J. Degen, V. Gieselmann, K. Sandhoff, K. Willecke, Adult Ceramide Synthase 2 (CERS2)-deficient Mice Exhibit Myelin Sheath Defects, Cerebellar Degeneration, and Hepatocarcinomas, Journal of Biological Chemistry, 284 (2009) 33549-33560.

[59] R. Jennemann, M. Rabionet, K. Gorgas, S. Epstein, A. Dalpke, U. Rothermel, A. Bayerle, F. van der Hoeven, S. Imgrund, J. Kirsch, W. Nickel, K. Willecke, H. Riezman, H.-J. Gröne, R. Sandhoff, Loss of ceramide synthase 3 causes lethal skin barrier disruption, Human Molecular Genetics, 21 (2012) 586-608.

[60] T.D. Mullen, S. Spassieva, R.W. Jenkins, K. Kitatani, J. Bielawski, Y.A. Hannun, L.M. Obeid, Selective knockdown of ceramide synthases reveals complex interregulation of sphingolipid metabolism, Journal of Lipid Research, 52 (2011) 68-77.

[61] C.E. Chalfant, K. Rathman, R.L. Pinkerman, R.E. Wood, L.M. Obeid, B. Ogretmen, Y.A. Hannun, De Novo Ceramide Regulates the Alternative Splicing of Caspase 9 and Bcl-x in A549 Lung Adenocarcinoma Cells: DEPENDENCE ON PROTEIN PHOSPHATASE-1, Journal of Biological Chemistry, 277 (2002) 12587-12595.

[62] Z.-H. Lu, Y.-M. Mu, B.-A. Wang, X.-L. Li, J.-M. Lu, J.-Y. Li, C.-Y. Pan, T. Yanase, H. Nawata, Saturated free fatty acids, palmitic acid and stearic acid, induce apoptosis by stimulation of ceramide generation in rat testicular Leydig cell, Biochemical and Biophysical Research Communications, 303 (2003) 1002-1007.

[63] S.-T. Huang, R.-C. Yang, M.-Y. Chen, J.-H.S. Pang, Phyllanthus urinaria induces the Fas receptor/ligand expression and ceramide-mediated apoptosis in HL-60 cells, Life Sciences, 75 (2004) 339-351.

[64] J. Jin, T.D. Mullen, Q. Hou, J. Bielawski, A. Bielawska, X. Zhang, L.M. Obeid, Y.A. Hannun, Y.-T. Hsu, AMPK inhibitor Compound C stimulates ceramide production and promotes Bax redistribution and apoptosis in MCF7 breast carcinoma cells, Journal of Lipid Research, 50 (2009) 2389-2397.

[65] L.J. Siskind, T.D. Mullen, K. Romero Rosales, C.J. Clarke, M.J. Hernandez-Corbacho, A.L. Edinger, L.M. Obeid, The BCL-2 Protein BAK Is Required for Long-chain Ceramide Generation during Apoptosis, Journal of Biological Chemistry, 285 (2010) 11818-11826.

[66] X. Deng, X. Yin, R. Allan, D.D. Lu, C.W. Maurer, A. Haimovitz-Friedman, Z. Fuks, S. Shaham, R. Kolesnick, Ceramide Biogenesis Is Required for Radiation-Induced Apoptosis in the Germ Line of C. elegans, Science, 322 (2008) 110-115.

[67] K. Kitatani, J. Idkowiak-Baldys, Y.A. Hannun, The sphingolipid salvage pathway in ceramide metabolism and signaling, Cellular Signalling, 20 (2008) 1010-1018.

[68] D. Hartmann, J. Lucks, S. Fuchs, S. Schiffmann, Y. Schreiber, N. Ferreirós, J. Merkens, R. Marschalek, G. Geisslinger, S. Grösch, Long chain ceramides and very long chain ceramides have opposite effects on human breast and colon cancer cell growth, The International Journal of Biochemistry & Cell Biology, 44 (2012) 620-628.

[69] T.D. Mullen, R.W. Jenkins, C.J. Clarke, J. Bielawski, Y.A. Hannun, L.M. Obeid, Ceramide Synthase-dependent Ceramide Generation and Programmed Cell Death: Involvement of Salvage Pathway in Regulating Postmitochondrial Events, Journal of Biological Chemistry, 286 (2011) 15929-15942.

[70] M. Sawada, S. Nakashima, Y. Banno, H. Yamakawa, K. Takenaka, J. Shinoda, Y. Nishimura, N. Sakai, Y. Nozawa, Influence of Bax of Bcl-2 overexpression on the ceramide-dependent apoptotic pathway in glioma cells, Oncogene, 19 (2000) 3508-3520.

[71] S.-i. Yoshimura, Y. Banno, S. Nakashima, K. Takenaka, H. Sakai, Y. Nishimura, N. Sakai, S. Shimizu, Y. Eguchi, Y. Tsujimoto, Y. Nozawa, Ceramide Formation Leads to Caspase-3 Activation during Hypoxic PC12 Cell Death: Inhibitory Effects of Bcl-2 on Ceramide Formation and Caspase-3 Activation, Journal of Biological Chemistry, 273 (1998) 6921-6927.

[72] Y. Okamoto, L.M. Obeid, Y.A. Hannun, Bcl-xL interrupts oxidative activation of neutral sphingomyelinase, FEBS letters, 530 (2002) 104-108.

[73] M. Bektas, P.S. Jolly, C. Muller, J. Eberle, S. Spiegel, C.C. Geilen, Sphingosine kinase activity counteracts ceramide-mediated cell death in human melanoma cells: role of Bcl-2 expression, Oncogene, 24 (2005) 178-187.

[74] T.A. Taha, W. Osta, L. Kozhaya, J. Bielawski, K.R. Johnson, W.E. Gillanders, G.S. Dbaibo, Y.A. Hannun, L.M. Obeid, Down-regulation of Sphingosine Kinase-1 by DNA Damage: Dependence on Proteases and p53, Journal of Biological Chemistry, 279 (2004) 20546-20554.

[75] D.A. Wiesner, J.P. Kilkus, A.R. Gottschalk, J. Quintáns, G. Dawson, Anti-immunoglobulin-induced Apoptosis in WEHI 231 Cells Involves the Slow Formation of Ceramide from Sphingomyelin and Is Blocked by bcl-xL, Journal of Biological Chemistry, 272 (1997) 9868-9876.

[76] C. von Haefen, T. Wieder, B. Gillissen, L. Stärck, V. Graupner, B. Dörken, P.T. Daniel, Ceramide induces mitochondrial activation and apoptosis via a Bax-dependent pathway in human carcinoma cells, Oncogene, 21 (2002) 4009-4019.

[77] J.A. Rotolo, J.G. Maj, R. Feldman, D. Ren, A. Haimovitz-Friedman, C. Cordon-Cardo, E.H.Y. Cheng, R. Kolesnick, Z. Fuks, Bax and Bak Do Not Exhibit Functional Redundancy in Mediating Radiation-Induced Endothelial Apoptosis in the Intestinal Mucosa, International Journal of Radiation Oncology • Biology • Physics, 70 (2008) 804-815.

[78] K. Gottlob, N. Majewski, S. Kennedy, E. Kandel, R.B. Robey, N. Hay, Inhibition of early apoptotic events by Akt/PKB is dependent on the first committed step of glycolysis and mitochondrial hexokinase, Genes & Development, 15 (2001) 1406-1418.

[79] N. Majewski, V. Nogueira, R.B. Robey, N. Hay, Akt Inhibits Apoptosis Downstream of BID Cleavage via a Glucose-Dependent Mechanism Involving Mitochondrial Hexokinases, Molecular and Cellular Biology, 24 (2004) 730-740.

[80] N.N. Danial, C.F. Gramm, L. Scorrano, C.-Y. Zhang, S. Krauss, A.M. Ranger, S. Robert Datta, M.E. Greenberg, L.J. Licklider, B.B. Lowell, S.P. Gygi, S.J. Korsmeyer, BAD and glucokinase reside in a mitochondrial complex that integrates glycolysis and apoptosis, Nature, 424 (2003) 952-956.

[81] N.N. Danial, BAD: undertaker by night, candyman by day, Oncogene, 27 (2009) S53-S70.

[82] A. Giménez-Cassina, L. Garcia-Haro, Cheol S. Choi, Mayowa A. Osundiji, E.A. Lane, H. Huang, Muhammed A. Yildirim, B. Szlyk, Jill K. Fisher, K. Polak, E. Patton, J. Wiwczar, M. Godes, Dae H. Lee, K. Robertson, S. Kim, A. Kulkarni, A. Distefano, V. Samuel, G. Cline, Y.-B. Kim, Gerald I. Shulman, Nika N. Danial, Regulation of Hepatic Energy Metabolism and Gluconeogenesis by BAD, Cell Metabolism, 19 (2014) 272-284.

[83] N.N. Danial, L.D. Walensky, C.-Y. Zhang, C.S. Choi, J.K. Fisher, A.J.A. Molina, S.R. Datta, K.L. Pitter, G.H. Bird, J.D. Wikstrom, J.T. Deeney, K. Robertson, J. Morash, A. Kulkarni, S. Neschen, S. Kim, M.E. Greenberg, B.E. Corkey, O.S. Shirihai, G.I. Shulman, B.B. Lowell, S.J. Korsmeyer, Dual role of proapoptotic BAD in insulin secretion and beta cell survival, Nat Med, 14 (2008) 144-153.

[84] Y.-P. Zhou, J.C. Pena, M.W. Roe, A. Mittal, M. Levisetti, A.C. Baldwin, W. Pugh, D. Ostrega, N. Ahmed, V.P. Bindokas, L.H. Philipson, D. Hanahan, C.B. Thompson, K.S. Polonsky, Overexpression of Bcl-xL in β-cells prevents cell death but impairs mitochondrial signal for insulin secretion, American Journal of Physiology - Endocrinology and Metabolism, 278 (2000) E340-E351.

[85] M.A. de Pablo, S.A. Susin, E. Jacotot, N. Larochette, P. Costantini, L. Ravagnan, N. Zamzami, G. Kroemer, Palmitate induces apoptosis via a direct effect on mitochondria, Apoptosis, 4 (1999) 81-87.

[86] M.B. Paumen, Y. Ishida, M. Muramatsu, M. Yamamoto, T. Honjo, Inhibition of Carnitine Palmitoyltransferase I Augments Sphingolipid Synthesis and Palmitate-induced Apoptosis, Journal of Biological Chemistry, 272 (1997) 3324-3329.

[87] M.B. Paumen, Y. Ishida, H. Han, M. Muramatsu, Y. Eguchi, Y. Tsujimoto, T. Honjo, Direct Interaction of the Mitochondrial Membrane Protein Carnitine Palmitoyltransferase I with Bcl-2, Biochemical and Biophysical Research Communications, 231 (1997) 523-525.

[88] A. Giordano, M. Calvani, O. Petillo, P. Grippo, F. Tuccillo, M.A.B. Melone, P. Bonelli, A. Calarco, G. Peluso, tBid induces alterations of mitochondrial fatty acid oxidation flux by malonyl-CoA-independent inhibition of carnitine palmitoyltransferase-1, Cell Death Differ, 12 (2005) 603-613.

[89] M. Karbowski, K.L. Norris, M.M. Cleland, S.-Y. Jeong, R.J. Youle, Role of Bax and Bak in mitochondrial morphogenesis, Nature, 443 (2006) 658-662.

[90] G. Yeretssian, R.G. Correa, K. Doiron, P. Fitzgerald, C.P. Dillon, D.R. Green, J.C. Reed, M. Saleh, Non-apoptotic role of BID in inflammation and innate immunity, Nature, 474 (2011) 96-99.

[91] L.D. Walensky, E. Gavathiotis, BAX unleashed: the biochemical transformation of an inactive cytosolic monomer into a toxic mitochondrial pore, Trends in Biochemical Sciences, 36 (2011) 642-652.

[92] H.M. Roche, Fatty acids and the metabolic syndrome, Proceedings of the Nutrition Society, 64 (2005) 23-29.

[93] P.L. Huang, A comprehensive definition for metabolic syndrome, Disease Models & Mechanisms, 2 (2009) 231-237.

[94] F. Karpe, J.R. Dickmann, K.N. Frayn, Fatty Acids, Obesity, and Insulin Resistance: Time for a Reevaluation, Diabetes, 60 (2011) 2441-2449.

[95] P.J. Randle, P.B. Garland, C.N. Hales, E.A. Newsholme, The Glucose Fatty-Acid Cycle its Role in Insulin Sensitivity and the Metabolic Disturbances of Diabetes Mellitus, The Lancet, 281 (1963) 785-789.

[96] M. Lafontan, D. Langin, Lipolysis and lipid mobilization in human adipose tissue, Progress in Lipid Research, 48 (2009) 275-297.

[97] K. Evans, G.C. Burdge, S.A. Wootton, M.L. Clark, K.N. Frayn, Regulation of Dietary Fatty Acid Entrapment in Subcutaneous Adipose Tissue and Skeletal Muscle, Diabetes, 51 (2002) 2684-2690.

[98] S.E. McQuaid, L. Hodson, M.J. Neville, A.L. Dennis, J. Cheeseman, S.M. Humphreys, T. Ruge, M. Gilbert, B.A. Fielding, K.N. Frayn, F. Karpe, Downregulation of Adipose Tissue Fatty Acid Trafficking in Obesity: A Driver for Ectopic Fat Deposition?, Diabetes, 60 (2011) 47-55.

[99] M.D. Jensen, M. Caruso, V. Heiling, J.M. Miles, Insulin Regulation of Lipolysis in Nondiabetic and IDDM Subjects, Diabetes, 38 (1989) 1595-1601.

[100] R.H. Eckel, S.M. Grundy, P.Z. Zimmet, The metabolic syndrome, The Lancet, 365 1415-1428.

[101] Y.-B. Kim, G.I. Shulman, B.B. Kahn, Fatty Acid Infusion Selectively Impairs Insulin Action on Akt1 and Protein Kinase C λ/ζ but Not on Glycogen Synthase Kinase-3, Journal of Biological Chemistry, 277 (2002) 32915-32922.

[102] J.A. Chavez, T.A. Knotts, L.-P. Wang, G. Li, R.T. Dobrowsky, G.L. Florant, S.A. Summers, A Role for Ceramide, but Not Diacylglycerol, in the Antagonism of Insulin Signal Transduction by Saturated Fatty Acids, Journal of Biological Chemistry, 278 (2003) 10297-10303.

[103] H. Cao, K. Gerhold, J.R. Mayers, M.M. Wiest, S.M. Watkins, G.S. Hotamisligil, Identification of a Lipokine, a Lipid Hormone Linking Adipose Tissue to Systemic Metabolism, Cell, 134 (2008) 933-944.

[104] D.Y. Oh, S. Talukdar, E.J. Bae, T. Imamura, H. Morinaga, W. Fan, P. Li, W.J. Lu, S.M. Watkins, J.M. Olefsky, GPR120 Is an Omega-3 Fatty Acid Receptor Mediating Potent Anti-inflammatory and Insulin-Sensitizing Effects, Cell, 142 687-698.

[105] D.Y. Oh, S. Talukdar, E.J. Bae, T. Imamura, H. Morinaga, W. Fan, P. Li, W.J. Lu, S.M. Watkins, J.M. Olefsky, GPR120 Is an Omega-3 Fatty Acid Receptor Mediating Potent Anti-inflammatory and Insulin-Sensitizing Effects, Cell, 142 (2010) 687-698.

[106] S. Kersten, B. Desvergne, W. Wahli, Roles of PPARs in health and disease, Nature, 405 (2000) 421-424.

[107] T.C. Leone, C.J. Weinheimer, D.P. Kelly, A critical role for the peroxisome proliferator-activated receptor α (PPARα) in the cellular fasting response: The PPARα-null mouse as a model of fatty acid oxidation disorders, Proceedings of the National Academy of Sciences, 96 (1999) 7473-7478.

[108] S. Kersten, J. Seydoux, J.M. Peters, F.J. Gonzalez, B. Desvergne, xE, atrice, W. Wahli, Peroxisome proliferator–activated receptor α mediates the adaptive response to fasting, The Journal of Clinical Investigation, 103 (1999) 1489-1498.

[109] S.Y. Moya-Camarena, J.P.V. Heuvel, S.G. Blanchard, L.A. Leesnitzer, M.A. Belury, Conjugated linoleic acid is a potent naturally occurring ligand and activator of PPARα, Journal of Lipid Research, 40 (1999) 1426-1433.

[110] M.A. Belury, S.Y. Moya-Camarena, M. Lu, L. Shi, L.M. Leesnitzer, S.G. Blanchard, Conjugated linoleic acid is an activator and ligand for peroxisome proliferator-activated receptor-gamma (PPARγ), Nutrition Research, 22 (2002) 817-824.

[111] K.L. Houseknecht, J.P.V. Heuvel, S.Y. Moya-Camarena, C.P. Portocarrero, L.W. Peck, K.P. Nickel, M.A. Belury, Dietary Conjugated Linoleic Acid Normalizes Impaired Glucose

Tolerance in the Zucker Diabetic Fattyfa/faRat, Biochemical and Biophysical Research Communications, 244 (1998) 678-682.

[112] M.T. Nakamura, T.Y. Nara, Structure, Function, AND Dietary Regulation of Δ6, Δ5, and Δ9 Desaturases, Annual Review of Nutrition, 24 (2004) 345-376.

[113] J. Rigaudy, S.P. Klesney, Nomenclature of Organic Chemistry, Pergamon (1979).

[114] P.R. Shepherd, L. Gnudi, E. Tozzo, H. Yang, F. Leach, B.B. Kahn, Adipose cell hyperplasia and enhanced glucose disposal in transgenic mice overexpressing GLUT4 selectively in adipose tissue, Journal of Biological Chemistry, 268 (1993) 22243-22246.

[115] E. Tozzo, P.R. Shepherd, L. Gnudi, B.B. Kahn, Transgenic GLUT-4 overexpression in fat enhances glucose metabolism: preferential effect on fatty acid synthesis, American Journal of Physiology - Endocrinology and Metabolism, 268 (1995) E956-E964.

[116] K.W. Yip, J.C. Reed, Bcl-2 family proteins and cancer, Oncogene, 27 (2008) 6398-6406.

[117] D. Mérino, P. Bouillet, The Bcl-2 family in autoimmune and degenerative disorders, Apoptosis, 14 (2009) 570-583.

[118] O. Takeuchi, J. Fisher, H. Suh, H. Harada, B.A. Malynn, S.J. Korsmeyer, Essential role of BAX,BAK in B cell homeostasis and prevention of autoimmune disease, Proceedings of the National Academy of Sciences of the United States of America, 102 (2005) 11272-11277.

[119] N. Vinayavekhin, E.A. Homan, A. Saghatelian, Exploring Disease through Metabolomics, ACS Chemical Biology, 5 (2009) 91-103.

[120] N. Vinayavekhin, A. Saghatelian, Untargeted Metabolomics, in: Current Protocols in Molecular Biology, John Wiley & Sons, Inc., 2001.

[121] Y.-G. Kim, A. Saghatelian, Functional Analysis of Protein Targets by Metabolomic Approaches, in: S.A. Sieber (Ed.) Activity-Based Protein Profiling, vol. 324, Springer Berlin Heidelberg, 2012, pp. 137-162.

[122] V.E. Kagan, G.G. Borisenko, Y.Y. Tyurina, V.A. Tyurin, J. Jiang, A.I. Potapovich, V. Kini, A.A. Amoscato, Y. Fujii, Oxidative lipidomics of apoptosis: redox catalytic interactions of cytochrome c with cardiolipin and phosphatidylserine, Free Radical Biology and Medicine, 37 (2004) 1963-1985.

[123] V.E. Kagan, Y.Y. Tyurina, H. Bayir, C.T. Chu, A.A. Kapralov, I.I. Vlasova, N.A. Belikova, V.A. Tyurin, A. Amoscato, M. Epperly, J. Greenberger, S. DeKosky, A.A. Shvedova, J. Jiang, The “pro-apoptotic genies” get out of mitochondria: Oxidative lipidomics and redox activity of cytochrome c/cardiolipin complexes, Chemico-Biological Interactions, 163 (2006) 15-28.

[124] V. Tyurin, Y. Tyurina, V. Ritov, A. Lysytsya, A. Amoscato, P. Kochanek, R. Hamilton, S. DeKosky, J. Greenberger, H. Bayir, V. Kagan, Oxidative Lipidomics of Apoptosis: Quantitative Assessment of Phospholipid Hydroperoxides in Cells and Tissues, in: R.M. Uppu, S.N. Murthy, W.A. Pryor, N.L. Parinandi (Eds.) Free Radicals and Antioxidant Protocols, vol. 610, Humana Press, 2010, pp. 353-374.

[125] V.A. Tyurin, Y.Y. Tyurina, P.M. Kochanek, R. Hamilton, S.T. DeKosky, J.S. Greenberger, H. Bayir, V.E. Kagan, Chapter Nineteen Oxidative Lipidomics of Programmed Cell Death, in: Z.Z.R.A.L. Roya Khosravi-Far, P. Mauro (Eds.) Methods in Enzymology, vol. Volume 442, Academic Press, 2008, pp. 375-393.

[126] L.J. Sparvero, A.A. Amoscato, P.M. Kochanek, B.R. Pitt, V.E. Kagan, H. Bayır, Mass-spectrometry based oxidative lipidomics and lipid imaging: applications in traumatic brain injury, Journal of Neurochemistry, 115 (2010) 1322-1336.

[127] S.U. Bajad, W. Lu, E.H. Kimball, J. Yuan, C. Peterson, J.D. Rabinowitz, Separation and quantitation of water soluble cellular metabolites by hydrophilic interaction chromatography-tandem mass spectrometry, Journal of Chromatography A, 1125 (2006) 76-88.

[128] J.G. McDonald, D.D. Smith, A.R. Stiles, D.W. Russell, A comprehensive method for extraction and quantitative analysis of sterols and secosteroids from human plasma, Journal of Lipid Research, 53 (2012) 1399-1409.

[129] J.G. McDonald, B.M. Thompson, E.C. McCrum, D.W. Russell, Extraction and Analysis of Sterols in Biological Matrices by High Performance Liquid Chromatography Electrospray Ionization Mass Spectrometry, in: H.A. Brown (Ed.) Methods in Enzymology, vol. Volume 432, Academic Press, 2007, pp. 145-170.

[130] J. Bielawski, Z.M. Szulc, Y.A. Hannun, A. Bielawska, Simultaneous quantitative analysis of bioactive sphingolipids by high-performance liquid chromatography-tandem mass spectrometry, Methods, 39 (2006) 82-91.

[131] M. Valsecchi, L. Mauri, R. Casellato, S. Prioni, N. Loberto, A. Prinetti, V. Chigorno, S. Sonnino, Ceramide and sphingomyelin species of fibroblasts and neurons in culture, Journal of Lipid Research, 48 (2007) 417-424.

[132] C.A. Haynes, J.C. Allegood, H. Park, M.C. Sullards, Sphingolipidomics: Methods for the comprehensive analysis of sphingolipids, Journal of Chromatography B, 877 (2009) 2696-2708.

Chapter 2

Regulation of mitochondrial ceramide distribution by members of the BCL-2 family

2.1. Introduction

The mitochondrial apoptotic pathway follows a highly regulated sequence of events and is dependent on BCL-2 proteins [1]. Named after its founding member, the anti-apoptotic B-cell lymphoma-2 [2-4], the BCL-2 family includes pro and anti-apoptotic members whose interactions regulate the balance between cell death and survival [1]. BCL-2 members are classified based on structure and function into multidomain anti-apoptotic, multidomain pro-apoptotic and BH3 domain-only pro-apoptotic proteins [1]. A wide range of death signals recruits distinct BH3-domain only proteins to activate the executioner proteins BAX and BAK [1]. Oligomerization of BAX and BAK in the mitochondrial outer membrane leads to mitochondrial outer membrane permeabilization (MOMP), releasing cytochrome c (cyt c) and other apoptogenic factors to promote caspase activation and proteolysis [1, 5, 6]. Dysregulated expression of BCL-2 proteins is associated with cancer [7], autoimmune and neurodegenerative diseases [8, 9].

Murine knockout models of BCL-2 members have proven useful in understanding the cellular functions of these proteins [9, 10]. Lymphocytes and fibroblasts from *Bax*$^{-/-}$, *Bak*$^{-/-}$ (DKO) mice are resistant to apoptosis induced by a range of death signals, supporting an indispensable role for these proteins in mitochondrial apoptosis [9, 11, 12]. Cells from *Bak*$^{-/-}$ mice could activate both extrinsic and intrinsic apoptotic pathways [11], and either BAX or BAK was sufficient for anoikis or serum deprivation-induced cell death [12], implying some degree of functional redundancy between these two proteins. At the molecular level, activation of BH3-domain only proteins in response to death stimuli is believed to activate BAX and BAK either directly or *via* deactivation of anti-apoptotic proteins sequestering BAX and BAK [13]. Upon activation, conformational changes in cytosolic BAX trigger its mitochondrial targeting and

subsequent oligomerization; BAK is localized to the mitochondrial outer membrane under physiological conditions and oligomerizes upon activation by BH3 domain-only proteins [13, 14].

While much of apoptosis research has focused on protein components, evidences support equally important functions for lipids in promoting or inhibiting apoptosis at the mitochondria [15-19]. Successful execution of the mitochondrial apoptotic program requires mobilization of key protein factors such as BCL-2 members and cyt c, which requires structural reorganization within the lipid bilayer [16, 19]. The mitochondrial lipid cardiolipin (CL) tethers cyt c to the inner mitochondrial membrane such that CL peroxidation during apoptosis is a crucial step toward cyt c release [20, 21], and more recently, *in vitro* reconstitution studies revealed cooperation of distinct portions of the sphingolipid metabolic pathway with BAX and BAK in promoting membrane permeabilization [22]. It is also interesting to note that aside from their role in apoptosis, recent finding supports an additional function for BAX and BAK in mitochondrial morphogenesis [23]. BAX and BAK co-localized with mitofusin 2 and the mitochondrial fission mediator dynamin-related protein 1 at sites of mitochondrial division during apoptosis; DKO MEFs displayed shorter, more fragmented mitochondria and lower fusion rates relative to WT [23]. This connection between mitochondrial dynamics and lipid composition [24-28] suggests that BCL-2 proteins such as BAX and BAK may also modulate lipid metabolism at the mitochondria.

Lipids can also influence BAX function through direct lipid-protein binding [22]. Hexadecenal, the breakdown product of sphingosine *via* sphingosine lyase, has been shown to interact with BAX in a chloroform-spotted array and promote BAX oligomerization in large unilamellar vesicles [22]. Altered mitochondrial morphology in DKO MEFs, role of lipids in apoptosis and maintenance of membrane structure [16], and cooperation between lipids and

BCL-2 proteins support a potential function for BAX and BAK in modulating mitochondrial lipid levels *via* regulation of lipid metabolism, with impacts on both mitochondrial morphology and apoptosis. To test this hypothesis, we performed unbiased, comparative global lipidomic analysis of WT and DKO MEFs using a quantitative liquid chromatography (LC)–mass spectrometry (MS) platform. Our analysis revealed specific differences in mitochondrial lipid composition between DKO and WT MEFs, supporting a role for BAX and BAK in mitochondrial lipid metabolism.

2.2. Results

2.2.1. Comparative metabolite profiling reveals elevated level of unsaturated C16 ceramide in DKO mitochondria

Lipids were extracted [29] from WT and DKO MEF mitochondria isolated using a standard protocol [30] and subjected to LC–MS (Figure 2.1A). Data were analyzed *via* two separate approaches: a targeted approach that quantifies known lipids and an untargeted approach that identifies changes in unknown metabolites. For the targeted approach, extracted ion chromatographs (EICs) corresponding to the exact mass-to-charge ratios (m/z) of common lipids were manually integrated to yield ion counts corresponding to relative lipid abundances. For the untargeted approach, WT and DKO sample files were sorted into two groups and analyzed by XCMS [31], which detects metabolites common to all data files through retention time alignment and statistically compares abundances of detected metabolites between assigned groups [31], enabling identification of both novel and known metabolites not included in the targeted analysis.

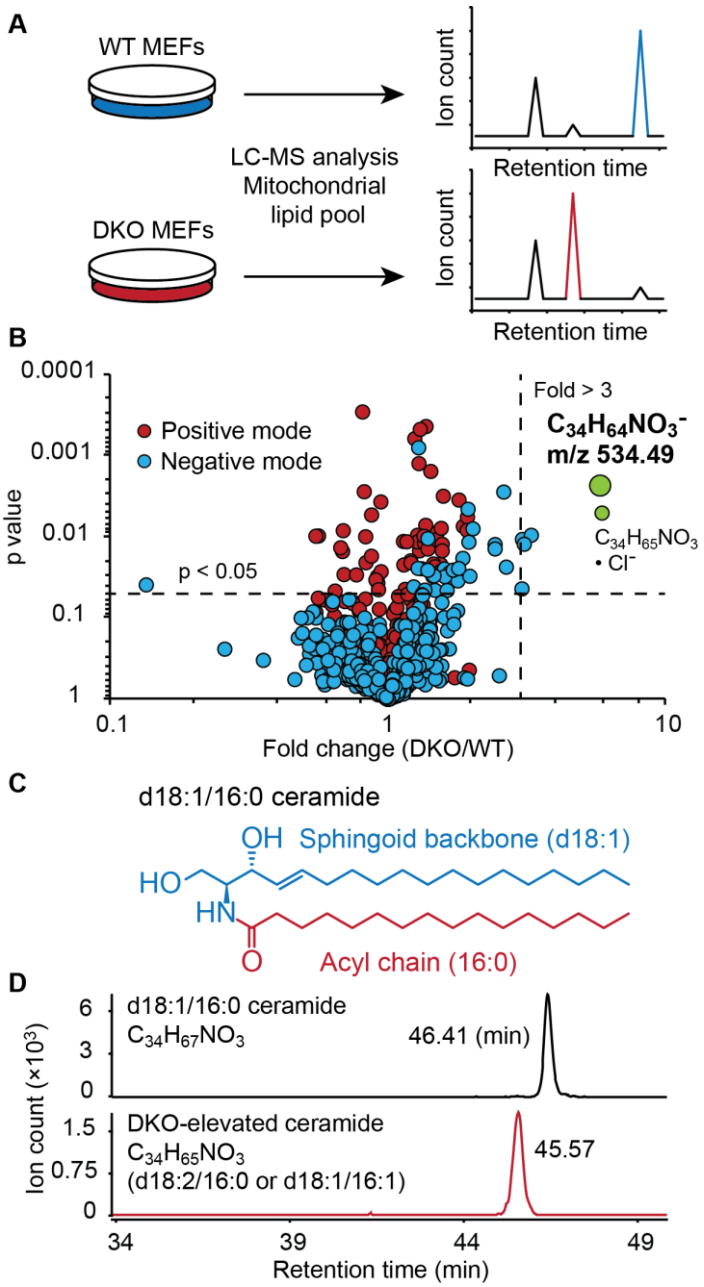

Figure 2.1. Comparative metabolite profiling of WT and DKO MEF mitochondria. A) Schematic of unbiased, comparative global lipidomic analysis of WT and DKO MEF mitochondrial lipid pools, allowing identification of metabolite changes between WT and DKO samples. B) Volcano plot of XCMS-detected parent ions between 5-50 min; each ion is plotted by its DKO/WT fold change and associated p-value. The DKO-elevated m/z 534 metabolite (predicted unsaturated C16 ceramide) and its chlorine adduct are in green. C) Structure of d18:1/16:0 ceramide. D) The DKO-elevated ceramide elutes ~1 min before d18:1/16:0 ceramide. Two-tailed Student's t-test, n=3.

The targeted list included free fatty acids, phospholipids, sphingolipids, acylglycerols, acylcarnitines, ether lipids, cholesterol and cholesterol esters. Targeted metabolite levels were largely unaltered between WT and DKO MEFs (Table 2.1), revealing that majority of lipid metabolic pathways were unaltered in the absence of BAX and BAK. Untargeted XCMS analysis in negative ionization mode uncovered a metabolite with detected m/z 534.4886 that was consistently elevated in DKO mitochondria relative to WT (Figure 2.1B). Discovery of a changing metabolite in a background of mostly unaltered metabolites demonstrates specificity in the metabolic pathway affected by loss of BAX and BAK.

Database search (LIPID MAPS [32] and METLIN [33]) with the exact neutral mass of the DKO-elevated metabolite afforded the molecular formula $C_{34}H_{65}NO_3$, which is characteristic of the sphingolipid ceramide. One of the major mammalian ceramide species, d18:1/16:0 ceramide (Figure 2.1C) [34, 35], has the molecular formula $C_{34}H_{67}NO_3$ that differs from the DKO-elevated ceramide by two hydrogen atoms. This difference corresponds to an additional unsaturation site in the DKO-elevated ceramide either in the sphingoid backbone (d18:2/16:0 ceramide) or acyl chain (d18:1/16:1 ceramide) in addition to the C4-C5 *trans* double bond common to the sphingoid backbone of all mature ceramides (Figure 2.1C) [36-38]. A decrease of ~1 min in retention time was also observed for the DKO-elevated ceramide relative to d18:1/16:0 ceramide (Figure 2.1D) in agreement with the typical phenomenon of decreasing retention time with increasing unsaturation in reversed-phase lipid chromatography [39], providing further evidence that the DKO-elevated metabolite belongs to the ceramide family. To conclusively identify the structure of the DKO-elevated ceramide we performed tandem MS and chemical synthesis.

Lipid class Acyl chain length	DKO/WT
Free fatty acid	
14:0	0.7
16:1	1.0
16:0	0.6
18:1	0.8
18:0	0.8
Phospholipid	
34:1 PA	0.8
36:2 PA	0.9
34:1 PE	1.0
36:2 PE	1.0
34:1 PC	0.9
36:3 PC	1.0
36:2 PC	0.9
34:1 PS	0.8
36:2 PS	0.9
Acylglycerol	
16:0 MAG	0.8
18:1 MAG	0.7
34:1 DAG	0.9
36:2 DAG	0.9
52:2 TAG	0.8
54:3 TAG	0.9
56:2 TAG	0.8
Cholesterol	1.2
Cholesterol ester	0.9

Table 2.1. Comparative metabolite profiling of WT and DKO MEF mitochondria revealed no significant change in the levels of most common lipids. PA: phosphatidic acid; PE: phosphatidylethanolamine; PC: phosphatidylcholine; PS: phosphatidylserine; MAG: monacylglycerol; DAG: diacylglycerol and TAG: triacylglycerol.

2.2.2. DKO-elevated metabolite is d18:2/16:0 ceramide

Tandem MS was performed on d18:1/16:0 and DKO-elevated ceramides to determine the location of the unsaturation site. Fragmentation of d18:1/16:0 ceramide in positive ionization mode yielded known product ions at m/z 282, 264 and 252 (Figure 2.2A, B) [40-42], all of which

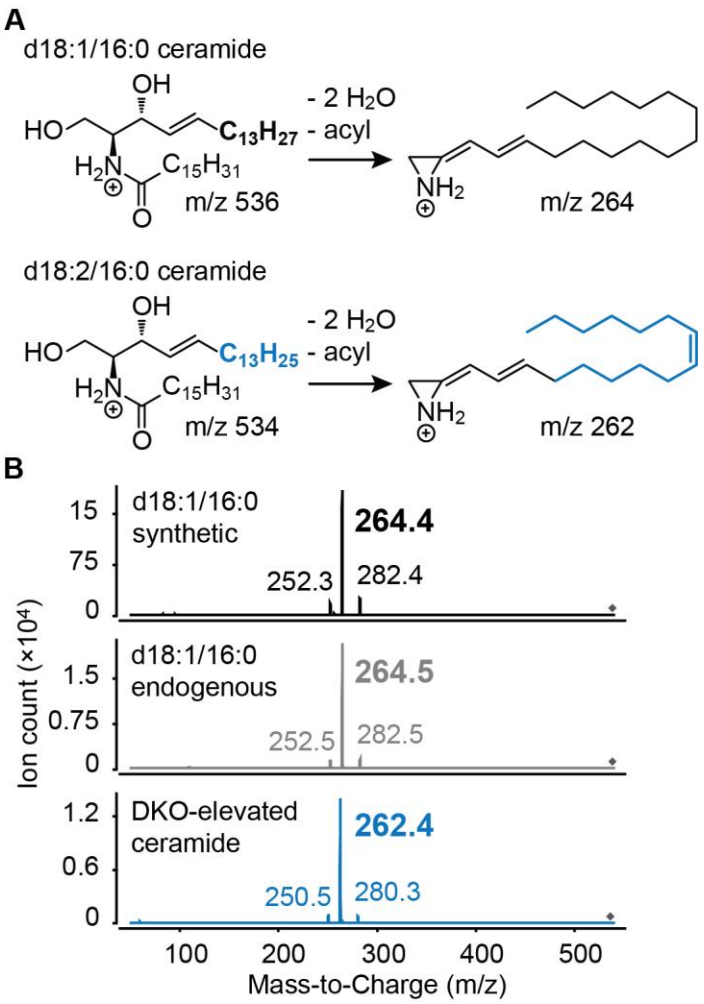

Figure 2.2. Tandem MS of differently saturated ceramides. A) Predicted major product ions for d18:1/16:0 and d18:2/16:0 ceramides in positive mode, corresponding to loss of two water molecules and acyl chain [40, 43]. B) Positive mode tandem MS of synthetic and endogenous d18:1/16:0 ceramide (m/z 538), and the DKO-elevated ceramide (m/z 536).

derive from the sphingoid backbone [40]. Tandem MS of the DKO-elevated ceramide yielded a similar group of product ions at m/z 280, 262 and 250, with each ion 2 Da (i.e. an additional unsaturation site) lower than its corresponding ion in the d18:1/16:0 spectrum (Figure 2.2B); this shift in all sphingoid-derived fragments suggests that the additional unsaturation site is located predominantly in the backbone such that the major isomer of the DKO-elevated ceramide is

d18:2/16:0 rather than d18:1/16:1. The d18:2/16:0 structural assignment was further validated by tandem MS in negative ionization mode, where the acyl chain-derived product ion (m/z 280) corresponds to a saturated (C16:0) acyl chain (Figure 2.3).

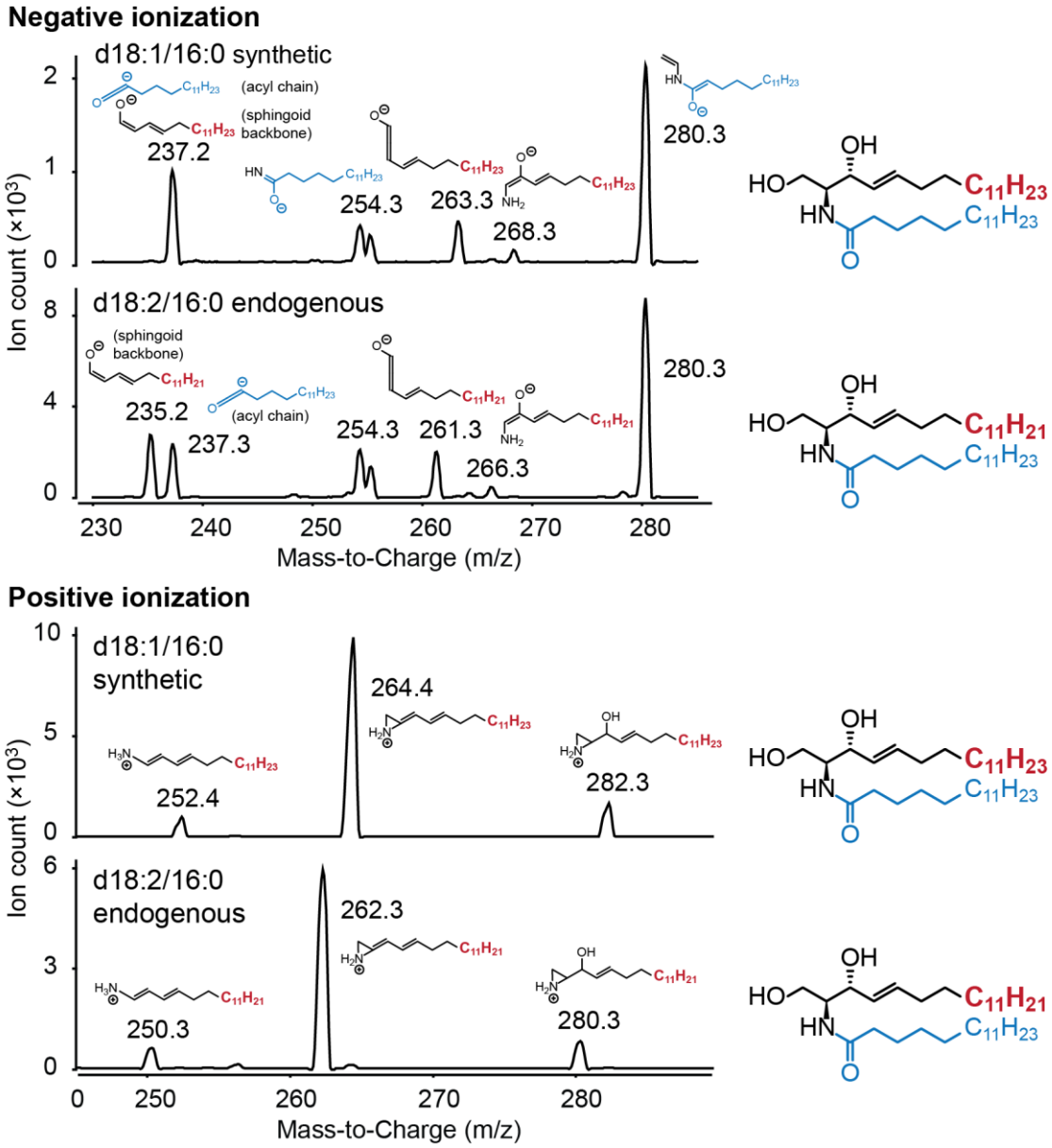

Figure 2.3. Tandem MS of synthetic d18:1/16:0 ceramide and DKO-elevated ceramide in negative and positive modes. Structures are based on published ceramide fragmentation predictions [40, 42-47].

2.2.3. *De novo* biosynthesis of d18:2/16:0 ceramide from palmitoleic acid

De novo ceramide biosynthesis occurs *via* coupling of palmitoyl (C16:0)-CoA to serine by serine palmitoyltransferase (SPT), reduction of 3-keto-sphinganine to sphinganine, acylation at the amine and desaturation of the resulting dihydroceramide at C4-C5 of the sphingoid backbone to yield mature d18:1 ceramide (Figure 2.4A) [35, 36]. This sequence implies two possible pathways for d18:2/16:0 ceramide biosynthesis: coupling of hexadecenoyl (16:1)-CoA to serine in place of palmitoyl-CoA, or presence of desaturases capable of forming additional double bonds across the sphingoid backbone. Given no additional mammalian desaturases are known to directly desaturate dihydroceramides [48], we tested the hypothesis that palmitoleic (16:1, *cis*-Δ^9) acid, the dominant 16:1 fatty acid isomer in murine tissues [49], can be incorporated into d18:2/16:0 ceramide through the *de novo* pathway.

Tolerance of the *de novo* ceramide biosynthetic pathway for palmitoleic acid was examined *via* stable isotope-labeled palmitoleic acid ($^2H_{14}$-16:1 FA, Figure 2.4B) feeding to MEFs. $^2H_{14}$-C16:1 FA was added to DKO MEFs in cell culture and the cells were harvested at 2 h and 21 h post-addition. A peak corresponding to $^2H_{12}$-d18:2/16:0 ceramide was observed at both 2 h and 21 h in fatty acid-treated MEFs but not DMSO controls (Figure 2.4B), indicating that palmitoleic acid can be incorporated into the *de novo* biosynthetic pathway in place of palmitic acid to generate d18:2 ceramide.

2.2.4. Structure validation of d18:2/16:0 ceramide with synthesized standards

d18:2/16:0 and d18:1/16:1 ceramides (Figure 2.5A) were chemically synthesized for further validation of the d18:2/16:0 ceramide structural assignment. The *cis* double bond in the d18:2/16:0 standard was installed at C11-C12 given this position would derive from the

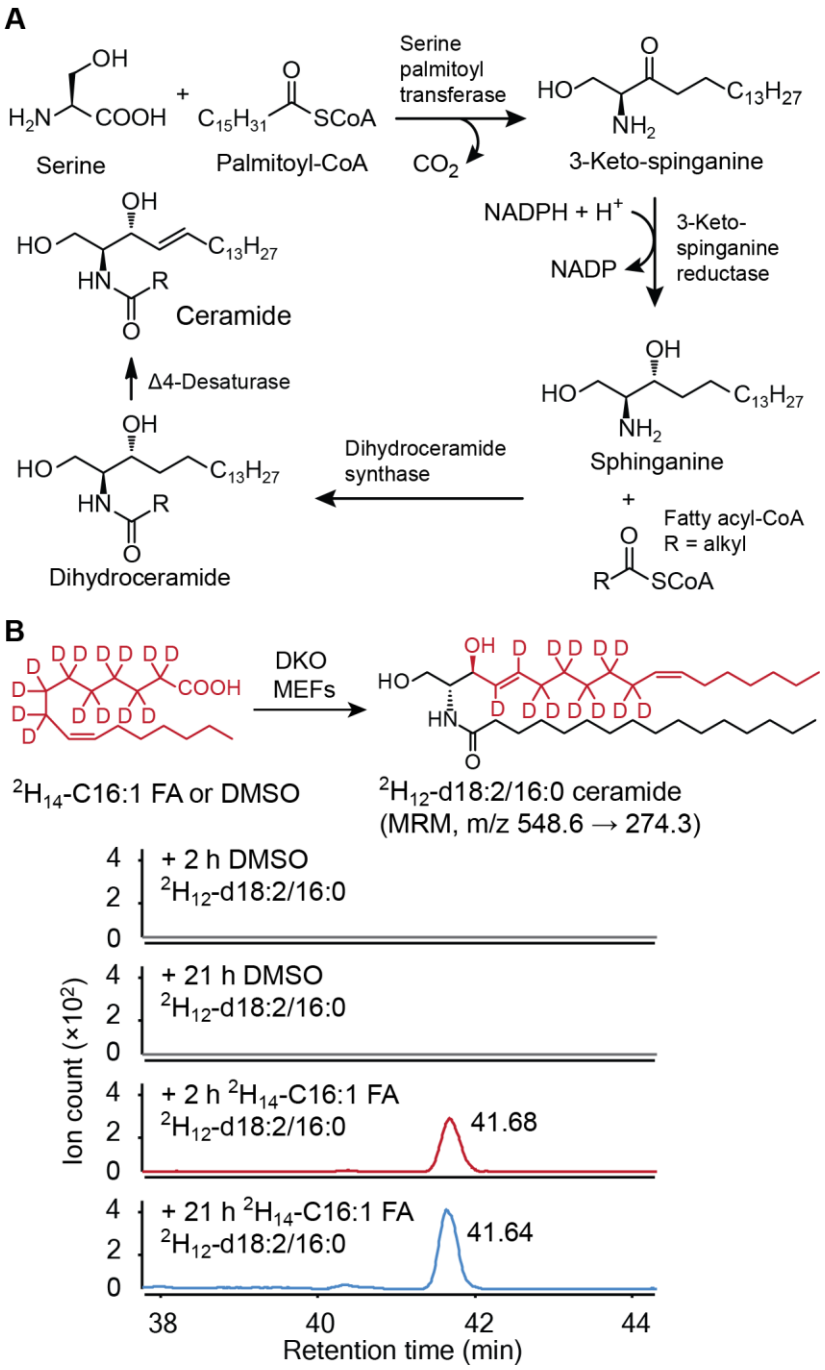

Figure 2.4. *De novo* biosynthesis of unsaturated ceramide from unsaturated fatty acid. A) Ceramide biosynthesis. B) Production of $^{2}H_{12}$-d18:2/16:0 ceramide (m/z 548.6 → 274.3) in DKO MEFs treated with $^{2}H_{14}$-palmitoleic acid.

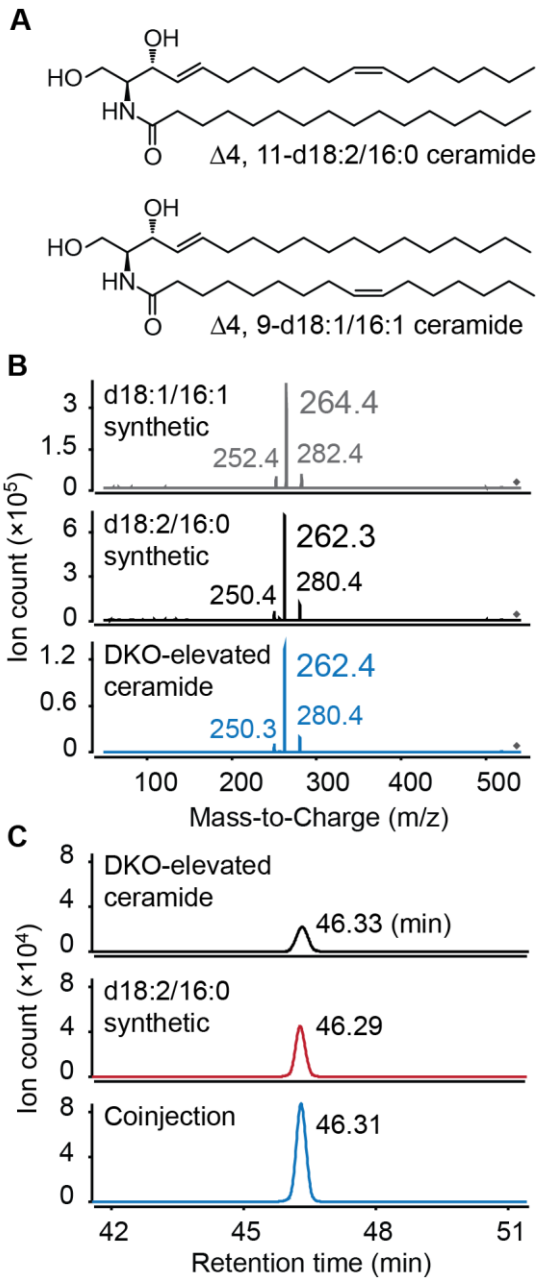

Figure 2.5. Structure validation of d18:2/16:0 ceramide with synthesized standards. A) Structures of synthesized d18:2/16:0 and d18:1/16:1 ceramides with unsaturation sites as shown. B) Positive mode tandem MS of synthetic d18:1/16:1 and d18:2/16:0 ceramides, and the DKO-elevated ceramide. C) Co-injection experiment for d18:2/16:0 ceramide.

incorporation of palmitoleic acid during *de novo* biosynthesis. Product ions (m/z 280, 262 and 250) from the fragmentation of synthetic Δ4, 11-d18:2/16:0 ceramide matched those of the

endogenous DKO-elevated ceramide as strong support of the latter's structure (Figure 2.5B). Importantly, fragmentation of the d18:1/16:1 isomer afforded the product ions m/z 282, 264 and 252 that did not match those from the DKO-elevated ceramide.

A co-injection experiment was also performed to verify that chromatographic retention of the DKO-elevated ceramide was consistent with that of the synthetic Δ4, 11-d18:2/16:0 ceramide. Endogenous lipid extract was mixed and co-injected with the Δ4, 11-d18:2/16:0 standard. Multiple reaction monitoring (MRM) targeting d18:2/16:0 ceramide (m/z 534.5 → 280.3) yielded a single peak with similar retention time and approximately twice the ion count of either the endogenous lipid extract or standard injected alone (Figure 2.5C), further supporting the Δ4-*trans*, 11-*cis*-d18:2/16:0 isomer as the most likely contributor toward the unsaturated C16 ceramide pool. Taken together, our data indicate that the major unsaturated C16 ceramide isomer in MEFs is d18:2/16:0 rather than d18:1/16:1 (or the dihydroceramide d18:0/16:2), with palmitoleic acid incorporation being a feasible pathway toward generation of the DKO-elevated ceramide. It is possible for the additional unsaturation site to be on a different backbone position that is beyond the resolution of our current chromatographic method; however, the prevalence of palmitoleic acid over additional 16:1 isomers [49] suggests that the majority of d18:2/16:0 ceramides is likely to be Δ4, 11-d18:2/16:0.

2.2.5. Unsaturated ceramides are selectively upregulated in DKO MEF mitochondria

Elevated d18:2/16:0 ceramide level in DKO MEF mitochondria relative to WT raises the question of whether a similar trend is present in additional ceramide species. To account for less abundant ceramide species not identified during untargeted XCMS analysis, absolute levels of saturated and unsaturated C16-C24 ceramides were determined by isotope-dilution MS (IDMS).

A $^{2}H_{31}$-d18:1/16:0 ceramide standard was added to biological samples during lipid extraction, allowing ratiometric quantification of endogenous ceramides. For each acyl chain both the saturated and unsaturated species were considered. We define saturated ceramide as any ceramide with a single double bond (i.e. d18:1/16:0) and unsaturated ceramide as species with two double bonds (i.e. d18:2/16:0 or d18:1/16:1, collectively designated d18:1/16:0 - 2H).

Of all detectable ceramides (Figure 2.6), species with C16 acyl chains occurred at highest levels (~300-1400 pmol/mg protein), followed by ceramides with C24 acyl chains (~120-600 pmol/mg protein) (Figure 2.7A). A decrease in abundance was observed for C18 and C20 ceramides (~4-17 pmol/mg protein), corresponding to a ~100-fold decrease relative to C16 ceramides (Figure 2.7A). Levels of most saturated ceramides (i.e. d18:1/16:0) were unchanged between DKO and WT mitochondria. By contrast, a significant increase (~2-4.5-fold) in most unsaturated ceramides was observed in the absence of BAX and BAK (Figure 2.7A).

Summing individual ceramide changes revealed a ~2-fold elevation in unsaturated-to-saturated (unsat/sat) total ceramide ratio in DKO MEF mitochondria relative to WT (Figure 2.7B), which was also observed for individual acyl chains (Figure 2.7C). No changes were observed in free palmitic and palmitoleic acid or in sphingadienine, sphingosine, sphinganine and sphingomyelins (Table 2.1, Figure 2.8A, B), suggesting that changes in ceramides were not the direct result of alteration in fatty acid composition or in ceramide derivatives along the sphingolipid metabolic pathway. No changes in ceramides were observed in the mitochondria of BAX and BAK single knockout (SKO) MEFs (Figure 2.9A-C), implying compensation between BAX and BAK in the regulation of ceramide distribution. A similar dependence on both BAX and BAK occurs in the case of mitochondrial morphogenesis, where DKO, but not SKO MEFs

displayed a short, fragmented mitochondrial morphology with reduced number of elongated tubules relative to WT [23].

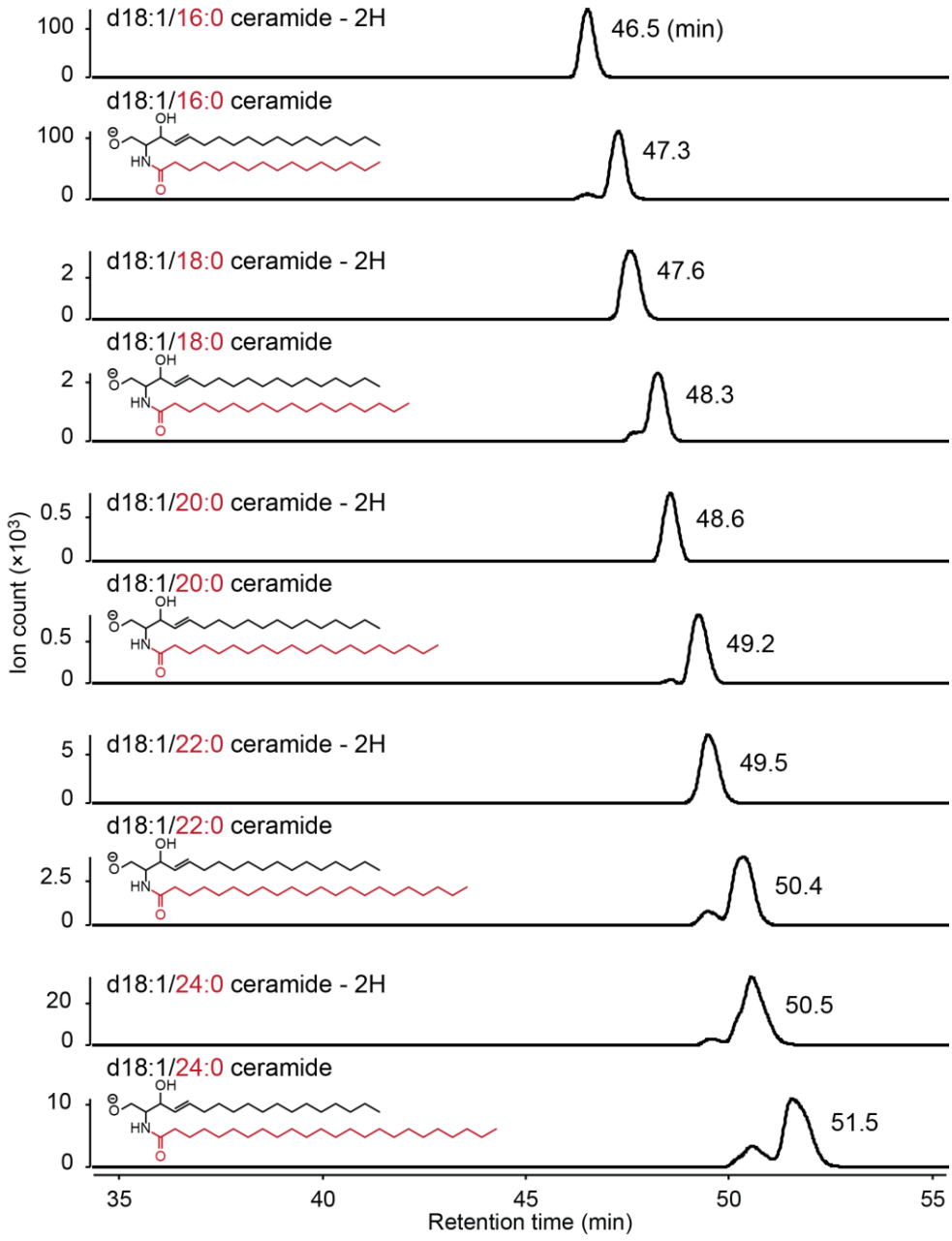

Figure 2.6. Detectable ceramides in MEFs.

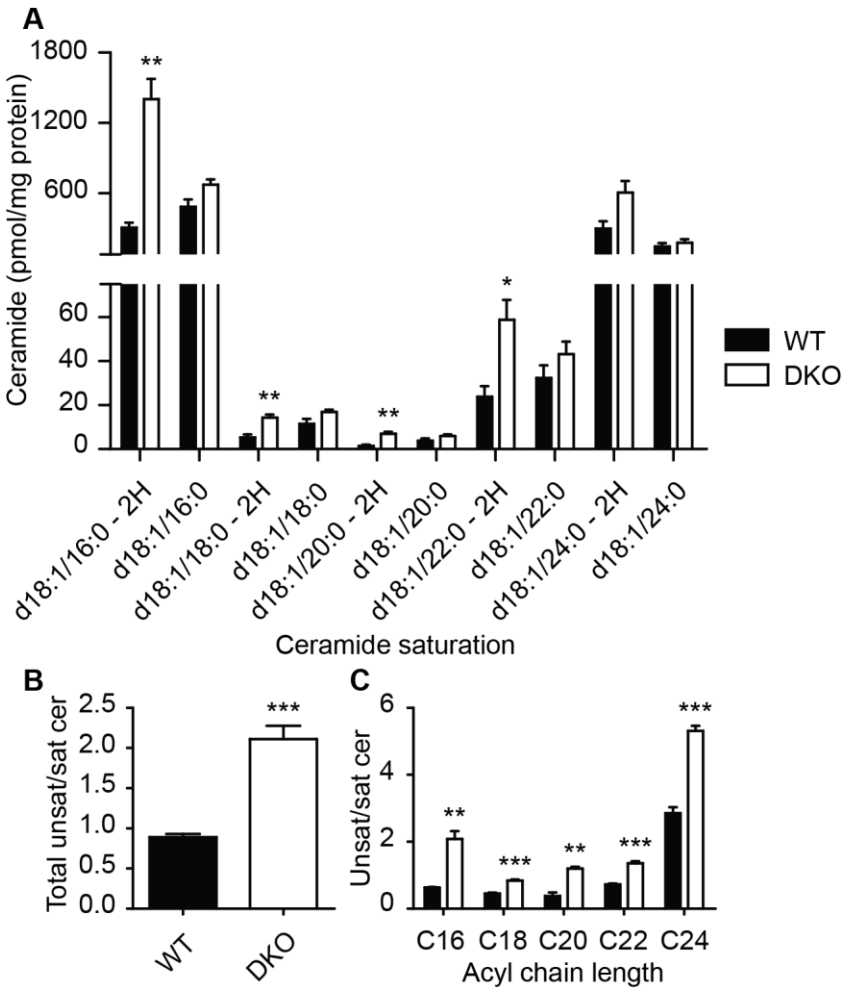

Figure 2.7. Absolute quantification of ceramides reveals elevated unsaturated-to-saturated ceramide ratio in DKO MEFs relative to WT. A) Absolute quantification of C14-C24 ceramides by IDMS, using $^{2}H_{31}$-d18:1/16:0 ceramide as standard. B) Unsaturated-to-saturated total mitochondrial ceramide ratio for WT and DKO MEFs. C) Unsaturated-to-saturated mitochondrial ceramide ratio by ceramide acyl chain length. *, $p \leq 0.05$, **, $p \leq 0.01$, ***, $p \leq 0.001$. Two-tailed Student's t test, SEM, n=3.

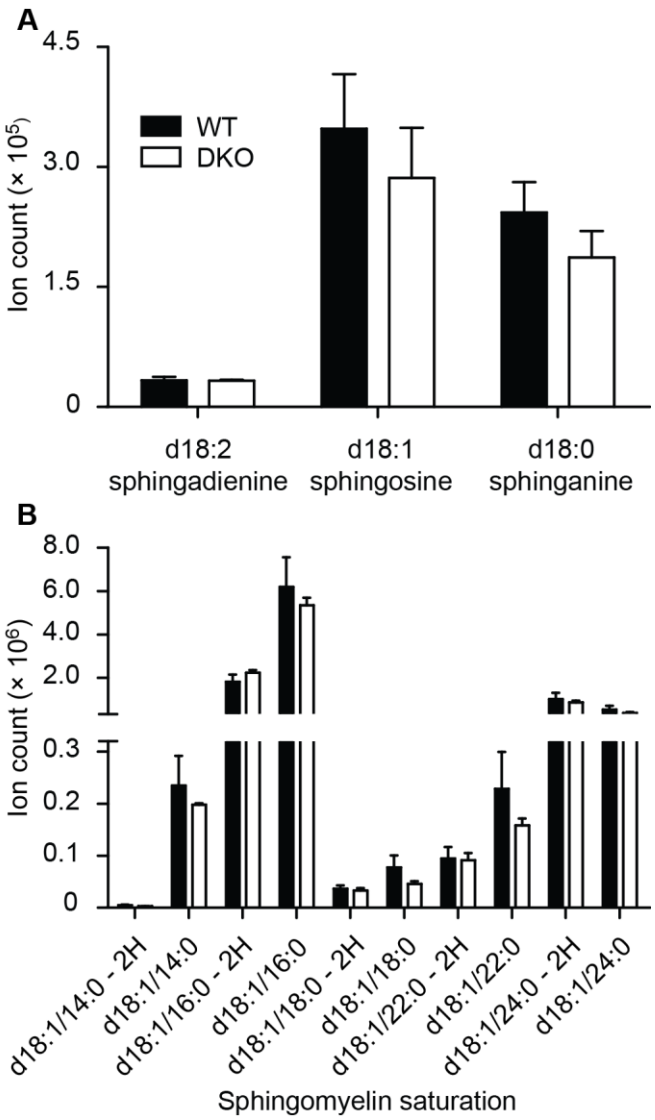

Figure 2.8. Relative levels of additional sphingolipids in WT and DKO MEF mitochondria. A) Sphingadienine, sphingosine and sphinganine levels in WT and DKO MEF mitochondria. B) Sphingomyelin levels in WT and DKO MEF mitochondria. No statistically significant changes were observed. Two-tailed Student's t test, SEM, n=3.

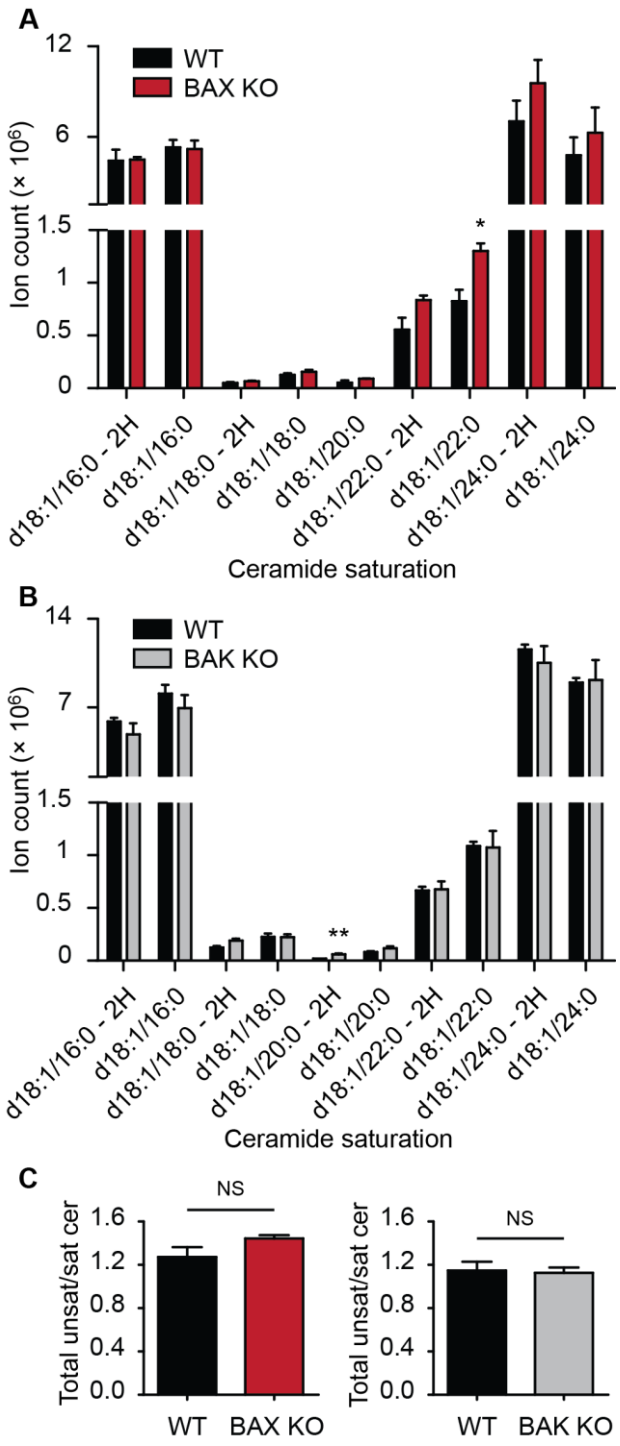

Figure 2.9. Ceramide levels in WT and SKO MEF mitochondria. A) C16-C24 ceramide levels in WT and BAX KO MEF mitochondria. B) C16-C24 ceramide levels in WT and BAK KO MEF mitochondria. C) Unsaturated-to-saturated total ceramide ratios in WT and SKO MEF mitochondria. Two-tailed Student's t test, SEM, n=3.

2.2.6. Increase in unsaturated ceramides is driven by upregulation of d18:2 ceramides in MEFs and iBMKs

The DKO-elevated unsaturated-to-saturated ceramide ratio in the case of the C16 acyl chain (Figure 2.7C) could be largely attributed to elevation in the d18:2/16:0 ceramide isomer based on tandem MS (Figure 2.2B). To test if absence of BAX and BAK selectively upregulated the d18:2 isomer for all DKO-elevated unsaturated ceramides, location of the additional unsaturation site (i.e. backbone or acyl chain) was determined for C16-C24 ceramides *via* MRM in negative mode, where the product ion corresponds to the acyl chain (Figures 2.3, 2.10A). By measuring levels of unique product ions generated from precursor ions the relative abundances of different unsaturated ceramide isomers (i.e. d18:2/16:0 and d18:1/16:1) could be determined.

Distinguishing two isobaric ceramide isomers requires two unique MRM transitions. d18:2/16:0 and d18:1/16:1 ceramides, for example, share the parent ion m/z 534, but generate distinct product ions upon fragmentation in negative mode. Fragmentation of d18:2/16:0 ceramide produces the major product ion m/z 280 corresponding to a saturated (16:0) acyl chain (Figures 2.3, 2.10A), thus allowing unambiguous identification and quantification of this isomer by monitoring its characteristic precursor-to-product ion transition m/z 534 → 280. Fragmentation of d18:1/16:1 ceramide affords the product ion m/z 278 corresponding to an unsaturated (16:1) acyl chain, and the transition m/z 534 → 278. Taken together, MRM allows simultaneous quantification of all saturated and unsaturated C16-C24 ceramides with different degrees and locations of unsaturation, given the unique transition associated with each isomer (Table 2.2). The increased sensitivity of MRM also enables detection of ceramide isomers on the whole cell (~10^7 cells) level in addition to mitochondria (isolated from ~2.5×10^8 cells).

Ceramide isomer	Precursor ion	Product ion	Fragmentor (V)	CE (V)
C18:0/C16:2	534.5	276.2	132	26
C18:1/C16:1	534.5	278.2	132	26
C18:2/C16:0	534.5	280.3	132	26
C18:1/C16:0	536.5	280.3	132	26
C18:0/C18:2	562.5	304.3	132	26
C18:1/C18:1	562.5	306.3	132	26
C18:2/C18:0	562.5	308.3	132	26
C18:1/C18:0	564.5	308.3	132	26
C18:0/C20:2	590.6	332.3	132	26
C18:1/C20:1	590.6	334.3	132	26
C18:2/C20:0	590.6	336.3	132	26
C18:1/C20:0	592.6	336.3	132	26
C18:0/C22:2	618.6	360.3	132	26
C18:1/C22:1	618.6	362.3	132	26
C18:2/C22:0	618.6	364.3	132	26
C18:1/C22:0	620.6	364.3	132	26
C18:0/C24:2	646.6	388.4	132	26
C18:1/C24:1	646.6	390.4	132	26
C18:2/C24:0	646.6	392.4	132	26
C18:1/C24:0	648.6	392.4	132	26

Table 2.2. List of MRM transitions and instrument parameters for quantification of C16-C24 ceramide isomers.

Following MRM quantification of individual ceramide isomers, the unsaturated-to-saturated ratio between DKO and WT MEFs was calculated with the unsaturated fraction being either ceramides containing an unsaturated (d18:2) backbone ($sph_{unsat/sat}$) or those with a sphingosine (d18:1) backbone and unsaturated acyl chain ($acyl_{unsat/sat}$). The unsaturated-to-saturated ratio was calculated for both total ceramides (Figure 2.10B) and isomers of individual acyl chains on the mitochondrial (Figure 2.10C) and whole cell (Figure 2.10D) levels. Absence of BAX and BAK preferentially increased the $sph_{unsat/sat}$ ratio for acyl chains C16-C24, but did not consistently alter $acyl_{unsat/sat}$ ratios (Figure 2.10C, D); this change was less pronounced on the whole cell level relative to mitochondria, implying that this effect may be more localized to an organelle.

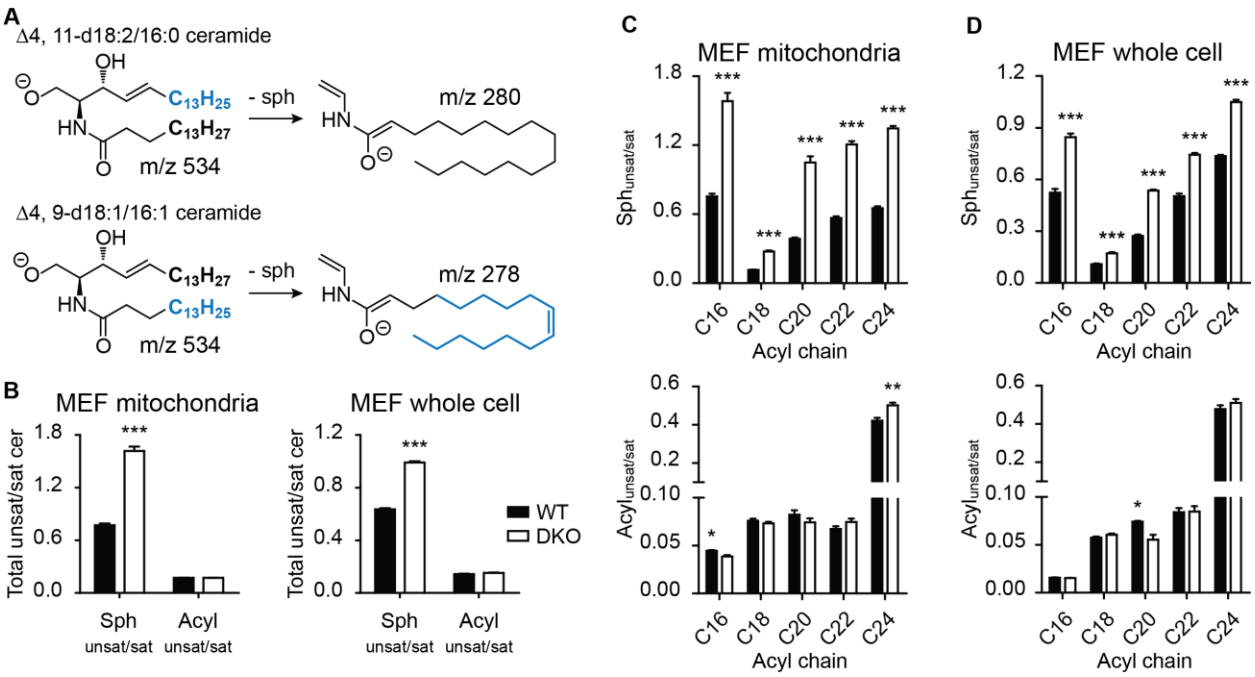

Figure 2.10. Selective regulation of MEF unsaturated ceramide pools by BAX and BAK. A) Predicted major fragments for d18:1/16:1 and d18:2/16:0 ceramides in negative mode, corresponding to loss of the sphingoid backbone [44, 47]. B) Unsaturated-to-saturated total mitochondrial and whole cell ceramide ratios for WT and DKO MEFs. The unsaturated ceramide fraction was calculated as either the sum of all d18:2 ceramides ($Sph_{unsat/sat}$) or as the sum of all unsaturated d18:1 ceramides with the additional unsaturation site in the acyl chain ($Acyl_{unsat/sat}$). C) MEF mitochondrial $Sph_{unsat/sat}$ and $Acyl_{unsat/sat}$ ratios for individual acyl chains. D) MEF whole cell $Sph_{unsat/sat}$ and $Acyl_{unsat/sat}$ ratios for individual acyl chains. *, $p \leq 0.05$, **, $p \leq 0.01$, ***, $p \leq 0.001$. Two-tailed Student's t test, SEM, n=3-5.

To assess the generality of our observation, MRM quantification of ceramide isomers was repeated in mitochondrial (Figure 2.11A) and whole cell (Figure 2.11B) fractions of WT and DKO immortalized baby mouse kidney epithelial cells (iBMKs). iBMKs were chosen given availability of the BAX, BAK double knockout model and usage of this cell line in previous study of ceramides in apoptosis [50]. Importantly, absence of BAX and BAK preferentially increased the $sph_{unsat/sat}$ ratio for most C16-C24 acyl chains in iBMKs, in agreement with observation in MEFs (Figure 2.11A, B). A corresponding decrease in $acyl_{unsat/sat}$ ratio was also detected for several acyl chains in DKO iBMK mitochondria (Figure 2.11A), a potential

consequence of diversion of the unsaturated fatty acid pool toward d18:2 ceramide biosynthesis. Taken together, our findings suggest that BAX and BAK selectively modulate the metabolism of distinct unsaturated ceramide pools in different cell types.

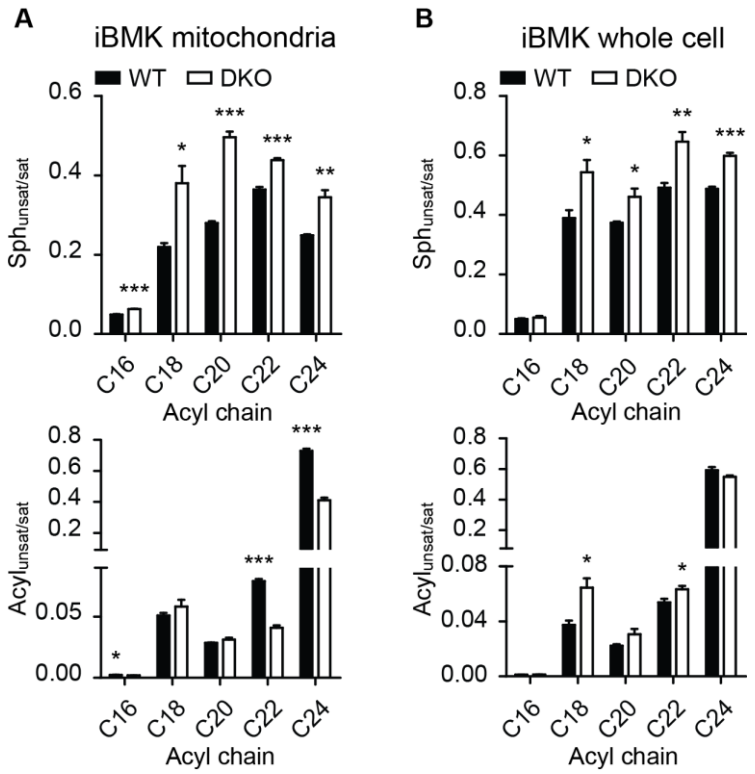

Figure 2.11. Selective regulation of iBMK unsaturated ceramide pools by BAX and BAK. A) iBMK mitochondrial $Sph_{unsat/sat}$ and $Acyl_{unsat/sat}$ ratios for individual acyl chains. B) iBMK whole cell $Sph_{unsat/sat}$ and $Acyl_{unsat/sat}$ ratios for individual acyl chains. *, $p \leq 0.05$, **, $p \leq 0.01$, ***, $p \leq 0.001$. Two-tailed Student's t test, SEM, n=3-5.

2.2.7. Serum starvation raises unsaturated-to-saturate ceramide ratio in MEFs

Selective upregulation of d18:2 ceramides in unperturbed DKO cells raises the question of whether this altered lipid state could be affected by cellular stress or apoptosis. Ceramide elevation is a widely observed phenomenon across multiple cell types in response to serum starvation [51], UV irradiation [50, 52] or chemical treatments [53-55]. To address the question

of whether stress-induced ceramide upregulation correlates with ceramide unsaturation, WT and DKO MEFs were deprived of FBS for 13 h, and resulting changes in ceramide isomer levels relative to control quantified by MRM. In agreement with literature [37, 51], serum starvation raised total ceramide levels in WT and DKO MEFs (Figure 2.12A) with contribution from both saturated and unsaturated species (data not shown). Importantly, serum starvation also increased

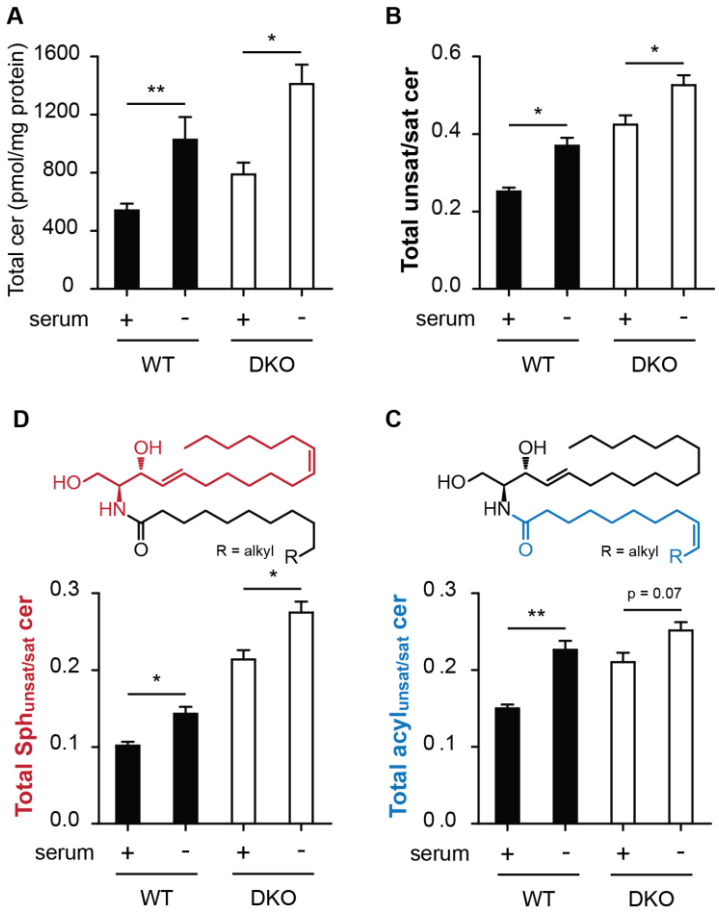

Figure 2.12. Serum starvation raises unsaturated-to-saturated ceramide ratio in MEFs. A) Total ceramide level in non-serum starved and serum starved MEFs. B) Total unsaturated-to-saturated ceramide ratio in non-serum starved and serum starved MEFs. Total unsaturated ceramide is the sum of Sph_{unsat} and $Acyl_{unsat}$ species. C) Total $Sph_{unsat/sat}$ ratios in non-serum starved and serum starved MEFs, structure of sphingoid backbone-unsaturated (red) ceramide is on top of graph. D) Total $Acyl_{unsat/sat}$ ratios in non-serum starved and serum starved MEFs, structure of acyl chain-unsaturated (blue) ceramide is on top of graph. *, $p \leq 0.05$, **, $p \leq 0.01$, ***, $p \leq 0.001$, two-tailed Student's t test, SEM, n=5.

the total unsaturated-to-saturated ceramide ratio (Figure 2.12B) by raising the levels of both backbone-unsaturated (Figure 2.12C) and acyl chain-unsaturated ceramides (Figure 2.12D) to a greater extent than saturated species. Our findings lead to the hypothesis that differently saturated ceramides are differentially regulated due to their distinct biological actions.

2.2.8. d18:2/16:0 ceramide treatment of MEFs and iBMKs leads to greater viability loss than d18:1/16:0 ceramide

The selective upregulation of endogenous d18:2 ceramides in the absence of BAX and BAK and during serum starvation, in combination with previous studies demonstrating increased resistance of DKO cells toward apoptosis, [9, 11, 12] suggest that differently saturated ceramides may exert distinct influences over cellular viability. To test this hypothesis, WT and DKO MEFs and iBMKs were treated with d18:2/16:0 or d18:1/16:0 ceramide at varying doses for 24 h, and viability assessed by ATP measurement. d18:2/16:0 ceramide treatment led to significantly higher dose-dependent viability loss than d18:1/16:0 ceramide treatment in both MEFs and iBMKs (Figure 2.13). Taken together, our findings suggest that BAX and BAK could regulate cell fate by tuning the ratio of ceramide pools with different effects on cellular viability.

2.3. Discussion

A global lipidomics approach was used to identify metabolite changes in the absence of the key pro-apoptotic proteins BAX and BAK. Given the additional role of BAX and BAK in mitochondrial morphogenesis and the fact that oligomerized BAX and BAK act at the mitochondria to facilitate MOMP during apoptosis [6, 23], we hypothesized that these proteins could be modulating lipid levels at the mitochondrial membrane, resulting in altered lipid

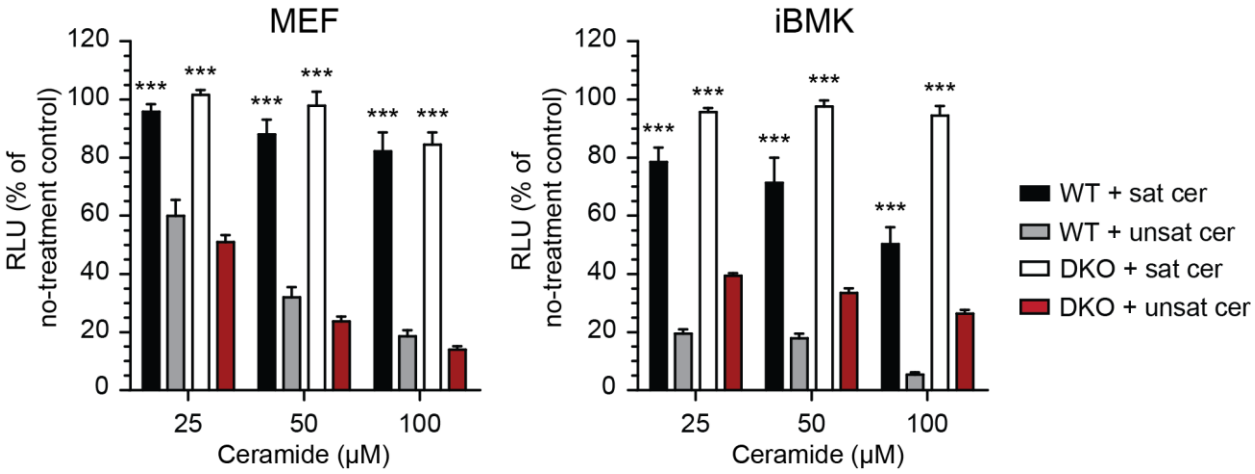

Figure 2.13. Viability of MEFs and iBMKs treated with d18:2/16:0 or d18:1/16:0 ceramide. *, $p \leq 0.05$, **, $p \leq 0.01$, ***, $p \leq 0.001$, two-tailed Student's t test, SEM, n=5.

composition and subsequently, the changes in membrane structure necessary for successful propagation of the apoptotic signal. In support of our hypothesis, LC–MS analysis of whole cell and mitochondrial lipids from WT and DKO MEFs revealed selective upregulation of d18:2 ceramides in the absence of BAX and BAK.

The roles of ceramides in apoptosis have been examined in multiple experimental settings [17, 19]. Modeling and experimental studies in liposomes and isolated mitochondria support assembly of saturated C2 and C16 ceramides into channels to facilitate protein release [56-58]. Ceramides act synergistically with BAX to cause membrane permeabilization [59], while anti-apoptotic BCL-2 proteins promote channel disassembly [60]. Interestingly, dihydroceramides have been shown to hinder channel formation [61], suggesting that distinct ceramide metabolites could exert opposing influences over apoptosis. Endogenous ceramide level increases in response to a wide range of apoptotic signals in multiple cell types [19], and ceramide macrodomains in the mitochondrial outer membrane have been shown to act as preferential sites of BAX translocation and oligomerization during irradiation-induced apoptosis [62].

While the link between ceramide and apoptosis has been confirmed in different biological systems, it is important to note that most studies have focused on saturated ceramides [50, 56-58, 61, 62], thus the effect of ceramide unsaturation on the lipid's ability to influence apoptosis remains unclear. Interestingly, comprehensive measurement of ceramide isomers in human fibroblasts revealed that > 90% of d18:2 ceramides were present in the detergent-soluble fraction while the major ceramide species (d18:1/16:0) localized partially (~42 %) to the detergent-resistant fraction [34], in agreement with ceramide participation in membrane rafts and macrodomains that facilitate apoptosis [62-64]. This is not surprising when considered in the context of lipid structure, as the *cis* double bond introduces bending in the d18:2 backbone that could hinder tight packing of d18:2 ceramides into detergent-insoluble structures.

Our LC–MS analysis revealed selective upregulation of unsaturated ceramides in the absence of BAX and BAK, which could be attributed to elevation in the d18:2 ceramide isomer. To our knowledge this is the first report of BAX and BAK regulation of endogenous sphingolipid metabolism, and more specifically, selective regulation of ceramides based on their backbone structure. It is difficult to obtain these results using traditional ceramides analysis tools that do not allow simultaneous quantification of differently saturated isomers. Consequently, the selective regulation of d18:2 ceramides may be a more general phenomenon, and the current strategy could aid in the discovery of similar lipid alterations in different biological settings. This is of particular interest toward the study of apoptosis, where ceramides have been known to regulate this process. Modeling and empirical evidences support ceramide assembly into lipid domains or channels that facilitate BAX activation and protein diffusion during apoptosis [56, 57, 62], and ceramide release has been observed in multiple cell types in

response to a range of apoptotic stimuli [19, 50-55]; it may be of interest to revisit these studies to determine the effect of ceramide unsaturation on these processes.

Interaction between sphingolipids and BCL-2 proteins has also been examined [22]. Sphingosine-1-phosphate and the sphingosine breakdown product hexadecenal cooperated with BAK and BAX respectively to promote membrane permeabilization in *in vitro* reconstitution studies [22]. Importantly, hexadecenal, but not the saturated hexadecanal, was shown to physically associate with BAX in a chloroform-spotted array [22]. The cooperation of different sphingolipids with BAX and BAK in promoting membrane permeabilization implies that it may also be possible for distinct ceramide species to cooperate with BAX and BAK in regulating the cell state.

Serum starvation raised unsaturated-to-saturated ceramide ratio in MEFs, and d18:2/16:0 ceramide addition to MEFs and iBMKs resulted in significantly higher viability loss than d18:1/16:0 ceramide species. While the d18:1 backbone of saturated ceramides may facilitate more efficient assembly into pro-apoptotic lipid domains, preferential localization of d18:2 ceramides in the detergent-soluble fraction [34] also suggests that unsaturated ceramides may be less sequestered in membranes and therefore more freely shuttled across the cytosol as mediators of cellular homeostasis. Mechanisms of ceramide-induced cell death are complex and include caspase-dependent and independent pathways [65-67]. Ceramides have been implicated in THFα-induced apoptosis [68], and serum starvation or exogenous C2 ceramide addition led to JNK/SAPK activation and apoptosis of WT Jurkat cells, but not Fas-resistant mutant clones, suggesting that ceramides may also function in the Fas pathway [69]. Ceramides trigger autophagy in rich media [37, 70, 71] and starve cells to death *via* nutrient transporters down-regulation [37]. The sequential nature of apoptosis and autophagy, in combination with

preferential localizations of ceramide species based on structure [34], suggest that successful propagation of these events may require temporal regulation by different ceramide populations. In the context of our findings, DKO-dependent upregulation of ceramides that more potently reduces cellular viability may be a compensatory mechanism toward hindering excessive cellular survival in the absence of BAX and BAK, and suggests that these proteins could regulate cell fate by tuning the relative abundances of distinct ceramide populations with different impacts on cellular homeostasis (Figure 2.14).

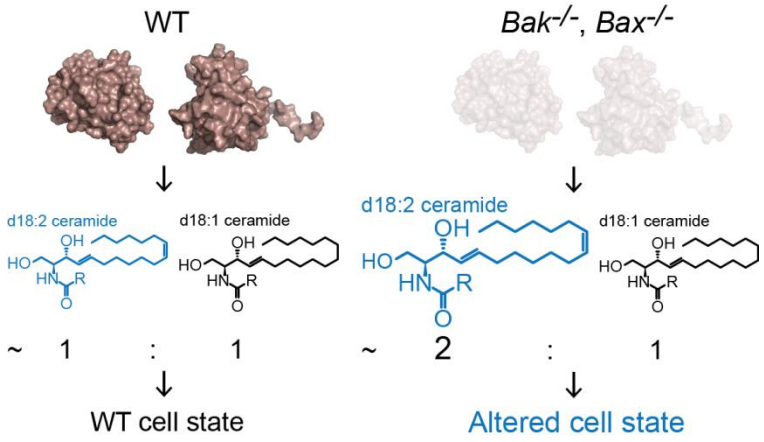

Figure 2.14. A model illustrating selective up-regulation of d18:2 ceramides in the absence of BAX and BAK, which may alter downstream cellular phenotypes. PDB ID for BAK (right): 2JCN; PDB ID for BAX (left): 1F16.

Our findings also raise key questions including the cellular mechanism that links BCL-2 proteins to ceramide metabolism. Ceramide elevation in response to apoptotic stimuli has been attributed to sphingomyelin hydrolysis, *de novo* biosynthesis and/or sphingosine salvage depending on apoptotic signal and cell type [19]. BAK, but not BAX was recently shown to be required for UV-C-induced long chain ceramide generation *via* CerS in multiple cell types [50]; interestingly, no change in *CerS* mRNA or protein was observed in the absence of BAK, suggesting that BAK may be regulating CerS post-translationally [50]. Given the complexity in

the biochemical regulation of ceramide levels that encompasses multiple production pathways, a comprehensive approach will be needed to fully explain the connection between ceramides and BCL-2 proteins.

2.4. Conclusion

While the mitochondrial apoptotic pathway relies heavily on its protein machinery, evidences support an equally important role for lipids and lipid metabolism in promoting or inhibiting apoptosis at the mitochondria [16, 19]. To understand the interplay between lipids and the key pro-apoptotic proteins BAX and BAK, we used a comparative lipidomics approach to identify metabolite changes in WT and DKO MEFs. Our analysis revealed selective upregulation of the unsaturated ceramide pool in DKO MEFs, which could be further extended into iBMKs. Interestingly, the additional unsaturation site is present more frequently in the sphingoid backbone than the acyl chain, and absence of BAX and BAK selectively upregulates d18:2 ceramides. Addition of heavy-labeled palmitoleic acid to MEFs led to production of the corresponding heavy-labeled d18:2/16:0 ceramide, supporting *de novo* biosynthesis from unsaturated fatty acid as a potential pathway toward unsaturated ceramide generation. We also demonstrate that serum starvation raises the total unsaturated-to-saturated ceramide ratio in MEFs, and d18:2/16:0 ceramide treatment leads to greater loss of MEFs and iBMKs viability than d18:1/16:0 ceramide. Our findings identify an additional function for BAX and BAK in modulating endogenous ceramide distribution, and suggest that BCL-2 proteins could influence cellular biology through regulation of lipid metabolism.

2.5. Methods

2.5.1. Materials

Grubbs second generation catalyst, N-succinimidyl palmitate, palmitoleic acid and triethylamine, vinyl magnesium bromide, and anhydrous tetrahydrofuran were purchased from Sigma-Aldrich. (*S*)-*Garner* aldehyde was from TCI America. Oct-7-enal was from Novel Chemical Solutions. Heptyltriphenylphosphonium bromide, sodium *bis*(trimethylsilyl)amide and oxalyl chloride were from Alfa Aesar. (2*S*, 3*R*, *E*)-2-aminooctadec-4-ene-1, 3-diol (d18:1 sphingosine) was from Avanti Polar Lipids. Pyridine was from Mallinckrodt Chemicals and all additional solvents were from EMD Chemicals.

For mass spectrometry, ammonium formate (516961) and ammonium hydroxide (338818) were purchased from Sigma-Aldrich. Formic acid (06440) was from Fluka. Water (365-4), methanol (230-4), isopropanol (323-4), acetonitrile (017-4) and chloroform (049-1L) were from Honeywell Burdick & Jackson. All analytical columns were from Phenomenex. The precolumn (C-130B) and C18 silica (C-603) were from Upchurch Scientific. C4 silica (214TPB1520) was from Western Analytical Products.

2.5.2. Tissue culture and harvest

MEFs were maintained at 37 ºC with 5 % CO_2 in Dulbecco's Modified Eagle Medium (4.5 g/ml glucose, without sodium pyruvate) supplemented with FBS (10 %), penicillin, streptomycin, non-essential amino acids and L-glutamine (final concentration is 6 mM). To ensure consistent cell growth between WT and DKO MEFs, all cells were passaged at least three times and re-plated based on cell count at each passage. Cells were harvested at confluency by

scraping and mitochondria were isolated immediately upon harvest. A cell count of ~2.5×10^8 is necessary to ensure successful mitochondria preparation.

2.5.3. Mitochondria isolation and lipid extraction

Mitochondria were isolated from MEFs following known protocol [30], using a sucrose isolation buffer (250 mM sucrose, 10 mM Tris-HCl, 0.1 mM EGTA · 4 Na, pH 7.4). Lipid extraction was performed with modifications on the Bligh and Dyer procedure [29]. Mitochondrial or whole cell pellets were Dounce homogenized in a 2:1:1 mixture of chloroform:methanol:citric acid buffer (100 mM trisodium citrate, 1 M NaCl, pH 3.6). The samples were centrifuged at 2200 g, 4 °C for 6 min in a glass vial, allowing separation between organic (bottom) and aqueous (top) layers. The organic layer was carefully removed with a glass Pasteur pipet, transferred to a new glass vial and concentrated under a gentle stream of nitrogen. Lipids were reconstituted in chloroform, and 1/4-1/8 of sample used for LC–MS analysis.

2.5.4. LC–MS general profiling of WT, DKO and SKO MEFs

General profiling was performed on an Agilent 6220 LC-ESI-TOF instrument and data were acquired in both positive and negative ionization modes. For negative mode a Gemini (Phenomenex) C18 column (5 µm, 4.6 mm × 50 mm) was used with a precolumn (C18, 3.5 µm, 2 mm × 20 mm). Solvent A was 95: 5 water: methanol with 0.1 % ammonium hydroxide, and solvent B was 60:35:5 isopropanol:methanol:water with 0.1 % ammonium hydroxide. For positive mode a Luna (Phenomenex) C5 column (5 µm, 4.6 mm × 50 mm) was used with a precolumn (C4, 3.5 µm, 2 mm × 20 mm). Solvent A was 95: 5 water: methanol with 0.1 % formic acid and 5 mM ammonium formate, and solvent B was 60:35:5

isopropanol:methanol:water with 0.1 % formic acid and 5 mM ammonium formate. Identical gradient was used for both modes. The gradient was held at 0 % B between 0 and 5 min, changed to 20 % B at 5.1 min, increased linearly from 20 % B to 100 % B between 5.1 min and 45 min, held at 100 % B between 45.1 min and 53 min, and returned to 0 % B at 53.1 min and held at 0 % B between 53.1 min and 60 min to allow column re-equilibration. The flow rate was maintained at 0.1 mL/min between 0 and 5 min to counter pressure increase due to chloroform injection. The flow rate was 0.4 mL/min between 5.1 min and 45 min, and 0.5 mL/min between 45.1 min and 60 min. The injection volume was 30 µL. The capillary, fragmentor and skimmer voltages were 3.5 kV, 100 V and 60 V, respectively. The drying gas temperature was 350 °C, the drying gas flow rate was 10 L min^{-1} and the nebulizer pressure was 45 psi. Data were collected in both profile and centroid modes using a mass range of 100-1500 Da.

Data were analyzed *via* targeted and untargeted approaches. For the targeted approach, manual integration of EICs corresponding to exact m/z of known metabolites was performed in Agilent Quantitative Analysis. Statistical significance was determined by two-tailed Student's t-test. For the untargeted approach, raw data were converted from .d into .mzXML format *via* trapper [72]; WT and knockout samples were sorted into two groups and analyzed by XCMS [31]. Following filtering of XCMS output files by statistical significance, fold change and reproducibility across independent data sets, the remaining metabolite changes were further verified by manual integration in Qualitative Analysis and two-tailed Student's t-test. Confirmed unknown metabolites could then be identified through database search and tandem MS.

2.5.5. Synthesis of d18:2/16:0 ceramide

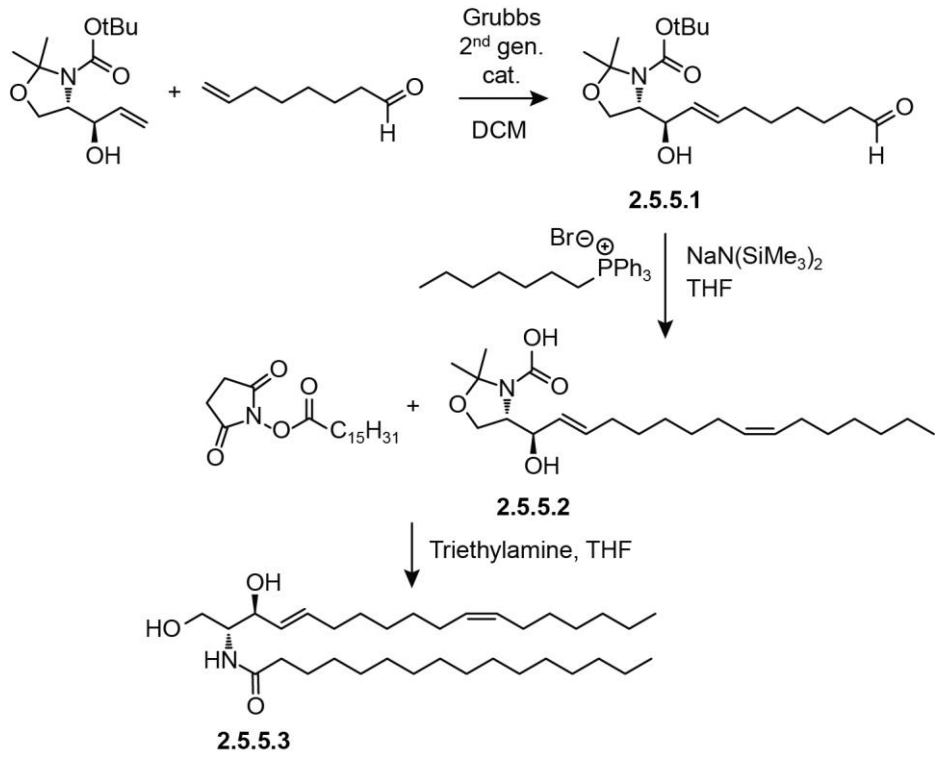

Figure 2.15. synthesis of d18:2/16:0 ceramide.

2.5.5.1. Synthesis of (*S*)-*tert*-butyl 4-((*R, E*)-1-hydroxy-9-oxonon-2-en-1-yl)-2, 2-dimethyloxazolidine-3-carboxylate

Stereoselective addition of vinyl magnesium bromide to (*S*)-*Garner* aldehyde was carried out in THF and the crude product purified by silica gel chromatography based on known procedures [73, 74] to yield (*S*)-*tert*-butyl 4-((*R*)-1-hydroxyallyl)-2,2-dimethyloxazolidine-3-carboxylate for synthesis of d18:2/16:0 ceramide.

To a solution of (*S*)-*tert*-butyl 4-((*R*)-1-hydroxyallyl)-2, 2-dimethyloxazolidine-3-carboxylate (280 mg, 1.1 mmol, 1 eq.) in dry DCM (10 mL) were added oct-7-enal (549 mg, 660 μL, 4.4 mmol, 4 eq.) and Grubbs second generation catalyst (23 mg, 0.027 mmol, 0.025 eq.).

The solution was refluxed overnight (approximately 16 h) and completion of reaction confirmed by TLC (40: 60 ethyl acetate: hexanes, PMA stain, R_f = 0.35-0.4). The reaction was concentrated and purified by silica gel chromatography (35: 65 ethyl acetate: hexanes). Fractions containing product were concentrated to afford (*S*)-*tert*-butyl 4-((*R*, *E*)-1-hydroxy-9-oxonon-2-en-1-yl)-2, 2-dimethyloxazolidine-3-carboxylate (190 mg, 41 % yield) as a colorless oil. ^{1}H-NMR (500 MHz, $CDCl_3$): 1.19-1.54 (*m*, 21H), 1.94 (*dt*, 2H), 2.31 (*t*, 2H), 3.73-4.07 (*m*, 5H including OH), 5.35 (*dd*, J = 15.3, 6.3, 1H), 5.9 (*m*, 1H), 9.64 (*s*, 1H). ESI-MS: exact mass calculated for $C_{19}H_{33}NO_5Na^+$ (sodium adduct): 378.2251, mass detected: 378.2224, ppm difference 7.14.

2.5.5.2. Synthesis of (*S*)-*tert*-butyl 4-((*R*, 2*E*, 9*Z*)-1-hydroxyhexadeca-2, 9-dien-1-yl)-2, 2-dimethyloxazolidine-3-carboxylate

To a suspension of heptyltriphenylphosphonium bromide (330 mg, 0.75 mmol, 3 eq.) in dry THF (10 mL) at 0 °C was added sodium *bis*(trimethylsilyl)amide (725 μL of 1 M solution in dry THF, 2.9 mmol, 2.9 eq.). The solution immediately turned orange and was allowed to stir at 0 °C for 30 min. The solution was then cooled to -78 °C and a THF solution (2 mL) of (*S*)-*tert*-butyl 4-((*R*, *E*)-1-hydroxy-9-oxonon-2-en-1-yl)-2,2-dimethyloxazolidine-3-carboxylate (90 mg, 0.25 mmol, 1 eq.) was added. The reaction was allowed to proceed overnight where it warmed from -78 °C to room temperature (rt) and the color dissipated until white. Saturated aqueous sodium bicarbonate was added, and the aqueous phase was extracted three times with diethyl ether (10 mL). The combined organic phases were washed with brine, dried over anhydrous sodium sulfate, concentrated and purified by silica gel chromatography (15: 85 ethyl acetate: hexanes, R_f = 0.3) to yield (*S*)-*tert*-butyl 4-((*R*, 2*E*, 9*Z*)-1-hydroxyhexadeca-2, 9-dien-1-yl)-2, 2-

dimethyloxazolidine-3-carboxylate (36 mg, 32 % yield) as a colorless oil. ^{1}H-NMR (400 MHz, $CDCl_3$): 0.88 (*t*, 3H), 1.25-1.62 (*m*, 29H), 2.02 (*m*, 6H), 3.83 (*m*, 1H), 4.02 (*m*, 1H), 4.14 (*m*, 2H), 5.34 (m, 2H), 5.44 (*dd*, J = 15.3, 5.2, 1H), 5.73 (*m*, 1H). ESI-MS: mass calculated for $C_{26}H_{47}NO_4Na^+$ (sodium adduct): 460.3397, mass detected: 460.3388, ppm difference 1.96.

2.5.5.3. Synthesis of *N*-((2*S*, 3*R*, 4*E*, 11*Z*)-1, 3-dihydroxyoctadeca-4, 11-dien-2-yl)palmitamide

A solution of (*S*)-*tert*-butyl 4-((*R*, 2*E*, 9*Z*)-1-hydroxyhexadeca-2, 9-dien-1-yl)-2, 2-dimethyloxazolidine-3-carboxylate (33 mg, 0.076 mmol, 1 eq.) in 1 M HCl (0.75 mL) and dioxane (0.75 mL) was heated at 100 °C for 1 h. The mixture was cooled to rt and neutralized with 1 M NaOH (1 mL). This mixture was then extracted twice with ethyl acetate (3 mL) and the organic layer was sent through a plug of sodium sulfate and concentrated to yield crude sphingosine. The yellowish solid was then dissolved in THF (0.5 mL) and N-succinimidyl palmitate (40 mg, 0.11 mmol, 1.5 eq.) was added followed by triethylamine (22 μL). After stirring overnight, 1 M HCl (1 mL) was added and the mixture extracted twice with ethyl acetate (2 mL). The combined organic phases were dried over anhydrous sodium sulfate, concentrated and purified by silica gel chromatography (66: 34 ethyl acetate: hexanes, R_f = 0.5) to yield *N*-((2*S*, 3*R*, 4*E*, 11*Z*)-1, 3-dihydroxyoctadeca-4, 11-dien-2-yl)palmitamide (17 mg, 41 % yield) as a white solid. ^{1}H-NMR (500 MHz, $CDCl_3$): 0.88 (*m*, 6H), 1.25-1.35 (*m*, 46H), 1.63 (*m*, 2H), 2.00-2.08 (*m*, 6H), 2.25 (*t*, J = 7.5, 2H), 2.88 (s, 1H), 3.70 (m, 1H), 3.88-3.96 (m, 2H), 4.3 (*m*, 1H), 5.34 (m, 1H), 5.53 (*dd*, J = 15.5, 6.5, 1H), 5.78 (*m*, 1H), 6.29 (d, J = 7.5, 1H). ESI-MS: mass calculated for $C_{34}H_{66}NO_3^+$ (hydrogen adduct): 536.5037, mass detected: 536.5029, ppm difference 1.49.

2.5.6. Synthesis of d18:1/16:1 ceramide [(*Z*)-N-((2*S*, 3*R*, *E*)-1, 3-dihydroxyoctadec-4-en-2-yl)hexadec-9-enamide]

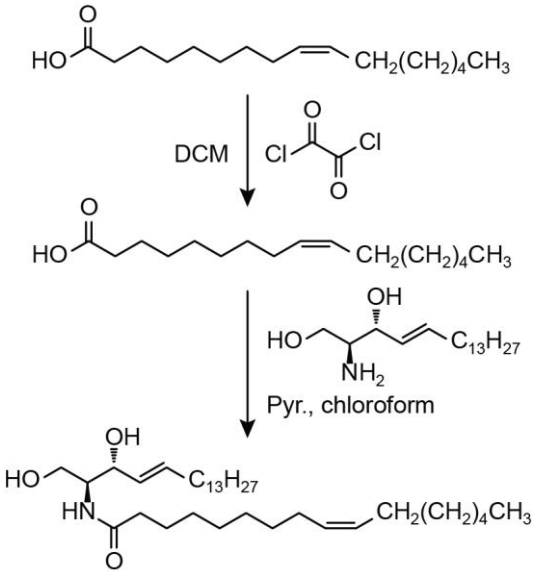

Figure 2.16. Synthesis of d18:1/16:1 ceramide.

To a stirring solution of (*Z*)-hexadec-9-enoic acid (9.7 mg, 0.038 mmol, 1eq.) at RT was added oxalyl dichloride (1 mL, excess). Formation of bubbles was observed over the next 30 min, and the reaction was stirred overnight at rt before being concentrated to afford the crude (*Z*)-hexadec-9-enoyl chloride. The crude acyl chloride was dried under vacuum for 3 h, dissolved in a mixture of pyridine (15.1 µL, 0.195 mmol, 5 eq. assuming 100 % yield for previous reaction) and chloroform (0.5 mL), and added dropwise to a stirring solution of (2*S*, 3*R*, *E*)-2-aminooctadec-4-ene-1, 3-diol (14.7 mg, 0.049 mmol, 1.3 eq. assuming 100 % yield for previous reaction) in chloroform (4 mL). The reaction was stirred at rt for 5 h, water was added and the resulting mixture was extracted three times with chloroform. The combined organic layers were washed with brine, dried with sodium sulfate, filtered and concentrated to afford the crude (*Z*)-N-((2*S*, 3*R*, *E*)-1, 3-dihydroxyoctadec-4-en-2-yl)hexadec-9-enamide, which was used

directly for targeted tandem MS. ESI-MS: mass calculated for $C_{34}H_{64}NO_3^-$ (loss of hydrogen): 534.4892, mass detected: 534.4903, ppm difference 2.06.

2.5.7. Absolute quantification, co-injection and tandem MS

A $^2H_{31}$-d18:1/16:0 ceramide standard (Avanti Polar Lipids) was used for absolute quantification of C16-C24 ceramides on the TOF instrument, using the same instrument, solvent and gradient conditions as general profiling. The standard was added to chloroform prior to lipid extraction to account for metabolite loss during extraction. Tandem MS was performed on an Agilent 6410 Triple Quad LC/MS instrument in Product Ion mode. d18:1/16:0 ceramide standard was from Avanti Polar Lipids; d18:1/16:1 and d18:2/16:0 ceramide standards were synthesized. The precursor ions were m/z 538.5 (d18:1/16:0 ceramide) and m/z 536.5 (d18:2/16:0 and d18:1/16:1 ceramides) in positive mode, and m/z 536.5 (d18:1/16:0 ceramide) and m/z 534.5 (d18:2/16:0 and d18:1/16:1 ceramides) in negative mode. The time filter width was 0.07 min. The fragmentor voltage and collision energy were 132 V and 26 V unless otherwise indicated. The skimmer voltage and ΔEMV were 15 V and 400 V, respectively. Tandem MS range was initially set to 50-540 Da to capture the entire ceramide fragmentation range, and lowered to 230-290 Da to capture the region containing the greatest number of identifiable fragments. The injection volume was 30 µL. Tandem MS was recorded for mitochondrial and whole cell lipids from both WT and DKO MEFs to ensure presence of the same ceramide isomers in all sample fractions. The same triple quadrupole instrument operated in MRM mode was used for co-injection; MEF whole cell lipid extract was used as sample, 25 pmol of synthetic d18:2/16:0 ceramide was used as standard, and a combination of the sample and standard used for co-injection. All samples were dissolved in chloroform such that the final

volume was 10 µL. The fragmentor and collision energy were same as Product Ion. The transition in negative mode was m/z 534.5 → m/z 280.3; ΔEMV was 400 V; MS1 resolution was set to Wide and MS2 resolution to Unit. The capillary voltage was 4.0 kV, the skimmer voltage was 15 V, the drying gas temperature was 350 °C, the drying gas flow rate was 8 L min^{-1} and the nebulizer pressure was 35 psi for all Triple Quad measurements. Gradient and solvents were identical to general profiling.

2.5.8. Cellular production of $^{2}H_{12}$-d18:2/16:0 ceramide

For each sample, 20 µL of $^{2}H_{14}$-palmitoleic acid (Cayman Chemical) in DMSO (83 mM) was mixed with 10.5 mL media, and 10 mL of the media introduced to DKO MEFs in a 10 cm tissue culture dish. 20 µL of DMSO was used as control. The treated cells were incubated at 37 °C for 2 h or 21 h prior to harvest by scraping. Lipids were extracted from cell pellets and the presence of $^{2}H_{12}$-d18:2/16:0 ceramide product confirmed by dynamic MRM using the transition m/z 548.6 → 274.3 in positive mode. The retention time was 42.55 min and the retention window was 10 min. All other instrument, solvent and gradient conditions were identical to co-injection and tandem MS.

2.5.9. Quantification of ceramide isomers by MRM

Individual ceramide isomers were quantified on the Triple Quad instrument using the same solvent, gradient and instrument parameters as tandem MS. List of targeted transitions is provided in Table 2.2. 1/4-1/8 of mitochondrial sample (mitochondrial lipid extract from ~2.5 × 10^{8} cells) or 1/3-1/6 of whole cell sample (lipid extract from ~1.5 × 10^{7} cells) was used for analysis.

2.5.10. Serum starvation

WT and DKO MEFs were plated and passaged three times. The media was replaced with FBS-free media 48 h after the third passage. No media was changed for control cells. All cells were harvested by scraping 61 h after the third passage (13 h serum starvation).

2.5.11. Cellular viability assay

d18:2/16:0 and d18:1/16:0 ceramides (10 mM in DMSO, stored at -80 °C) were thawed at rt for 20 min (d18:2/16:0 ceramide is a clear solution at rt while d18:1/16:0 ceramide is a gel) before being warmed briefly in a water bath (70 °C, 2-5 min). 52.2 μL ceramide was transferred into a 15 mL Falcon tube at 70 °C, and 5 mL media (pre-warmed at 37 °C) added and immediately mixed with the ceramide to allow complete solubilization. The resulting media was diluted serially as needed (for final ceramide concentrations of 25 μM, 50 μM and 100 μM, with final DMSO concentration maintained at 1 %) and the resulting dilutions added to 96-well plate (100 μL/well); media without DMSO and media containing 1 % DMSO without ceramide were used as controls. MEFs (1000 cells in 5 μL media for each well) or iBMKs (2500 cells in 5 μL media for each) were added to the 96-well plate containing media with or without ceramides, and the plate incubated in a 37 °C incubator with 5 % CO_2 for 24 h. Viability was accessed *via* CellTiter-Glo® Lumiescent Cell Viability Assay (Promega) based on manufacturer's instruction. Luminescence was measured on a Spectramax L plate reader (Molecular Devices).

2.6. References

[1] L.D. Walensky, BCL-2 in the crosshairs: tipping the balance of life and death, Cell Death Differ, 13 (2006) 1339-1350.

[2] Y. Tsujimoto, J. Gorham, J. Cossman, E. Jaffe, C. Croce, The t(14;18) chromosome translocations involved in B-cell neoplasms result from mistakes in VDJ joining, Science, 229 (1985) 1390-1393.

[3] A. Bakhshi, J.P. Jensen, P. Goldman, J.J. Wright, O.W. McBride, A.L. Epstein, S.J. Korsmeyer, Cloning the chromosomal breakpoint of t(14;18) human lymphomas: clustering around Jh on chromosome 14 and near a transcriptional unit on 18, Cell, 41 (1985) 899-906.

[4] M.L. Cleary, J. Sklar, Nucleotide sequence of a t(14;18) chromosomal breakpoint in follicular lymphoma and demonstration of a breakpoint-cluster region near a transcriptionally active locus on chromosome 18, Proceedings of the National Academy of Sciences, 82 (1985) 7439-7443.

[5] J.I. Fletcher, D.C.S. Huang, BH3-only proteins: orchestrating cell death, Cell Death Differ, 13 (2006) 1268-1271.

[6] E. Gavathiotis, M. Suzuki, M.L. Davis, K. Pitter, G.H. Bird, S.G. Katz, H.-C. Tu, H. Kim, E.H.Y. Cheng, N. Tjandra, L.D. Walensky, BAX activation is initiated at a novel interaction site, Nature, 455 (2008) 1076-1081.

[7] K.W. Yip, J.C. Reed, Bcl-2 family proteins and cancer, Oncogene, 27 (2008) 6398-6406.

[8] D. Mérino, P. Bouillet, The Bcl-2 family in autoimmune and degenerative disorders, Apoptosis, 14 (2009) 570-583.

[9] O. Takeuchi, J. Fisher, H. Suh, H. Harada, B.A. Malynn, S.J. Korsmeyer, Essential role of BAX,BAK in B cell homeostasis and prevention of autoimmune disease, Proceedings of the National Academy of Sciences of the United States of America, 102 (2005) 11272-11277.

[10] J.C. Reed, Proapoptotic multidomain Bcl-2//Bax-family proteins: mechanisms, physiological roles, and therapeutic opportunities, Cell Death Differ, 13 (2006) 1378-1386.

[11] T. Lindsten, A.J. Ross, A. King, W.-X. Zong, J.C. Rathmell, H.A. Shiels, E. Ulrich, K.G. Waymire, P. Mahar, K. Frauwirth, Y. Chen, M. Wei, V.M. Eng, D.M. Adelman, M.C. Simon, A. Ma, J.A. Golden, G. Evan, S.J. Korsmeyer, G.R. MacGregor, C.B. Thompson, The Combined Functions of Proapoptotic Bcl-2 Family Members Bak and Bax Are Essential for Normal Development of Multiple Tissues, Molecular Cell, 6 (2000) 1389-1399.

[12] W.-X. Zong, T. Lindsten, A.J. Ross, G.R. MacGregor, C.B. Thompson, BH3-only proteins that bind pro-survival Bcl-2 family members fail to induce apoptosis in the absence of Bax and Bak, Genes & Development, 15 (2001) 1481-1486.

[13] L.D. Walensky, E. Gavathiotis, BAX unleashed: the biochemical transformation of an inactive cytosolic monomer into a toxic mitochondrial pore, Trends in Biochemical Sciences, 36 (2011) 642-652.

[14] H. Kim, H.-C. Tu, D. Ren, O. Takeuchi, J.R. Jeffers, G.P. Zambetti, J.J.D. Hsieh, E.H.Y. Cheng, Stepwise Activation of BAX and BAK by tBID, BIM, and PUMA Initiates Mitochondrial Apoptosis, Molecular Cell, 36 (2009) 487-499.

[15] J.R. Van Brocklyn, J.B. Williams, The control of the balance between ceramide and sphingosine-1-phosphate by sphingosine kinase: Oxidative stress and the seesaw of cell survival and death, Comparative Biochemistry and Physiology Part B: Biochemistry and Molecular Biology, 163 (2012) 26-36.

[16] M. Crimi, M.D. Esposti, Apoptosis-induced changes in mitochondrial lipids, Biochimica et Biophysica Acta (BBA) - Molecular Cell Research, 1813 (2011) 551-557.

[17] B.J. Pettus, C.E. Chalfant, Y.A. Hannun, Ceramide in apoptosis: an overview and current perspectives, Biochimica et Biophysica Acta (BBA) - Molecular and Cell Biology of Lipids, 1585 (2002) 114-125.

[18] J.B. McMillin, W. Dowhan, Cardiolipin and apoptosis, Biochimica et Biophysica Acta (BBA) - Molecular and Cell Biology of Lipids, 1585 (2002) 97-107.

[19] T. Zhang, A. Saghatelian, Emerging roles of lipids in BCL-2 family-regulated apoptosis, Biochimica et Biophysica Acta (BBA) - Molecular and Cell Biology of Lipids.

[20] V.E. Kagan, V.A. Tyurin, J. Jiang, Y.Y. Tyurina, V.B. Ritov, A.A. Amoscato, A.N. Osipov, N.A. Belikova, A.A. Kapralov, V. Kini, I.I. Vlasova, Q. Zhao, M. Zou, P. Di, D.A. Svistunenko, I.V. Kurnikov, G.G. Borisenko, Cytochrome c acts as a cardiolipin oxygenase required for release of proapoptotic factors, Nat Chem Biol, 1 (2005) 223-232.

[21] V.E. Kagan, H.A. Bayır, N.A. Belikova, O. Kapralov, Y.Y. Tyurina, V.A. Tyurin, J. Jiang, D.A. Stoyanovsky, P. Wipf, P.M. Kochanek, J.S. Greenberger, B. Pitt, A.A. Shvedova, G. Borisenko, Cytochrome c/cardiolipin relations in mitochondria: a kiss of death, Free Radical Biology and Medicine, 46 (2009) 1439-1453.

[22] Jerry E. Chipuk, Gavin P. McStay, A. Bharti, T. Kuwana, Christopher J. Clarke, Leah J. Siskind, Lina M. Obeid, Douglas R. Green, Sphingolipid Metabolism Cooperates with BAK and BAX to Promote the Mitochondrial Pathway of Apoptosis, Cell, 148 (2012) 988-1000.

[23] M. Karbowski, K.L. Norris, M.M. Cleland, S.-Y. Jeong, R.J. Youle, Role of Bax and Bak in mitochondrial morphogenesis, Nature, 443 (2006) 658-662.

[24] C. Osman, D.R. Voelker, T. Langer, Making heads or tails of phospholipids in mitochondria, The Journal of Cell Biology, 192 (2011) 7-16.

[25] F. Furt, P. Moreau, Importance of lipid metabolism for intracellular and mitochondrial membrane fusion/fission processes, The International Journal of Biochemistry & Cell Biology, 41 (2009) 1828-1836.

[26] H. Huang, M.A. Frohman, Chapter 7 - Visualizing Mitochondrial Lipids and Fusion Events in Mammalian Cells, in: P. Gilbert Di, R.W. Markus (Eds.) Methods in Cell Biology, vol. Volume 108, Academic Press, 2012, pp. 131-145.

[27] M. Perkins, J.M. Haslam, A.W. Linnane, Biogenesis of mitochondria. The effects of physiological and genetic manipulation of Saccharomyces cerevisiae on the mitochondrial transport systems for tricarboxylate-cycle anions, Biochem. J., 134 (1973) 923-934.

[28] T.K. Rostovtseva, P.A. Gurnev, M.-Y. Chen, S.M. Bezrukov, Membrane Lipid Composition Regulates Tubulin Interaction with Mitochondrial Voltage-dependent Anion Channel, Journal of Biological Chemistry, 287 (2012) 29589-29598.

[29] E.G. Bligh, W.J. Dyer, A Rapid Method of Total Lipid Extraction and Purification, Canadian Journal of Biochemistry and Physiology, 37 (1959) 911-917.

[30] C. Frezza, S. Cipolat, L. Scorrano, Organelle isolation: functional mitochondria from mouse liver, muscle and cultured filroblasts, Nat. Protocols, 2 (2007) 287-295.

[31] C.A. Smith, E.J. Want, G. O'Maille, R. Abagyan, G. Siuzdak, XCMS: Processing Mass Spectrometry Data for Metabolite Profiling Using Nonlinear Peak Alignment, Matching, and Identification, Analytical Chemistry, 78 (2006) 779-787.

[32] LIPID MAPS Structure Database (LMSD) (2014), http://www.lipidmaps.org/data/structure/index.html.

[33] Scripps Center for Metabolomics: Metabolite and Tandem MS Database (METLIN), (2003) http://metlin.scripps.edu/.

[34] M. Valsecchi, L. Mauri, R. Casellato, S. Prioni, N. Loberto, A. Prinetti, V. Chigorno, S. Sonnino, Ceramide and sphingomyelin species of fibroblasts and neurons in culture, Journal of Lipid Research, 48 (2007) 417-424.

[35] The AOCS Lipid Library (2014), http://lipidlibrary.aocs.org.

[36] A.H. Futerman, H. Riezman, The ins and outs of sphingolipid synthesis, Trends in Cell Biology, 15 (2005) 312-318.

[37] G.G. Guenther, E.R. Peralta, K.R. Rosales, S.Y. Wong, L.J. Siskind, A.L. Edinger, Ceramide starves cells to death by downregulating nutrient transporter proteins, Proceedings of the National Academy of Sciences, 105 (2008) 17402-17407.

[38] A.H. Futerman, Y.A. Hannun, The complex life of simple sphingolipids, EMBO Rep, 5 (2004) 777-782.

[39] E. Jahangir, Lipid Analysis by HPLC, in: Encyclopedia of Chromatography, Second Edition, vol. null, Taylor & Francis, 2011, pp. 960-964.

[40] H.H. Yoo, J. Son, D.-H. Kim, Liquid chromatography–tandem mass spectrometric determination of ceramides and related lipid species in cellular extracts, Journal of Chromatography B, 843 (2006) 327-333.

[41] B. Colsch, C. Afonso, I. Popa, J. Portoukalian, F. Fournier, J.-C. Tabet, N. Baumann, Characterization of the ceramide moieties of sphingoglycolipids from mouse brain by ESI-MS/MS: identification of ceramides containing sphingadienine, Journal of Lipid Research, 45 (2004) 281-286.

[42] M.H. Lee, G.H. Lee, J.S. Yoo, Analysis of ceramides in cosmetics by reversed-phase liquid chromatography/electrospray ionization mass spectrometry with collision-induced dissociation, Rapid Communications in Mass Spectrometry, 17 (2003) 64-75.

[43] F.-F. Hsu, J. Turk, M. Stewart, D. Downing, Structural studies on ceramides as lithiated adducts by low energy collisional-activated dissociation tandem mass spectrometry with electrospray ionization, Journal of the American Society for Mass Spectrometry, 13 (2002) 680-695.

[44] H. Farwanah, B. Pierstorff, C.E.H. Schmelzer, K. Raith, R.H.H. Neubert, T. Kolter, K. Sandhoff, Separation and mass spectrometric characterization of covalently bound skin ceramides using LC/APCI-MS and Nano-ESI-MS/MS, Journal of Chromatography B, 852 (2007) 562-570.

[45] X. Han, Characterization and Direct Quantitation of Ceramide Molecular Species from Lipid Extracts of Biological Samples by Electrospray Ionization Tandem Mass Spectrometry, Analytical Biochemistry, 302 (2002) 199-212.

[46] F.-F.u. Hsu, J. Turk, Characterization of ceramides by low energy collisional-activated dissociation tandem mass spectrometry with negative-ion electrospray ionization, Journal of the American Society for Mass Spectrometry, 13 (2002) 558-570.

[47] Q. Ann, J. Adams, Structure-specific collision-induced fragmentations of ceramides cationized with alkali-metal ions, Analytical Chemistry, 65 (1993) 7-13.

[48] G. Fabrias, J. Muñoz-Olaya, F. Cingolani, P. Signorelli, J. Casas, V. Gagliostro, R. Ghidoni, Dihydroceramide desaturase and dihydrosphingolipids: Debutant players in the sphingolipid arena, Progress in Lipid Research, 51 (2012) 82-94.

[49] D.S. Kelley, G.L. Bartolini, J.W. Newman, M. Vemuri, B.E. Mackey, Fatty acid composition of liver, adipose tissue, spleen, and heart of mice fed diets containing t10, c12-, and c9, t11-conjugated linoleic acid, Prostaglandins, Leukotrienes and Essential Fatty Acids, 74 (2006) 331-338.

[50] L.J. Siskind, T.D. Mullen, K. Romero Rosales, C.J. Clarke, M.J. Hernandez-Corbacho, A.L. Edinger, L.M. Obeid, The BCL-2 Protein BAK Is Required for Long-chain Ceramide Generation during Apoptosis, Journal of Biological Chemistry, 285 (2010) 11818-11826.

[51] S. Jayadev, B. Liu, A.E. Bielawska, J.Y. Lee, F. Nazaire, M.Y. Pushkareva, L.M. Obeid, Y.A. Hannun, Role for Ceramide in Cell Cycle Arrest, Journal of Biological Chemistry, 270 (1995) 2047-2052.

[52] Q. Dai, J. Liu, J. Chen, D. Durrant, T.M. McIntyre, R.M. Lee, Mitochondrial ceramide increases in UV-irradiated HeLa cells and is mainly derived from hydrolysis of sphingomyelin, Oncogene, 23 (2004) 3650-3658.

[53] M. Sawada, S. Nakashima, Y. Banno, H. Yamakawa, K. Hayashi, K. Takenaka, Y. Nishimura, H. Sakai, Y. Nozawa, Ordering of ceramide formation, caspase activation, and Bax/Bcl-2 expression during etoposide-induced apoptosis in C6 glioma cells, Cell Death Differ, 7 (2000) 761-772.

[54] M.A. Mikati, M. Zeinieh, R.A. Habib, J. El Hokayem, A. Rahmeh, M. El Sabban, J. Usta, G. Dbaibo, Changes in sphingomyelinases, ceramide, Bax, Bcl2, and caspase-3 during and after experimental status epilepticus, Epilepsy Research, 81 (2008) 161-166.

[55] C. Dumitru, I. Sandalcioglu, M. Wagner, M. Weller, E. Gulbins, Lysosomal ceramide mediates gemcitabine-induced death of glioma cells, J Mol Med, 87 (2009) 1123-1132.

[56] V. Ganesan, M. Colombini, Regulation of ceramide channels by Bcl-2 family proteins, FEBS letters, 584 (2010) 2128-2134.

[57] M. Colombini, Ceramide channels and their role in mitochondria-mediated apoptosis, Biochimica et Biophysica Acta (BBA) - Bioenergetics, 1797 (2010) 1239-1244.

[58] L.J. Siskind, M. Colombini, The Lipids C2- and C16-Ceramide Form Large Stable Channels: Implications for Apoptosis, Journal of Biological Chemistry, 275 (2000) 38640-38644.

[59] V. Ganesan, M. Perera, D. Colombini, D. Datskovskiy, K. Chadha, M. Colombini, Ceramide and activated Bax act synergistically to permeabilize the mitochondrial outer membrane, Apoptosis, 15 (2010) 553-562.

[60] L.J. Siskind, L. Feinstein, T. Yu, J.S. Davis, D. Jones, J. Choi, J.E. Zuckerman, W. Tan, R.B. Hill, J.M. Hardwick, M. Colombini, Anti-apoptotic Bcl-2 Family Proteins Disassemble Ceramide Channels, Journal of Biological Chemistry, 283 (2008) 6622-6630.

[61] J. Stiban, D. Fistere, M. Colombini, Dihydroceramide hinders ceramide channel formation: Implications on apoptosis, Apoptosis, 11 (2006) 773-780.

[62] H. Lee, J.A. Rotolo, J. Mesicek, T. Penate-Medina, A. Rimner, W.-C. Liao, X. Yin, G. Ragupathi, D. Ehleiter, E. Gulbins, D. Zhai, J.C. Reed, A. Haimovitz-Friedman, Z. Fuks, R. Kolesnick, Mitochondrial Ceramide-Rich Macrodomains Functionalize Bax upon Irradiation, PLoS ONE, 6 (2011) e19783.

[63] J. Kilkus, R. Goswami, F.D. Testai, G. Dawson, Ceramide in rafts (detergent-insoluble fraction) mediates cell death in neurotumor cell lines, Journal of Neuroscience Research, 72 (2003) 65-75.

[64] E. Martínez-Abundis, F. Correa, N. Pavón, C. Zazueta, Bax distribution into mitochondrial detergent-resistant microdomains is related to ceramide and cholesterol content in postischemic hearts, FEBS Journal, 276 (2009) 5579-5588.

[65] J. Park, M. Kim, Y. Kim, J. Woo, Ceramide induces apoptosis via caspase-dependent and caspase-independent pathways in mesenchymal stem cells derived from human adipose tissue, Arch Toxicol, 85 (2011) 1057-1065.

[66] S. Zhao, Y.-N. Yang, J.-G. Song, Ceramide induces caspase-dependent and -independent apoptosis in A-431 cells, Journal of Cellular Physiology, 199 (2004) 47-56.

[67] L. Thon, H. Möhlig, S. Mathieu, A. Lange, E. Bulanova, S. Winoto-Morbach, S. Schütze, S. Bulfone-Paus, D. Adam, Ceramide mediates caspase-independent programmed cell death, The FASEB Journal, 19 (2005) 1945-1956.

[68] L. Obeid, C. Linardic, L. Karolak, Y. Hannun, Programmed cell death induced by ceramide, Science, 259 (1993) 1769-1771.

[69] R. Caricchio, L. D'Adamio, P.L. Cohen, Fas, ceramide and serum withdrawal induce apoptosis via a common pathway in a type II Jurkat cell line, Cell Death Differ, 9 (2002) 574-580.

[70] S. Daido, T. Kanzawa, A. Yamamoto, H. Takeuchi, Y. Kondo, S. Kondo, Pivotal Role of the Cell Death Factor BNIP3 in Ceramide-Induced Autophagic Cell Death in Malignant Glioma Cells, Cancer Research, 64 (2004) 4286-4293.

[71] F. Scarlatti, C. Bauvy, A. Ventruti, G. Sala, F. Cluzeaud, A. Vandewalle, R. Ghidoni, P. Codogno, Ceramide-mediated Macroautophagy Involves Inhibition of Protein Kinase B and Up-regulation of Beclin 1, Journal of Biological Chemistry, 279 (2004) 18384-18391.

[72] trapper (MassHunter converter) (2009), http://sourceforge.net/projects/sashimi/files.

[73] G. Kumar, S. Kaur, V. Singh, Efficient Synthesis of a Styryl Analogue of (2S,3R,4E)-N2-Octadecanoyl-4-tetradecasphingenine via Cross-Metathesis Reaction, Helvetica Chimica Acta, 94 (2011) 650-655.

[74] I. Ojima, E.S. Vidal, Rhodium-Catalyzed Cyclohydrocarbonylation: Application to the Synthesis of (+)-Prosopinine and (−)-Deoxoprosophylline†, The Journal of Organic Chemistry, 63 (1998) 7999-8003.

Chapter 3

A non-apoptotic role for BAX and BAK in COX-2 regulation

3.1. Introduction

The balance between apoptosis and survival is essential for maintenance of homeostasis and health in living systems [1, 2]. Apoptosis is an intricately regulated mechanism that proceeds through different cell type and signal-dependent pathways [2]. The mitochondrial apoptotic pathway is modulated by pro- and anti-apoptotic BCL-2 family members whose interactions in response to a diverse set of cellular signals regulate cell fate [1, 3, 4]. The anti-apoptotic B-cell lymphoma-2 (BCL-2) is the founding member of the BCL-2 family, and its role in cancer was established when transgenic mice expressing a *Bcl-2-lg* minigene were found to accumulate B cells and develop lymphoma [1, 5-7]. Co-immunoprecipitation with BCL-2 led to identification of BAX, the first pro-apoptotic BCL-2 protein [8]. More than 20 BCL-2 members have been identified to date, and are classified based on structure and function into multidomain pro-apoptotic, multidomain anti-apoptotic and BH3 domain-only pro-apoptotic proteins [1, 9, 10].

In addition to their roles in cell death, recent evidence points to novel, non-apoptotic functions for several BCL-2 members in metabolism [11-13], immunity [14] and mitochondrial morphogenesis [15]. Proteomics of mouse liver mitochondrial fractions identified a functional holoenzyme complex that included BAD and glucokinase [11]. BAD was required for complex assembly, and $Bad^{-/-}$ mice displayed reduced glucose tolerance and abnormal glucose homeostasis [11]. More recently, genome-wide siRNA screen identified BID as a regulator of innate immunity; BID was found to interact with nucleotide-binding and oligomerization domains 1 and 2 (NOD1 and NOD2) in an inflammatory complex, and $Bid^{-/-}$ mice displayed blunted response upon NOD agonist treatment [14]. These examples highlight the potential for

individual BCL-2 proteins to partake in unexpected biology, and suggest that other BCL-2 members may also have non-apoptotic functions.

BAX and BAK are key multidomain pro-apoptotic proteins required for the mitochondrial apoptotic pathway [1]. BAX and BAK oligomerization leads to mitochondrial outer membrane permeabilization (MOMP), a crucial step in apoptosis [1, 16]. Interestingly, BAX and BAK were also found to regulate mitochondrial morphogenesis; BAX and BAK double knockout (DKO) mouse embryonic fibroblasts (MEFs) displayed a short, fragmented mitochondrial morphology while BAX or BAK single knockout (SKO) MEFs did not exhibit this phenotype [15]. Given evidences supporting a role for lipids in activation of BCL-2 proteins during apoptosis [17, 18] and the close connection between membrane morphology and lipid composition [19, 20], we reasoned that BAX and BAK could participate in mitochondrial morphogenesis by interacting with mitochondrial lipids and/or regulating cellular lipid metabolism. To test this hypothesis, we used an unbiased, global lipidomics approach to identify differences in lipid profiles among WT, DKO and SKO MEFs.

3.2. Results

3.2.1. Lipidomics uncovers a connection between BCL-2 proteins and eicosanoid metabolism

Lipids from WT and DKO MEF mitochondria were subjected to liquid chromatography–mass spectrometry (LC–MS) analysis (Figure 3.1A). Data were analyzed by XCMS [21], which aligns, quantifies and statistically ranks fold changes of all detectable ions common to WT and DKO groups (Figure 3.1B). Analysis of major lipid classes including free fatty acids, phospholipids, acylglycerols, acylcarnitines, glycerol ethers, cardiolipins, cholesterol and

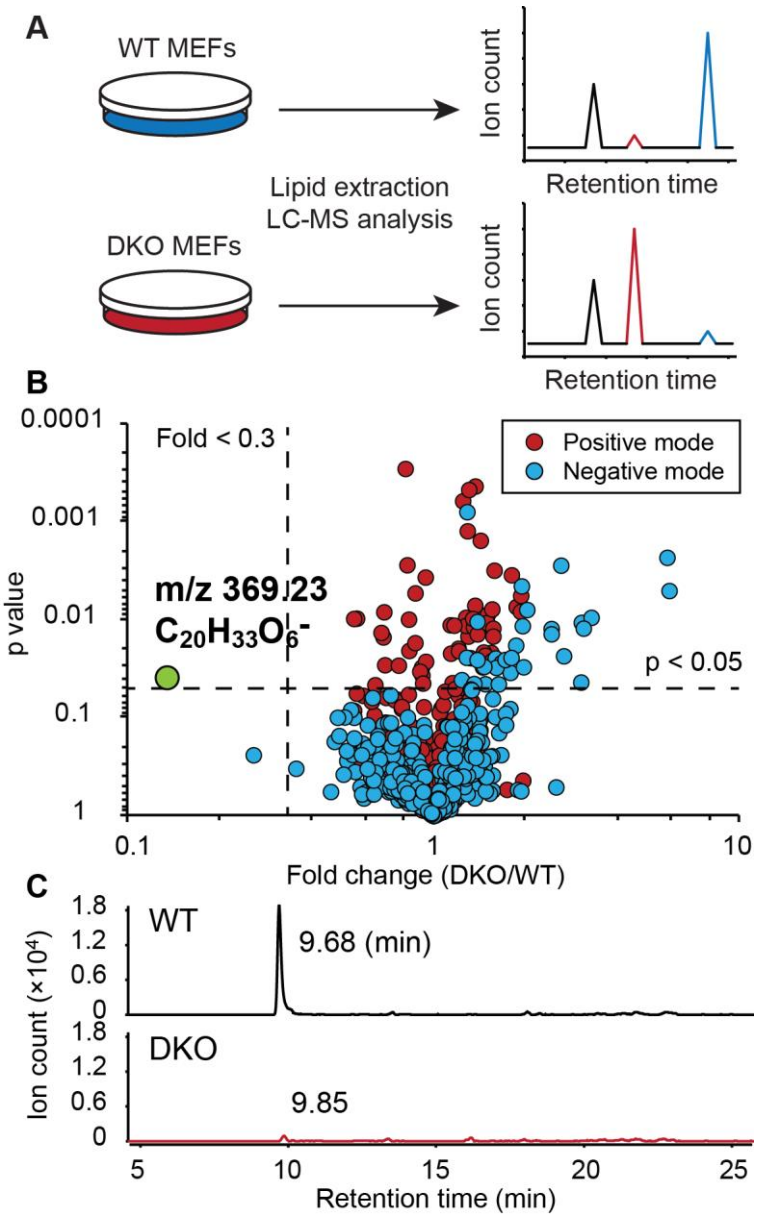

Figure 3.1. Comparative lipidomic profiling of WT and DKO MEF mitochondria. A) Schematic of unbiased, comparative global lipidomic analysis of WT and DKO MEF mitochondrial lipid pools, allowing identification of metabolite changes between WT and DKO samples. B) Volcano plot of all XCMS-detectable ions from WT and DKO MEF mitochondria. The m/z 369.23 ion, which is consistently down-regulated in DKO mitochondria relative to WT, is in green. C) Extracted chromatographs of the m/z 369.23 metabolite in WT and DKO MEF mitochondria. Two-tailed Student's t-test, n=3.

cholesterol esters yielded no significant changes based on our criteria (≥ 3-fold change, p-value ≤ 0.05) (Table 2.1). While metabolites from major lipid classes were unaltered, an unidentified metabolite (m/z: 369.2255, calculated formula: $C_{20}H_{34}O_6$) was consistently down-regulated in DKO MEF mitochondria relative to WT (Figure 3.1B, C). Importantly, perturbation in the level of a single metabolite in a background of unchanging lipids supports specifity in the pathway that is altered.

Database searches (Lipid Maps [22] and KEGG [23]) uncovered six known eicosanoids (6-keto-prostaglandin $F_{1\alpha}$, 16, 5-diketo-13, 14-dihydroxy-prostaglandin $F_{1\alpha}$, 20-hydroxy-prostaglandin $F_{2\alpha}$, thromboxane B_2, 19(R)-hydroxy-prostaglandin $F_{2\alpha}$ and 19(R)-hydroxy-prostaglandin E_1) that matched the calculated molecular formula (Figure 3.2). Structural

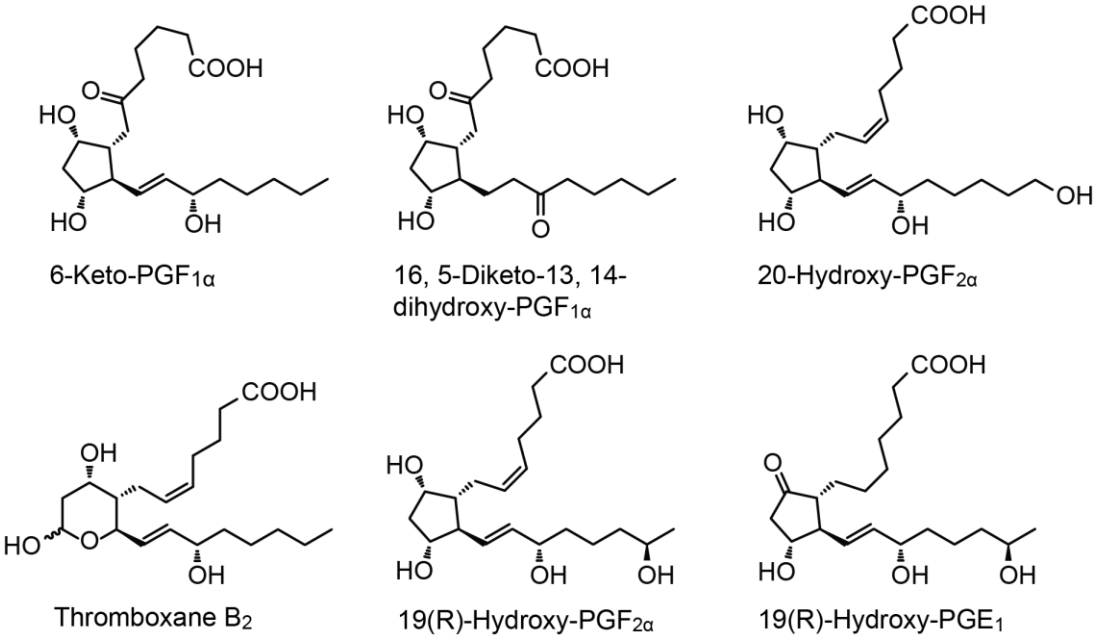

Figure 3.2. Structures of eicosanoids with formula $C_{20}H_{34}O_6$.

similarities among these candidates presented a challenge toward characterizing the unidentified metabolite. While our non-high resolution global lipidomics method allows injection of

relatively large sample volumes and simultaneous quantification of lipids from a wide range of lipid classes, this method is not suited to more sensitive resolution of the structurally similar eicosanoids, leaving open the possibility that the unidentified metabolite is a mixture of multiple species. To address this question we performed tandem MS and chromatography optimization.

3.2.2. Unidentified metabolite is 6-keto-$PGF_{1\alpha}$

Comparison between tandem MS spectra of candidate eicosanoid standards and endogenous m/z 369.23 metabolite strongly suggests that the latter is predominantly 6-keto-prostaglandin $F_{1\alpha}$, (6-keto-$PGF_{1\alpha}$) (Figure 3.3A, B). Based on our tandem MS findings we developed a robust chromatographic method enabling baseline separation of 6-keto-$PGF_{1\alpha}$ away from additional eicosanoids (Figure 3.3B). A column with increased length and decreased internal diameter and particle size than the global lipidomics column was chosen to achieve higher resolution of the structurally similar eicosanoids. A water-acetonitrile solvent system was chosen over the previous water-methanol-isopropanol system to improve resolution and retention while countering increased column backpressure; addition of formic acid also significantly improved 6-keto-$PGF_{1\alpha}$ peak shape (Figure 3.3C). Co-injection of 6-keto-$PGF_{1\alpha}$ standard with endogenous sample using the improved chromatographic method yielded a single peak corresponding to the m/z of 6-keto-$PGF_{1\alpha}$ (Figure 3.3D). The combination of tandem MS and co-injection provides strong evidence that the unidentified metabolite is 6-keto-$PGF_{1\alpha}$.

3.2.3. Elevated arachidonic acid levels in DKO and SKO MEFs support BCL-2 regulation of prostaglandin biosynthesis

Prostaglandins are produced *de novo* in most cell types from arachidonic (C20:4) acid in response to mechanical trauma or inflammatory stimuli [24]. Upon release from membrane phospholipids by phospholipases, arachidonic acid is converted to the intermediate prostaglandin H_2 and further processed into downstream eicosanoids by cell type-specific enzymes [24, 25] (Figure 3.4A). Within this pathway, 6-keto-$PGF_{1\alpha}$ is the hydrolysis breakdown product of the vasodilator and potent platelet activation inhibitor prostaglandin I_2 (prostacyclin) (Figure 3.4A) [26, 27]. The relative stability of 6-keto-$PGF_{1\alpha}$ has allowed its measurement as a marker for eicosanoid metabolism [28].

Reduced 6-keto-$PGF_{1\alpha}$ levels in DKO MEFs could be the result of decreased 6-keto-$PGF_{1\alpha}$ production or increased catabolism. In accordance with previous literature [29, 30], we did not observe significant amounts of additional prostaglandins, a possible consequence of the short half-lives of these metabolites [24, 31, 32]. Instead, we measured arachidonic acid levels in WT and DKO MEF mitochondria to determine if absence of BAX and BAK could have an impact over arachidonic acid metabolism. Our analysis revealed a two-fold ($p < 0.05$) elevation in arachidonic acid in DKO MEF mitochondria relative to WT, with no changes in additional common free fatty acids (Figure 3.4B). Decreased 6-keto-$PGF_{1\alpha}$ and elevated arachidonic acid levels in DKO MEFs support a reduction in the rate of prostaglandin biosynthesis in the absence of BAX and BAK.

To determine if BCL-2 regulation of eicosanoid metabolism requires both BAX and BAK, we extended our LC–MS analysis to include BAX and BAK single knockout (SKO) MEFs. 6-keto-$PGF_{1\alpha}$ was reduced in both DKO and *Bax*$^{-/-}$ MEF mitochondria relative to WT (Figure 3.4C); a similar but non-statistically significant trend was observed for the *Bak*$^{-/-}$ model (Figure 3.4C). Arachidonic acid was significantly elevated in DKO, *Bax*$^{-/-}$, and *Bak*$^{-/-}$ MEF

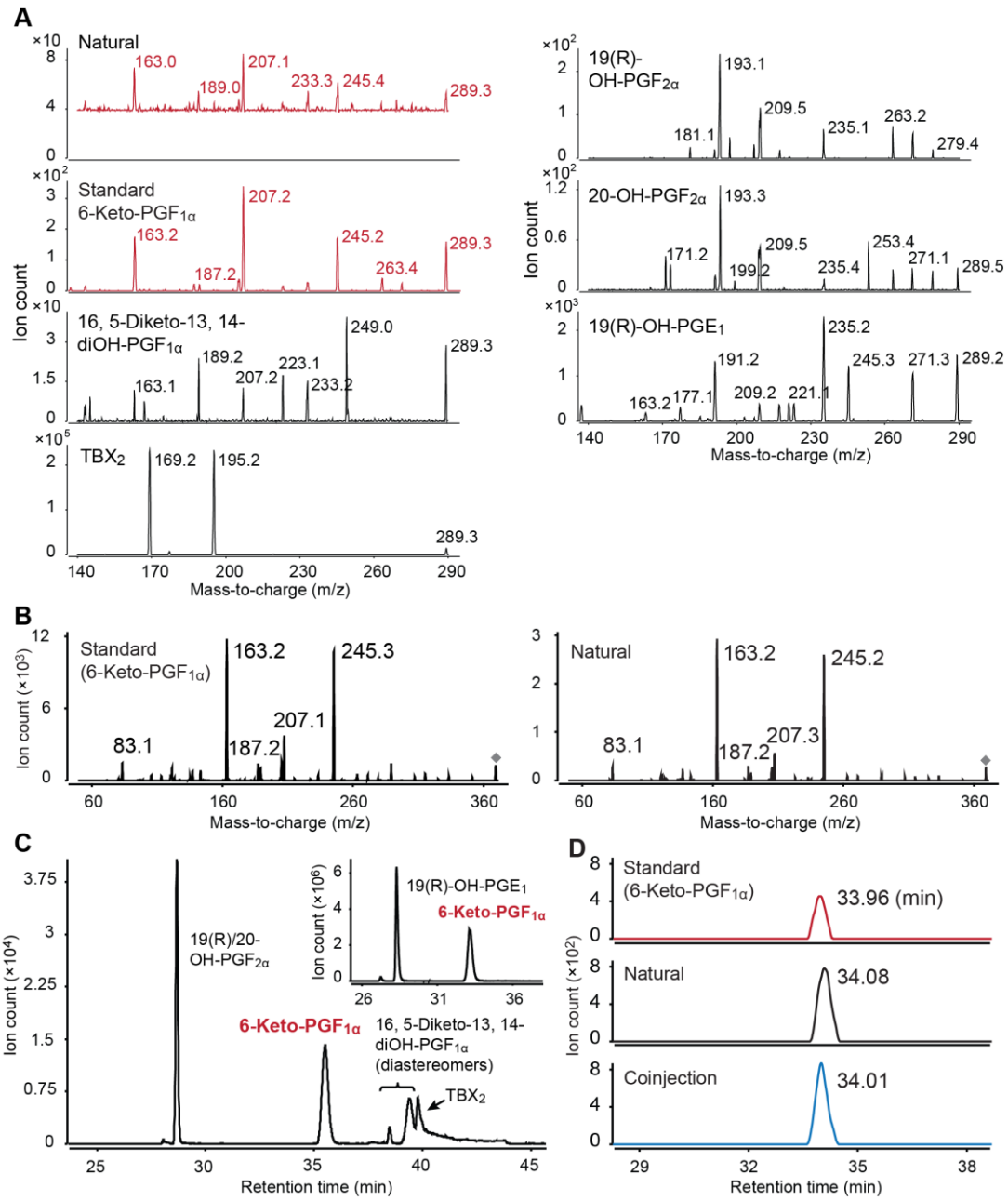

Figure 3.3. Unidentified metabolite is 6-keto-$PGF_{1\alpha}$. A) Preliminary tandem MS spectra of endogenous m/z 369.23 metabolite and candidate eicosanoid standards. Spectra of endogenous metabolite and 6-keto-$PGF_{1\alpha}$ standard are in red. Fragmentor voltage and collision energy are 140 V and 27 V, respectively, for 19(R)-OH-PGE_1, and 150 V and 10 V for all additional samples. B) Optimized tandem MS spectra for endogenous m/z 369.23 metabolite and 6-keto-$PGF_{1\alpha}$ standard. Fragmentor voltage and collision energy are 140 V and 27 V. C) Optimized chromatographic method for resolution of the six candidate eicosanoids, enabling baseline separation of 6-keto-$PGF_{1\alpha}$ from additional species. D) Co-injection of 6-keto-$PGF_{1\alpha}$ with endogenous sample.

mitochondria relative to WT, with more significant metabolite change present in the absence of BAX than BAK (Figure 3.4C). 6-keto-$PGF_{1\alpha}$ and arachidonic acid were further quantified in whole cell extracts to determine if the observed metabolite differences were organelle-specific. 6-keto-$PGF_{1\alpha}$ was reduced in DKO and *Bax*$^{-/-}$ whole cell extracts (Figure 3.4D) while arachidonic acid was elevated in SKO MEFs (Figure 3.4D). Taken together, our data demonstrate that BAX, and to a lesser extent BAK, regulate cellular eicosanoid metabolism, and imply that the levels or activities of eicosanoid biosynthetic enzymes are decreased in the absence of these proteins.

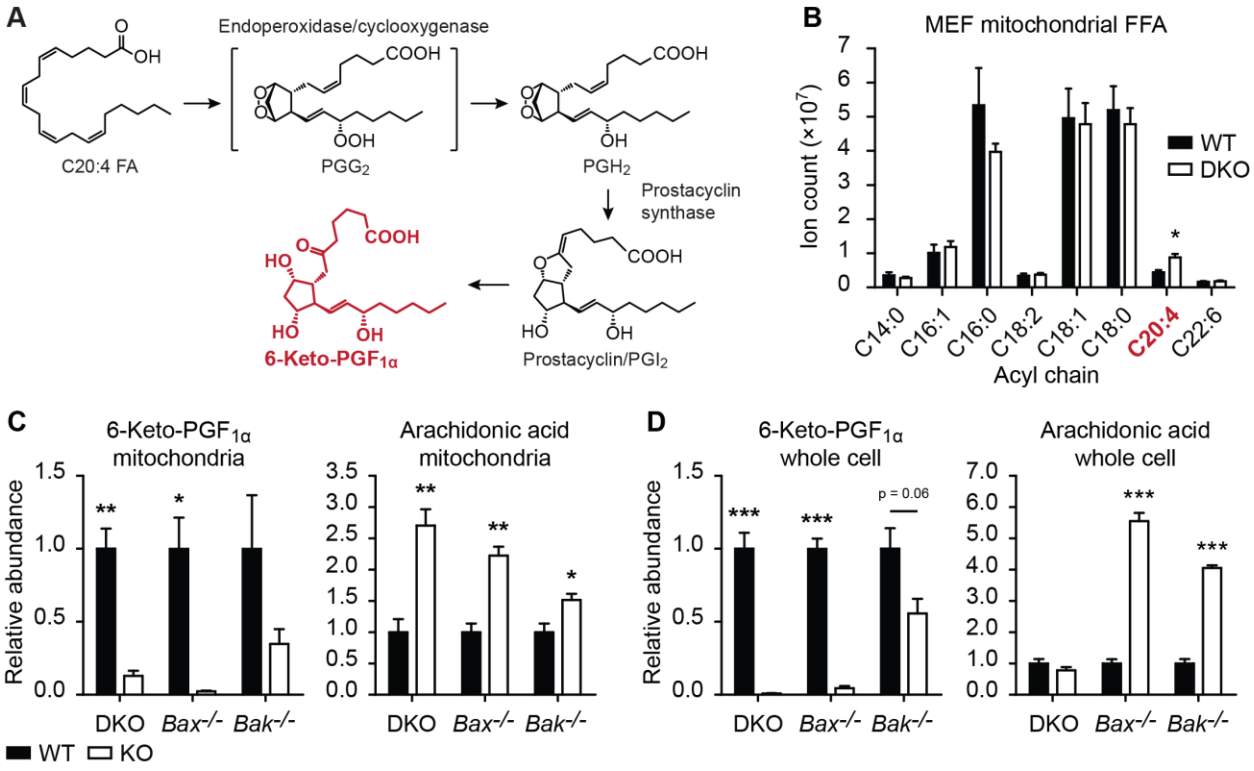

Figure 3.4. Absence of BAX and/or BAK reduces eicosanoid metabolism. A) Prostacyclin biosynthesis from arachidonic acid. B) Levels of common free fatty acids (FFAs) in WT and DKO MEF mitochondria (n = 3). C) 6-keto-$PGF_{1\alpha}$ levels in WT, DKO and SKO MEF mitochondria (n = 3). D) Arachidonic acid levels in WT, DKO and SKO MEF mitochondria (n = 3). E) 6-keto-$PGF_{1\alpha}$ levels in WT, DKO and SKO MEF whole cell lysates (n = 3-5). F) Arachidonic acid levels in WT, DKO and SKO MEF whole cell lysates (n =3-5). *, $p \leq 0.05$, **, $p \leq 0.01$, ***, $p \leq 0.001$. Two-tailed Student's t test, SEM.

3.2.4. BAX and/or BAK regulate COX levels

Conversion of arachidonic acid to prostaglandins is catalyzed by prostaglandin H synthase (PGHS, alternatively known as cyclooxygenase [COX]) at the ER and nuclear membranes [24]. Two COX isoforms are known; COX-1 is responsible for basal, constitutive prostaglandin production while COX-2 is an inducible enzyme that is activated by stress signals [24, 33]. Importantly, COX-2 is the primary target of non-steroidal anti-inflammatory drugs due to its physiological role in inflammation [33]. Elevated arachidonic acid and decreased 6-keto-$PGF_{1\alpha}$ levels in the absence of BAX and/or BAK could be a consequence of COX down-regulation. To test this hypothesis, COX expression in WT, DKO and SKO whole cell lysates was monitored by Western blot. While COX-1 level was unaltered, COX-2 expression was significantly reduced in DKO and SKO lysates relative to WT (Figure 3.5A). The extent of

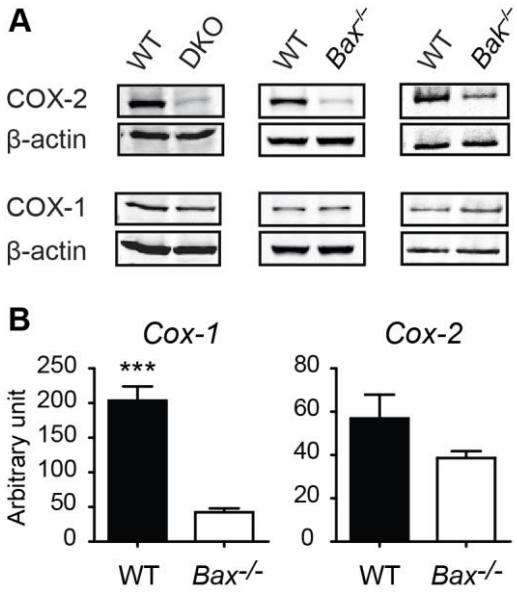

Figure 3.5. BAX and/or BAK regulate COX levels. A) Western blots against COX-1 and 2 in WT, DKO and SKO MEFs. B) RT-PCR of *Cox-1* and *2* in WT and *Bax*$^{-/-}$ MEFs

BCL-2 regulation of COX-2 correlated well with BCL-2-induced changes at the metabolic level, with absence of BAX causing stronger changes in both prostaglandin and COX-2 levels in comparison to BAK (Figure 3.4C, D; Figure 3.5A).

Given the most significant difference in COX-2 expression was observed between WT and *Bax*$^{-/-}$ MEFs (Figure 3.5A), we performed real time-PCR on *Cox-1* and *Cox-2* in these cells. Interestingly, *Cox* mRNA changes did not correlate with protein expression; *Cox-1* mRNA was reduced in *Bax*$^{-/-}$ MEFs while no change was observed in *Cox-2* mRNA (Figure 3.5B).

To compare WT and *Bax*$^{-/-}$ MEF transcriptional profiles more globally and map the resulting differences into known biological processes, we also performed RNA sequencing followed by gene set enrichment analysis (GSEA). GSEA of altered genes using the KEGG collection of canonical pathways (C2:CP:KEGG) revealed mapping into multiple gene sets including arachidonic acid metabolism and cytokine cytokine receptor interaction, both hallmarks of the cellular inflammatory response (Figure 3.6) and in agreement with our metabolomics and Western blot data.

3.2.5. BAX impairs COX-2 induction by LPS

COX-2 induction and subsequent increase in COX activity are key steps of the inflammatory cascade, as demonstrated by the success of COX-2 inhibitors in preventing inflammation [33]. A variety of agents stimulate COX-2 expression and inflammation, including *E. coli* lipopolysaccharide (LPS), a bacterial endotoxin and ligand for Toll-like receptor 4 (TLR4) [34]. While our data in MEFs clearly demonstrate BAX regulation of basal COX-2 expression, we also addressed the question of whether absence of BAX perturbs COX-2 induction by LPS, which would more accurately mimic an endogenous inflammatory response. WT and *Bax*$^{-/-}$

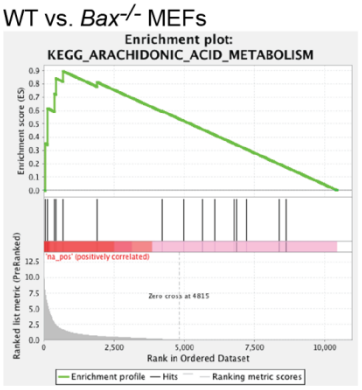

Core enrichment = Yes
PLA2G5
PLA2G2E
LTC4S
GGT1
CYP2J2

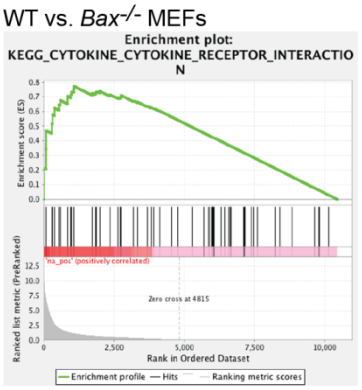

Core enrichment = Yes
TNFRSF11B
IL17RB
CXCL14
KITLG
TGFB2
INHBA
CSF3R
TGFB3
IL4R
PDGFRB
TNFRSF10A
TNFRSF25
GHR
VEFGB

Figure 3.6. GSEA of RNA-Seq results from WT and *Bax*$^{-/-}$ MEFs. Enrichment results are shown for the arachidonic acid metabolism and cytokine cytokine receptor interaction gene sets.

MEFs were harvested 0, 3 and 6 hours post-LPS treatment, and *Cox* mRNA and protein levels were measured (Figure 3.7A). LPS increased *Cox-2*, but not *Cox-1*, transcript and protein levels in WT MEFs (3.7B, C). Importantly, the *Cox-2* response in *Bax*$^{-/-}$ MEFs was significantly blunted, demonstrating a role for BAX in the cellular inflammatory response to LPS (Figure 3.7B, C). In addition, basal *Cox-1* transcription, but not expression, was reduced in the absence of BAX, suggesting that BAX could also modulate *Cox-1* transcription (Figure 3.5B; Figure 3.7B, C). Taken together, our data strongly support a diminished cellular inflammatory response through a marked reduction in COX-2 in the absence of BAX.

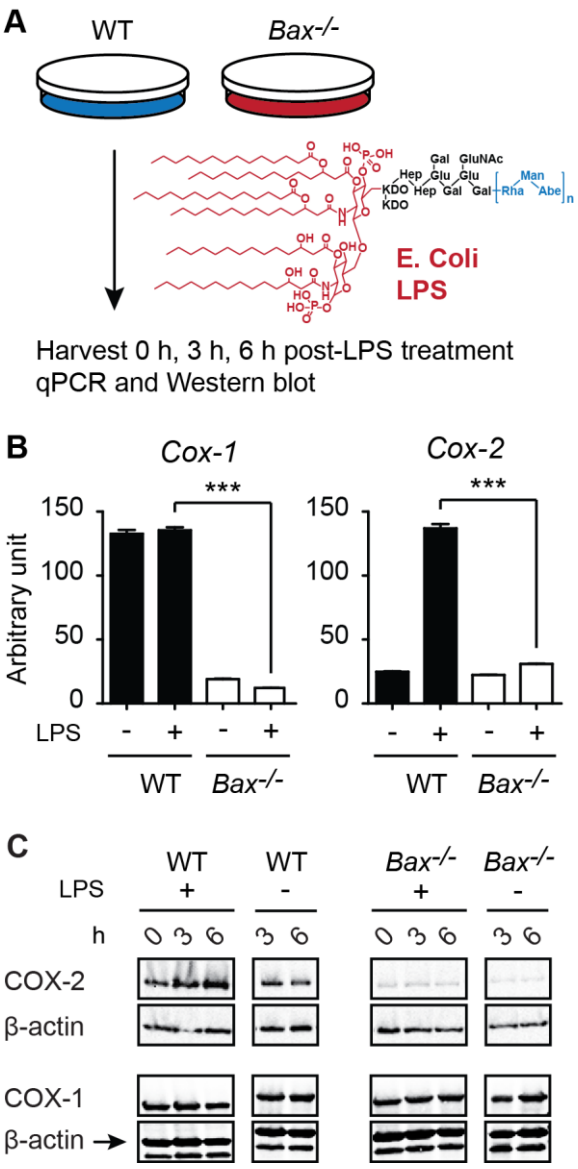

Figure 3.7. BAX impairs COX-2 induction by LPS. A) Schematic of E. Coli LPS addition to MEFs. B) RT-PCR of *Cox-1* and *2* in LPS or PBS-treated WT and *Bax*$^{-/-}$ MEFs. Cells (n=3) were treated with LPS (1 μg/mL) or PBS for 6 h. C) Western blots against COX-1 and 2 in LPS or PBS-treated WT and *Bax*$^{-/-}$ MEFs. Cells were treated with LPS (1 μg/mL) or PBS for 0, 3 or 6 h. *, $p \leq 0.05$, **, $p \leq 0.01$, ***, $p \leq 0.001$. Two-tailed Student's t test, SEM.

3.2.6. BAX modulates kinetics of TLR4 signaling

TLR4 belongs to the Toll-like receptor family, a well-characterized family of pattern recognition receptors (PRRs) involved in pathogen sensing [35]. TLR4 recognizes

lipopolysaccharide, a component of the outer membrane of Gram-negative bacteria [35]. LPS stimulation of TLR4 triggers recruitment of distinct adaptor proteins and assembly of downstream inflammatory complexes, resulting in activation of NFκB and MAP kinase (MAPK) cascades *via* TAK1, and subsequent transcription of inflammatory genes [35]. To determine if the blunted cellular response to LPS in the absence of BAX is attributable to a specific signaling pathway, WT and *Bax*$^{-/-}$ MEFs were harvested at 15-minute intervals following LPS addition, and time-dependent phosphorylation along the NFκB and MAPK pathways monitored by phospho-Western blot.

Activation of the TAK1, TAB1 and TAB2/3 complex leads to phosphorylation of NEMO and activation of an IKK complex; phosphorylation of IκBα induces its degradation, freeing NFκB to be phosphorylated and act as a transcription factor in the nucleus (Figure 3.8A) [35].

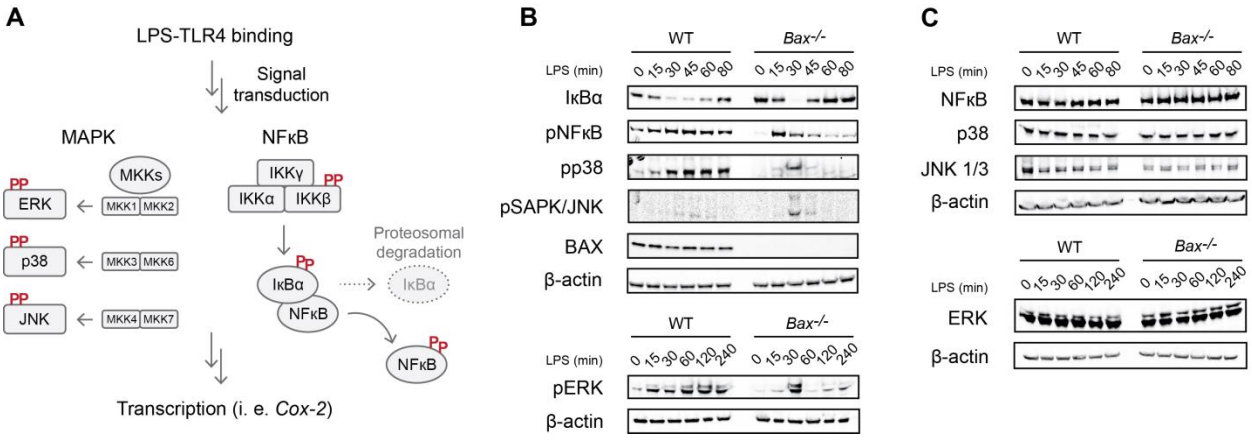

Figure 3.8. BAX modulates kinetics of TLR4 signaling. A) Schematic of NFκB and MAPK signaling in response to LPS stimulation of TLR4. B) Western blots demonstrating time-dependent activation of NFκB and MAPK pathways in response to LPS treatment. Cells were treated with LPS (2 μg/mL) at the indicated time points. Cells at 0 min were treated with PBS. C) Western blots against non-phosphorylated proteins in the NFκB and MAPK pathways.

TAK1 also activates the MAPK pathway (Figure 3.8A) by inducing phosphorylation of ERK, p38 and SAPK/JNK [35]. To assess response of these two pathways to LPS in the presence or

absence of BAX, we performed Western blot against IκBα, phosphorylated NFκB, and phosphorylated ERK, p38 and SAPK/JNK in LPS-treated WT and *Bax*$^{-/-}$ MEFs. LPS activated both NFκB and MAPK signaling in WT MEFs, as demonstrated by the time-dependent disappearance of IκBα and phosphorylation of NFκB and MAP kinases (Figure 3.8B). Interestingly, LPS-treated *Bax*$^{-/-}$ MEFs displayed altered kinetics in NFκB and MAPK signaling; absence of BAX resulted in a stronger, but short-lived activation of both NFκB and MAPK pathways relative to WT (Figure 3.8B). No significant differences in non-phosphorylated NFκB, ERK, p38 and JNK levels were observed between WT and *Bax*$^{-/-}$ MEFs (Figure 3.8C), suggesting that altered phosphorylation kinetics in the absence of BAX was not a direct result of changes in the levels of these proteins. Taken together, our findings suggest that BAX regulates COX-2 response to LPS by modulating the kinetics of NFκB and MAPK signaling.

3.2.7. BAX co-immunoprecipitation supports BAX-protein interactions

Altered NFκB and MAPK signaling in the absence of BAX raises the question of whether this effect is due to direct interaction between BAX and downstream inflammatory complexes that assemble upon LPS binding to TLR4. Similar changes in the kinetics of NFκB and MAPK signaling suggest that potential BAX-inflammasome interactions precede these two pathways and occur at or upstream of TAK1. To test this hypothesis, we performed co-immunoprecipitation against BAX in LPS-treated or untreated WT and *Bax*$^{-/-}$ MEFs. BAX was successfully precipitated in LPS-treated and untreated WT MEFs while no pulldown was observed in *Bax*$^{-/-}$ MEFs (Figure 3.9).

Proteins were precipitated from co-IP fractions, digested with trypsin and analyzed by LC–MS to identify potential interactors of BAX. Trypsin-digested samples were labeled with 6-

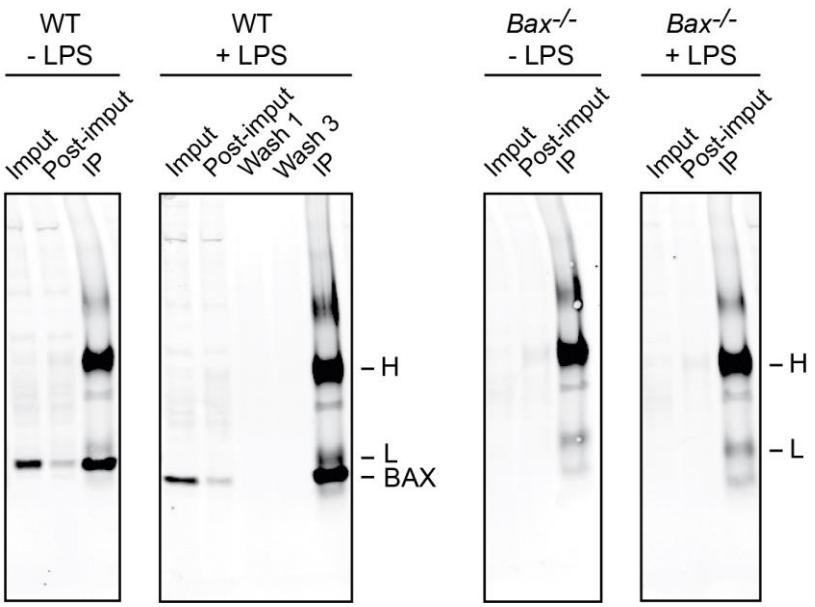

Figure 3.9. Co-immunoprecipitation of BAX in LPS-treated or untreated WT and *Bax*$^{-/-}$ MEFs.

plex tandem affinity tags (TMTs) to enable peptide quantification. A large WT/KO enrichment was observed for BAX (26-fold), in agreement with Western blot data (Figure 3.9, Table 3.1). Consistently enriched proteins and their detected fragments are listed in Table 3.1. Interactions between BAX and 14-3-3 proteins have been previously demonstrated through co-IP [36, 37]. Cytosolic localization of p53 induces apoptosis by directly activating BAX [38], and co-localization of p53 and activated BAX in response to the apoptotic agent staurosporine has been observed *via* confocal microscopy [39], supporting a direct BAX-p53 interaction. No BAX-TRIM21 interaction is known; however, TRIM21 is of particular interest given its role in acquired and innate immunity through regulation of NFκB and IRF signaling [40, 41]. We hope to further confirm these findings *via* Western blot and MRM targeting known peptide fragments of enriched proteins; effects of knockdowns of enriched proteins on the cellular inflammatory response will also be examined.

Name	Function (UniProt)	Detected sequences	Fold change
BCL2-associated X protein [Q8K3J2]	Apoptosis	**tGAFLLQGFIQDR**	**26.32**
Lysyl oxidase homolog 2 [P58022]	Lysine deamination, extracellular matrix protein crosslinking, transcription regulation	aYkPEQPLVR	4.88
		eLGFGTAk	**3.61**
		IGQGIGPIHLNEVQcTGTEk	3.51
		aYkPEQPLVR	3.09
		kAYkPEQPLVR	3.04
		kPVTEGYVEVk	2.96
		sWAASSSYGPGEGPIWLDNIYcTGk	1.84
α-Mannosidase 2 [P27046]	Complex N-glycans biosynthesis	vLLAPLGDDFR	3.26
		gIGLPcSTTqGk	**2.75**
		yYTDLnGYqIQPR	1.86
E3 ubiquitin-protein ligase TRIM21 [Q3U7K7]	Protein ubiquitination, cell cycle regulation, negative regulation of NFκB transcription factor activity	nQALQELISELER	7.41
		ecIFEVGk	**2.70**
Cellular tumor antigen p53 [Q3UGQ1]	Tumor repressor, apoptosis, cell cycle regulation	sVmcTYSPPLNk	2.78
		kPLDGEYFTLk	2.78
		lFcQLAk	**2.65**
		sVmcTYSPPLNk	2.59
14-3-3 protein δ/ζ [P63101]	Protein binding, regulation of general and specialized signaling pathways, cell death regulation	dIcNDVLSLLEk	3.00
		yLAEVAAGDDkk	**2.64**

Table 3.1. List of consistently enriched proteins from co-immunoprecipitation of BAX. The most abundant detected peptide and its WT/KO enrichment for each protein are in bold. Protein functions are based on UniProt (http://www.uniprot.org) search.

3.3. Discussion

The recent emergence of non-apoptotic functions for several BCL-2 proteins suggests that other members of this family might also be involved in biology outside of cell death [11, 14, 15]. Here, we demonstrate that BAX and BAK regulate the magnitude of the cellular inflammatory response, as measured by NFκB and MAPK signaling, COX-2 expression and prostaglandin production. Importantly, altered inflammatory response was present in both DKO and SKO MEFs, suggesting that BAX and BAK cannot compensate for each other in this function, which stands in contrast to their capacity to subserve each other's pro-apoptotic and

mitochondrial morphogenesis roles [15, 42]. Thus, BAX and BAK are likely modulating the cellular inflammatory response through a separate pathway from their regulation of mitochondrial morphology and apoptosis, which are dependent on both proteins. Differences in prostaglandin level and basal COX-2 expression were more pronounced in *Bax*$^{-/-}$ than *Bak*$^{-/-}$ MEFs, leading us to focus on the role of BAX in COX-2 regulation.

Endogenously, COX-2 expression is induced in response to inflammatory signals. LPS treatment of macrophages leads to COX-2 upregulation and prostaglandin E_2 production [43]. Prostaglandin accumulation is also associated with increased COX-2 expression in inflamed tissues in rat models of adjuvant arthritis [44]. To mimic these conditions in MEFs we monitored changes in COX protein and RNA levels following LPS treatment. Given the inducible nature of COX-2, significant differences in *Cox-2* mRNA were only observed between WT and *Bax*$^{-/-}$ MEFs in the presence of LPS (Figure 3.7B). Absence of BAX inhibited the upregulation in *Cox-2* mRNA and protein following LPS treatment (Figure 3.7B, C). Taken together, our data clearly indicate that BAX regulates COX-2 at both transcriptional and translational levels in response to LPS.

Paradoxically, *Cox-1* mRNA was reduced in *Bax*$^{-/-}$ MEFs while COX-1 expression was unaltered between WT and *Bax*$^{-/-}$ cells in the presence or absence of LPS (Figure 3.5B; Figure 3.7B, C). While it is possible for BAX to regulate *Cox-1* transcriptionally, the role of the latter in basal prostaglandin biosynthesis implies significant change in the level of the COX-1 enzyme could be detrimental to the cell. Consequently, similarity in COX-1 expression between WT and *Bax*$^{-/-}$ MEFs could be a translational or post-translational compensatory mechanism on the part of *Bax*$^{-/-}$ cells to restore COX-1 production to wild type levels. RNA sequencing of WT and

Bax$^{-/-}$ MEFs followed by GSEA revealed mapping to pathways associated with inflammation as further support of our observations on the metabolite and enzyme levels (Figure 3.6).

To our knowledge, this is the first report linking BAX and BAK to the regulation of prostaglandins, COX-2 and inflammation; however, the BCL-2 family member BID was recently shown to have a role in inflammation and innate immunity [14], suggesting that there may be a general connection between inflammation and the BCL-2 family. BID is downstream of NOD1 activation, which has been implicated in intestinal inflammation [14]. Together with Toll-like receptors and two other receptor families, the NOD proteins belong to a group of pattern recognition receptors (PRRs) that recognize a variety of ligands associated with microbial infection or tissue damage [35]. BID mediates formation of the NOD signalome upon NOD activation, leading to production of inflammatory cytokines and chemokines; NOD activation in the absence of BID results in significantly blunted inflammatory response, as demonstrated by reduced NFκB and MAPK signaling, and cytokine production [14].

Based on our finding that BAX is upstream of LPS-induced COX-2 upregulation we hypothesize that BAX could also be participating in the assembly of downstream inflammatory complexes upon LPS binding to TLR4; absence of BAX could lead to complex destabilization and subsequently, reduced NFκB and MAPK signaling, and COX-2 translation [45]. Surprisingly, LPS treatment of *Bax*$^{-/-}$ MEFs induced significantly more rapid activation but also deactivation of both NFκB and MAPK pathways (Figure 3.8B), and no detectable increase in COX-2 (Figure 3.7C), relative to WT. We hypothesize that absence of BAX could increase the kinetics of inflammatory complex assembly due to the presence of fewer components in the complex; however, assembled complexes lacking BAX could also be more destabilized and prone to degradation than WT, resulting in the altered signaling kinetics in *Bax*$^{-/-}$ MEFs (Figure

3.10). It is worth noting that in the NOD pathway, removal of BAX had no impact on inflammatory response [14], indicating that different BCL-2 proteins may regulate distinct inflammatory pathways initiated by different PRRs. The elucidation of these connections represents a new frontier in understanding the non-apoptotic roles of BCL-2 proteins and supports a more general function for the BCL-2 family in immunity.

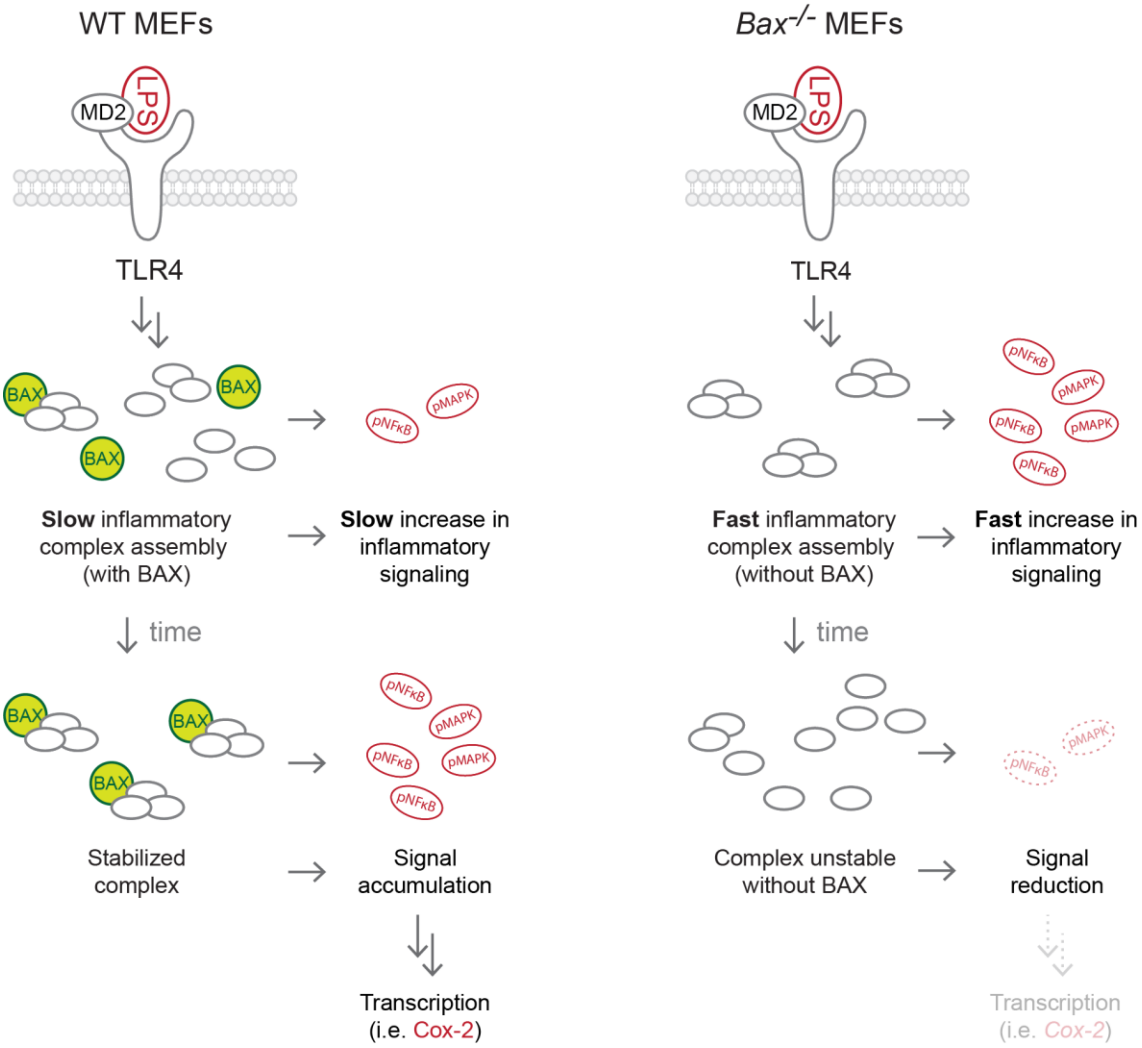

Figure 3.10. A model illustrating altered kinetics of LPS-induced TLR4 signaling in the absence of BAX.

Co-immunoprecipitation of BAX identified five consistently WT-enriched proteins (Table 3.1). TRIM21 is of particular interest given its roles in innate and acquired immunity [46]. TRIM21, also known as Ro52, is an autoantigen involved in autoimmune diseases such as systemic lupus erythematosus [46, 47]. TRIM21 has E3 ubiquitin ligase activity and regulates the levels of type I interferons and cytokines in response to viral or bacterial infection *via* ubiquitination of the interferon regulatory factors IRF3, 5 7 and 8 [47]. TRIM21 is tyrosine phosphorylated upon TLR3 or TLR4 stimulation, suggesting interaction between this protein and TLR signaling [48]. Interestingly, MEFs isolated from *Trim21*$^{-/-}$ mice displayed higher levels of LPS-induced cytokine production relative to WT; luciferase reporter analysis revealed elevated NFκB activity in LPS-treated *Trim21*$^{-/-}$ MEFs relative to WT, supporting negative regulation of NFκB signaling by TRIM21 [41, 46]. It is worth noting that in a separate study demonstrating a PRR-independent role for TRIM21 in intracellular antibody recognition, no LPS induction of NFκB was observed in WT or *Trim21*$^{-/-}$ MEFs, although this could be attributable to differences in the concentration of LPS used [40]. The overlap of multiple inflammatory pathways both at the level of ligand binding and at NFκB suggests the possibility of TRIM21 involvement in different receptor signaling pathways depending on cell state; BAX interaction with TRIM21 could affect the latter's regulation of inflammatory responses through perturbations in NFκB and/or additional signaling pathways.

3.4. Conclusion

Global lipidomics of WT, BAX and BAK-double knockout, and BAX or BAK single knockout MEFs revealed down-regulation of 6-keto-$PGF_{1\alpha}$ and accumulation of the eicosanoid precursor arachidonic acid in DKO and SKO MEFs relative to WT. In agreement with

metabolite data, expression of the inducible prostaglandin biosynthetic enzyme COX-2 was significantly decreased in DKO and SKO MEFs relative to WT. Absence of BAX resulted in blunted LPS-induced COX-2 upregulation by altering the kinetics of TLR4 signaling through both NFκB and MAPK pathways, supporting potential BAX-inflammasome interactions downstream of LPS binding to TLR4. Co-immunoprecipitation followed by proteomics identified five potential interactors of BAX, including the protein-ubiquitin ligase TRIM21 with known roles in immunity [40, 41]. Knockdown of these proteins in mammalian cells and extension of our study into murine models could yield additional information on BAX-inflammasome interactions and their effects on cytokine production and COX-2 regulation.

These studies uncover a novel role of BAX that will strongly impact the current understanding of COX-2 regulation. COX-2 is the predominant enzyme responsible for the production of inflammatory prostaglandins. Inhibition of this COX isoform formed the basis for the development of COX-2 inhibitors as drugs for treatment of inflammatory diseases such as rheumatoid arthritis [49]. Unfortunately, these drugs were ultimately recognized to increase cardiovascular risks most likely due to their effects on prostacyclin production [49]. The discovery of COX-2 regulation by BAX raises new questions and possibilities; the presence of this pathway in specific cell types or tissues could allow for controlled targeting of COX-2 without diminishing its cardioprotective roles. Future work will aim to elucidate the molecular mechanism linking BCL-2 proteins to COX-2, and explore potential applications of these insights toward the development of therapeutics.

3.5. Methods

3.5.1. Materials

Ammonium formate (516961), ammonium acetate (372331), ammonium hydroxide (338818) and lipopolysaccharides from *E. coli* 0111:B4 (L4391) were purchased from Sigma-Aldrich. Formic acid (06440) was from Fluka. Water (365-4), methanol (230-4), isopropanol (323-4), acetonitrile (017-4) and chloroform (049-1L) for lipid extraction and LC–MS were from Honeywell Burdick & Jackson. 6-keto-prostaglandin $F_{1\alpha}$ (10007219), 16, 5-diketo-13, 14-dihydroxy-prostaglandin $F_{1\alpha}$ (15270), 20-hydroxy-prostaglandin $F_{2\alpha}$ (16950), thromboxane B_2 (19030), 19(R)-hydroxy-prostaglandin $F_{2\alpha}$ (16910) and 19(R)-hydroxy-prostaglandin E_1 (13910) were from Cayman Chemical. Mouse anti-COX-1 (ab695), rabbit anti-COX-2 (ab15191), mouse anti-β-actin (ab8226) and rabbit anti-VDAC (ab15895) primary antibodies were from Abcam. Mouse anti-cytochrome c antibody (556433) was from BD Pharmingen. NF-κB Pathway Sampler Kit (9936), MAPK Family Antibody Sampler Kit (9926) and phospho-MAPK Family Antibody Sampler Kit (9910) were from Cell Signaling Technology. Protein A/G PLUS-Agarose (sc-2003), rabbit anti-JNK1/3 (sc-474) and rabbit anti-BAX (sc-493) primary antibodies were from Santa Cruz Biotechnology. IRDye 680LT donkey anti-rabbit (926-68023) and IRDye 800CW goat anti-mouse (926-32210) secondary antibodies were from LI-COR. RIPA buffer (89901) was from Thermo Scientific.

3.5.2. Tissue culture and harvest

Mouse embryonic fibroblasts were maintained in 5 % CO_2 at 37 °C in Dulbecco's Modified Eagle's Medium (Life Technologies, 11965) supplemented with 10 % fetal bovine serum (Hyclone, SH300070.03), penicillin (70 µg/mL), streptomycin (110 µg/mL), non-essential amino acids (1X) and L-glutamine (final concentration 6 mM). All cells were passaged (1:4-1:6) at least three times by trypsinization and harvested 36-40 h after the last passage by scraping.

Cell pellets were frozen at -80 °C except for mitochondria preparation, in which case mitochondria were isolated from cells immediately upon harvesting.

3.5.3. Mitochondria isolation and lipid extraction

Mitochondria were isolated from ~2.5×10^8 cells based on known protocol [50] using a sucrose isolation buffer (250 mM sucrose, 10 mM Tris-HCl, 0.1 mM EGTA · 4 Na, pH 7.4). Lipids were extracted from either mitochondria (from ~2.5×10^8 cells) or whole cell (~10^7 cells) pellets with modifications on known protocols [51, 52]. Pellets were either Dounce homogenized 30-40 times on ice or shaken for 30 s at rt (comparable extraction efficiencies were observed for the two methods by LC–MS [data not shown]) in 2:1:1 chloroform:methanol:citric acid buffer (100 mM trisodium citrate, 1 M NaCl, pH 3.6), vortexed (in glass vials) for 15-30 s and centrifuged at 2200 g, 4 °C for 6 min to allow separation between aqueous (top) and organic (bottom) layers. The organic fraction was transferred to a new glass vial and concentrated under a gentle stream of nitrogen. Dried lipids were stored at -80 °C and reconstituted in chloroform (unless otherwise indicated) for LC–MS.

3.5.4. Global lipidomics of WT, DKO and SKO MEF mitochondria

Global LC–MS profiling was performed on an Agilent 6220 LC-ESI-TOF instrument in positive and negative ionization modes with modifications on known protocol [53]. For negative mode a Gemini (Phenomenex) C18 column (5 µm, 4.6 mm × 50 mm) was used with a precolumn (C18, 3.5 µm, 2 mm × 20 mm). Solvent A was 95: 5 water: methanol with 0.1 % ammonium hydroxide, and solvent B was 60:35:5 isopropanol:methanol:water with 0.1 % ammonium hydroxide. For positive mode a Luna (Phenomenex) C5 column (5 µm, 4.6 mm × 50 mm) was

used with a precolumn (C4, 3.5 µm, 2 mm × 20 mm). Solvent A was 95: 5 water: methanol with 0.1 % formic acid and 5 mM ammonium formate, and solvent B was 60:35:5 isopropanol:methanol:water with 0.1 % formic acid and 5 mM ammonium formate. Identical gradient was used for both ionization modes. The gradient was held at 0 % B between 0 and 5 min, changed to 20 % B at 5.1 min, increased linearly from 20 % B to 100 % B between 5.1 min and 45 min, held at 100 % B between 45.1 min and 53 min, and returned to 0 % B at 53.1 min and held at 0 % B between 53.1 min and 60 min to allow column re-equilibration. Flow rate was maintained at 0.1 mL/min between 0 min and 5 min to counter pressure increase due to the chloroform injection. The flow rate was 0.4 mL/min between 5.1 min and 45 min, and 0.5 mL/min between 45.1 min and 60 min. Injection volume was 30 µL. Capillary voltage was 3.5 kV and fragmentor and skimmer voltages were 100 V and 60 V, respectively. Drying gas temperature was 350 °C, drying gas flow rate was 10 L/min and nebulizer pressure was 45 psi. Data were collected in both profile and centroid modes using a mass range of 100-1500 Da.

Data from general profiling were analyzed *via* targeted and untargeted approaches. For the targeted approach, extracted ion chromatograms (EICs) corresponding to the m/z of known metabolites were manually integrated in MassHunter Quantitative Analysis (Agilent Technologies), and the resulting ion counts compared between WT and KO groups to give relative quantification for known lipids. Statistical significance was determined by two-tailed Student's t-test. All errors were standard errors of the mean. For the untargeted approach, LC–MS raw data were converted from .d to .mzXML format with trapper-4.3.1 (http://sourceforge.net/projects/sashimi/files). WT and KO samples were sorted into two groups and analyzed *via* XCMS [21]. Following filtering of XCMS output files by statistical significance (p-value ≤ 0.05), fold change (≥ 3) and reproducibility across four independent data

sets, the remaining metabolite changes were further confirmed by manual integration in Qualitative Analysis and Student's t-test. Molecular formulae for unidentified metabolites were generated using formula calculator in Quantitative Analysis.

3.5.5. Co-injection and tandem MS

Co-injection for 6-keto-$PGF_{1\alpha}$ was performed in negative mode on the Agilent 6220 LC-ESI-TOF instrument. A Luna (Phenomenex) C18(2) column (3 µm, 250 mm × 2.00 mm) was used. Solvent A was 90: 10 water: acetonitrile with 5 mM ammonium acetate and 0.1 % formic acid, and solvent B was 50: 50 water: acetonitrile with 5 mM ammonium acetate and 0.1 % formic acid. The gradient was held at 0 % B between 0 and 5 min, increased linearly from 0 % B to 100 % B between 5.1 min and 45 min, held at 100 % B between 45.1 min and 53 min, and returned to 0 % B at 53.1 min and held at 0 % B between 53.1 min and 70 min to allow column re-equilibration. The flow rate was maintained at 0.1 mL/min between 0 min and 5 min, increased to 0.25 mL/min at 5.1 min and maintained at 0.25 mL/min for the rest of the run. 1.7 pmol 6-keto-$PGF_{1\alpha}$ was used as standard and a mixture of WT and *Bak*$^{-/-}$ MEF mitochondrial lipid extracts was used as sample; for co-injection, the endogenous lipid extract and standard were combined and half of the mixture was injected. The injection volume was 3 µL and all samples were reconstituted in 1:1 chloroform. Tandem MS was performed on an Agilent 6410 Triple Quad LC/MS instrument operated in Product Ion mode. The precursor ion was m/z 369.2 in negative mode. MS2 range was set to 50-371 Da to capture the entire fragmentation range of the targeted metabolite. Time filter width was 0.07 min. Fragmentor voltage and collision energy were 140 V and 27 V, respectively. ΔEMV was 400 V. Capillary voltage was 4.0 kV, skimmer voltage was 15 V, drying gas temperature was 350 °C, drying gas flow rate was 8

L/min and nebulizer pressure was 35 psi. All additional parameters were identical to co-injection.

3.5.6. Quantification of 6-keto-$PGF_{1\alpha}$ and arachidonic acid in whole cell lysates

6-keto-$PGF_{1\alpha}$ and arachidonic acid were measured on the Agilent 6410 Triple Quad LC/MS instrument operated in multiple reaction monitoring (MRM) mode. Fragmentor voltages for 6-keto-$PGF_{1\alpha}$ and arachidonic acid were 140 V and 113 V, respectively. Precursor-to-product ion transitions for arachidonic acid were m/z 303.2 → m/z 59.0 (CE = 19 V), m/z 303.2 → m/z 259.2 (CE = 4 V) and m/z 303.2 → m/z 205.2 (CE = 4 V), and the transitions for 6-keto-$PGF_{1\alpha}$ were m/z 369.2 → m/z 163.0 (CE = 27 V) and m/z 369.2 → m/z 245.2 (CE = 27 V). All transitions yielded similar DKO/WT fold changes for each metabolite. Ion counts from the m/z 303.2 → m/z 59.0 and m/z 369.2 → m/z 163.0 transitions were used for quantification. Additional parameters were identical to tandem MS. Arachidonic acid was monitored with the same column and gradient as global profiling. 6-Keto-$PGF_{1\alpha}$ was monitored with both the global profiling gradient and the optimized acetonitrile-water gradient used for co-injection, yielding comparable results.

3.5.7. Real time-PCR

Total RNA was isolated from WT and *Bax*$^{-/-}$ MEFs with the RNeasy Mini Kit (Qiagen) and reverse transcribed with the QuantiTect Reverse Transcription Kit (Qiagen) following manufacturer's instructions. Primers for *Cox-1* (NM_008969), *Cox-2* (NM_011198) and *Bax* (NM_007527) were from Qiagen. Quantification for genes of interest was performed with the QuantiTect SYBR Green PCR Kit (Qiagen) on a MX3000p thermal cycler (Stratagene).

Relative mRNA levels were calculated using the comparative Ct method with *Gapdh* (forward: 5'-GTG AGG CCG GTG CTG AGT AT-3', reverse: 5'-TCA TGA GCC CTT CCA CAA TG-3', Integrated DNA Technologies) as reference gene [54].

3.5.8. RNA sequencing and gene set enrichment analysis (GSEA)

RNA sequencing for WT, DKO and SKO MEFs was performed by the sequencing facility at Center for Cancer Computational Biology (Dana Farber Cancer Institute, Boston, MA). Assembled .gtf files were imputed into Cuffdiff (http://cufflinks.cbcb.umd.edu) to generate a list of detectable genes and corresponding KO/WT fold changes, which was used for GSEA. GSEA was performed by Dr. Arthur Liberzon (GSEA and MSigDB Team, Broad Institute, Cambridge, MA) using the C2:CP:KEGG, C2:CP, C2:CGP and C5:BP collections.

3.5.9. LPS treatment

WT and *Bax*$^{-/-}$ MEFs were passaged (1:4-1:6) at least three times by trypsinization and treated with LPS (1 mg/mL solution in PBS) 24-40 h after the last passage. Final LPS concentration was 1 µg/mL. Equal volumes of PBS were used as negative control. Cells were harvested on ice by scraping into cold PBS 0, 3 and 6 h post-LPS addition and stored at -80 °C prior to real time-PCR and Western blot against COX-1/2. For phospho-Western blot against NFκB and MAPK pathways, WT and *Bax*$^{-/-}$ MEFs were treated with LPS (1 mg/mL solution in PBS, final concentration 2 µg/mL) and harvested on ice by scraping into cold PBS either 15, 30, 45, 60 and 80 min or 15, 30, 60, 120 and 240 min post-LPS addition. Each harvested pellet was frozen immediately at -80 °C before the next time point. Cells for the 0 min time point were

treated with PBS without LPS and harvested by scraping immediately prior to LPS addition to the other samples.

3.5.10. Western blot

Protein concentrations were recorded in Quick Start 1X Bradford dye reagent (Bio-Rad, 500-0205). Cell pellets (~200-400 μg protein) were diluted in PBS with protease inhibitors (1.5X inhibitor cocktail [87786, Thermo Scientific], 10 mM sodium fluoride, 10 mM sodium orthovanadate), mixed with 3X Laemmli buffer, sonicated at 4 °C and boiled at 100 °C for ~5 min. The resulting samples were aliquoted (30-60 μg/gel) and stored at -80 °C prior to being loaded onto gels. Western blots were performed following standard protocol. PVDF membranes were imaged on an Odyssey Infrared Imager (LI-COR).

3.5.11. Co-immunoprecipitation and protein precipitation

WT and *Bax*$^{-/-}$ MEFs (~10^8 cells/sample) were treated with either PBS or LPS (1 mg/mL solution in PBS, final concentration 1 μg/mL) for 30 min and quickly harvested by scraping into PBS at RT. All subsequent steps were performed in cold room. Cell pellets were lysed in RIPA buffer (1 mL/sample) with protease inhibitors (1X EDTA-free inhibitor cocktail [11836170001, Roche], 5 mM sodium fluoride, 1 mM sodium orthovanadate) for 10 min with rotation and centrifuged at 14000 g for 10 min. 40 μL rabbit anti-BAX antibody and 100 μL A/G PLUS-Agarose beads were added to the supernatant, and the mixture incubated with rotation in cold room overnight. Beads were pelleted by centrifugation (1000 g, 3 min) and washed three times with RIPA buffer with protease inhibitors (1 mL each time). Washed beads were boiled in 30 μL 3X Laemmli buffer, centrifuged at 14000 g for 10 min, and the supernatant stored at -80 °C.

Proteins from Laemmli buffer were precipitated with ethanol and chloroform for proteomic analysis. To ensure presence of visible protein pellets, samples from three individual co-IP experiments were combined (total volume ~100 μL) on ice. 5X cold ethanol (pre-chilled overnight at -80 °C) was added, and the samples were mixed briefly by inversion and immediately incubated at -20 °C for 30 min. 1X room temperature chloroform was then added, at which point precipitates were observed immediately. The resulting samples were mixed briefly by inversion and incubated at -20 °C for an additional 30 min. Precipitated proteins were pelleted by centrifugation (20000 g, 10 min, 4 °C) and stored at -80 °C prior to proteomic analysis.

3.5.12. Proteomics

Sample preparation and LC–MS were performed by Dr. Bogdan Budnick at the Mass Spectrometry and Proteomics Resource Laboratory (FAS Center for Systems Biology, Harvard University, Cambridge, MA). Precipitated proteins were alkylated, digested with trypsin and labeled using commercially available 6-plex tandem affinity tags (TMTs) for quantification. Samples were injected onto a nanoACQUITY UPLC system (Waters) equipped with a 5 cm × 100 μm capillary trapping column (New Objective) packed with 5 μm C18 AQUA beads (Waters) and a PicoFrit SELF/P analytical column (15-μm tip, 25-cm length, New Objective) packed with 3 μm C18 AQUA beads (Waters). The UPLC system was online with a LTQ-Orbitrap Elite (Thermo Fisher) instrument configured with nanospray ESI interface and HCD cell. Data analysis was performed in Proteome Discoverer (Thermo Scientific) or IP2 (Integrated Proteomics Applications) to yield comparable results.

3.6. References

[1] L.D. Walensky, BCL-2 in the crosshairs: tipping the balance of life and death, Cell Death Differ., 13 (2006) 1339–1350.

[2] D.R. Green, J.C. Reed, Mitochondria and Apoptosis, Science, 281 (1998) 1309–1312.

[3] P.S. Schwartz, D.M. Hockenbery, Bcl-2-related survival proteins, Cell Death Differ., 13 (2006) 1250–1255.

[4] J.C. Reed, Proapoptotic multidomain Bcl-2//Bax-family proteins: mechanisms, physiological roles, and therapeutic opportunities, Cell Death Differ., 13 (2006) 1378–1386.

[5] T.J. McDonnell, G. Nunez, F.M. Platt, D. Hockenberry, L. London, J.P. McKearn, S.J. Korsmeyer, Deregulated Bcl-2-immunoglobulin transgene expands a resting but responsive immunoglobulin M and D-expressing B-cell population, Molecular and Cellular Biology, 10 (1990) 1901-1907.

[6] T.J. McDonnell, S.J. Korsmeyer, Progression from lymphoid hyperplasia to high-grade malignant lymphoma in mice transgenic for the t(14;18), Nature, 349 (1991) 254-256.

[7] T.J. McDonnell, N. Deane, F.M. Platt, G. Nunez, U. Jaeger, J.P. McKearn, S.J. Korsmeyer, bcl-2-Immunoglobulin transgenic mice demonstrate extended B cell survival and follicular lymphoproliferation, Cell, 57 (1989) 79-88.

[8] Z.N. Oltval, C.L. Milliman, S.J. Korsmeyer, Bcl-2 heterodimerizes in vivo with a conserved homolog, Bax, that accelerates programed cell death, Cell, 74 (1993) 609-619.

[9] J.C. Reed, M. Pellecchia, Apoptosis-based therapies for hematologic malignancies, Blood, 106 (2005) 408-418.

[10] M.H. Kang, C.P. Reynolds, Bcl-2 Inhibitors: Targeting Mitochondrial Apoptotic Pathways in Cancer Therapy, Clinical Cancer Research, 15 (2009) 1126-1132.

[11] N.N. Danial, C.F. Gramm, L. Scorrano, C.-Y. Zhang, S. Krauss, A.M. Ranger, S. Robert Datta, M.E. Greenberg, L.J. Licklider, B.B. Lowell, S.P. Gygi, S.J. Korsmeyer, BAD and glucokinase reside in a mitochondrial complex that integrates glycolysis and apoptosis, Nature, 424 (2003) 952-956.

[12] A. Giordano, M. Calvani, O. Petillo, P. Grippo, F. Tuccillo, M.A.B. Melone, P. Bonelli, A. Calarco, G. Peluso, tBid induces alterations of mitochondrial fatty acid oxidation flux by malonyl-CoA-independent inhibition of carnitine palmitoyltransferase-1, Cell Death Differ., 12 (2005) 603–613.

[13] R.M. Perciavalle, D.P. Stewart, B. Koss, J. Lynch, S. Milasta, M. Bathina, J. Temirov, M.M. Cleland, S. Pelletier, J.D. Schuetz, R.J. Youle, D.R. Green, J.T. Opferman, Anti-apoptotic MCL-1 localizes to the mitochondrial matrix and couples mitochondrial fusion to respiration, Nat Cell Biol, advance online publication (2012).

[14] G. Yeretssian, R.G. Correa, K. Doiron, P. Fitzgerald, C.P. Dillon, D.R. Green, J.C. Reed, M. Saleh, Non-apoptotic role of BID in inflammation and innate immunity, Nature, 474 (2011) 96-99.

[15] M. Karbowski, K.L. Norris, M.M. Cleland, S.-Y. Jeong, R.J. Youle, Role of Bax and Bak in mitochondrial morphogenesis, Nature, 443 (2006) 658-662.

[16] E. Gavathiotis, M. Suzuki, M.L. Davis, K. Pitter, G.H. Bird, S.G. Katz, H.-C. Tu, H. Kim, E.H.Y. Cheng, N. Tjandra, L.D. Walensky, BAX activation is initiated at a novel interaction site, Nature, 455 (2008) 1076-1081.

[17] F. Gonzalvez, Z.T. Schug, R.H. Houtkooper, E.D. MacKenzie, D.G. Brooks, R.J.A. Wanders, P.X. Petit, F.M. Vaz, E. Gottlieb, Cardiolipin provides an essential activating platform for caspase-8 on mitochondria, J. Cell Biol., 183 (2008) 681–696.

[18] M. Colombini, Ceramide channels and their role in mitochondria-mediated apoptosis, Biochimica et Biophysica Acta (BBA) - Bioenergetics, 1797 (2010) 1239-1244.

[19] P. Sengupta, B. Baird, D. Holowka, Lipid rafts, fluid/fluid phase separation, and their relevance to plasma membrane structure and function, Seminars in Cell & Developmental Biology, 18 (2007) 583-590.

[20] G. van Meer, D.R. Voelker, G.W. Feigenson, Membrane lipids: where they are and how they behave, Nat Rev Mol Cell Biol, 9 (2008) 112-124.

[21] C.A. Smith, E.J. Want, G. O'Maille, R. Abagyan, G. Siuzdak, XCMS: processing mass spectrometry data for metabolite profiling using nonlinear peak alignment, matching, and identification, Anal. Chem., 78 (2006) 779–787.

[22] M. Sud, E. Fahy, D. Cotter, A. Brown, E.A. Dennis, C.K. Glass, A.H. Merrill, Jr., R.C. Murphy, C.R. Raetz, D.W. Russell, S. Subramaniam, LMSD: LIPID MAPS structure database, Nucleic Acids Res., 35 (2007) D527–D532.

[23] M. Kanehisa, S. Goto, M. Hattori, K.F. Aoki-Kinoshita, M. Itoh, S. Kawashima, T. Katayama, M. Araki, M. Hirakawa, From genomics to chemical genomics: new developments in KEGG, Nucleic Acids Res., 34 (2006) D354–D357.

[24] C.D. Funk, Prostaglandins and Leukotrienes: Advances in Eicosanoid Biology, Science, 294 (2001) 1871-1875.

[25] H. Harizi, J.-B. Corcuff, N. Gualde, Arachidonic-acid-derived eicosanoids: roles in biology and immunopathology, Trends Mol. Med., 14 (2008) 461–469.

[26] Y. Cheng, S.C. Austin, B. Rocca, B.H. Koller, T.M. Coffman, T. Grosser, J.A. Lawson, G.A. FitzGerald, Role of Prostacyclin in the Cardiovascular Response to Thromboxane A2, Science, 296 (2002) 539-541.

[27] B. Rosenkranz, C. Fischer, K.E. Weimer, J.C. Frölich, Metabolism of prostacyclin and 6-keto-prostaglandin F1 alpha in man, J. Biol. Chem., 255 (1980) 10194–10198.

[28] A.R. Brash, E.K. Jackson, C.A. Saggese, J.A. Lawson, J.A. Oates, G.A. FitzGerald, Metabolic disposition of prostacyclin in humans, Journal of Pharmacology and Experimental Therapeutics, 226 (1983) 78-87.

[29] S. Durant, D. Duval, F. Homo-Delarche, Mouse embryo fibroblasts in culture: characteristics of arachidonic acid metabolism during early passages, Prostaglandins Leukot. Essent. Fatty Acids, 32 (1988) 129–137.

[30] C. Ody, C. Seillan, F. Russo-Marie, 6-Ketoprostaglandin F1α, prostaglandins E2, F2α and thromboxane B2 production by endothelial cells, smooth muscle cells and fibroblasts cultured from piglet aorta, Biochim. Biophys. Acta - Lipids and Lipid Metabolism, 712 (1982) 103–110.

[31] M.J. Garrity, E.P. Brass, R.P. Robertson, Kinetics of prostaglandin E metabolism in isolated hepatocytes, Biochim. Biophys. Acta - Lipids and Lipid Metabolism, 796 (1984) 136–141.

[32] R. Schuligoi, R. Schmidt, G. Geisslinger, M. Kollroser, B.A. Peskar, A. Heinemann, PGD2 metabolism in plasma: Kinetics and relationship with bioactivity on DP1 and CRTH2 receptors, Biochem. Pharmacol., 74 (2007) 107–117.

[33] W.L. Smith, D.L. DeWitt, R.M. Garavito, CYCLOOXYGENASES: Structural, Cellular, and Molecular Biology, Annu. Rev. Biochem., 69 (2000) 145–182.

[34] S.I. Miller, R.K. Ernst, M.W. Bader, LPS, TLR4 and infectious disease diversity, Nat. Rev. Micro., 3 (2005) 36–46.

[35] O. Takeuchi, S. Akira, Pattern Recognition Receptors and Inflammation, Cell, 140 (2010) 805-820.

[36] F. Ge, W.-L. Li, L.-J. Bi, S.-C. Tao, Z.-P. Zhang, X.-E. Zhang, Identification of Novel 14-3-3ζ Interacting Proteins by Quantitative Immunoprecipitation Combined with Knockdown (QUICK), Journal of Proteome Research, 9 (2010) 5848-5858.

[37] M. Nomura, S. Shimizu, T. Sugiyama, M. Narita, T. Ito, H. Matsuda, Y. Tsujimoto, 14-3-3 Interacts Directly with and Negatively Regulates Pro-apoptotic Bax, Journal of Biological Chemistry, 278 (2003) 2058-2065.

[38] J.E. Chipuk, T. Kuwana, L. Bouchier-Hayes, N.M. Droin, D.D. Newmeyer, M. Schuler, D.R. Green, Direct Activation of Bax by p53 Mediates Mitochondrial Membrane Permeabilization and Apoptosis, Science, 303 (2004) 1010-1014.

[39] Y. Geng, K.C. Walls, A.P. Ghosh, R.S. Akhtar, B.J. Klocke, K.A. Roth, Cytoplasmic p53 and Activated Bax Regulate p53-dependent, Transcription-independent Neural Precursor Cell Apoptosis, Journal of Histochemistry & Cytochemistry, 58 (2010) 265-275.

[40] W.A. McEwan, J.C.H. Tam, R.E. Watkinson, S.R. Bidgood, D.L. Mallery, L.C. James, Intracellular antibody-bound pathogens stimulate immune signaling via the Fc receptor TRIM21, Nat Immunol, 14 (2013) 327-336.

[41] R. Yoshimi, T.-H. Chang, H. Wang, T. Atsumi, H.C. Morse, K. Ozato, Gene Disruption Study Reveals a Nonredundant Role for TRIM21/Ro52 in NF-κB-Dependent Cytokine Expression in Fibroblasts, The Journal of Immunology, 182 (2009) 7527-7538.

[42] T. Lindsten, A.J. Ross, A. King, W.-X. Zong, J.C. Rathmell, H.A. Shiels, E. Ulrich, K.G. Waymire, P. Mahar, K. Frauwirth, Y. Chen, M. Wei, V.M. Eng, D.M. Adelman, M.C. Simon, A. Ma, J.A. Golden, G. Evan, S.J. Korsmeyer, G.R. MacGregor, C.B. Thompson, The Combined Functions of Proapoptotic Bcl-2 Family Members Bak and Bax Are Essential for Normal Development of Multiple Tissues, Molecular Cell, 6 (2000) 1389-1399.

[43] A.G. Eliopoulos, C.D. Dumitru, C.-C. Wang, J. Cho, P.N. Tsichlis, Induction of COX-2 by LPS in macrophages is regulated by Tpl2-dependent CREB activation signals, EMBO J, 21 (2002) 4831-4840.

[44] G.D. Anderson, S.D. Hauser, K.L. McGarity, M.E. Bremer, P.C. Isakson, S.A. Gregory, Selective inhibition of cyclooxygenase (COX)-2 reverses inflammation and expression of COX-2 and interleukin 6 in rat adjuvant arthritis, The Journal of Clinical Investigation, 97 (1996) 2672-2679.

[45] M. Fukata, M.T. Abreu, Role of Toll-like receptors in gastrointestinal malignancies, Oncogene, 27 (2008) 234-243.

[46] R. Yoshimi, Y. Ushigatsubo, K. Ozato, Autoantigen TRIM21/Ro52 as a Possible Target for Treatment of Systemic Lupus Erythematosus, International Journal of Rheumatology, 2012 (2012) Article ID 718237.

[47] V. Oke, M. Wahren-Herlenius, The immunobiology of Ro52 (TRIM21) in autoimmunity: A critical review, Journal of Autoimmunity, 39 (2012) 77-82.

[48] K.B. Stacey, E. Breen, C.A. Jefferies, Tyrosine Phosphorylation of the E3 Ubiquitin Ligase TRIM21 Positively Regulates Interaction with IRF3 and Hence TRIM21 Activity, PLoS ONE, 7 (2012) e34041.

[49] D. Mukherjee, S.E. Nissen, E.J. Topol, Risk of cardiovascular events associated with selective COX-2 inhibitors, JAMA : the journal of the American Medical Association, 286 (2001) 954–959.

[50] C. Frezza, S. Cipolat, L. Scorrano, Organelle isolation: functional mitochondria from mouse liver, muscle and cultured filroblasts, Nat. Protocols, 2 (2007) 287-295.

[51] A. Saghatelian, S.A. Trauger, E.J. Want, E.G. Hawkins, G. Siuzdak, B.F. Cravatt, Assignment of endogenous substrates to enzymes by global metabolite profiling, Biochemistry, 43 (2004) 14332–14339.

[52] E.G. Bligh, W.J. Dyer, A Rapid Method of Total Lipid Extraction and Purification, Canadian Journal of Biochemistry and Physiology, 37 (1959) 911-917.

[53] E.A. Homan, Y.-G. Kim, J.P. Cardia, A. Saghatelian, Monoalkylglycerol Ether Lipids Promote Adipogenesis, Journal of the American Chemical Society, 133 (2011) 5178-5181.

[54] F.E. Erfurth, R. Popovic, J. Grembecka, T. Cierpicki, C. Theisler, Z.-B. Xia, T. Stuart, M.O. Diaz, J.H. Bushweller, N.J. Zeleznik-Le, MLL protects CpG clusters from methylation within the Hoxa9 gene, maintaining transcript expression, Proc. Natl. Acad. Sci. , 105 (2008) 7517–7522.

Chapter 4

Development of a LC–MS-based workflow for characterization of a novel lipid class involved in type 2 diabetes

4.1. Introduction

Type 2 diabetes mellitus (T2D) is a metabolic syndrome affecting more than 300 million people worldwide [1, 2]. T2D is characterized at its early stage by insulin resistance and fasting hyperinsulinemia, progressing toward the clinical presentation of fasting or postprandial hyperglycemia [3]; long term complications include blindness, kidney failure, amputation and cardiovascular disease [1]. Correlation between obesity and T2D [1, 4, 5], along with altered carbohydrate usage and fatty acid oxidation observed in insulin resistant populations [3, 6, 7], suggest that metabolic changes associated with T2D are complex and involve interactions among all major branches of central metabolism. Paradoxically, mice overexpressing GLUT4, the major glucose transporter in insulin-sensitive tissues, display enhanced insulin sensitivity but also increased lipogenesis, suggesting that the protective effect of GLUT4 overexpression could be due to altered lipid profile [8, 9]. A comprehensive comparison of lipid profiles from WT and adipose-specific GLUT4 overexpressor (AG4OX) mice could yield valuable information on the connection between GLUT4 upregulation and lipid metabolism in the promotion of insulin sensitivity.

Liquid chromatography–mass spectrometry (LC–MS) has emerged as an important technique of metabolomics with applications in numerous biological settings [10-12]. Coupling of LC to MS-based detection methods allows time-dependent resolution of metabolite classes, enabling targeted or untargeted analysis of a large number of metabolites from one biological sample [10]. Untargeted global lipidomics of WT and fatty acid amide hydrolase (FAAH) knockout mice led to discovery of N-acyl taurines, a novel lipid class regulated by FAAH in murine nervous system and peripheral tissues [13]. Recent advancements in reproducibility and resolution of chromatography-based techniques, coupled with significant improvement in MS

sensitivity, have also enabled comprehensive targeted quantification of hydrophilic and hydrophobic metabolites at higher sensitivity than targeted approaches [10, 14, 15].

The comprehensiveness and high sensitivity of LC–MS-based metabolomics suggest this technique is a suitable choice for comparison of lipid profiles from WT and AG4OX mice. Lipidomics undertaken by Homan *et al.* revealed significant upregulation of a novel class of lipids comprised of fatty acids conjugated to hydroxy fatty acids (fatty acid hydroxy fatty acid, designated FAHFA) in AG4OX subcutaneous (SQ) white adipose tissue (WAT) relative to WT (Figure 4.1). Of the multiple FAHFA family members detected, the authors chose to focus on

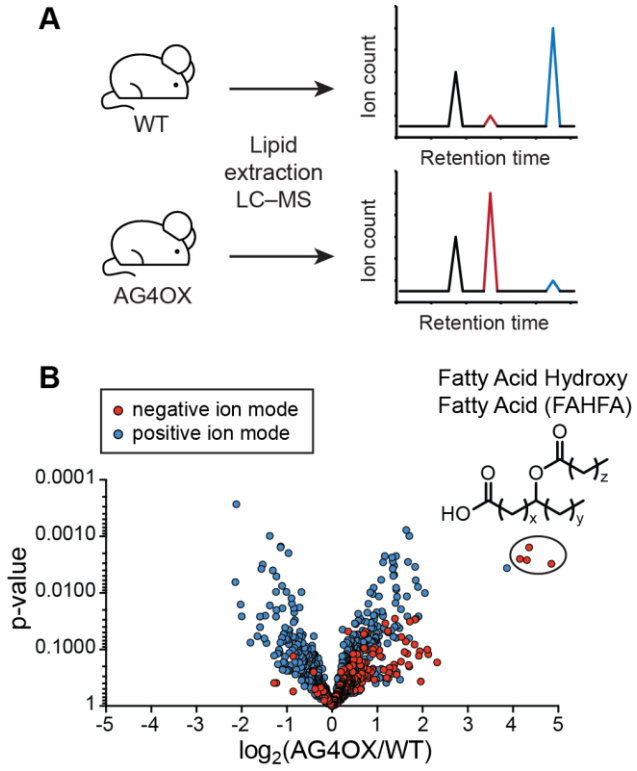

Figure 4.1. Comparative lipidomics of SQ WAT from WT and AG4OX mice. A) Schematic of unbiased, comparative global lipidomic analysis of WT and AG4OX murine lipids, allowing identification of metabolite changes. B) Volcano plot of ions (>10^5 ion count, 10-50 min) from WT and AG4OX SQ WAT lipids. Ions corresponding to fatty acid hydroxy fatty acids (FAHFAs), which are consistently elevated in AG4OX SQ WAT relative to WT, are circled in black. Two-tailed Student's t-test.

palmitic acid hydroxy stearic acid (PAHSA) given its high AG4OX/WT fold change (data not shown) and lack of unsaturation site, which eliminates data set complexity associated with double bond isomers.

PAHSA is comprised of palmitic acid (PA) esterified to the internal hydroxyl group in hydroxystearic acid (HSA). PAHSA positional isomers are designated 2-PAHSA through 18-PAHSA, based on location of the hydroxylated stearic carbon from the carboxylic acid. The structure of 9-PAHSA is shown in Figure 4.2, where palmitic acid is esterified to HSA at the ninth stearic carbon from the carboxylic acid. Alternative locations of hydroxylation are numbered in Figure 4.2.

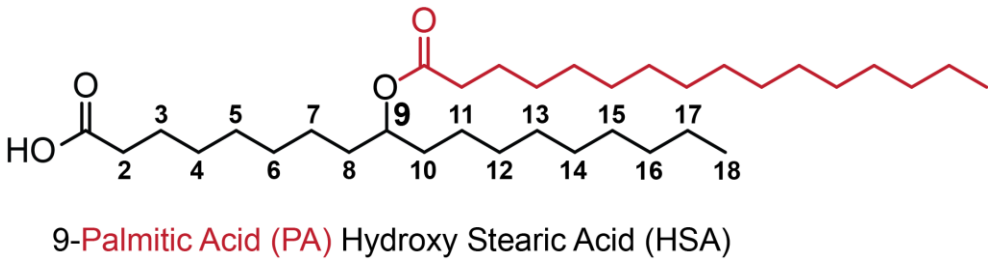

Figure 4.2. Structure of 9-palmitic acid hydroxy stearic acid (9-PAHSA). All possible locations of hydroxylation are numbered.

Potential existence of multiple PAHSA isomers raises the question of whether these species could be differentially regulated in the context of GLUT4 overexpression, which is the first step toward understanding the roles of these novel lipids in type 2 diabetes. To answer this question, quantification of individual PAHSA isomers in serum and tissues is crucial; unfortunately, this was not achieved with our untargeted global lipidomics method due to limited sensitivity and lack of chromatographic resolution for individual isomers. In this work, we present the development of a targeted LC–MS workflow for analysis of PAHSA isomers and additional FAHFA family members. Implementation this method in human and murine sera and

multiple murine tissues yielded sensitive, reproducible quantification of PAHSA isomers and additional FAHFAs, demonstrating selective regulation of distinct FAHFA pools in a tissue and subject-dependent manner.

4.2. Results

4.2.1. Optimization of multiple reaction monitoring (MRM) parameters for PAHSA detection

Global lipidomics through liquid chromatography (LC)–time of flight (TOF) mass spectrometry (MS) enabled targeted and untargeted analyses of known and novel metabolites with high mass accuracy; however, relatively low biological abundance of PAHSAs presented a challenge for measurement of these lipids across multiple murine tissue types [11]. To reduce quantity of samples necessary for analysis and improve data consistency, we switched to a targeted approach using a triple quadrupole mass spectrometer operated in multiple reaction monitoring (MRM) mode.

MRM has emerged as a powerful analytical technique that enables targeted, simultaneous quantification of multiple metabolites with high sensitivity [11, 14-16]. By subjecting the metabolite of interest (precursor ion) to an optimized set of fragmentation conditions and monitoring a specific fragment (product ion) that consistently originates from the precursor, MRM takes advantage of the characteristic precursor-to-product ion transition specific to each metabolite, allowing unambiguous identification and detection of known metabolites with high signal-to-noise ratio [11, 16]. As most metabolites with distinct structures will generate unique transitions, it is possible for many species to be monitored at once. Given many metabolites

fragment to yield multiple product ions at consistent ratios, multiple transitions could be optimized and monitored for each metabolite to increase the confidence of identification.

Tandem MS of 9-PAHSA (precursor ion m/z 537) yielded three characteristic fragments (product ions) at m/z 255, 299 and 281, corresponding to precursor-to-product ion transitions m/z 537 → 255, m/z 537 → 281 and m/z 537 → 299 (Figure 4.3). Fragmentor voltage for the precursor ion and collision energies (CEs) for all fragments were optimized manually to maximize signal-to-noise ratio for each transition. Of the fragments observed, m/z 255 corresponds to palmitic acid, m/z 299 to hydroxystearic acid, and m/z 281 to the hydroxystearic acid dehydration product C18:1 fatty acid (Figure 4.3). It is important to note that 9-PAHSA

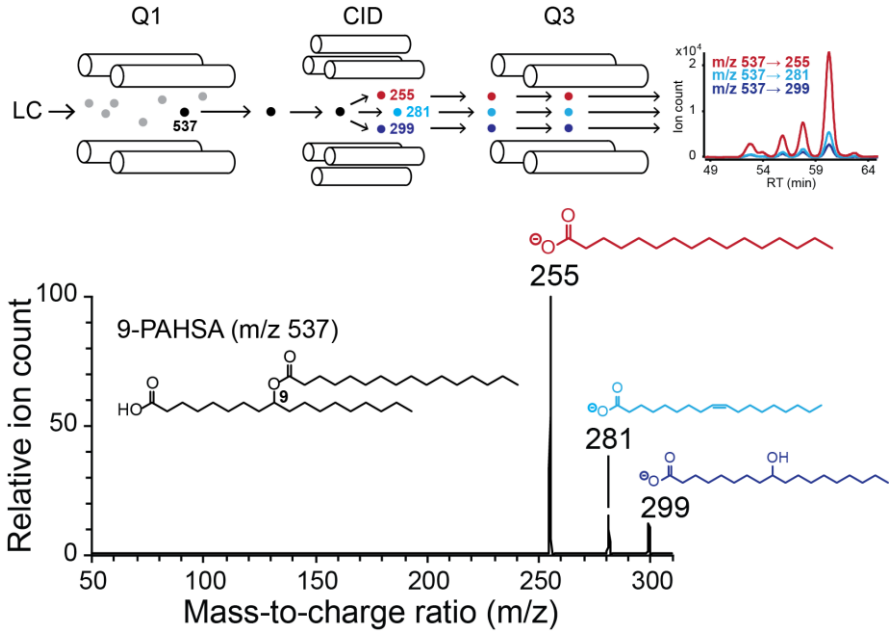

Figure 4.3. MRM of 9-PAHSA. MRM parameters are optimized based on characteristic fragmentation of 9-PAHSA (m/z 537) into palmitic acid (m/z 255), hydroxystearic acid (m/z 299) and C18:1 fatty acid (m/z 281).

consistently fragments with the relative fragment abundances m/z 255 > 281 > 299, which is reflected in the relative abundances of the corresponding precursor-to-product ion transitions

(m/z 537 → 255 > m/z 537 → 281 > m/z 537 → 299, Figure 4.3). Consequently, appearances of peaks from all three transitions with identical retention times and at PAHSA-characteristic ratios are importance criteria for the PAHSA structural assignment.

4.2.2. Chromatography optimization for resolution of PAHSA isomers

Presence of nearly identical major fragments in the tandem MS spectra of PAHSAs with different positions of fatty acid conjugation implies that MRM cannot distinguish PAHSA isomers (data not shown). Consequently, quantification of individual PAHSA isomers requires baseline chromatographic resolution. All optimizations were performed on a solution of synthesized 4, 5, 6, ^{13}C-8 (all ^{13}C standards are uniformly heavy-labeled on palmitic acid), 9, ^{13}C-9, 10, 11 and 12-PAHSA standards using a C18 column (3 μm, 100 Å, 2.0 × 250 mm) online with a triple quadrupole mass spectrometer in MRM mode. We hypothesized that the combination of column length and small particle size could sharpen standard peaks while allowing time for isomer resolution. A methanol-water system was initially tested, and 0.01 % ammonium hydroxide was added to all solvents to improve ion generation. Preliminary tests with water-to-methanol gradient elution did not yield good isomer resolution; comparable result was obtained with 90:10 methanol:water isocratic elution (Figure 4.4A). Significantly improved resolution was observed with 89.5:10.5 methanol:water, where reduced flow rate and addition of ammonium acetate led to increased peak retention and separation (Figure 4.4A); unfortunately, peak broadening and tailing also occurred, while the significantly delayed retention times (110-190 min) rendered analysis of large numbers of samples impractical, prompting us to further adjust the methanol:water ratio.

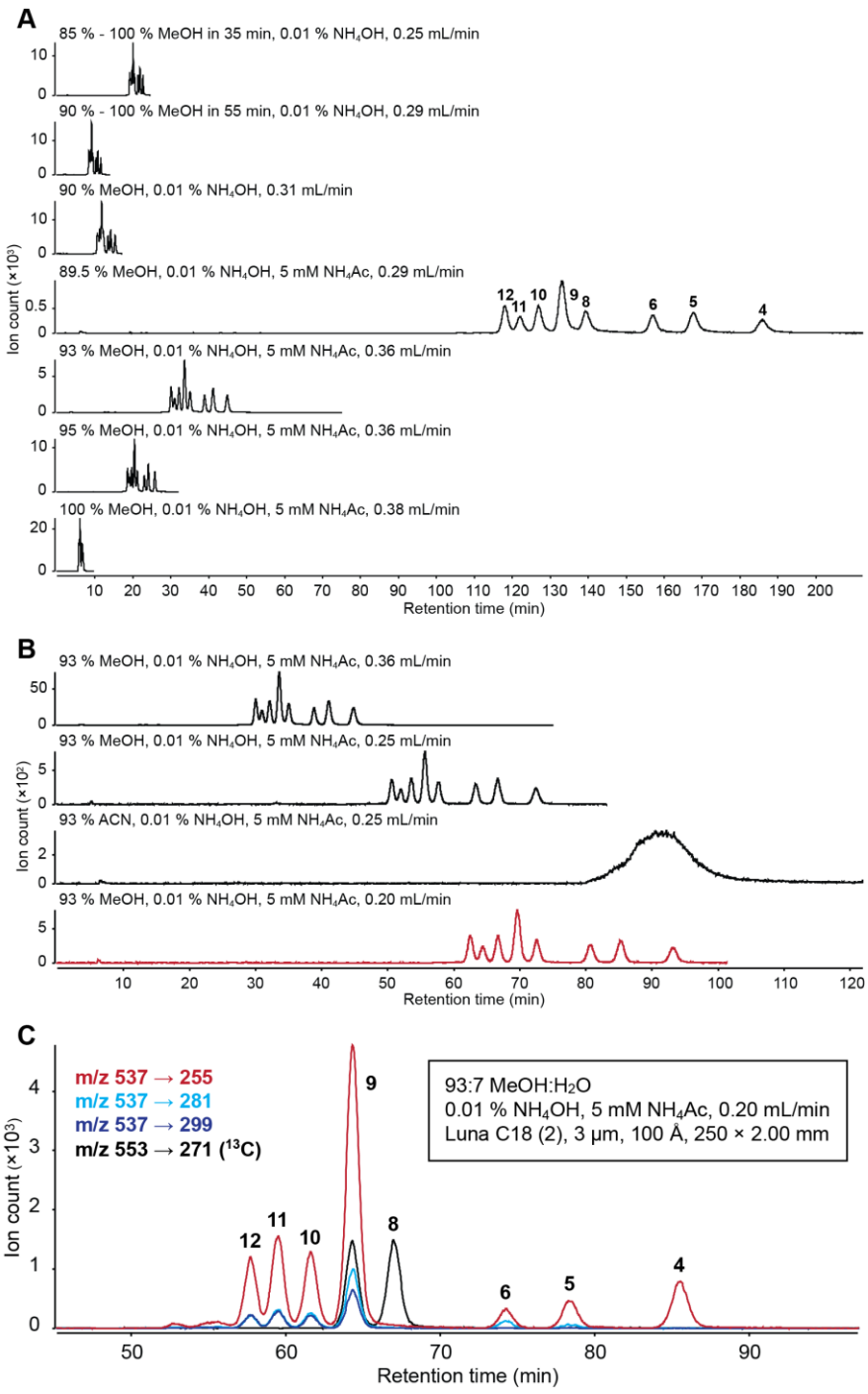

Figure 4.4. Chromatography optimization for resolution of PAHSA isomers. A) Comparison between methanol:water gradient and isocratic elutions and among different isocratic methanol:water ratios. B) Optimization of flow rate for the 93:7 methanol:water isocratic system and replacement test with 97:3 acetonitrile:water at 0.25 mL/min. C) Finalized LC method enabling resolution of 4, 5, 6, ^{13}C-8, 9, ^{13}C-9, 10, 11 and 12-PAHSA standards.

Methanol:water ratios from 89:11 to 100:0 were examined while maintaining the concentration of ammonium hydroxide and acetate. In comparison to the 89.5:10.5 methanol:water isocratic system, 93:7 methanol:water at 0.36 mL/min yielded significantly sharpened peaks at the cost of slightly decreased resolution (Figure 4.4A). While we had maintained a high flow rate (0.36 mL/min) in the 93:7 methanol:water system for the purpose of minimizing peak broadening and sample analysis time, we hypothesized that decreasing the flow rate could increase sample resolution. A range of flow rates was tested while maintaining the 93:7 methanol:water ratio and concentration of solvent modifiers (Figure 4.4B). 93:7 acetonitrile:water was also tested to yield no observable peak separation (Figure 4.4B). Reduction in flow rate significantly improved peak resolution for the 93:7 methanol:water ratio, and baseline separation was achieved for almost all PAHSAs at 0.20 mL/min (Figure 4.4B). Figure 4.4C illustrates measurement of 4, 5, 6, ^{13}C-8, 9, ^{13}C-9, 10, 11 and 12-PAHSA standards using the optimized LC method coupled to MRM. Similar to the 9-PAHSA standard used during MRM optimization (Figure 4.3), m/z 536 → 255 is the dominant transition for all PAHSA standards tested (Figure 4.4C).

In conjunction with chromatography optimization, effect of injection volume on resolution was also evaluated. Injection of standards in more than 3 μL chloroform significantly compromised resolution (Figure 4.5A), a potential consequence of unfavorable solvent-solvent interactions and polarity difference between the carrier and elution solvents. When the carrier solvent was switched to methanol, no significant resolution loss was observed between 2 μL and 15 μL (Figure 4.5B); 6 μL 1:1 methanol:chloroform was also tolerated (Figure 4.5C).

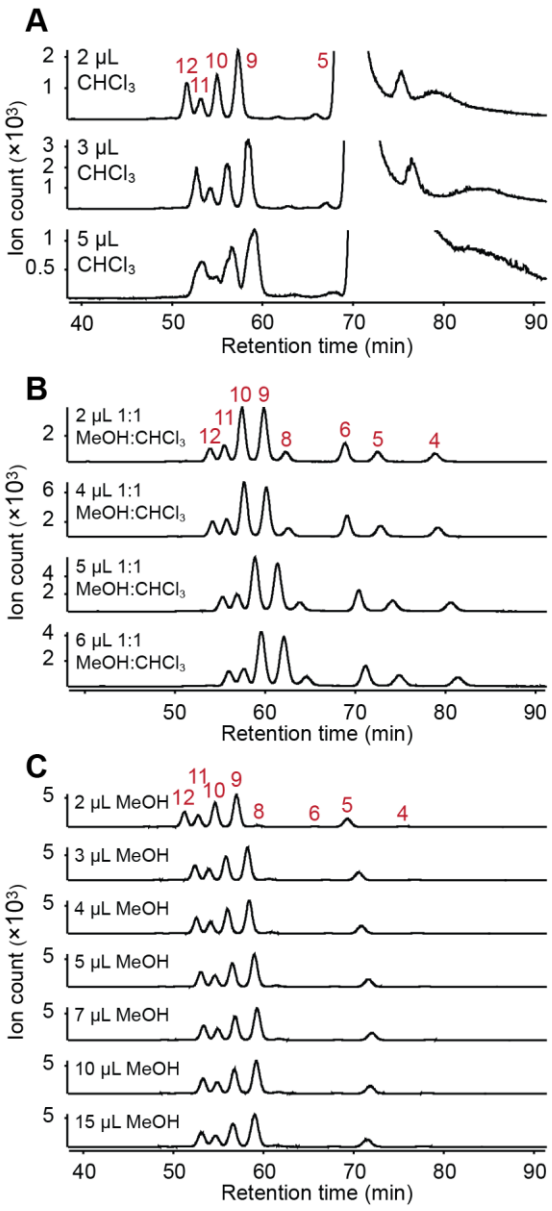

Figure 4.5. Effect of injection volume on PAHSA isomer resolution. A) Injection volume tests with chloroform. B) Injection volume tests with methanol. C) Injection volume tests with 1:1 methanol:chloroform.

4.2.3. Preliminary PAHSA analysis in PG WAT

The optimized LC–MS workflow was applied toward PAHSA analysis in WT murine perigonadal (PG) white adipose tissue (WAT). Lipid extraction was performed with slight modification on the Bligh-Dyer method [17], enabling extraction of major lipid classes including

fatty acids, phospholipids, sphingolipids, acyglycerols, cardiolipins, cholesterol and cholesterol esters. Lipids were isolated from 130 mg tissue, reconstituted in 30 or 60 µL chloroform, and 2 µL sample subjected to analysis. While 13/12, 11, 10 and 9-PAHSAs were detected in both samples ion counts were low for all species (Figure 4.6). This was due to high concentrations of nonpolar lipids such as triglycerides (TGs) in WAT [18]; TGs contributed significant volume toward the reconstituted sample, limiting the percentage of sample that could be injected while increasing ion suppression. Insolubility of TGs in methanol also restricted the carrier solvent to chloroform, preventing injection of larger sample volumes. To address this problem we performed solid phase extraction.

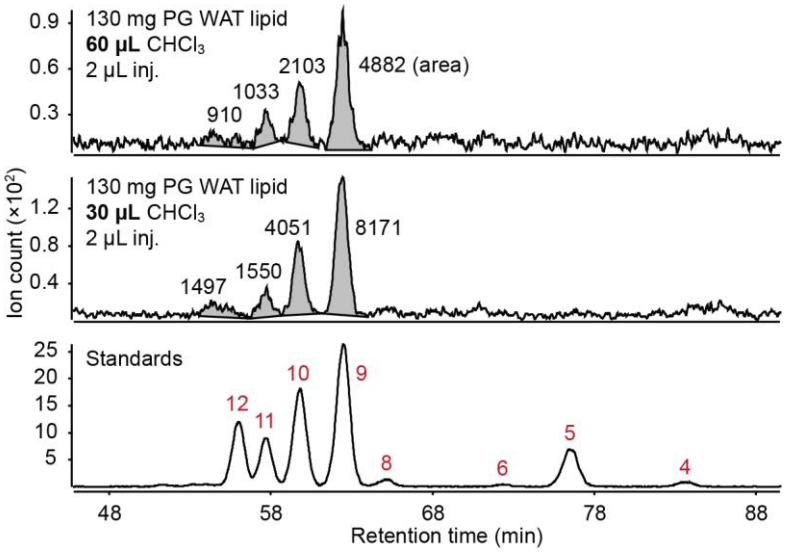

Figure 4.6. Preliminary test of optimized LC–MS workflow on WT murine PG WAT lipids.

4.2.4. Optimization of solid phase extraction for PAHSA enrichment

Solid phase extraction (SPE) is a widely used technique that separates analytes in solution based on their interactions with a solid support [19]. In the context of metabolomics, SPE enables enrichment of specific metabolite pools while removing other metabolites and

contaminants that could cause signal suppression and/or impair chromatographic resolution [11, 20]. SPE workflow for FAHFA enrichment is illustrated in Figure 4.7A. This method was tested on a solution of 4, 5, 6, ^{13}C-8, 9, ^{13}C-9, 10, 11 and 12-PAHSA standards. Ethyl acetate eluent (18 mL total) was collected in 1 mL fractions, and presence of PAHSAs in each fraction determined by MRM (Figure 4.7B). PAHSAs eluted rapidly across the first two ethyl acetate fractions with no significant carryover into addition fractions; no PAHSAs were observed in the 95:5 hexane: ethyl acetate fraction (Figure 4.7B).

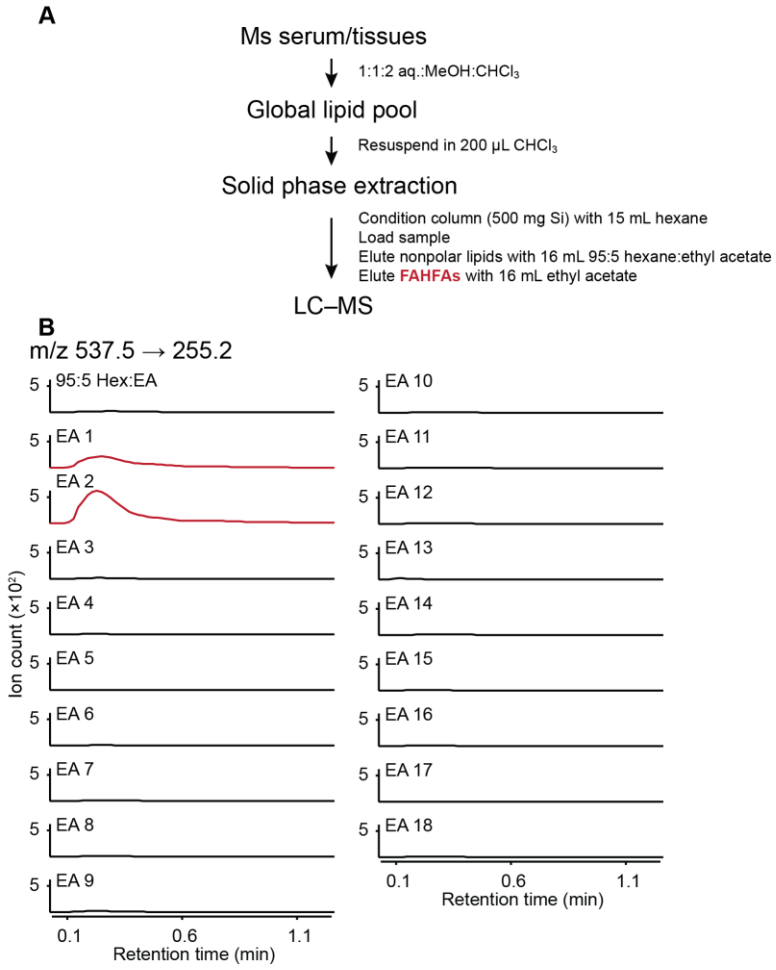

Figure 4.7. Solid phase extraction for FAHFA enrichment. A) SPE workflow. B) MRM of total (16 mL as one fraction) 95: 5 hexane: ethyl acetate (nonpolar lipids) fraction and 1 mL ethyl acetate (FAHFA) fractions. All fractions were concentrated to dryness and 1/3 of each sample used for analysis.

Metabolite recovery was calculated for each PAHSA standard (Figure 4.8). Fractionation did not lead to loss of 8, 9, 10, 11 and 12-PAHSAs; slight increase in ion count for these species in the fractionated sample relative to unfractionated could be due to decreased ion suppression through removal of impurities. Fractionation led to some loss of 6, 5 and 4-PAHSAs (23-66 %).

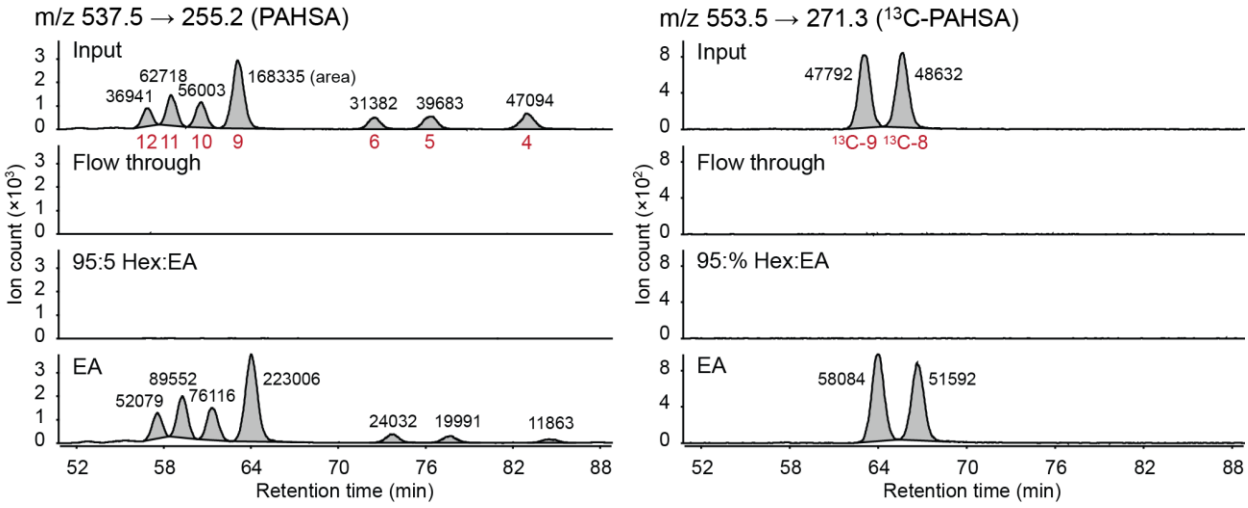

Figure 4.8. Metabolite recovery from fractionation for individual PAHSA isomers. All fractions were concentrated to dryness and 1/3 of each sample used for analysis.

While fractionation led to loss of 4, 5 and 6-PAHSA standards, it is worth noting that influence of different PAHSA isomer positions on lipid-matrix interactions could be more pronounced in the absence of lipid background. Consequently, metabolite recovery should be evaluated in the presence of background lipids as a more accurate representation of the endogenous system. To address this question, we compared recovery of 4, 5, 6 and ^{13}C-9-PAHSA standards using WT murine liver lipids as background; liver was chosen for its relatively simple PAHSA profile (preliminary analysis in WT liver revealed only presence of 13/12 and 9-PAHSAs, data not shown). A solution of 4, 5, 6 and ^{13}C-9-PAHSAs (input) was analyzed without fractionation (Figure 4.9A). An aliquot of the same PAHSA solution was

added to liver tissue, and the resulting tissue extracted, fractionated and analyzed by LC–MS; lack of significant amount of endogenous 4, 5 and 6-PAHSAs in liver provided a clean background for detection of the added standards (Figure 4.9B). ^{13}C-9/4, ^{13}C-9/5 and ^{13}C-9/6-PAHSA ratios were calculated for the unfractionated input (Figure 4.9A) and the standards in fractionated liver (Figure 4.9B), and results compared between the two groups (Figure 4.9C). ^{13}C-9/4, ^{13}C-9/5 and ^{13}C-9/6-PAHSA ratios changed only slightly between input and fractionated liver, suggesting that in a complex lipid environment, fractionation efficiency is only minimally dependent on PAHSA isomer positions (Figure 4.9C).

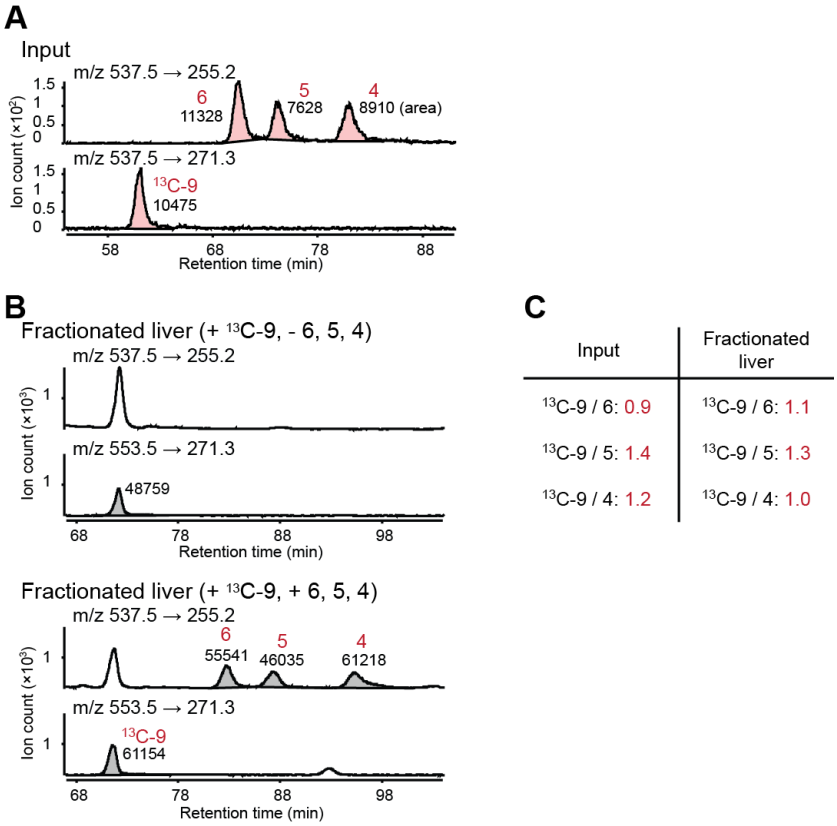

Figure 4.9. Metabolite recovery from fractionation for PAHSA isomers in the presence of background lipid. A) Unfractionated PAHSA standards as input. B) Detection of exogenous ^{13}C-9, 4, 5 and 6-PAHSA standards (same solution as input) in WT murine liver lipids following fractionation. C) Comparison of ^{13}C-9/6, ^{13}C-9/5 and ^{13}C-9/4-PAHSA ratios between unfractionated input and fractionated input in liver lipids.

4.2.5. Evaluation of lipid recovery and solvent effect in murine adipose tissues

Prior to implementation of our SPE workflow on a wider scale, we evaluated PAHSA recovery following fractionation of WT murine brown adipose tissue (BAT). Fractionated or unfractionated BAT lipids were analyzed by LC–MS and quantified with an internal ^{13}C-9-PAHSA standard. Fractionation did not lead to significant PAHSA loss, and enabled detection of additional low-abundance PAHSA isomers (5, 7 and 8) in BAT (Figure 4.10A).

As mentioned in section 4.2.3, TGs in unfractionated WAT reduced solubility in methanol and limited injection volume to 2 μL chloroform (Figure 4.6). TG removal allowed sample reconstitution in methanol and injection of higher volumes. To ensure no solvent-dependent PAHSA loss, fractionated WT PG WAT lipids were solubilized in either methanol (10 μL injection) or chloroform (2 μL injection), and absolute PAHSA quantifications compared between the two groups to yield similar results (Figure 4.10B). Importantly, injection of larger

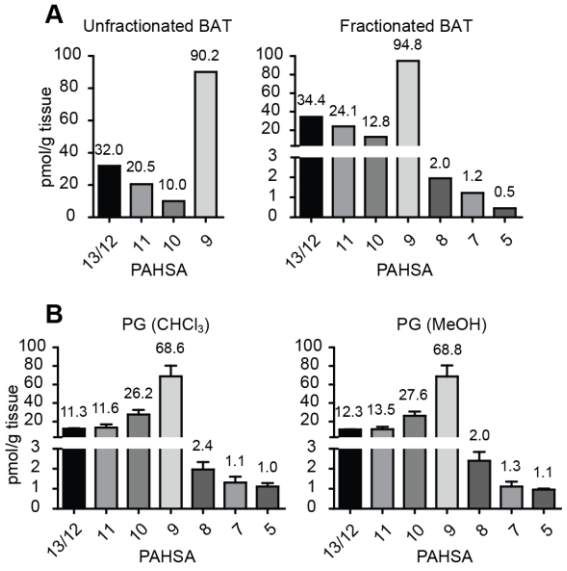

Figure 4.10. Tests of fractionation efficiency and carrier solvents in murine adipose tissues. A) Comparison of PAHSA isomer levels between unfractionated and fractionated WT murine BAT (n=1). B) Comparison of PAHSA isomer levels between chloroform and methanol-reconstituted fractionated WT murine PG WAT lipids (n=5).

sample volumes increased the quantity of sample that could be analyzed on-column, significantly improving signal-to-noise ratio and enabling measurement of low-abundance PAHSAs not detectable in unfractionated samples. The finalized workflow is in Figure 4.11.

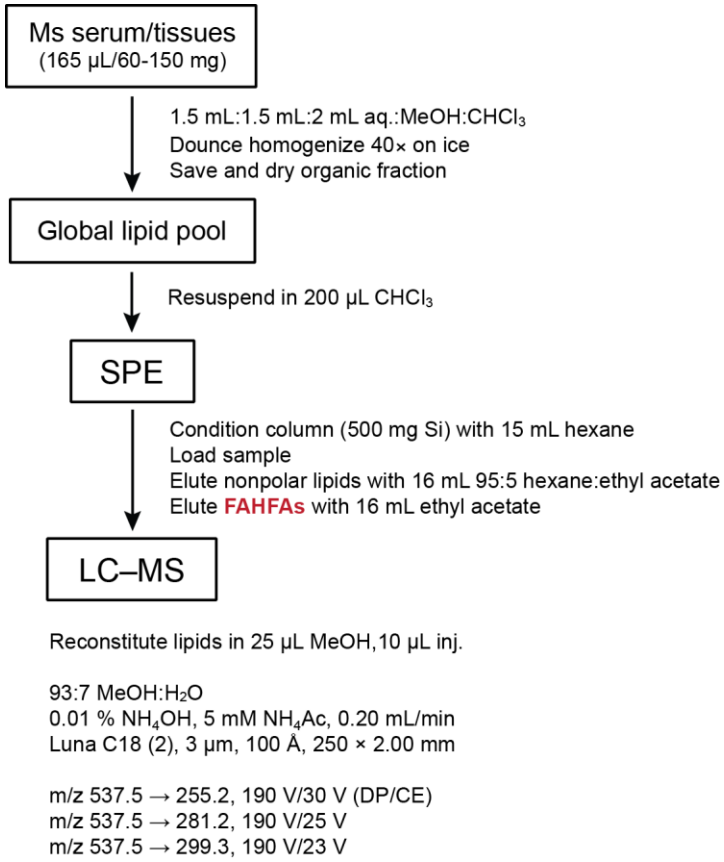

Figure 4.11. Finalized workflow for PAHSA isomer analysis.

4.2.6. PAHSA isomer distribution in murine serum, tissues and diets

Using our finalized LC–MS workflow, PAHSA isomers were quantified in WT murine serum, PG and SQ WATs, BAT, liver, pancreas, kidney, heart, gastrocnemius muscle (GNM) and brain. A ^{13}C-9-PAHSA internal standard was used for absolute quantification. Extracted ion chromatographs of the m/z 536 → 255 transition are shown for all samples in Figure 4.12A. 9-PAHSA is the major isomer in majority of samples (Figure 4.12A, B). Highest total PAHSA

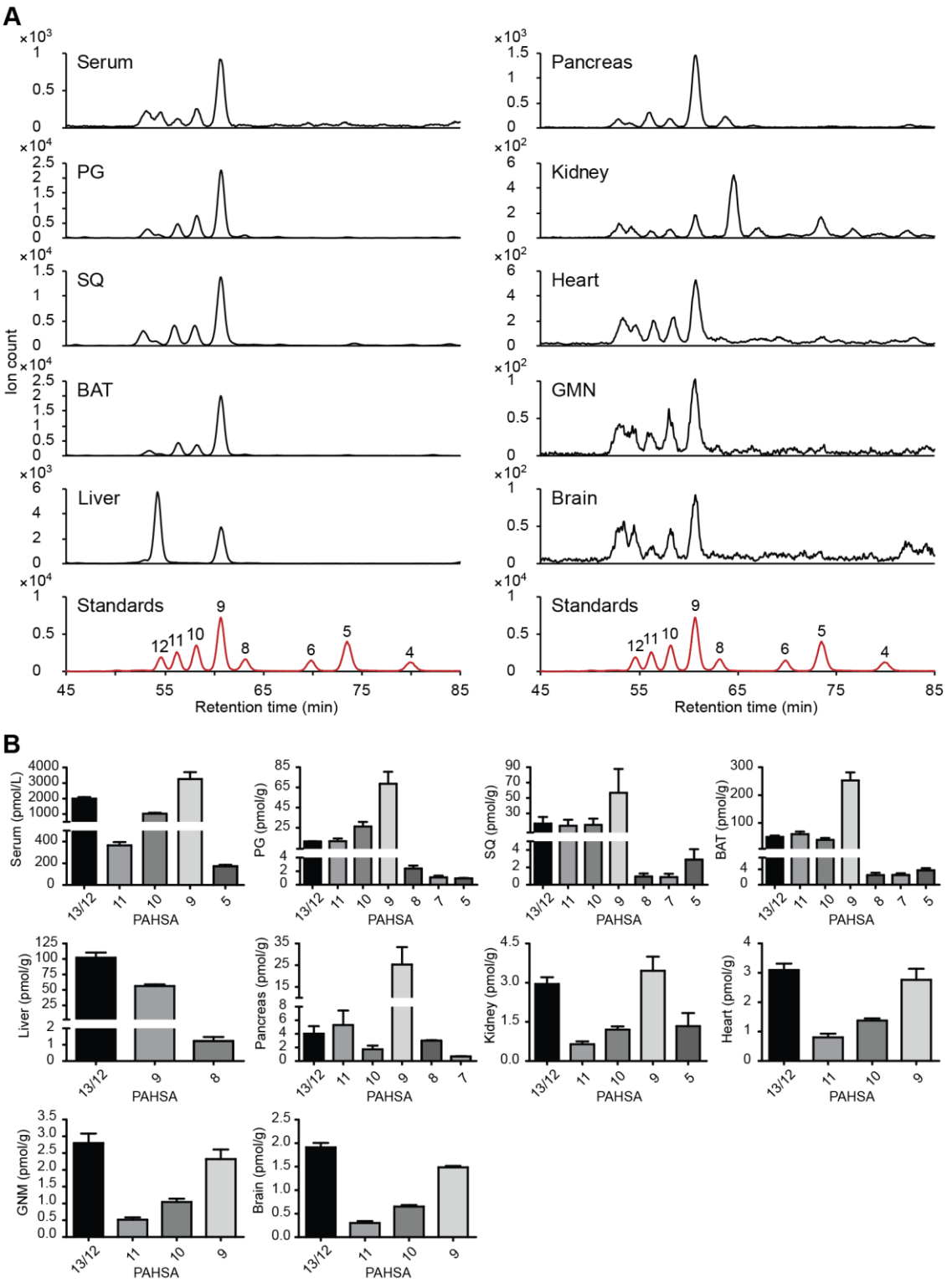

Figure 4.12. PAHSA isomer distribution in WT murine serum and tissues. A) Extracted ion chromatographs (m/z 537 → 255) of WT murine serum and tissues. B) PAHSA isomer levels in WT murine serum and tissues (n=4-5).

level is found in BAT, with adipose tissues displaying widest isomeric range; 13/12, 9 and 8-PAHSAs were the only detectable isomers in liver (Figure 4.12 A, B). Variability in PAHSA distribution across tissue types implies tissue-dependent metabolism and/or trafficking.

PAHSA analysis was also performed in food to assess the diet-dependence of *in vivo* PAHSA distribution. LC–MS of fractionated lipids from apple, broccoli, beef, chicken, egg white and yolk revealed significant variation in both the major isomer and relative isomeric ratios across dietary sources (Figure 4.13A). PAHSA level in egg yolk was significantly higher

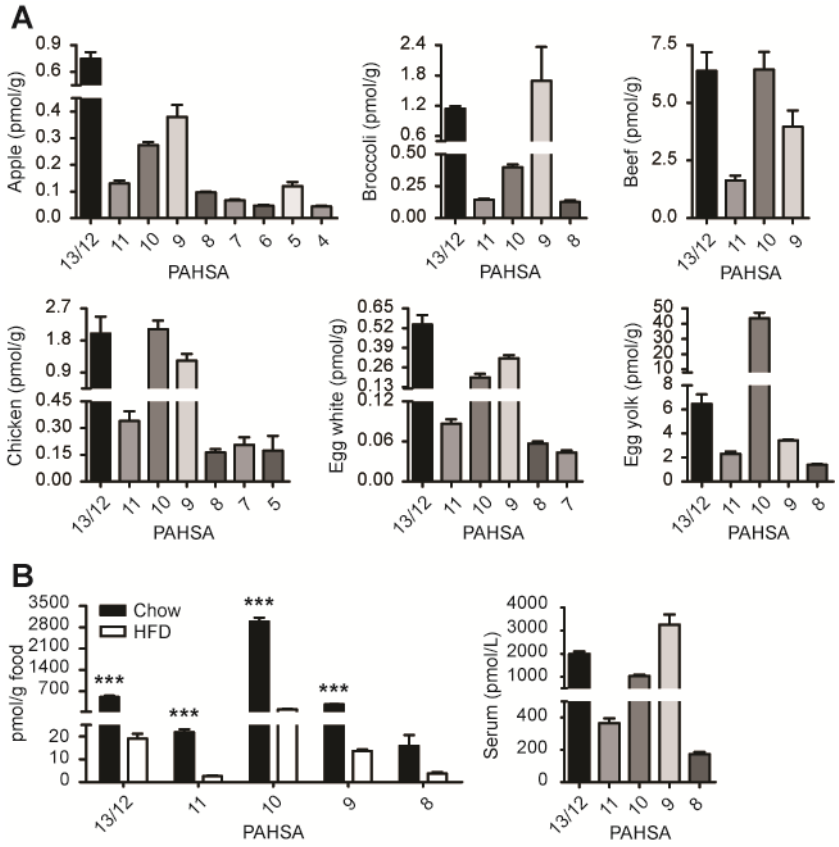

Figure 4.13. PAHSA isomer distribution in dietary sources. A) PAHSA isomer levels in fruit, vegetable, meat and egg (n=3). B) PAHSA isomer levels in chow and high fat murine diets (n=3). *, $p \leq 0.05$, **, $p \leq 0.01$, ***, $p \leq 0.001$. Two-tailed Student's t test, SEM.

(approximately one to two orders of magnitude) than all other dietary sources examined (Figure 4.13A).

PAHSAs were also detected in murine chow and high fat diet (HFD) (Figure 4.13B). Significantly higher PAHSA levels were observed in chow relative to HFD, a possible consequence of low conjugated fatty acid level in the HFD fat source. Importantly, major PAHSA isomer in chow and HFD is 10-PAHSA while the major isomer in WT murine serum and most tissues is 9-PAHSA (Figure 4.13B). Taken together, our data demonstrate that murine serum and tissue PAHSA distribution is not a direct reflection of diet, supporting generation of additional PAHSA species through *in vivo* metabolism.

4.2.7. Analysis of additional FAHFA family members

While we have focused on PAHSAs based on detectability during global lipidomics and ease of isomer analysis in the absence of unsaturation sites, complexity in the structures of free fatty acids in mammalian systems could translate into similar complexity in the range of possible FAHFA family members [21, 22], raising the question of whether different FAHFAs are selectively regulated in a tissue-specific manner or in the context of GLUT4 overexpression. To answer these questions, we expanded our MRM method to include additional FAHFAs.

Given all FAHFAs are comprised of a fatty acid (FA) conjugated to hydroxy fatty acid (HFA), variability in FAHFA structure is a direct reflection of variability in the FA and HFA chains. Candidate FAs and HFAs are shown in Figure 4.14A. Palmitoleic acid (16:1), palmitic acid (16:0), oleic acid (18:1) and stearic acid (18:0) were selected due to their abundance in mammalian tissues [21, 22]. Arachidonic acid (20:4) and docosahexaenoic acid (22:6) were

included given their roles in inflammation and interaction with G-protein coupled receptors [23-27]. Selection of six candidates for FA and six candidates for HFA implies a total of 36

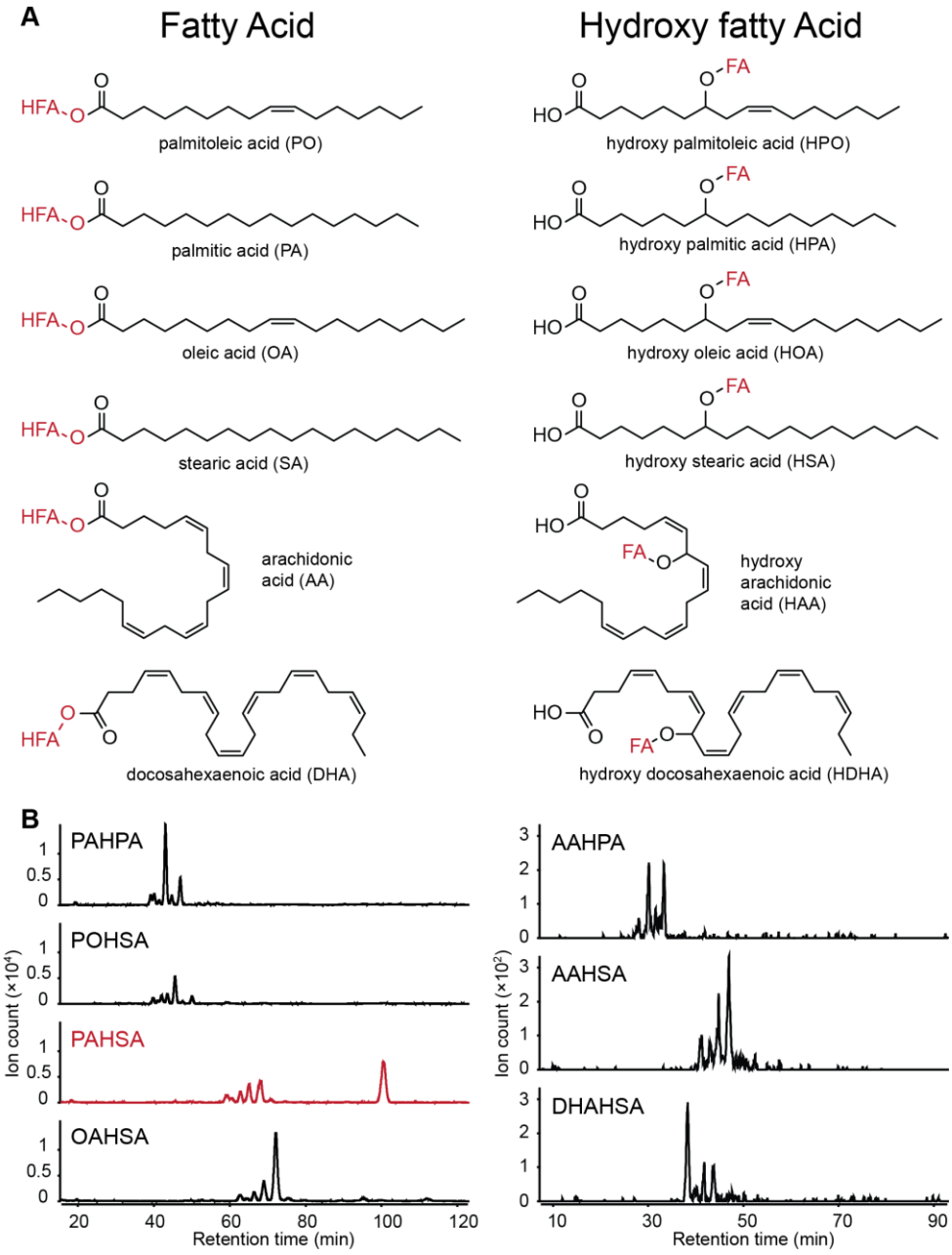

Figure 4.14. Additional FAHFA family members. A) Candidate structures for fatty acid and hydroxy fatty acid. B) Extracted ion chromatographs (m/z 537 → 255) of selected FAHFAs in WT murine PG WAT.

structurally distinct FAHFAs. MRM transitions were calculated for these candidates based on PAHSA parameters, and two transitions were monitored for each FAHFA. Selected spectra are in Figure 4.14B. Similar to PAHSA, multiple peaks were observed for each additional FAHFA, suggesting presence of multiple isomers (Figure 4.14B).

Using the expanded MRM method, 16 FAHFAs with different combinations of 16:1, 16:0, 18:1 and 18:0 acyl chains, and nine PAHSAs with 20:4 or 22:6 as one of the two acyl chains, were detected in WT murine PG WAT (Figure 4.15A). As a direct reflection of relative free fatty acid levels in murine tissues [21], 20:4 and 22:6 acyl chain-containing FAHFAs were approximately 50 to 100 fold lower in abundance than FAHFAs without these acyl chains (Figure 4.15A). Similar analysis in human sera taken from three individuals revealed variation in FAHFA distribution and selective regulation of different FAHFA pools in a subject-dependent manner (Figure 4.15B). Importantly, comparison of FAHFA levels between WT and AG4Ox murine sera revealed selective elevation of multiple FAHFA members in AG4Ox serum, with all elevated species containing either HPA or HSA (Figure 4.15C). Taken together, our data demonstrate successful implementation of our LC–MS workflow in the analysis of serum and tissue PAHSAs and FAHFAs. Further investigation into FAHFA metabolism and biology will yield valuable information on the roles of these novel lipids in type 2 diabetes and other disease states.

4.3. Discussion

Global lipidomics of WT and AG4OX SQ WAT revealed upregulation of palmitic acid hydroxy stearic acids (PAHSAs) under adipose-specific GLUT4 overexpression (Figures 4.1, 4.2). To determine PAHSA isomer distribution in serum and tissues, we optimized a LC–MS-

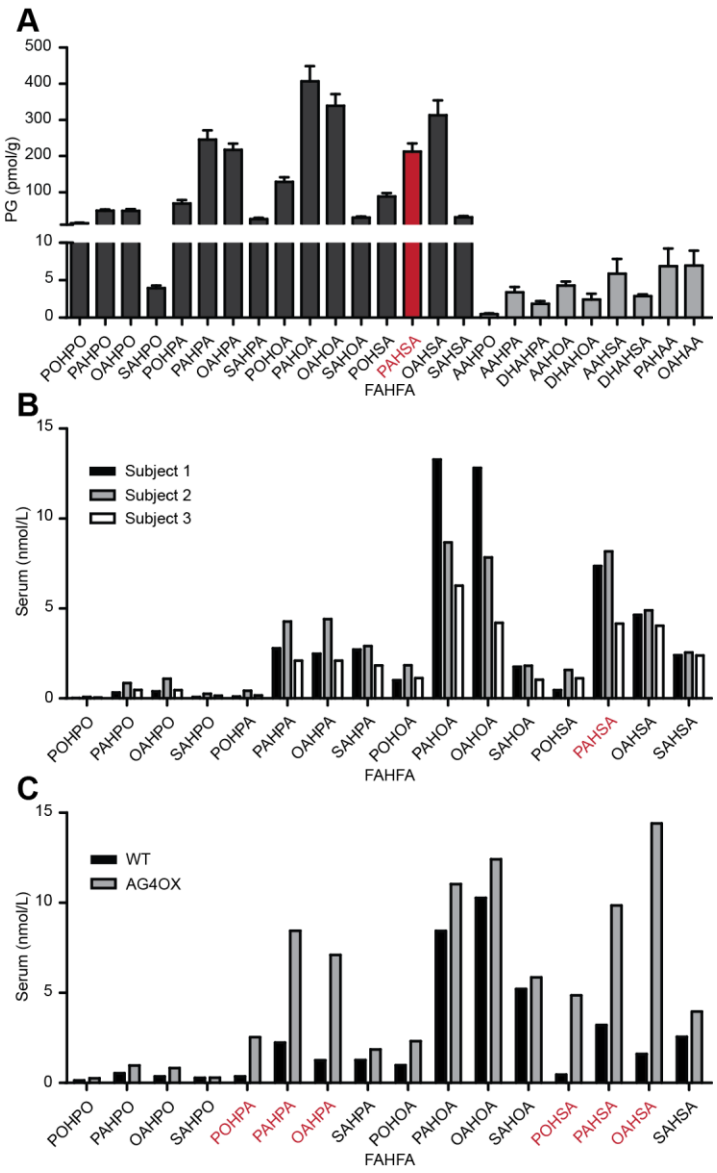

Figure 4.15. FAHFA levels in sera and adipose tissue. A) FAHFA levels in WT murine PG WAT (n=4). B) FAHFA levels in sera taken from three individuals (n=3). C) FAHFA levels in sera from WT and AG4OX mice (n=1).

based workflow enabling sensitive targeted detection of PAHSAs by multiple reaction monitoring; baseline resolution of majority of PAHSA isomers between 4 and 13 allowed quantification of individual isomers indistinguishable by MRM due to their nearly identical fragmentation mechanisms.

Tandem MS of 9-PAHSA yielded three major fragments at m/z 255, 299 and 281 (Figure 4.3), corresponding to precursor-to-product ion transitions m/z 537 → 255, m/z 537 → 299 and m/z 537 → 281. The m/z 537 → 255 transition yielded the highest ion count in all PAHSA (4, 5, 6, 9, 10, 11 and12) standards tested (Figure 4.4C), a likely consequence of stability of the palmitic (m/z 255) ion relative to the more chemically labile hydroxystearic (m/z 299) ion, which undergoes further fragmentation to yield unsaturated C18 fatty acid (m/z 281). It is worth noting that while m/z 537 → 255 is the major transition for all PAHSA standards, relative ratios of detected transitions (537 → 255/537 → 281, 537 → 255/537 → 299 and 537 → 281/537 → 299) are slightly dependent on isomer position. A lower 537 → 255/537 → 281 ratio was found for 6-PAHSA relative to 9-12-PAHSAs (Figure 4.4C) while m/z 537 → 255 was the only detectable transition for 4-PAHSA (Figure 4.4C). These differences could be attributed to differences in stability among the 9, 6 and 4-hydroxystearic (m/z 299) product ions as well as the 9, 6 and 4-unsaturated C18 fatty acids (m/z 281), where hydroxyl group or double bond distance from carboxylic acid could be a determinant of stability. It is unknown if efficiency of generation for the palmitic (m/z 255) product ion is dependent on isomer position; however, lack of unsaturation in palmitic acid implies that all generated ions will exhibit identical stability profile regardless of precursor, and suggests that the m/z 537 → 255 transition is the most reliable choice for use in quantification. Accuracy of absolute quantification could be improved through use of multiple PAHSA internal standards.

While MRM targets the precursor-to-product ion transition unique to each metabolite, lack of exact mass could lead to false positives in cases where two different metabolites share similar precursor and product ion masses. Consequently, monitoring of multiple transitions per metabolite increases the confidence of identification. For majority of PAHSA isomers,

appearances of peaks for all three transitions at identical retention times and with the major peak corresponding to m/z 537 → 255 are important criteria for the PAHSA structure assignment; simultaneous monitoring of all three transitions enables elimination of contaminant peaks. As Figure 4.16 illustrates, initial survey of WT murine kidney *via* the m/z 537 → 255 transition (black line) indicates that the major isomer is 8-PAHSA; however, overlay of all three transitions revealed significantly higher m/z 537 → 281 (red line) ion count than m/z 537 → 255 for the two peaks eluting after 9-PAHSA (Figure 4.16). While our MRM method has not been tested on a 8-

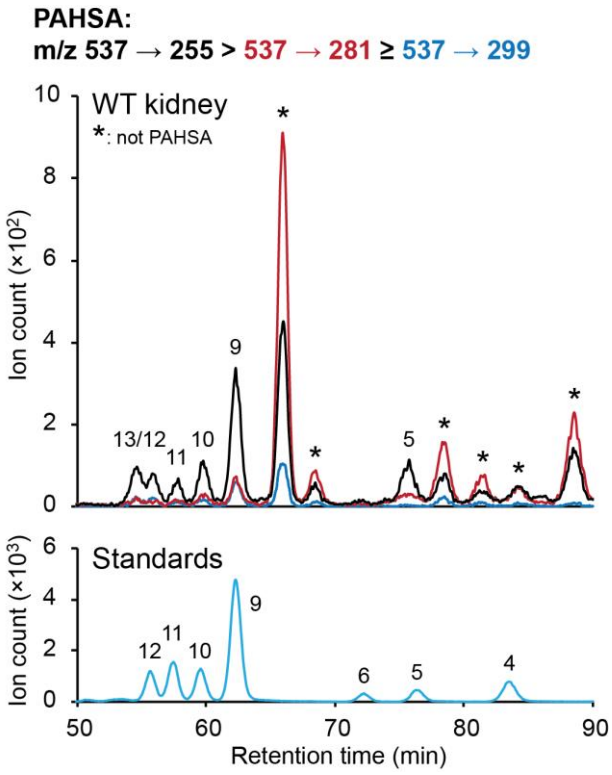

Figure 4.16. PAHSA profile of WT murine kidney. Relative abundances of transitions for majority of PAHSA isomers are m/z 537 → 255 > m/z 537 → 281 ≥ m/z 537 → 291.

PAHSA standard, dominance of the m/z 537 → 255 transition in all PAHSA standards (4, 5, 6, 9, 10, 11 and 12) examined (Figure 4.4C) implies a complete reversal of this trend for PAHSAs (7

and 8) in the middle of the isomer series is unlikely, and suggests that the two peaks eluting after 9-PAHSA in kidney are potential contaminants that should be excluded from analysis.

LC–MS of murine serum and tissues also revealed a highly abundant peak at ~95 min with higher m/z 537 → 281 ion count than m/z 537 → 255 (GNM is shown as example in Figure 4.17A). Importantly, tandem MS of the 95 min peak yielded fragments closely matching those from d18:1/16:0 ceramide (Figure 4.17B). It is worth noting that the loss-of-proton precursor ion for d18:1/16:0 ceramide is m/z 536, consequently, the 95 min peak (detected under PAHSA MRM parameters with m/z 537 as precursor) represents naturally occurring ^{13}C or ^{2}D-d18:1/16:0 ceramides; presence of ^{13}C or ^{2}D at different locations on the ceramide backbone or acyl chain leads to characteristic one-Dalton mass shifts in the tandem MS fragments of the 95 min peak (Figure 4.17B). Co-injection with GMN and d18:1/16:0 ceramide standard using ceramide-specific or PAHSA-specific MRM parameters yielded one peak as strong support that the 95 min peak is isotopic d18:1/16:0 ceramide rather than 2 or 3-PAHSA (Figure 4.17C).

Presence of ceramide in fractionated murine lipids was not surprising, given ethyl acetate elution during SPE was not FAHFA-specific, and could lead to co-elution of additional lipids with similar lipid-matrix interactions. Fractionation successfully removed nonpolar lipids such as TGs, allowing higher injection volume in methanol and analysis of larger quantity of sample on-column. Importantly, TG removal reduced column contamination, prolonging column lifetime and eliminating the need for exhaustive washing between sample runs. A more thorough survey of fractionation conditions could improve the specifity of FAHFA isolation and minimize co-elution of additional lipids.

Variability in PAHSA isomer distribution across murine tissues in a diet-independent manner raises questions on FAHFA metabolism *in vivo* (Figures 4.12, 4.13). Sampling of

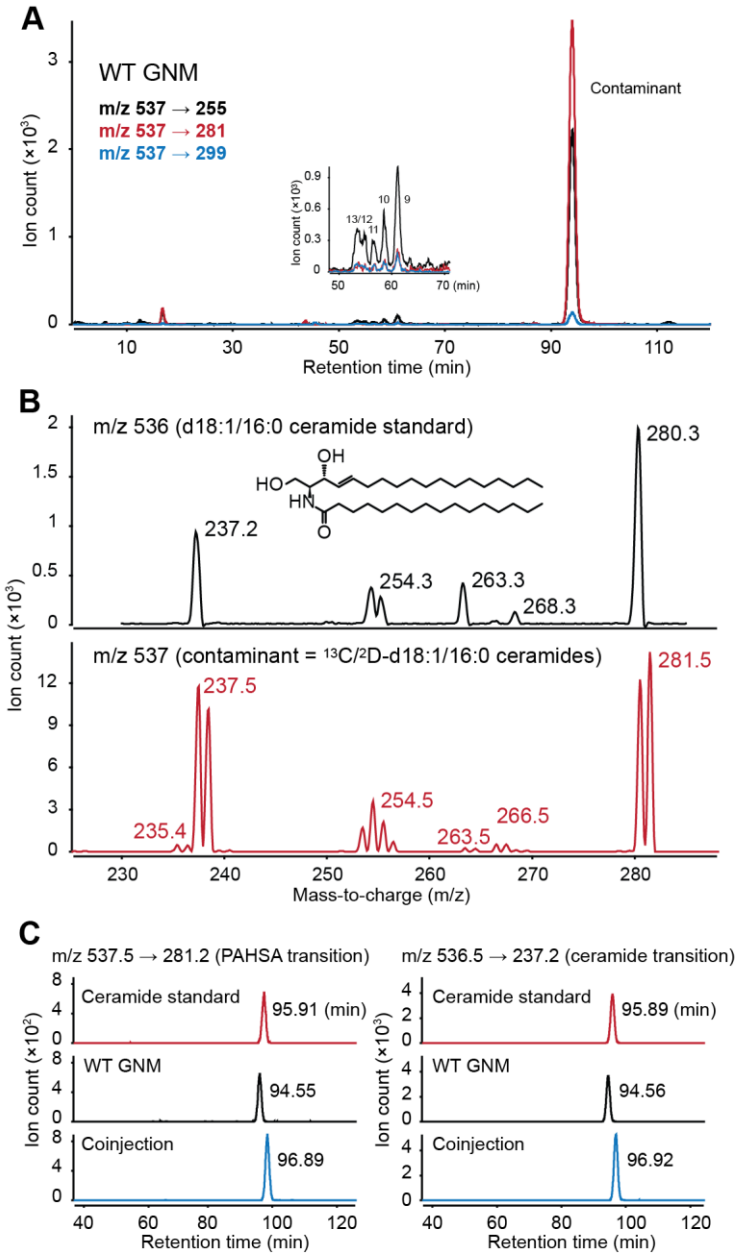

Figure 4.17. Identification of contaminant peak in PAHSA analysis of murine lipids. A) Extracted ion chromatographs of WT murine GNM. B) Tandem MS of d18:1/16:0 ceramide standard and contaminant peak at ~95 min. C) Co-injection of WT murine GNM lipids with d18:1/16:0 ceramide standard monitored by ceramide-characteristic and PAHSA-characteristic transitions.

FAHFA family members in sera from three individuals revealed selective regulation of distinct FAHFA pools in a subject-specific manner, and selective upregulation of HSA and HPA-

containing FAHFAs was observed in AG4OX serum relative to WT. It would be of interest to investigate the biological functions of different FAHFAs in the context of GLUT4 knockdown or overexpression. Comprehensive FAHFA measurements in insulin sensitive and resistant populations could also yield valuable information on the roles of these lipids in humans with potential therapeutic implications.

4.4. Conclusion

A LC–MS workflow was optimized to enable sensitive quantification of palmitic acid hydroxy stearic acid (PAHSA) isomers and additional fatty acid hydroxy fatty acids (FAHFAs), members of a novel lipid class upregulated in adipose tissue of AG4OX mice. MRM parameters were optimized with 9-PAHSA standard to yield three precursor-to-product ion transitions. A methanol-water isocratic solvent system was optimized to achieve baseline resolution of almost all PAHSA isomers between 4 and 13. Solid phase extraction of serum and tissue lipids removed nonpolar lipids such as TGs and significantly enriched FAHFAs, enabling measurement of low-abundance PAHSA isomers undetectable in unfractionated samples. Our workflow was successfully implemented to yield reproducible, robust quantification of PAHSA isomers and FAHFA family members in serum and tissues. Further investigation into the biological functions of this novel lipid class in murine GLUT4 knockout or overexpression models and in humans will bear significant implications over the roles of lipids in disease and development of therapeutics.

4.5. Methods

4.5.1. Materials

Ammonium formate (516961), ammonium acetate (372331) and ammonium hydroxide (338818) were from Sigma-Aldrich. Formic acid (06440) was from Fluka. Water (365-4), methanol (230-4), isopropanol (323-4), acetonitrile (017-4), hexane (212-4), ethyl acetate (100-4) and chloroform (049-1L) for lipid extraction, SPE and LC–MS were from Honeywell Burdick & Jackson. Solid phase extraction cartridges (HyperSep Silica, 500 mg/6 mL) were from Thermo Scientific (60108-411). Organic solvents for chemical syntheses were from EMD Millipore (Billerica, MA). (R)-9-hydroxystearic acid was from Indofine Chemical Company, Inc. (Hillsborough, NJ) and $^{13}C_{16}$-palmitic acid was from Cambridge Isotopes Laboratories, Inc. (Andover, MA). All additional chemicals for syntheses were from Sigma-Aldrich unless otherwise stated.

4.5.2. Animal studies

AG4OX mice (FVB background) were previously described [9, 28]. Female WT FVB mice were used in all LC–MS analyses, and age and gender-matched to AG4OX mice for all comparative lipidomic studies. Animals were euthanized with CO_2, the tissues dissected, flash frozen in liquid nitrogen and stored at -80 °C prior to lipid extraction. All animal care and use procedures were in strict accordance with the standing committee on the use of animals in research and teaching at Harvard University and at the Beth Israel Deaconess Medical Center Animal Research Facility.

.

4.5.3. Lipid extraction

Lipid extraction was performed with modification on the Bligh-Dyer method [17]. All glasswares were chilled on ice for at least 5 min prior to extraction. Murine tissues and frozen

meat for dietary analysis were kept on dry ice to avoid thawing, quickly sectioned with razor blade and weighed (60-150 mg) before being Dounce homogenized immediately on ice for 40 strokes in 1.5 mL:1.5 mL:3 mL citric acid buffer (100 mM trisodium citrate, 1 M NaCl, pH 3.6):methanol:chloroform. Apple, broccoli and egg (140-210 mg) were sectioned with razor blade at room temperature before being processed in the same way as tissues. ^{13}C-9-PAHSA standard (0.5-8 pmol per sample depending on sample type) was added to chloroform prior to extraction. The resulting mixture was poured into a glass vial on ice, the Douncer was washed with 0.5 mL chloroform without standard, and the wash combined with the Dounced mixture (total volume ~6.5 mL). The mixture was centrifuged at 2200 g, 6 min, 4 ºC to separate organic and aqueous phases, and the organic (bottom) phase containing lipids was transferred into a glass vial with a Pasteur pipet, dried under a gentle stream of N_2 and stored at -80 ºC prior to solid phase extraction (SPE). Frozen serum was thawed on ice and citric acid buffer was added to a final volume of 1-1.75 mL based on volume of serum used, followed by addition of 1-1.75 mL methanol and 2-3.5 mL chloroform; the resulting mixture was shaken vigorously for 30 s and vortexed for 15 s before being centrifuged and processed in the same way as tissues and food items. 165 μL murine serum was used for PAHSA isomer analysis, 265 μL murine serum and 450-900 μL human serum were used for analysis of additional FAHFA family members.

4.5.4. SPE

SPE was performed at room temperature *via* gravity flow. The column was conditioned with 15 mL hexane. Extracted lipids (in 200 μL chloroform) were loaded onto column. Nonpolar lipids were eluted with 16 mL 5 % ethyl acetate in hexane, followed by elution of free

fatty acids and FAHFAs with 16 mL ethyl acetate. FAHFA fractions were dried under a gentle stream of N_2 and stored at -80 ºC prior to LC–MS.

4.5.5. Targeted LC–MS

FAHFAs were measured on an Agilent 6410 Triple Quad LC/MS instrument *via* multiple reaction monitoring (MRM) in negative ionization mode, using a Luna C18 (2) (Phenomenex, 00G-4251-B0) column with an in-line filter (Phenomenex, AF0-8497). The solvent was 93:7 methanol:water with 5 mM ammonium acetate and 0.01 % ammonium hydroxide, and PAHSA isomers were resolved by isocratic elution at 0.2 mL/min for 120 min. Each extracted and fractionated sample (from 165-900 μL serum, 60-150 mg tissue, or 140-210 mg food) was reconstituted in 25 μL methanol and 10 μL was injected for analysis when possible. In cases where large quantities of fractionated lipids were observed, or lipids were not completely soluble in methanol, the sample was reconstituted in 20 μL chloroform and 2 μL was injected. Transitions for endogenous PAHSAs were m/z 537.5 → m/z 255.2 (CE = 30 V), m/z 537.5 → m/z 281.2 (CE = 25 V) and m/z 537.5 → m/z 299.3 (CE = 23 V), and transition for ^{13}C-9-PAHSA was m/z 553.5 → m/z 271.3 (CE = 30 V). Fragmentor voltage and dwell time were 205 V and 300 ms, respectively, for each transition. Skimmer voltage was 15 V and ΔEMV was 400 V. MS1 resolution was set to Wide and MS2 resolution to Unit. Capillary voltage was 4.0 kV, drying gas temperature was 350 °C, drying gas flow rate was 8 L min^{-1} and nebulizer pressure was 35 psi. Identical gradient and instrument parameters were used for detection of all additional FAHFAs with the exception of dwell time, which was reduced to 30 ms to accommodate additional transitions. All FAHFA transitions are in Table 4.1.

Transition	Precursor ion	Product ion	CE
POHPO_transition1	505.4	253.2	30
POHPO_transition2	505.4	251.2	25
POHPA_transition1	507.4	253.2	30
POHPA_transition2	507.4	271.2	23
PAHPO_transition1	507.4	255.2	30
PAHPO_transition2	507.4	251.2	25
PAHPA_transition1	509.5	255.2	30
PAHPA_transition2	509.5	253.2	25
POHOA_transition1	533.5	253.2	30
POHOA_transition2	533.5	279.2	25
OAHPO_transition1	533.5	281.2	30
OAHPO_transition2	533.5	251.2	25
PAHOA_transition1	535.5	255.2	30
PAHOA_transition2	535.5	279.2	25
OAHPA_transition1	535.5	281.2	30
OAHPA_transition2	535.5	253.2	25
POHSA_transition1	535.5	253.2	30
POHSA_transition2	535.5	281.2	25
SAHPO_transition1	535.5	283.2	30
SAHPO_transition2	535.5	251.2	25
PAHSA_transition1	**537.5**	**255.2**	**30**
PAHSA_transition2	**537.5**	**281.2**	**25**
PAHSA_transition3	**537.5**	**299.3**	**23**
^{13}C-PAHSA	**553.5**	**271.3**	**30**
SAHPA_transition1	537.5	283.2	30
SAHPA_transition2	537.5	253.2	25
OAHOA_transition1	561.5	281.2	30
OAHOA_transition2	561.5	279.2	25
OAHSA_transition1	563.5	281.2	30
OAHSA_transition2	563.5	299.3	23
SAHOA_transition1	563.5	283.3	30
SAHOA_transition2	563.5	279.2	25
SAHSA_transition1	565.5	283.3	30
SAHSA_transition2	565.5	281.2	25
AAHPO_transition1	555.4	303.2	30
AAHPO_transition2	555.4	251.2	25
POHAA_transition1	555.4	253.2	30
POHAA_transition2	555.4	301.2	25
AAHPA_transition1	557.5	303.2	30
AAHPA_transition2	557.5	253.2	25

PAHAA_transition1	557.5	255.2	30
PAHAA_transition2	557.5	301.2	25
AAHOA_transition1	583.5	303.2	30
AAHOA_transition2	583.5	279.2	25
OAHAA_transition1	583.5	281.2	30
OAHAA_transition2	583.5	301.2	25
AAHSA_transition1	585.5	303.2	30
AAHSA_transition2	585.5	281.2	25
SAHAA_transition1	585.5	283.2	30
SAHAA_transition2	585.5	301.2	25
AAHAA_transition1	605.5	303.2	30
AAHAA_transition2	605.5	301.2	25
DHAHPO_transition1	579.4	327.2	30
DHAHPO_transition2	579.4	251.2	25
POHDHA_transition1	579.4	253.2	30
POHDHA_transition2	579.4	325.2	25
DHAHPA_transition1	581.5	327.2	30
DHAHPA_transition2	581.5	253.2	25
PAHDHA_transition1	581.5	255.2	30
PAHDHA_transition2	581.5	325.2	25
DHAHOA_transition1	607.5	327.2	30
DHAHOA_transition2	607.5	279.2	25
OAHDHA_transition1	607.5	281.2	30
OAHDHA_transition2	607.5	325.2	25
DHAHSA_transition1	609.5	327.2	30
DHAHSA_transition2	609.5	281.2	25
SAHDHA_transition1	609.5	283.2	30
SAHDHA_transition2	609.5	325.2	25
AAHDHA_transition1	629.5	303.2	30
AAHDHA_transition2	629.5	325.2	25
DHAHAA_transition1	629.5	327.2	30
DHAHAA_transition2	629.5	301.2	25
DHAHDHA_transition1	653.5	327.2	30
DHAHDHA_transition2	653.5	325.2	25

Table 4.1. FAHFA transitions and collision energies. PAHSA parameters are in red.

4.5.6. Global lipidomics of WT and AG4OX SQ WAT

Global LC–MS profiling was performed on an Agilent 1200 series binary pump online with an Agilent 6220 ESI-TOF spectrometer in positive and negative ionization modes with modifications on known protocol [29]. For negative mode a Gemini (Phenomenex) C18 column (5 µm, 4.6 mm × 50 mm) was used with a C18 precolumn (3.5 µm, 2 mm × 20 mm, Western Analytical). Solvent A was 95:5 water:methanol with 0.1 % ammonium hydroxide, and solvent B was 60:35:5 isopropanol:methanol:water with 0.1 % ammonium hydroxide. For positive mode a Luna (Phenomenex) C5 column (5 µm, 4.6 mm × 50 mm) was used with a C4 precolumn (3.5 µm, 2 mm × 20 mm, Western analytical). Solvent A was 95: 5 water: methanol with 0.1 % formic acid and 5 mM ammonium formate, and solvent B was 60:35:5 isopropanol:methanol:water with 0.1 % formic acid and 5 mM ammonium formate. Identical gradient was used for both ionization modes. The gradient was held at 0 % B between 0 and 5 min, changed to 20 % B at 5.1 min, increased linearly from 20 % B to 100 % B between 5.1 min and 45 min, held at 100 % B between 45.1 min and 53 min, and returned to 0 % B at 53.1 min and held at 0 % B between 53.1 min and 60 min to allow column re-equilibration. Flow rate was maintained at 0.1 mL/min between 0 min and 5 min to counter pressure increase due to the chloroform injection. The flow rate was 0.4 mL/min between 5.1 min and 45 min, and 0.5 mL/min between 45.1 min and 60 min. Injection volume was 30 µL. Capillary voltage was 3.5 kV and fragmentor and skimmer voltages were 100 V and 60 V, respectively. Drying gas temperature was 350 °C, drying gas flow rate was 10 L/min and nebulizer pressure was 45 psi. Data were collected in both profile and centroid modes using a mass range of 100-1500 Da.

Data from general profiling were analyzed *via* targeted and untargeted approaches. For the targeted approach, extracted ion chromatograms (EICs) corresponding to the m/z of known

metabolites were manually integrated in MassHunter Quantitative Analysis (Agilent Technologies), and the resulting ion counts compared between WT and AG4OX groups to give relative quantification for known lipids. Statistical significance was determined by two-tailed Student's t-test. All errors were standard errors of the mean. For the untargeted approach, LC–MS raw data were converted from .d to .mzXML format with mzStar. WT and AG4OX samples were sorted into two groups and analyzed *via* XCMS [30]. Following filtering of XCMS output files by ion count ($> 5 \times 10^4$) and statistical significance (p-value ≤ 0.05), the remaining metabolite changes were further confirmed by manual integration in Qualitative Analysis and Student's t-test. Molecular formulae for unidentified metabolites were generated using formula calculator in Quantitative Analysis.

4.5.7. Preliminary PAHSA structural characterization by Q-TOF

Tandem MS of PAHSAs was performed on an Agilent 1200 series binary pump online with an Agilent 6510 quadrupole-time of flight mass spectrometer with an ESI source. Total runtime of the global lipidomics LC method (section 4.5.6) was lowered to 45 min, and the linear gradient lowered to 30 min to reduce sample acquisition time; all solvent and column conditions were identical. Collision energy was 20 V for generation of the major fragments m/z 255, 281 and 299, and 50 V (for 12-PAHSA) for generation of additional diagnostic fragments from the hydroxystearic acyl chain at predictable locations around the hydroxylated carbon, based on previous tandem MS study of 12-HSA [31]. Target m/z was 537.488, MS scan range was 100-1000 Da and MS2 scan range was 50-1000 Da with an acquisition time of 1000 ms. Capillary voltage was 3.5 kV, fragmentor

voltage was 100 V and skimmer voltage was 60 V. Drying gas temperature was 350 C, drying gas flow rate was 10 L/min and nebulizer pressure was 45 psi.

4.5.8. Synthesis of PAHSA standards

All glasswares were oven dried for at least 24 h prior to synthesis. Reactions were performed under nitrogen atmosphere unless otherwise stated. Analytical thin-layer chromatography (TLC) was performed on precoated silica gel F-254 plates and visualized by phosphomolybdic acid (PMA) stain. Flash chromatography was performed using 230-400 mesh silica gel from EMD. ^{1}H NMR spectra were acquired at 400 MHz.

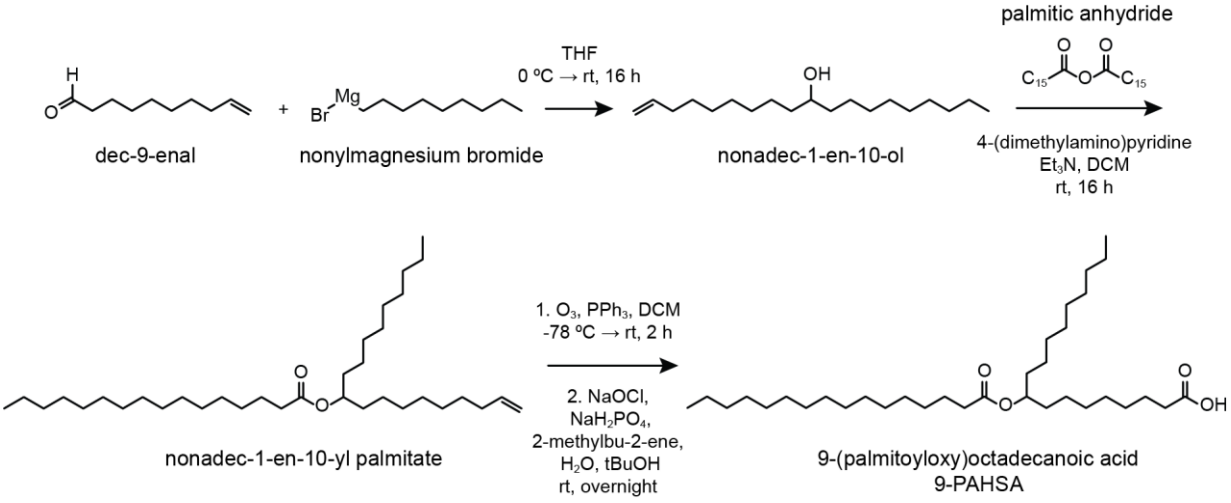

Figure 4.18. Synthesis of 9-PAHSA.

4.5.8.1. Synthesis of nonadec-1-en-6-ol

Pent-4-en-1-ylmagnesium bromide (0.5 M solution in THF, 21.2 mL, 10.6 mmol, 1.5 eq.) was added to a stirring solution of tetradecanal (1.5 g, 7.1 mmol, 1 eq.) in ice bath. The solution was stirred and allowed to warm to room temperature (rt) overnight (16 h). The reaction was quenched with saturated ammonium chloride (1 mL), concentrated onto

celite 545 (10 g) and purified by silica gel chromatography (85: 15 hexanes: ethyl acetate) to afford a white solid (570 mg, 28 %). R_f = 0.17, 90: 10 hexanes: ethyl acetate. ^{1}H NMR (400 MHz, $CDCl_3$): δ 5.846-5.761 (m, 1H), 5.022-4.920 (m, 2H), 3.584 (s, 1H), 2.070-2.055 (d, 2H), 1.42-1.24 (m, 29H), 0.863 (t, 3H). ESI+: found [$M+NH_4^+$], $C_{19}H_{42}NO^+$: m/z 300.3259, calculated $C_{19}H_{42}NO^+$: m/z 300.3261, ΔPPM = 0.67.

4.5.8.2. Synthesis of nonadec-1-en-6-yl palmitate

To a stirred solution of nonadec-1-en-6-ol (570 mg, 2 mmol, 1 eq.) in DCM (20 mL) was added palmitic anhydride (1.2 g, 2.4 mmol, 1.2 eq.), 4-(dimethylamino)pyridine (122 mg, 1 mmol, 0.5 eq.) and triethylamine (1.1 mL, 8 mmol, 4 eq.). The solution was stirred overnight (16 h) at rt. The reaction was concentrated onto celite 545 (10 g) and purified by silica gel chromatography (90: 10 hexanes: ethyl acetate) to afford a clear, colorless oil (750 mg, 71%). R_f = 0.33, 85: 15 hexanes: ethyl acetate. ^{1}H NMR (400 MHz, $CDCl_3$): δ 5.846-5.761 (m, 1H), 5.022-4.920 (m, 2H), 3.584 (s, 1H), 2.070-2.055 (d, 2H), 1.42-1.24 (m, 29H), 0.863 (t, 3H). ESI+: found [$M+H^+$], $C_{35}H_{69}O_2^+$: m/z 521.5302, calculated $C_{35}H_{69}O_2^+$: m/z 521.5292, ΔPPM = 1.92.

4.5.8.3. Synthesis of 5-PAHSA.

Ozone was bubbled into a stirred solution of nonadec-1-en-6-yl palmitate (104 mg, 0.2 mmol, 1 eq.) in DCM at -78 °C until the solution turned blue, oxygen was then bubbled until the reaction was colorless. Triphenylphosphine (104 mg, 0.4 mmol, 2 eq.) was added and the reaction warmed to rt. The reaction was concentrated after 2 h; sodium hypochlorite (112 mg of 80 % grade stock, 1 mmol, 5 eq.), sodium phosphate monobasic (138 mg, 1 mmol, 5 eq.), 2

methylbut-2-ene (1.6 mL,16 mmol, 80 eq.), water (3.6 mL) and *tert*-butanol (14 mL) were added and the reaction stirred overnight. The reaction was concentrated, taken up in DCM and washed with 10 % HCl in a separatory funnel. The organic layer was dried with sodium sulfate, filtered and rotovaped to yield a waxy solid bordering on oil. The crude product was dissolved in minimal volume of ethyl acetate and purified by silica gel chromatography (80: 20 hexanes: ethyl acetate) to afford a white solid (750 mg, 71%). R_f = 0.33, 85: 15 hexanes: ethyl acetate. ^{1}H NMR (400 MHz, $CDCl_3$): δ 5.846-5.761 (m, 1H), 5.022-4.920 (m, 2H), 3.584 (s, 1H), 2.070-2.055 (d, 2H), 1.42-1.24 (m, 29H), 0.863 (t, 3H). ESI-: found $[M - H]^-$, $C_{34}H_{65}O_4^-$: m/z 537.4905, calculated $C_{34}H_{65}O_4^-$: m/z 537.4888, ΔPPM = 3.16.

Syntheses of additional PAHSAs were performed with the same procedure as 5-PAHSA; the starting materials in section 4.5.8.1 were adjusted based on location of the hydroxylated carbon in the stearic acyl chain.

4.6. References

[1] T.R. Maher, Characterization of the metabolic pathway of a novel lipid family using liquid chromatography-mass spectrometry-based methods, undergraduate thesis, Harvard College, Cambridge, MA, (2010).

[2] A.B. Olokoba, O. Obateru, A., L.B. Olokoba, Type 2 Diabetes Mellitus: A Review of Current Trends, Oman Med. J., 27 (2012) 269-273.

[3] M.A. Herman, B.B. Kahn, Glucose transport and sensing in the maintenance of glucose homeostasis and metabolic harmony, The Journal of Clinical Investigation, 116 (2006) 1767-1775.

[4] A. Guilherme, J.V. Virbasius, V. Puri, M.P. Czech, Adipocyte dysfunctions linking obesity to insulin resistance and type 2 diabetes, Nat Rev Mol Cell Biol, 9 (2008) 367-377.

[5] S.E. Kahn, R.L. Hull, K.M. Utzschneider, Mechanisms linking obesity to insulin resistance and type 2 diabetes, Nature, 444 (2006) 840-846.

[6] D.E. Kelley, B. Goodpaster, R.R. Wing, J.-A. Simoneau, Skeletal muscle fatty acid metabolism in association with insulin resistance, obesity, and weight loss, American Journal of Physiology - Endocrinology and Metabolism, 277 (1999) E1130-E1141.

[7] L. Storlien, N.D. Oakes, D.E. Kelley, Metabolic flexibility, Proceedings of the Nutrition Society, 63 (2004) 363-368.

[8] E. Tozzo, P.R. Shepherd, L. Gnudi, B.B. Kahn, Transgenic GLUT-4 overexpression in fat enhances glucose metabolism: preferential effect on fatty acid synthesis, American Journal of Physiology - Endocrinology and Metabolism, 268 (1995) E956-E964.

[9] P.R. Shepherd, L. Gnudi, E. Tozzo, H. Yang, F. Leach, B.B. Kahn, Adipose cell hyperplasia and enhanced glucose disposal in transgenic mice overexpressing GLUT4 selectively in adipose tissue, Journal of Biological Chemistry, 268 (1993) 22243-22246.

[10] N. Vinayavekhin, E.A. Homan, A. Saghatelian, Exploring Disease through Metabolomics, ACS Chemical Biology, 5 (2009) 91-103.

[11] N. Vinayavekhin, A. Saghatelian, Untargeted Metabolomics, in: Current Protocols in Molecular Biology, John Wiley & Sons, Inc., 2001.

[12] I.J. Kurland, D. Accili, C. Burant, S.M. Fischer, B.B. Kahn, C.B. Newgard, S. Ramagiri, G.V. Ronnett, J.A. Ryals, M. Sanders, J. Shambaugh, J. Shockcor, S.S. Gross, Application of combined omics platforms to accelerate biomedical discovery in diabesity, Annals of the New York Academy of Sciences, 1287 (2013) 1-16.

[13] A. Saghatelian, M.K. McKinney, M. Bandell, A. Patapoutian, B.F. Cravatt, A FAAH-Regulated Class of N-Acyl Taurines That Activates TRP Ion Channels†, Biochemistry, 45 (2006) 9007-9015.

[14] S.U. Bajad, W. Lu, E.H. Kimball, J. Yuan, C. Peterson, J.D. Rabinowitz, Separation and quantitation of water soluble cellular metabolites by hydrophilic interaction chromatography-tandem mass spectrometry, Journal of Chromatography A, 1125 (2006) 76-88.

[15] J.G. McDonald, D.D. Smith, A.R. Stiles, D.W. Russell, A comprehensive method for extraction and quantitative analysis of sterols and secosteroids from human plasma, Journal of Lipid Research, 53 (2012) 1399-1409.

[16] D.M. Cox, F. Zhong, M. Du, E. Duchoslay, T. Sakuma, J.C. McDermott, Multiple Reaction Monitoring as a method for identifying protein posttranslational modifications J. Biomol. Tech., 16 (2005) 83-90.

[17] E.G. Bligh, W.J. Dyer, A Rapid Method of Total Lipid Extraction and Purification, Canadian Journal of Biochemistry and Physiology, 37 (1959) 911-917.

[18] X. Wei, X. Shi, W. Zhong, Y. Zhao, Y. Tang, W. Sun, X. Yin, B. Bogdanov, S. Kim, C. McClain, Z. Zhou, X. Zhang, Chronic Alcohol Exposure Disturbs Lipid Homeostasis at the Adipose Tissue-Liver Axis in Mice: Analysis of Triacylglycerols Using High-Resolution Mass Spectrometry in Combination with In Vivo Metabolite Deuterium Labeling, PLoS ONE, 8 (2013) e55382.

[19] A. Zwir-Ferenc, M. Biziuk, Solid Phase Extraction Technique - Trends, Opportunities and Applications Pol. J. Environ. Stud., 15 (2006) 677-690.

[20] M.Y. Mushtaq, Y.H. Choi, R. Verpoorte, E.G. Wilson, Extraction for Metabolomics: Access to The Metabolome, Phytochemical Analysis, (2014) doi: 10.1002/pca.2505.

[21] D.S. Kelley, G.L. Bartolini, J.W. Newman, M. Vemuri, B.E. Mackey, Fatty acid composition of liver, adipose tissue, spleen, and heart of mice fed diets containing t10, c12-, and c9, t11-conjugated linoleic acid, Prostaglandins, Leukotrienes and Essential Fatty Acids, 74 (2006) 331-338.

[22] E.R. Miraldi, H. Sharfi, R.H. Friedline, H. Johnson, T. Zhang, K.S. Lau, H.J. Ko, T.G. Curran, K.M. Haigis, M.B. Yaffe, R. Bonneau, D.A. Lauffenburger, B.B. Kahn, J.K. Kim, B.G. Neel, A. Saghatelian, F.M. White, Molecular network analysis of phosphotyrosine and lipid metabolism in hepatic PTP1b deletion mice, Integrative Biology, 5 (2013) 940-963.

[23] C.D. Funk, Prostaglandins and Leukotrienes: Advances in Eicosanoid Biology, Science, 294 (2001) 1871-1875.

[24] J.I. Odegaard, A. Chawla, Pleiotropic Actions of Insulin Resistance and Inflammation in Metabolic Homeostasis, Science, 339 (2013) 172-177.

[25] D.Y. Oh, S. Talukdar, E.J. Bae, T. Imamura, H. Morinaga, W. Fan, P. Li, W.J. Lu, S.M. Watkins, J.M. Olefsky, GPR120 Is an Omega-3 Fatty Acid Receptor Mediating Potent Anti-inflammatory and Insulin-Sensitizing Effects, Cell, 142 687-698.

[26] M.J. Sánchez-Martín, E. Ramon, J. Torrent-Burgués, P. Garriga, Improved Conformational Stability of the Visual G Protein-Coupled Receptor Rhodopsin by Specific Interaction with Docosahexaenoic Acid Phospholipid, ChemBioChem, 14 (2013) 639-644.

[27] A.D. Mancini, V. Poitout, The fatty acid receptor FFA1/GPR40 a decade later: how much do we know?, Trends in Endocrinology & Metabolism, 24 398-407.

[28] M.A. Herman, O.D. Peroni, J. Villoria, M.R. Schon, N.A. Abumrad, M. Bluher, S. Klein, B.B. Kahn, A novel ChREBP isoform in adipose tissue regulates systemic glucose metabolism, Nature, 484 (2012) 333-338.

[29] E.A. Homan, Y.-G. Kim, J.P. Cardia, A. Saghatelian, Monoalkylglycerol Ether Lipids Promote Adipogenesis, Journal of the American Chemical Society, 133 (2011) 5178-5181.

[30] C.A. Smith, E.J. Want, G. O'Maille, R. Abagyan, G. Siuzdak, XCMS: processing mass spectrometry data for metabolite profiling using nonlinear peak alignment, matching, and identification, Anal. Chem., 78 (2006) 779–787.

[31] M.K. Moe, M.B. Strøm, E. Jensen, M. Claeys, Negative electrospray ionization low-energy tandem mass spectrometry of hydroxylated fatty acids: a mechanistic study, Rapid Communications in Mass Spectrometry, 18 (2004) 1731-1740.

Appendix Chapter 1

Oxysterol metabolism in the absence of the Sonic hedgehog receptor Patched1

A1.1. Introduction

The Sonic hedgehog (Shh) pathway plays critical roles in cellular proliferation, development and stem cell function [1]. Shh signaling occurs through a series of repressive interactions [1-3]. In the absence of the secreted protein Shh, the 12-pass transmembrane receptor Patched1 (Ptc1) inactivates the 7-pass transmembrane receptor Smoothened (Smo); Shh binding to Ptc1 inhibits the latter and leads to Smo activation [1-3]. Smo inhibits Suppressor of Fused (SuFu), leading to downstream transcription *via* the Gli family of transcription factors [1-3]. Mutations in Shh signaling are associated with cancer and severe developmental defects in mice and humans [1, 4].

While key protein components of the Shh pathway have been identified, detailed mechanism of Ptc1 inhibition of Smo remains unclear [1, 5]. Shh treatment of murine fibroblasts induced Smo translocation into and Ptc1 disappearance from primary cilia, signal-sensing cell surface projections found on most vertebrate cells [6]; Smo translocation places Smo at the correct location for downstream signaling given presence of SuFu and Gli at the cilia [1, 6]. Importantly, oxygenated derivatives of cholesterol (oxysterols) with diverse functions in apoptosis, receptor signaling and platelet aggregation [7] have been shown to activate Shh signaling [1, 6, 8]. 20S-hydroxycholesterol (20S-OHC) induced Smo translocation into primary cilia [6] and significantly increased Shh signaling in a Shh luciferase reporter assay [9]; 25-OHC increased *Ptc1-LacZ* reporter activity in meduloblastomas isolated from mice with one copy of *Ptc1* replaced by *LacZ* [8]. More recently, use of affinity probes revealed binding of 20S-OHC and the 20S-OHC inhibitor 22-azacholesterol to the extracellular, cysteine-rich domain of Smo [5], a separate site from Smo's heptahelical bundle binding site that is the target of many small molecule Smo activators and inhibitors including SAG and cyclopamine [5, 10-12].

Two models for oxysterol-Shh pathway interactions have been proposed (Figure A1.1). Structural similarity of Smo to G-protein coupled receptors (GPCRs) and study of GPCR kinetics support existence of Smo in an active or inactive conformational state with different cellular localization [1, 13, 14] (Figure A1.1); Ptc1 inhibition leads to Smo activation and movement into the primary cilia, while inactive Smo is carried in intracellular vesicles [1, 15] (Figure A1.1). Ptc1 could inhibit Smo downstream signaling by down-regulating oxysterols that activate Smo (Figure A1.1, Model A); alternatively, oxysterols could activate the Shh pathway *via* direct Ptc1 inhibition (Figure A1.1, Model B). Oxysterol activation of Shh signaling in Ptc1-deficient cells and oxysterol-Smo binding support Model A [5, 8, 9]; however, Ptc1 also possesses a sterol-sensing domain necessary for regulation of Smo activity [16].

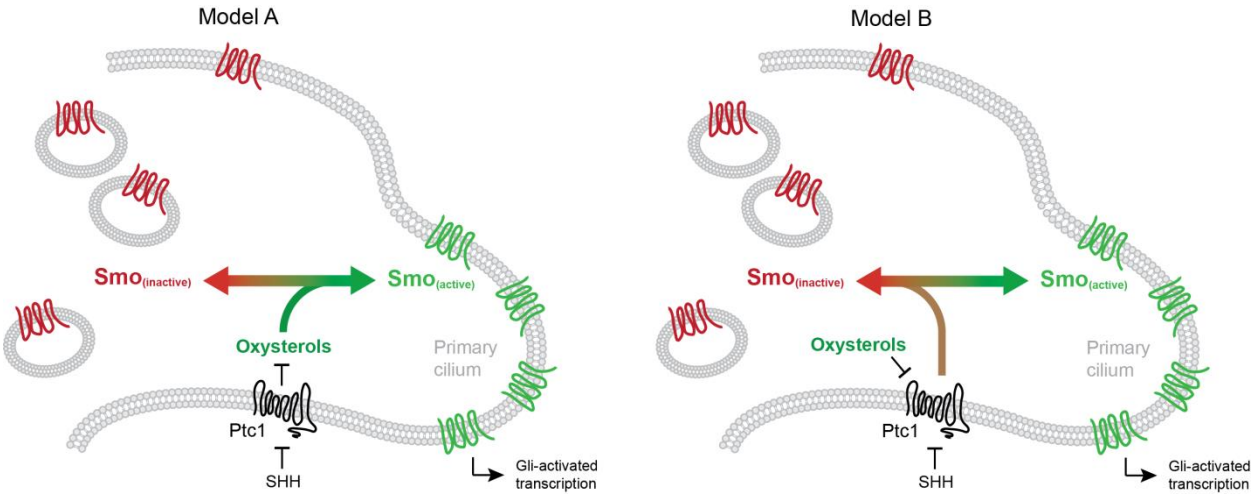

Figure A1.1. Two models for oxysterol-Shh pathway interactions. Models were adapted from Rothatgi *et al.* [1].

While dependence of Shh signaling on oxysterols has been demonstrated in multiple settings, the majority of methods involved treatment with exogenous oxysterols [5, 8, 9]. Consequently, effects of Shh activation or absence of key components of the Shh pathway on endogenous sterol levels remain unknown; evaluation of sterol profile in the absence of Ptc1

could yield valuable information on potential Ptc1 regulation of sterol metabolism, and help distinguish between the two models proposed in Figure A1.1. To address this important question, we performed targeted liquid chromatography (LC)–mass spectrometry (MS) analysis in WT and *Ptc1*$^{-/-}$ mouse embryonic fibroblasts (MEFs) using the method developed by McDonald *et al.* [17], which enables sensitive quantification of a wide range of sterols from one biological sample [17]. Our analysis revealed changes in levels of multiple oxysterols in the absence of Ptc1, suggesting that Ptc1 regulates Shh signaling through modulation of oxysterol metabolism.

A1.2. Results and discussions

WT and *Ptc1*$^{-/-}$ mouse embryonic fibroblasts (MEFs) and media from these cells were extracted with slight modifications on the Bligh-Dyer method [18]. We chose to profile both cells and media to determine if oxysterols could be released from cells. Solid phase extraction removed nonpolar metabolites such as cholesterol esters and triglycerides, enriching sterols for LC–MS [17]. A workflow is illustrated in Figure A1.2.

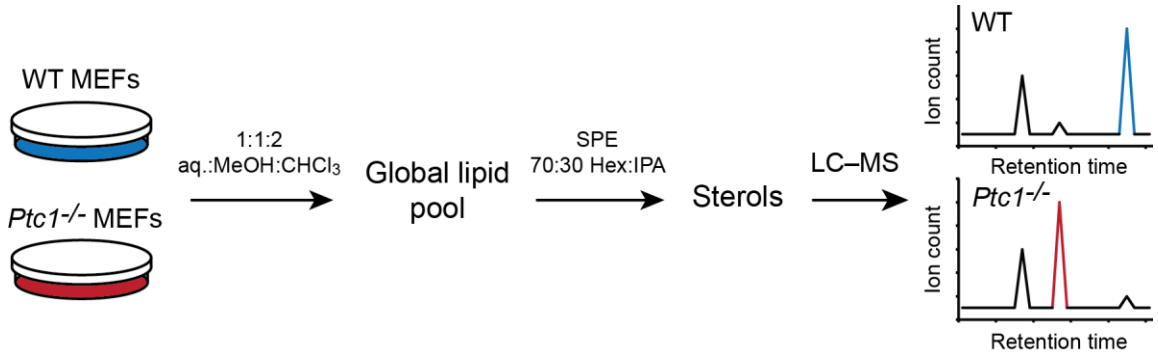

Figure A1.2. Workflow for sterol analysis.

Targeted LC–MS was performed based on the method of McDonald *et al.* on a triple quadrupole mass spectrometer operated in multiple reaction monitoring (MRM) mode [17]. As

stated in previous chapters, MRM quantifies characteristic product ions consistently generated from targeted precursor ions based on fragmentation parameters optimized for each precursor. Common sterol structures and precursor-to-product ion transitions with instrument parameters are in Figure A1.3A, B [17]. Targeted sterols include hydroxycholesterols, epoxycholesterols, ketocholesterol, cholesterol and cholesterol biosynthetic intermediates (Figure A1.3A, B). Either the $[M + H]^+$ or $[M + NH_4]^+$ species was monitored as the precursor ion [17]. Common fragmentation pathways include loss of ammonia and/or water [17].

Predicted fragment structures for 25-OHC are in Figure A1.3C. Ammonium adduct of 25-OHC ($[M + NH_4]^+$, precursor ion m/z 420.4) undergoes loss of ammonia and/or water to yield $[M + H]^+$ (m/z 402.4), $[M - H_2O + H]^+$ (m/z 385.3) and $[M - 2H_2O + H]^+$ (m/z 367.3) fragments [17, 19, 20]. Multiple fragmentation pathways translate to multiple precursor-to-product ion transitions (m/z 420 → 367, m/z 420 → 385 and m/z 385 → 367 were included in the method of McDonald *et al.*; m/z 385 → 367 could also be used to monitor some cholesterol biosynthetic intermediates) for each OHC; appearance of peaks corresponding to different transitions at the same retention time adds confidence to the OHC structure assignment. In agreement with instrument parameters used by McDonald *et al.*, intensity of the ammonium adduct is highly dependent on dry gas temperature [17]. In our optimization, stepwise reduction of drying gas temperature from 350 °C to 100 °C led to a corresponding increase in the strength of the ammonium adduct for $^2H_7$-cholesterol and all OHC standards examined. Figure A1.4A illustrates the scan spectra for $^2H_7$-cholesterol at 350 °C and 100 °C. Ammonium adduct (m/z 411.4) was clearly detected at 100 °C; the sodium adduct (m/z 416.4) present at higher temperatures could not be used as MRM precursor ion due to generation of a neutral product following loss of sodium ion during fragmentation. No drying gas temperatures below 100 °C

A

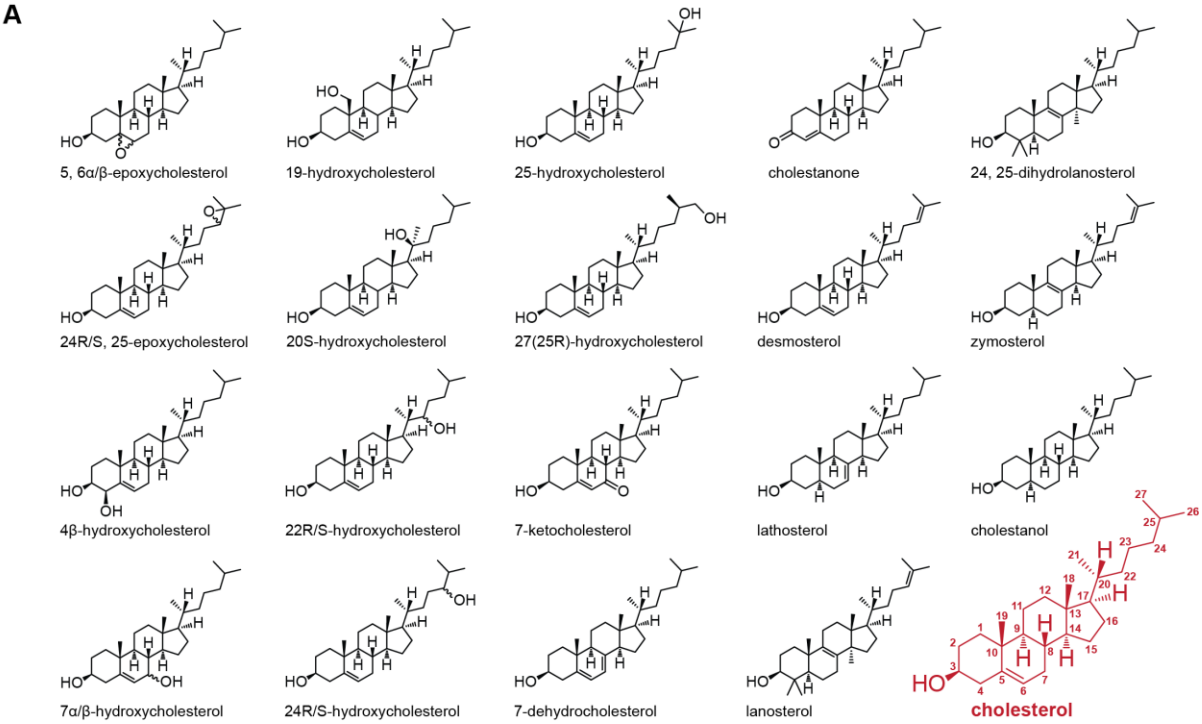

B

Major sterol(s) targeted	Precursor Ion	Product Ion	Dwell	DP (V)	CE (V)
Hydroxy/epoxycholesterols	420.4	367.3	110	50	15
Hydroxy/epoxycholesterols	420.4	385.3	110	50	15
Hydroxy/epoxycholesterols, chol. intermediates	385.3	367.3	110	50	15
Hydroxy/epoxycholesterols, chol. intermediates	385.3	367.3	110	85	15
24, 25-Epoxycholesterol	418.4	383.3	110	45	12
7-Ketocholesterol	401.3	383.3	110	80	35
Desmosterol	402.4	367.3	110	55	20
Cholesterol/lathosterol	404.4	369.4	110	110	13
$^{2}H_{7}$-Cholesterol	411.4	376.4	110	110	13
Cholestanol	406.4	371.4	110	110	13
Lanosterol	444.4	409.4	110	80	15
24-Dihydrolanosterol	429.4	411.4	110	100	17

C

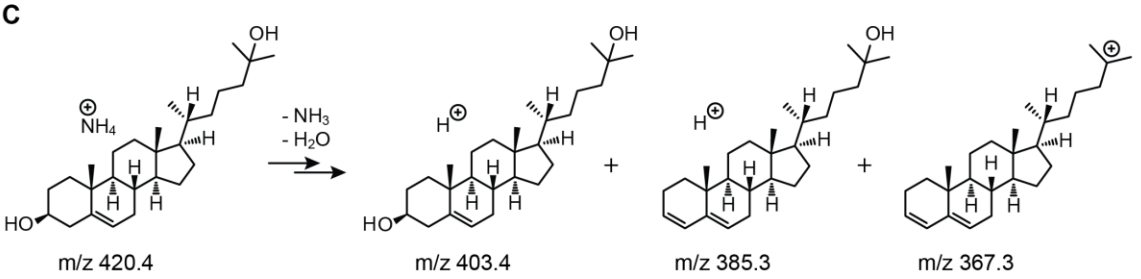

Figure A1.3. MRM analysis of sterols. A) Structures of common sterols. Structure of cholesterol with positional numbering is in red [17]. B) MRM transitions and instrument parameters for common sterols; parameters are taken from the method of McDonald *et al.* [17]. C) Predicted fragment structures for 25-hydroxycholesterol.

were tested due to inclusion of water in our solvent system, which could not be removed efficiently at lower temperatures.

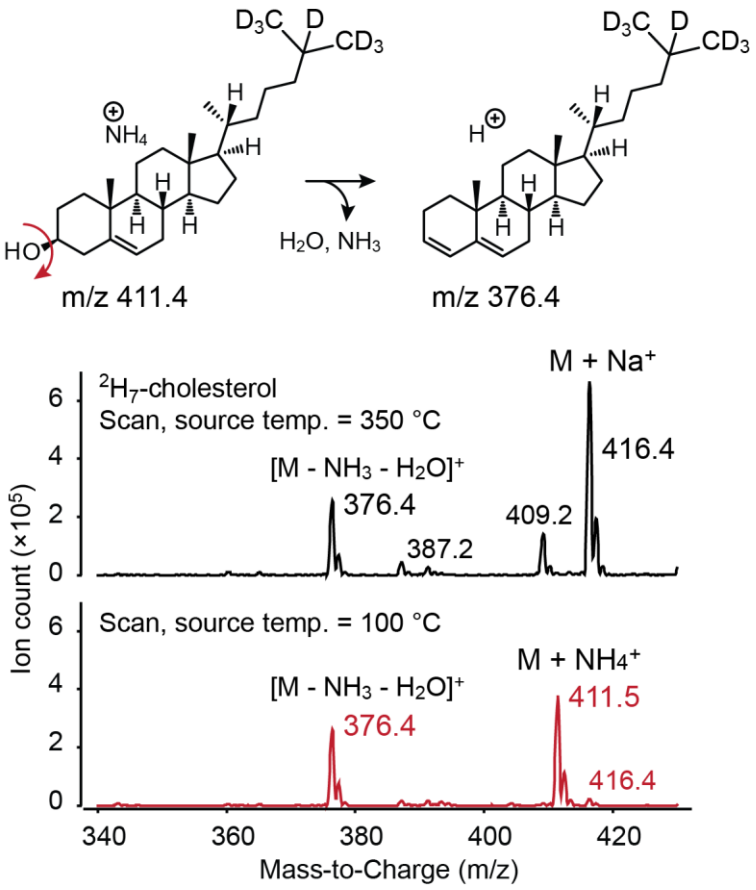

Figure A1.4. Effect of drying gas temperatures on $^{2}H_{7}$-cholesterol adducts formation.

Sterol profiles from WT and *Ptc1*$^{-/-}$ MEFs and media were evaluated by LC–MS using the transitions in Figure A1.3B. WT and *Ptc1*$^{-/-}$ extracted ion chromatographs (EICs) for each transition were overlaid, and changing peaks identified and integrated manually. For majority of transitions multiple peaks were observed (data not shown), a likely consequence of the diversity of sterols with slight differences in structure and identical fragmentation mechanisms. While losses of ammonia and water are common fragmentation pathways that could be shared by

multiple sterols, fragmentation within sterol rings, which could yield more information on subtle structural differences, is difficult due to the former's relative stability, which requires high collision energies and often generates inconsistent product ions [19, 21].

Of all transitions monitored, the largest number of statistically significant *Ptc1*$^{-/-}$-WT changes was present in the m/z 420 → 367 transition, corresponding to loss of ammonia and two water molecules from the ammonium adduct of OHC. This is in keeping with evidences supporting a role for OHCs in Shh signaling [1]. Overlaid m/z 420 → 367 spectra for WT and *Ptc1*$^{-/-}$ media (WT in black, *Ptc1*$^{-/-}$ in red) are in Figure A1.5; four consistent metabolite changes are present at 20.3 min (WT-elevated), 22.2 min (*Ptc1*$^{-/-}$ -elevated), 22.6 min (WT-elevated) and 28.8 min (*Ptc1*$^{-/-}$ -elevated). Similar changes were observed for cells (data not shown). Retention time comparison with OHC standards suggests that the 22.2 min and 22.6 min metabolites are 24S and 25-OHC, respectively; no matches were found for the 20.3 min and 28.8 min metabolites (Figure A1.5).

While retention time comparison between sample and external standards could facilitate structure assignment, retention time drifts across multiple sample runs hamper retention time alignment. Consequently, confirmation of structure requires co-elution of comparable quantities of sample and standard to yield one peak. To perform co-elution with 24S and 25-OHC standards, the chromatographic method from McDonald *et al.* was lengthened to increase separation among OHCs [17]. EICs for 20S, 22R/S, 24R/S, 25 and 27-OHC standards with the lengthened LC method are in Figure A1.6; close to baseline resolution allows co-elution for 24S and 25-OHCs to be carried out with minimal interference from adjacent peaks.

It is worth noting that for majority of standards, appearance of peaks corresponding to all three OHC transitions (m/z 420 → 367, m/z 420 → 385 and m/z 385 → 367) increases the confidence of identification (Figure A1.6) [17]. Relative intensities of OHC transitions depend

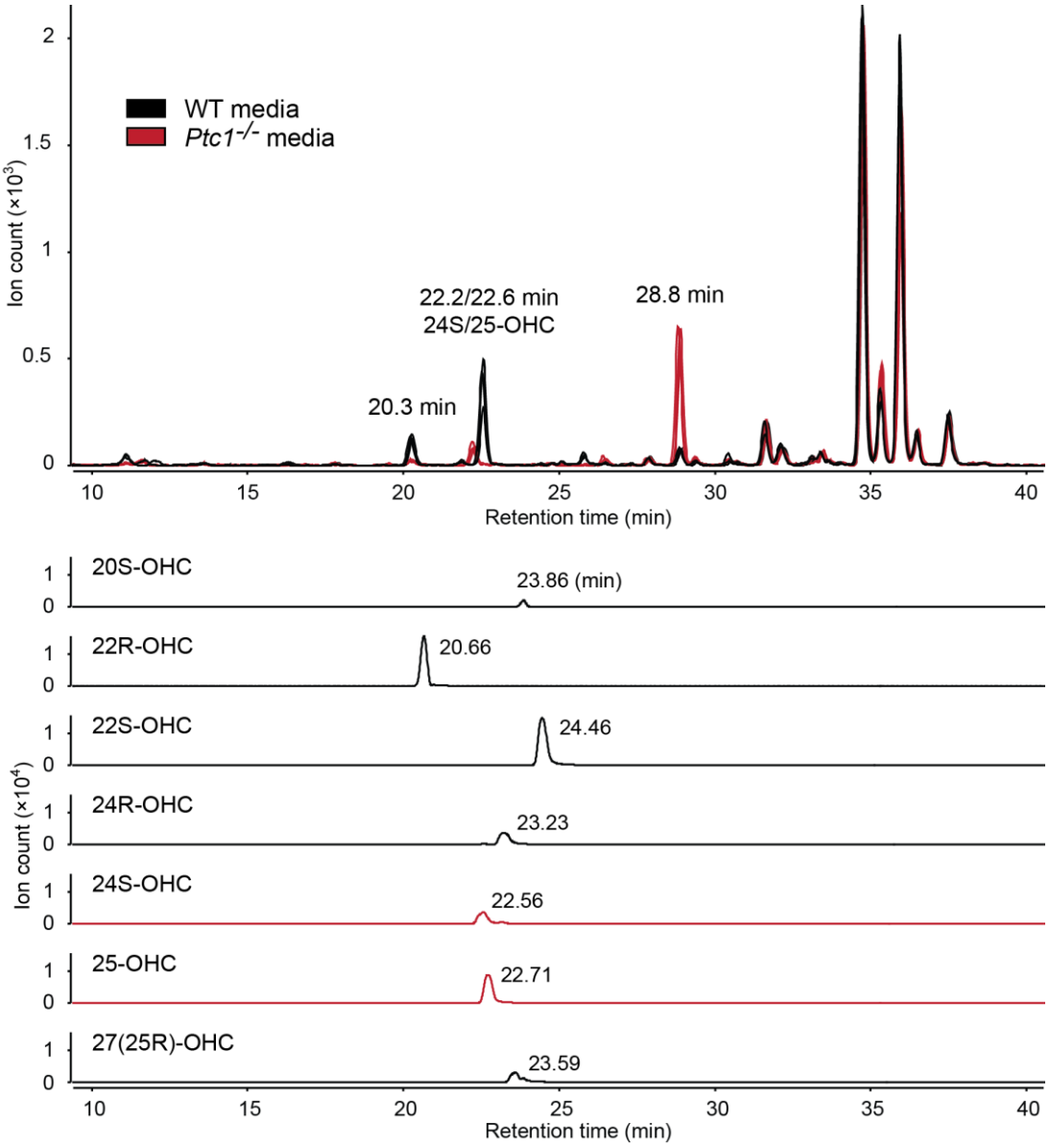

Figure A1.5. Altered hydroxysterol profile in the absence of Ptc1. m/z 420.4 → m/z 367.3 extracted ion chromatographs of WT and *Ptc1*$^{-/-}$ media are overlaid and changing peaks identified and integrated manually. Retention time comparison with external standards suggests that the 22.2 min and 22.6 min peaks are 24S and 25-hydroxycholesterol, respectively.

on position of hydroxylation; while the major transition for 22R/S, 24R/S and 25-OHCs is m/z 420 → 367, m/z 385 → 367 and m/z 420 → 385 are the major transitions for 20S and 27-OHC, respectively (Figure A1.6). Discrepancy in the major transition observed is a consequence of differences in relative stabilities of the m/z 420, m/z 385 and m/z 367 ions in different OHCs. Prevalence of the m/z 420 →385 transition (loss of one ammonia and one water) in 27-OHC could be due to unfavorable loss of the second hydroxyl group at carbon 27, which generates a primary cation (Figure A1.3A). Prevalence of the m/z 385 → 367 transition in 20S-OHC implies the major precursor ion is m/z 385 rather than the unfragmented ammonium adduct m/z 420, suggesting in-source fragmentation of the m/z 420 ion to m/z 385, which then undergoes collision-induced dissociation (CID) to yield the m/z 367 product ion; ready formation of the m/z 385 ion in the absence of CID suggests that the hydroxyl group at carbon 20 could be significantly more labile than other locations, which could be explained by stability of the resulting tertiary cation following fragmentation (Figure A1.3A).

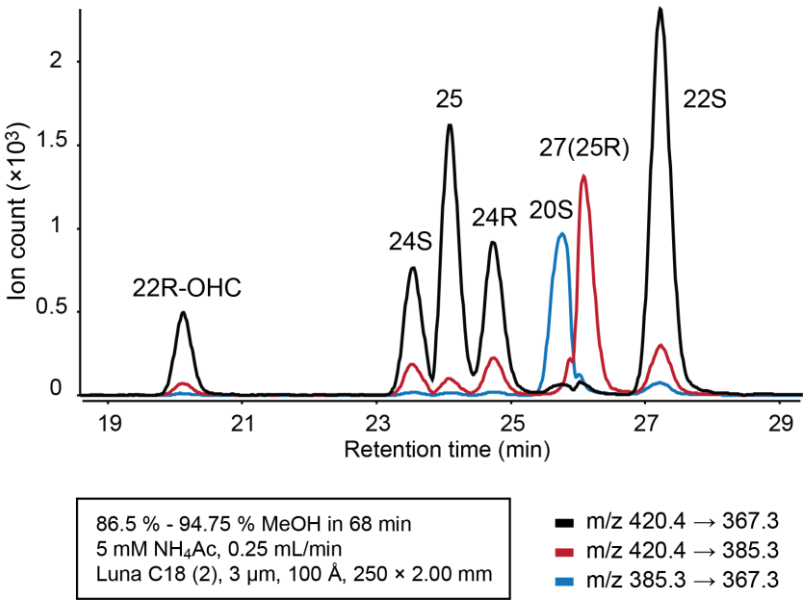

Figure A1.6. Chromatographic resolution of OHC standards. Gradient was optimized based on the LC method of McDonald *et al.* [17].

Co-injection was performed with the lengthened LC method by combining endogenous sample with either the 24S or 25-OHC standard, yielding one peak in both cases (Figure A1.7A).

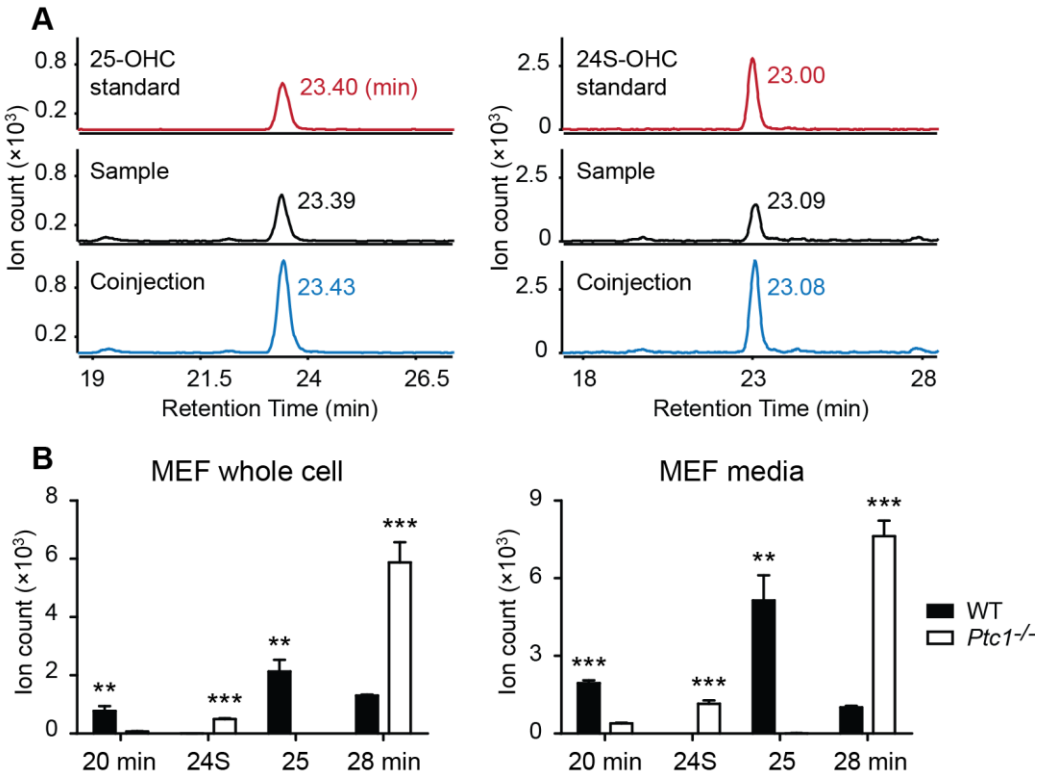

Figure A1.7. Structure confirmation and relative quantification of OHCs in WT and *Ptc1*$^{-/-}$ MEFs and media. A) Co-injection of sample with 24S or 25-hydroxycholesterol. B) Relative quantification of 24S-hydroxcholesterol, 25-hydroxycholesterol and unidentified hydroxycholesterols or related species in WT and *Ptc1*$^{-/-}$ MEFs and media.

Taken together, our data demonstrate down-regulation of 25-OHC and upregulation of 24S-OHC, as well as changes in two additional unidentified OHCs or related species, in *Ptc1*$^{-/-}$ media and cells relative to WT (Figure A1.7B). Observations of similar changes in cells and media suggest that OHCs could be released or trafficked across the plasma membrane as signaling lipids. Importantly, our findings demonstrate altered oxysterol metabolism in the absence of Ptc1, supporting model A (Figure A1.1) of oxysterols-Shh pathway interactions where Ptc1 inhibits

Smo through modulation of oxysterol levels and/or metabolism. 25-OHC has been shown to stimulate Shh signaling in multiple contexts [8, 9]; down-regulation of this species in *Ptc1*$^{-/-}$ MEFs could be a compensatory mechanism to reduce Shh signaling and excessive cellular proliferation. Alterations in different OHCs and OHC-related metabolites in the absence of Ptc1 also implies Ptc1 could regulate Shh signaling by tuning the ratios of distinct OHC pools depending on the homeostatic need of the cell; it might also be possible for some OHC populations to interact with Ptc1 as part of a Ptc1-sterol feedback loop. Identification of unknown OHCs and comprehensive analysis of sterol metabolism in the context of Shh pathway activation could yield addition information on the roles of different sterols in Shh signaling.

A1.3. Conclusion

Comparative lipidomics uncovered altered sterol profile in MEFs and MEF media in the absence of the Sonic hedgehog (Shh) receptor Ptc1, in agreement with previous findings supporting requirement of Shh signaling for sterol biosynthesis and roles of several oxysterols in Shh pathway activation [1, 5, 8]. Targeted LC–MS with slight modifications on the method of McDonald *et al.* enabled detection of a wide range of sterols including cholesterol, cholesterol biosynthetic intermediates, hydroxy, epoxy and ketocholesterols [17]. Our analysis uncovered down-regulation of 25-OHC and upregulation of 24S-OHC in *Ptc1*$^{-/-}$ MEFs and media relative to WT. Our findings suggest that Ptc1 could inhibit Smo downstream signaling by modulating cellular oxysterol distribution. Identification of additional altered sterols and evaluation of sterol metabolism and sterol-protein interactions in the context of Shh pathway activation could yield valuable information on the detailed connection between small molecules and proteins in the Sonic hedgehog pathway.

A1.4. Methods

A1.4.1. Materials

Ammonium acetate (372331) was from Sigma-Aldrich. Water (365-4), methanol (230-4), toluene (347-1L), isopropanol (323-4), hexane (212-4), chloroform (049-1L) and solid phase extraction cartridges (9050, 100 mg silica, 1 mL) were from Honeywell Burdick & Jackson. 22R-OHC (700058), 22S-OHC (700057), 24R-OHC (700071), 24S-OHC (700061), 25-OHC (700019), 27(25R)-OHC (700021), 7-ketocholesterol (700015), 5α, 6α-epoxycholesterol (700032) and 5β, 6β-epoxycholesterol (700033) were from Avanti Polar Lipids. 20α-OHC (sc-209393) was from Santa Cruz Biotechnologies.

A1.4.2. Tissue culture and harvest

Mouse embryonic fibroblasts (MEFs) and media for metabolite profiling were prepared by Dr. Yu Wang and Dr. Sherry Zhang at the laboratory of Prof. Andrew McMahon. MEFs were maintained in 5 % CO_2 at 37 °C in Phenyl Red-containing Dulbecco's Modified Eagle's Medium supplemented with 10 % fetal bovine serum, penicillin and streptomycin. Phenol Red-free media were used for media profiling to prevent dye contamination of LC–MS. Cells were harvested by scraping, and pellets frozen at -80 °C prior to lipid extraction. Media were removed from culture dishes, centrifuged to pellet residual cell debris and the supernatants frozen in 15 mL Falcon tubes at -80 °C prior to extraction.

A1.4.3. Lipid extraction

Lipids were extracted from MEFs (~10^7 cells from 10 cm dish) with slight modification on the Bligh-Dyer method [18]. Pellets were either Dounce homogenized 30-40 times on ice or

shaken for 30 s at room temperature (comparable extraction efficiencies were observed for the two methods by LC–MS [data not shown]) in 1 mL:1 mL:2 mL phosphate buffered saline:methanol:chloroform, vortexed (in glass vials) for 15-30 s and centrifuged at 2200 g, 4 °C for 6 min to allow separation between aqueous (top) and organic (bottom) layers. The organic fraction was transferred to a new glass vial and dried under a gentle stream of nitrogen. Dried lipids were either immediately taken through solid phase extraction or stored at -80 °C for no more than one week prior to solid phase extraction. Media were thawed at room temperature and extracted immediately upon thawing. 7-8 mL media were transferred into a glass vial on ice, followed by addition of 7-8 mL methanol and 14-16 mL chloroform. The resulting mixture was shaken for 30 s at room temperature, vortexed for 15-30 s and processed following identical procedure as cells. Internal standards were added to chloroform prior to extraction.

A1.4.4. Solid phase extraction

Solid phase extraction was performed based on known protocol [17]. Lipids from MEFs (~10^7 cells) or media (7-8 mL) were reconstituted in 1 mL toluene. Solid phase extraction cartridge (100 mg silica, 1 mL) was conditioned with 2 mL hexane. Lipids in 1 mL toluene were loaded onto column with a gentle vacuum. Nonpolar lipids such as triglycerides and cholesterol esters were eluted dropwise (~2-3 drops per s) with 1 mL hexane. Sterols were eluted dropwise (~2-3 drops per s) with 8 mL 30 % isopropanol in hexane. The sterol fraction was dried under a gentle stream of nitrogen and reconstituted in methanol for LC–MS.

A1.4.5. LC–MS

Targeted analysis of sterols was performed with an Agilent 1200 series LC online with an Agilent 6410 Triple Quad LC/MS with an ESI source in positive ionization mode, with slight modifications on the protocol of McDonald *et al.* [17, 19]. A Luna C18 (2) (Phenomenex, 00G-4251-B0) column with an in-line filter (Phenomenex, AF0-8497) was used. Solvent A was 15: 85 water: methanol with 5 mM ammonium acetate and solvent B was methanol with 5 mM ammonium acetate. The gradient was held at 0 % B between 0 and 2 min, increased linearly from 0 % B to 100 % B between 2 min and 35 min, held at 100 % B between 35 min and 55 min, returned to 0 % B at 55.1 min and held at 0 % B between 55.1 min and 68 min to allow column re-equilibration. Flow rate was 0.25 mL/min. Each sample (from 7-8 mL media or ~10^7 MEFs) was reconstituted in 30-40 μL methanol, and 10 μL injected for analysis. All transitions, dwell times, DP and CE are listed in Figure A1.3. Skimmer voltage was 15 V and ΔEMV was 400 V. MS1 resolution was set to Wide and MS2 resolution to Unit. Capillary voltage was 4.0 kV, drying gas temperature was 100 °C, drying gas flow rate was 8 L min^{-1} and nebulizer pressure was 35 psi.

For data analysis, extracted ion chromatographs of WT and *Ptc1*$^{-/-}$ replicates for each transition were overlaid, and peaks changing between WT and *Ptc1*$^{-/-}$ groups manually identified and integrated. Statistical significance was determined *via* two-tailed Student's t test. All errors were standard errors of the mean.

A1.4.6. Co-injection

For co-injection, the LC runtime from section A1.4.5 was lengthened to improve resolution of oxysterols. Solvent A was 15: 85 water: methanol with 5 mM ammonium acetate

and solvent B was methanol with 5 mM ammonium acetate. The gradient was held at 10 % B between 0 and 2 min, increased linearly from 10 % B to 65 % B between 2 min and 70 min, held at 65 % B between 70 min and 90 min, returned to 10 % B at 90.1 min and held at 10 % B between 90.1 min and 105 min to allow column re-equilibration. Flow rate was 0.25 mL/min. A mixture of sample and standard in 8 μL methanol was injected. All instrument parameters were identical to section A1.4.5, with the exceptions that only the four transitions for Hydroxy/epoxycholesterols and Hydroxy/epoxycholesterols, cholesterol derivatives (Figure A1.3) were included, and dwell time was raised to 200 ms for each transition.

A1.5. References

[1] R. Rohatgi, M.P. Scott, Patching the gaps in Hedgehog signalling, Nat Cell Biol, 9 (2007) 1005-1009.

[2] Y. Wang, A.P. McMahon, B.L. Allen, Shifting paradigms in Hedgehog signaling, Current Opinion in Cell Biology, 19 (2007) 159-165.

[3] J.E. Hooper, M.P. Scott, Communicating with Hedgehogs, Nat Rev Mol Cell Biol, 6 (2005) 306-317.

[4] A.E. Bale, Hedgehog Signaling and Human Disease, Annual Review of Genomics and Human Genetics, 3 (2002) 47-65.

[5] D. Nedelcu, J. Liu, Y. Xu, C. Jao, A. Salic, Oxysterol binding to the extracellular domain of Smoothened in Hedgehog signaling, Nat Chem Biol, 9 (2013) 557-564.

[6] R. Rohatgi, L. Milenkovic, M.P. Scott, Patched1 Regulates Hedgehog Signaling at the Primary Cilium, Science, 317 (2007) 372-376.

[7] G.J. Schroepfer, Oxysterols: Modulators of Cholesterol Metabolism and Other Processes, Physiological Reviews, 80 (2000) 361-554.

[8] R.B. Corcoran, M.P. Scott, Oxysterols stimulate Sonic hedgehog signal transduction and proliferation of medulloblastoma cells, Proceedings of the National Academy of Sciences, 103 (2006) 8408-8413.

[9] S. Nachtergaele, L.K. Mydock, K. Krishnan, J. Rammohan, P.H. Schlesinger, D.F. Covey, R. Rohatgi, Oxysterols are allosteric activators of the oncoprotein Smoothened, Nat Chem Biol, 8 (2012) 211-220.

[10] J.K. Chen, J. Taipale, K.E. Young, T. Maiti, P.A. Beachy, Small molecule modulation of Smoothened activity, Proceedings of the National Academy of Sciences, 99 (2002) 14071-14076.

[11] M. Frank-Kamenetsky, X. Zhang, S. Bottega, O. Guicherit, H. Wichterle, H. Dudek, D. Bumcrot, F. Wang, S. Jones, J. Shulok, L. Rubin, J. Porter, Small-molecule modulators of Hedgehog signaling: identification and characterization of Smoothened agonists and antagonists, Journal of Biology, 1 (2002) 10.

[12] J.K. Chen, J. Taipale, M.K. Cooper, P.A. Beachy, Inhibition of Hedgehog signaling by direct binding of cyclopamine to Smoothened, Genes & Development, 16 (2002) 2743-2748.

[13] J. Taipale, J.K. Chen, M.K. Cooper, B. Wang, R.K. Mann, L. Milenkovic, M.P. Scott, P.A. Beachy, Effects of oncogenic mutations in Smoothened and Patched can be reversed by cyclopamine, Nature, 406 (2000) 1005-1009.

[14] A. De Lean, J.M. Stadel, R.J. Lefkowitz, A ternary complex model explains the agonist-specific binding properties of the adenylate cyclase-coupled beta-adrenergic receptor, Journal of Biological Chemistry, 255 (1980) 7108-7117.

[15] Y. Nakano, S. Nystedt, A.A. Shivdasani, H. Strutt, C. Thomas, P.W. Ingham, Functional domains and sub-cellular distribution of the Hedgehog transducing protein Smoothened in Drosophila, Mechanisms of Development, 121 (2004) 507-518.

[16] V. Martín, G. Carrillo, C. Torroja, I. Guerrero, The sterol-sensing domain of Patched protein seems to control Smoothened activity through Patched vesicular trafficking, Current Biology, 11 601-607.

[17] J.G. McDonald, B.M. Thompson, E.C. McCrum, D.W. Russell, Extraction and Analysis of Sterols in Biological Matrices by High Performance Liquid Chromatography Electrospray Ionization Mass Spectrometry, in: H.A. Brown (Ed.) Methods in Enzymology, vol. Volume 432, Academic Press, 2007, pp. 145-170.

[18] E.G. Bligh, W.J. Dyer, A Rapid Method of Total Lipid Extraction and Purification, Canadian Journal of Biochemistry and Physiology, 37 (1959) 911-917.

[19] J.G. McDonald, D.D. Smith, A.R. Stiles, D.W. Russell, A comprehensive method for extraction and quantitative analysis of sterols and secosteroids from human plasma, Journal of Lipid Research, 53 (2012) 1399-1409.

[20] M.K. Pulfer, C. Taube, E. Gelfand, R.C. Murphy, Ozone Exposure in Vivo and Formation of Biologically Active Oxysterols in the Lung, Journal of Pharmacology and Experimental Therapeutics, 312 (2005) 256-264.

[21] V. Wewer, I. Dombrink, K. vom Dorp, P. Doermann, Quantification of sterol lipids in plants by quadrupole time of flight mass spectrometry, Journal of Lipid Research, (2011).